QUANTITATIVE STRUCTURE-FLUX RELATIONSHIPS OF MEMBRANE DISTILLATION MATERIALS FOR WATER DESALINATION

Submitted in partial fulfillment of the requirements for the degree of

DOCTOR OF PHILOSOPHY

in

CIVIL AND ENVIRONMENTAL ENGINEERING

Megan E. Leitch

B.S. Mechanical Engineering, Yale University
M.S. Civil and Environmental Engineering, Carnegie Mellon University

Carnegie Mellon University
Pittsburgh, PA 15213

May 2016

ABSTRACT

Membrane distillation (MD) is an emergent water desalination technology with potential for scalable, sustainable production of fresh water from highly concentrated brines. Wider adoption of MD technology depends upon improvements to process efficiency. In recent years, researchers have published a number of experimental papers seeking to improve mass and heat transport properties of MD membranes. However, an imperfect understanding of how intrinsic membrane geometry affects MD performance limits efforts to optimize membrane structure.

The objective of this dissertation is to help elucidate effects of membrane structure on MD flux, permeability, and thermal performance, with a focus on novel fibrous membranes. Mechanistic and empirical modeling methods were employed to relate the structural characteristics of bacterial nanocellulose and electrospun polymeric membranes to experimentally-measured MD performance. Through these experimental and modeling studies, three conclusions are reached.

First, the MD community can hasten the search for optimal membrane structures by improving the quality and reproducibility of reported experimental data. Review of published and newly-collected MD data shows that feed and permeate stream channel geometry and flow non-idealities can substantially affect measured performance metrics for MD membranes. If these factors are accounted for by careful characterization of convective heat transfer coefficients, membrane permeability and thermal efficiency can be definitively deduced. A new methodology is presented for determining convective heat transfer coefficient using experimentally-validated Nusselt correlations. Accurate reporting of cassette heat transfer metrics will facilitate inter-study experimental reproducibility and comparison.

Second, use of dimensional analysis to empirically model MD transport is effective for predicting vapor flux in fibrous membranes. Advantages of the model include its use of easily-measurable structural parameters tailored specifically for fibrous membranes and the incorporation of all relevant vapor, membrane, and system characteristics into a mathematically simple, yet theoretically sound, regression model. The new model predicts MD flux more accurately than the mechanistic Dusty Gas Model or previously published empirical MD models. Dimensional-analysis-based transport models may be generalizable for a variety of novel membrane types, lead to a more rigorous understanding of structural influences on vapor transport processes, and guide the development of high-performance membrane structures.

Finally, MD process efficiency can benefit by development of highly porous, scalable membrane materials. Bacterial nanocellulose aerogel membranes exhibit substantial improvements in intrinsic permeability and thermal efficiency as compared to traditional phase-inversion membranes, suggesting that there is an opportunity to advance MD process viability through improved membrane design. By mimicking the porosity and pore-interconnectivity of nanocellulose aerogels, novel membrane materials can achieve high thermal efficiency and low mass transport resistance.

This dissertation contributes experimental data and modeling techniques to improve knowledge of membrane structural effects on MD performance. These contributions have implications for the wider adoption of MD technology through better reproducibility of published experimental results, enhanced transport modeling to optimize membrane structure, and demonstrated thermal efficiency of a highly porous materials.

ACKNOWLEDGEMENTS

There are many people and agencies to thank for their support of my doctoral research. First, I'd like to acknowledge the generous monetary aid provided by federal and private sources. The Post-9/11 GI Bill, the National Science Foundation (NSF) Graduate Research Fellowship Program, and the NSF Integrative Graduate Education and Research Traineeship in Nanotechnology-Environmental Effects and Policy (IGERT NEEP) funded the bulk of my tuition and stipend from 2011 to 2016. I also am honored to have received the 2010 Prem Narain Srivastava Legacy Fellowship, the 2014 Neil and Jo Bushnell Fellowship, and financial support from the Center for Environmental Implications of Nanotechnology (CEINT), which I used to purchase supplies and laboratory equipment essential to this dissertation. Additionally, my Fall 2013 research trip to Aalto University, was jointly subsidized by an NSF Graduate Research Opportunities Worldwide travel grant and the Academy of Finland. This international collaboration jump-started my experimental membrane distillation research. It is quite a privilege to exit graduate school with such rich experiences and with negligible loan debt; I will consider it an obligation to "pay it forward" in my professional and personal life.

To my advisors, Greg Lowry and Meagan Mauter, thank you. At my defense presentation, I jokingly estimated your contribution to my PhD as "90 work-days" but we know that doesn't really quantify what your guidance has meant to me. I am deeply indebted to you for showing me how to perform rigorous scientific research, for sharing your knowledge and intellects, for your patience and enthusiasm …and for breaking up my run-on-sentences. Simultaneously experiencing your *somewhat* different advising styles has also been valuable for me. Greg, I especially appreciate the freedom you gave me to explore thesis topics, and your unwavering confidence that I would find the right project and do a good job. Meagan, you've re-defined the

phrase “high standard” for me, and it is inspiring to see how your demand for the best out of yourself and your students is leading to so much success. Thanks to both of your efforts I am certainly smarter and wiser than I was when entering this program.

Thanks to my committee members, Alan McGaughey and Bob Tilton, for all your help to improve this dissertation. Alan, you were instrumental to me finishing my degree this year. Without your willingness to meet with me and discuss potential sources of error in the membrane distillation (MD) heat transfer model, it would have taken me far longer to pinpoint the disconnect between my experimental and modeled MD results. Bob, via your presence in my CEINT meeting updates and my proposal committee, you have helped guide me through a variety of potential thesis topics. Your encyclopedic knowledge of surface and colloid chemistry has frankly been a treat to witness in research group meetings and I am grateful for your willingness to weigh-in on my research.

I’d also like to thank three other academics in particular for their mentorship in my academic career. Liz Casman, thank you for your insightful and witty feedback on my work in CEINT meetings, and for seeing me through the nanotechnology patenting project, substantially improving the manuscript. Jeanne VanBriesen, I was a student in your graduate level classes, a teaching assistant for you, and a trainee in your IGERT NEEP program, and greatly admire your leadership and ability to captivate a room. Thank you for sitting on my proposal committee and for your extensive guidance to my group on our IGERT capstone project. Olli Ikkala, my semester at Aalto University was more rewarding and valuable than any other in my graduate school experience. I am indebted to you for so generously allowing me to come to Finland and learn from the fun and brilliant members of your applied physics research group.

Thanks also to the two most patient people in the CMU Civil and Environmental Engineering department, Maxine Leffard and Ron Ripper. Maxine, thank you for the third reminder e-mail, the one with all caps and exclamation points that gets me to do the thing I should have done weeks ago, and for somehow forgiving me every time for my waywardness. Ron, you have been an amazing mentor and friend in the lab. I don't know anyone else with your talent for good-naturedly and expertly fielding 15 people's repetitive questions about things we should know already or could probably find out ourselves without interrupting your work. I will miss walking in your office to gripe about something tangential to labwork, and hearing funny stories about your family or politics at lunch.

There are several students who helped me collect data for this dissertation, but in particular I'd like to thank Chenkai Li, Yupeng Zhao, and Arpita Iddya for their work. I've really enjoyed getting to know each of you in our long hours at the lab. Together, we ran more than 150 experiments on the benchtop MD unit, and the analysis herein relied on your commitment and conscientious attention to detail. This dissertation is far better with your work than if I'd tried to do it on my own, thank you.

To my fellow graduate student buddies, thank you for making CMU an amazing place to work and play. I've learned from you, confided in you, and joked around with this brilliant, kind, and fun group of peers for so many years that I don't think its hit me yet that it's over. I am so lucky to know each of you, and will miss working with you daily.

Now for the people I love most. To all my family, thank you for supporting me in this endeavor. John and Kathy, you are the absolute best in-laws a person could ask for – I can't believe I got so lucky. Thank you for being such great cheerleaders, especially as I repeatedly revised my projected defense date. Mom and Dad, I would not have completed this degree without the

confidence that comes from the lifetime of steady encouragement and support you've given me. You knew I could do this, so I never questioned whether I would. Thank you for all the little and big things you did in the last six years to help me achieve this goal.

Greta, you motivate me to succeed more than any other person or idea. Thank you for being such a fun kid. And you're doing a good job with those Legos…keep it up!

To Jay, my chief enabler: I don't know how to thank you for being my partner through this long process. As I slogged away at school, you started and completed your MBA, then began climbing rungs up the corporate ladder. In the meantime we also travelled to four continents, bought a house, got a big slobbery dog, got married, and became parents. Thank you for always being on my side, for making me laugh, and for my happy life. I am lucky to share it with you and am excited for whatever comes next. I love you.

DISSERTATION COMMITTEE

Gregory V. Lowry, Ph.D. (Co-Chair)
Walter J. Blenko, Sr. Professor, Civil and Environmental Engineering
Carnegie Mellon University

Meagan S, Mauter (Co-Chair)
Assistant Professor, Civil and Environmental Engineering and Engineering & Public Policy
Carnegie Mellon University

Robert D. Tilton
Professor, Chemical Engineering and Biomedical Engineering
Carnegie Mellon University

Alan J.H. McGaughey
Professor, Mechanical Engineering
Carnegie Mellon University

TABLE OF CONTENTS

Abstract iii

Acknowledgements v

Dissertation Committee ix

Table of Contents x

List of Tables xiii

List of Figures xiv

Chapter 1 : Introduction, Problem Identification, and Research Objectives 1

Introduction 1

Chapter 2 : Reproduction and comparison of membrane distillation data requires well-characterized Nusselt Number 8

2.1 Abstract 8

2.2 Introduction 9

2.3 Convective heat transfer in MD membrane cassettes: relation to experimental outcomes and the use of Nusselt number for calculation 13

2.4 Existing Nusselt correlations must be carefully selected for application to MD feed and permeate channels 26

2.5. To accurately determine heat transfer rate in MD, existing Nusselt correlations should be modified using theoretical and experimental correction factors. 32

2.6 Application of theoretical correction factors to Nusselt number correlations 33

2.7 Experimental method to determine cassette-dependent Nusselt correction factor (NuCF) 41

2.8 Heat transfer reporting recommendations for MD experimental work 62

2.9 Conclusions and Future Work 63

Chapter 3 : Prediction of membrane distillation flux for fibrous membranes using Buckingham-Pi dimensional analysis 66

3.1 Abstract 66

3.2 Introduction 67

3.3 Methods and Materials 73

3.4 Results and Discussion 87

3.5 Conclusions and Future work 99

Chapter 4 : Bacterial nanocellulose aerogel membranes: Novel high-porosity materials for Membrane Distillation(Leitch et al., 2016) 101

4.1 Abstract 101

4.2 Introduction and Background 101

4.3 Materials and Methods 104

4.4 Results and Discussion 108

Chapter 5 : Conclusions, Research Contributions & Implications 116
5.1 Conclusions 116
5.2 Research Contributions and Implications 118
Chapter 6 : Future Work 121
6.1 Use of computational fluid dynamics to develop idealized Nusselt correlations specific to MD cassette conformations and operating conditions 121
6.2 Multi-laboratory collaborative studies to examine MD membrane permeability using the NuCF method. 124
6.3 Exploration of Buckingham Pi method generalizability and usefulness in determining dominant vapor transport mechanisms 129
6.4 Process modeling to show sensitivity of system-level MD performance and cost to membrane structural parameters. 132
Appendices 133
A. Appendix A 133
A.1 Experimentally-measured membrane permeability is dependent on heat transfer coefficient 133
A.2 Nusselt correlations 134
A.3 Calculation of Nusselt correction factor for rectangular duct 137
A.4 Calculation of Nusselt correction factor for simultaneously developing flow 143
A.5 Calculation of Nusselt correction factor for heat flux from one wall 145
B. Appendix B 146
B.1: Solution for B-P dimensionless coefficients 146
B.2 Correlation to estimate pore diameter for fibrous membranes 149
B.3 Tabulated experimental results 150
B.4 B-P regressions for alternate parameter sets 151
B.5 Supplemental SEM images for fibrous membranes 153
C. Appendix C 154
C.1. Detailed methods for fabricating BNCA membranes and discussion of various bacterial strains tested for this research 154
C.2 Gravimetric calculation of porosity 155
C.3 Characteristics and Schematic of Benchtop DCMD system 156
C.4 Theoretical, Modeling and Experimental Discussion of BNCA matrix stability under DCMD conditions 159
C.5 Calculation of parameters for DCMD mass and heat transport 167
C.6 Hydrophobization characterization 174
C.7 Capillary Flow Porometry Data and discussion of Liquid Entry Pressure 176

C.8 Experimental vs. Theoretical permeability of tested membranes 177
C.9 Revised data for BNCA study: DCMD metrics re-modeled using Ch2 Nusselt number correction factors 178
Nomenclature 180
References 183

LIST OF TABLES

Table 2.1. Dimensionless parameters relevant to heat and mass transport in MD feed and permeate channels 21
Table 2.2 Nusselt correlations for laminar internal flow 30
Table 2.3. Characterization of commercial phase inversion PVDF membrane (Millipore GVHP) and electrospun PTFE membrane (Zeus Filtriq). 50
Table 2.4 Calculations of intrinsic membrane permeability, $Bw, i\ kgm-1s-1Pa-1\times 1011\ at\ 40°C$ for two commercial membranes. 62
Table 3.1 Summary of Buckingham-Pi variable selection. 75
Table 3.2 – Regression analysis repeated by removing subsets of experimental results. 95
Table 4.1. Characterization of polymer benchmark and BNCA membranes. 110
Table 4.2 Comparison of flux, salt rejection, Temperature Polarization Coefficient (TPC) between membrane-types (error expressed as standard error of the mean for multiple experiments). There is significant variation in the BNCA membrane thickness from sample to sample. Similarly-sized samples were used for each temperature experiment, which minimized intra-experiment variability. 113
Table 6.1 Experimental series using NuCF method to determine relationships between membrane structure, experimental conditions, and transport mechanism 128
Table 6.2 Matrix of potential experiments to independently vary each B-P dimensionless parameter 130

Table A.1 Nusselt correlations for transitional *internal* or *external* flow 134
Table A.2 Nusselt correlations for turbulent *internal* or *external* flow 134
Table A.3 Nusselt correlations for laminar external flow 136
Table A.4 Raw data, reproduced from Wibulswas thesis data (Shah&London table 51) 137
Table A.5 Tabular correction factors: Ratio of rectangular duct Nusselt # to circular duct Nusselt # 138
Table A.6 Channel aspect ratio vs *f*Re* 139
Table A.7 Find Correction factor constant, "C" (Divide Tabular correction factors by $f \cdot \mathrm{Rerect}$) 139
Table A.8 Mean Nusselt number, "H1" constant heat flux boundary condition for simultaneously developing flow in a rectangular duct, $\alpha^* = 0.5$. 143
Table A.9 Tabular correction factors: Ratio of Nusselt# for simultaneously developing flow to Nusselt # for $Pr = \infty$ 143
Table A.10 Fully developed Nusselt numbers for flow in rectangular ducts with constant axial heat flux. 145
Table B.1 Structural, Flux, Nusselt Number, and Salt rejection data for Series A and Series B experiments 150
Table C.1 Measurements of advancing contact angle (ACA) of membranes before and after DCMD testing 165
Table C.2 Updated temperature polarization coefficients using NuCF to model heat transfer coefficients 178

LIST OF FIGURES

Figure 2.1. DCMD Flux results compiled from the literature.....11
Figure 2.2 The effect of average cassette hf and hp on A) modeled average membrane surface temperatures and B) predicted MD vapor flux and heat flux for a commercial phase inversion PVDF membrane (Millipore GVHP).....16
Figure 2.3 The effect of estimated average cassette h_f and h_p on A) modeled thermal efficiency and B) membrane permeability for a given DCMD flux measurement.....17
Figure 2.4 Schematic of laminar hydrodynamic and thermal profile development in MD feed channel.....22
Figure 2.5. Modeled DCMD flux trends for a commercial PVDF membrane with laminar counter-current feed/permeate flow in symmetrical, rectangular channels.....25
Figure 2.6. Nusselt correlation selection matrix for MD applications.....29
Figure 2.7 Combined effect of correction factors on Nusselt prediction in MD channels.....41
Figure 2.8 The relation of theoretical membrane permeability, $B_{w,i,}$ to average membrane temperature for two different commercial membranes.....45
Figure 2.9 Model of $B_{w,i,experimental}$ of commercial membrane (Millipore GVHP) vs average Nusselt Number.....47
Figure 2.10 Flux results for two membrane types with A) varying bulk feed temperature. B) varying cassette flow rate.....52
Figure 2.11 Power regressions of $B_{w.i,experimental}$ and $B_{w,i,theoretical}$ for different DCMD experiment series. $B_{w.i,experimental}$ calculated using three separate Nusselt correlations for comparison.....54
Figure 2.12 Power regressions of $B_{w.i,experimental}$ and $B_{w,i,theoretical}$ for different DCMD experiment series. $B_{w.i,experimental}$ calculated using Eq19*NuCF.....60
Figure 3.1 Representative images of electrospun membranes.....88
Figure 3.2 Structural characterization of isotropic fibrous membranes.....89
Figure 3.3 Membrane structural parameter, C_m, calculated for individual membranes using SEM thickness and gravimetric measurements vs gravimetric measurements only.....91
Figure 3.4 Buckingham-Pi regressions model.....92
Figure 3.5 Comparison of modeled predictions with experimental data.....98
Figure 4.1 Schematic of membrane cross-section in DCMD.....107
Figure 4.2. Images of typical BNCA and PVDF membrane samples.....109
Figure 4.3. Experimentally-measured intrinsic (thickness-normalized) membrane permeability and thermal efficiency.....112

Figure A.1 Experimental permeate flux for a phase inversion PVDF membrane (Millipore GVHP) versus modeled Δp_{vap} between membrane surfaces.....133
Figure A.1.2 A) Plot Data from Table A.4, Find correlations, B) Correlation for constant "C" slope in with respect to aspect ratio.....140
Figure A.2 Evaluation of Nusselt prediction using duct geometry correction factors.....142
Figure A.3 A) Regression of tabular correction factors for simultaneously developing flow vs x* B) Regression of slopes from A.....144
Figure A.4 Percent error in Nusselt calculations compared to Wibulswas thesis data.....144
Figure A.5 Tabular data plotted along with polynomial correlations of fully developed Nusselt number in a rectangular duct.....145
Figure B.1 Correlation of electrospun membrane characterization data from literature.....149

Figure B.2 B-P model correlation fit is poorer when porosity is used as a parameter instead of solid fraction 151
Figure B.3 Experimental data regressed for limited parameter sets. Shows full correlation is not a result of over-fitting: 152
Figure B.4 Presence of beading in 7% PVDF electrospun membrane samples 153
Figure C.1 Benchtop DCMD Schematic 156
Figure C.2 Images of DCMD cassette used for data collection. 156
Figure C.3 Schematic of MD cassette 157
Figure C.4 Variation in modeled DCMD flux of BNCA membrane if membranes are gradually and uniformly compressed (decrease in thickness and porosity, pore size held constant), or if they are slowly infiltrated from the feed and permeate sides with liquid water. 162
Figure C.5 Variation in modeled DCMD flux of BNCA membrane with uniform evaporative fiber aggregation 162
Figure C.6 Variation in modeled DCMD flux with partial compression of membrane, due to evaporative aggregation. 163
Figure C.7 Representative raw data from DCMD experiments 164
Figure C.8 Representative plot of BNCA salt rejection, 60°C bulk feed 165
Figure C.9 Feed-side of membrane before and after DCMD testing. 166
Figure C.10 Representative cross sectional images of a BNCA membrane subjected to static pressure, heat, water, and salt exposures 166
Figure C.11 Electrical analogue of mass transfer resistances in MD 172
Figure C.12 Representative FTIR spctra verifying silane modificaion of BNCA membranes 174
Figure C.13 Typical BNCA advancing contact angle measurement images. 175
Figure C.14 CFP pore size distribution for a hydrophobic BCNA membrane (36 hour growth) and Millipore GVHP membrane 176
Figure C.15 Comparison of experimental to modeled membrane permeability for characterized and tested membranes. 177
Figure C.16 Updated Permeability and thermal efficiency comparisons between BNCA and PVDF membranes. 178
Figure C.17 Updated comparison of theoretical vs experimental permeability of BNCA and PVDF membranes using NuCF method to calculate the heat transfer coefficient. 179

Chapter 1 : INTRODUCTION, PROBLEM IDENTIFICATION, AND RESEARCH OBJECTIVES

Introduction

Global freshwater demand is projected to increase 55% by 2050, driven by energy production, manufacturing, and households uses (OECD, 2012). A portfolio of sustainable thermal, pressure-based, and electrochemical desalination technologies can help alleviate water scarcity. Solution conditions, process energy availability, and scale are three primary factors that determine the optimal desalination method for a given freshwater requirement.

One promising thermal desalination technology is Membrane Distillation (MD). MD is unlike typical membrane water treatment processes, where liquid feed water travels through a hydrophilic membrane and contaminants are excluded based on pore size and membrane chemistry. In MD, the membrane is hydrophobic, preventing liquid water from entering the pores. Raised temperature on the "feed" side of the membrane or vacuum pressure applied to the "permeate" side of the membrane causes a vapor pressure gradient in the membrane pores. This creates the driving force for liquid water from the feed stream to evaporate at the membrane surface, travel through the membrane pores, and condense on the permeate side of the membrane.

Process advantages of MD include its efficiency treating highly concentrated solutions, the use of low grade heat as the primary energy source, and its inherent scalability as a membrane-based technology. Given the high enthalpy input required to evaporate water and the difficulty of completely recovering this energy for re-use, MD and other thermal desalination processes are unlikely to compete commercially with reverse osmosis (RO) as stand-alone municipal-scale

seawater desalination methods.(Semiat, 2008; Elimelech, 2011; Mistry et al., 2011) However, the MD process has strengths where other desalination technologies are weak. Energy required for physical or electrochemical salt separation increases significantly with feed concentration, but in MD the effect is minimal; total dissolved solids concentration has only a weak effect on solution vapor pressure. Likewise, the mechanical strength (i.e. burst pressure) of RO membranes limits process applicability for highly-salty feed waters, whereas no such limitation exists for MD. MD is therefore a logical desalination option for concentrated waste streams or as a brine treatment step in standard desalination processes. In circumstances where low-grade heat is abundant, membrane distillation may be preferable to technologies that require high-grade electrical or thermal energy to drive desalination. MD could feasibly be coupled to industrial or energy production processes that generate waste heat.(Gingerich and Mauter, 2015) Membrane distillation could also prove valuable for deployment to remote locations with limited conventional power or water resources, as demonstrated by the construction of pilot MD plants (Song et al., 2008) and commercially available field-scale units.(SolarSpring, Aquaver)

Wider adoption of MD technology depends upon improvements to process efficiency. As with any desalination technology, a design goal is to minimize energy required per volume of produced fresh water while maintaining reasonable capital cost. The thermodynamic minimum energy to separate water from a salt solution is a function of the feed solution composition and the percent recovery of fresh water from the feed stream. It is independent of the method used for desalination. For example, the thermodynamic minimum separation energy for 50% recovery of seawater is 1.06 kWh/m^3, assuming a reversible process(Elimelech, 2011). By comparison, state-of-the-art municipal-scale reverse osmosis plants use about ~3 kWh/m^3 for the same recovery(Elimelech, 2011), and separation energy for 60°C seawater in single-stage direct

contact membrane distillation (DCMD) was calculated to be 27.6 kWh/m^3(Lin et al., 2014). A way to substantially improve energy efficiency for thermal desalination systems is to recover and reuse the heat of vaporization multiple times. Therefore, any fundamental research that facilitates the reuse of vapor enthalpy while limiting conductive heat losses in the MD process may lead to more widespread adoption of the desalination technology.

Membrane design is important to minimizing MD process irreversibilities. Researchers have published exploratory studies on multi-stage MD systems that reuse vapor enthalpy and thus reduce volumetric energy requirements (Lu and Chen, 2011; Chung et al., 2016). Membranes that maximize permeate flux will maximize the recoverable energy per stage. High permeability, low thermal conductivity membrane materials can simultaneously reduce membrane area required in a given stage and reduce conductive heat loss. A well-designed MD membrane therefore can reduce the size and number of MD stages required to achieve a given fresh water flux, thus improving energy efficiency and process viability.

From the first published demonstration of MD in 1967(Findley, 1967) until the mid-2000's, study of the MD process was performed almost exclusively by co-opting commercial membranes designed for liquid separation(Khayet, 2011). However, vapor transport theory indicates MD performance will increase if membrane structure can be adapted from the dense polymeric conformations tested in the first decades of research. In recent years, a number of experimental papers have been published by researchers seeking to improve mass and heat transport properties of MD membranes. Many creative structures have been tested, such as nanotube and graphene sheets(Dumée et al., 2010, 2011), and nanospiked glass(Ma et al., 2009). Currently, the most promising scalable "novel" membrane structures to decrease mass transport resistance are asymmetric membranes and fibrous membranes, which have shown substantial flux

improvements over commercial benchmarks(Qtaishat et al., 2009a; Essalhi and Khayet, 2012; Su et al., 2012; Liao et al., 2014b; Tijing et al., 2014b; Yao et al., 2016).

1.2 Problem Identification

Novel fibrous or asymmetric membrane structures show promise to improve the viability of MD desalination technology, but researchers and engineers lack the tools to optimize them. There are a few reasons for this knowledge gap:

A) Heat transport in the feed and permeate streams is poorly characterized, preventing reproducibility of results and quantitative comparison of membrane performance between studies. A majority of published MD research is experimental work describing how membrane, solution, and system characteristics affect MD flux.(Web of Science, 2014) For the MD community to efficiently leverage information from these studies, results must be reproducible and easily compared. Research groups use different bench-top system configurations, membrane cassette geometries, flow rates, fluid temperatures, etc. Each of these design choices has an effect on temperature profiles in the feed and permeate channels, and thus on MD flux and process efficiency. In existing literature, these effects are not consistently accounted for, making assessment of membrane properties inaccurate, and making comparisons of flux or membrane properties determined in different cassettes impossible.

Nusselt number is a dimensionless parameter used to characterize thermal boundary layers. Applied to MD, it describes the temperature gradient alongside the membrane. A high Nusselt number is the result of a steep thermal gradient at the membrane surface, signifying efficient heat transfer between the surface and the bulk fluid streams, and leads to high MD vapor flux.

Because permeate flux is proportional to Nusselt number, cassette design choices and operating conditions that affect Nusselt number also affect measured flux. Yet Nusselt number is rarely reported. This may be, in part, because published relationships for Nusselt number are not appropriate for the geometry of most cassettes used for MD research. In its absence, commonly published membrane, bulk solution, and bench top system parameters fail to fully characterize the experimental heat transfer characteristics in the feed and permeate streams. Thus, results are difficult to compare between MD studies because flux and process efficiency metrics cannot be conclusively attributed to membrane design, system design, or operating condition.

B) Existing MD membrane transport models are overly simplified and inappropriate for novel fibrous membranes, limiting researchers' ability to explain or predict membrane performance. Current empirical and theoretical models assume a simplified membrane structure in order to predict vapor transport performance. Empirical models either ignore membrane structure entirely (Khayet et al., 2007; Onsekizoglu et al., 2010; Khayet and Cojocaru, 2012, 2013) or are trained exclusively using conventional phase inversion membranes(Rao et al., 2014). Theoretical (i.e. mechanistic) models employ structural parameters that are problematic for novel membranes. Often, modeled pore geometry is highly simplified (e.g. cylindrical, non-interconnected pores, uniform characteristics throughout membrane) (Mason and Malinauskas, 1983; Schofield et al., 1987, 1990; Lawson et al., 1995; Lawson and Lloyd, 1997; Martínez et al., 2003; Phattaranawik et al., 2003a; Khayet et al., 2004; Xu et al., 2009; Charfi et al., 2010; Hwang et al., 2011; Khayet, 2011; Field et al., 2013; Soukane et al., 2014) so models are not sensitive to mass transport benefits of interconnected or asymmetrical pore networks. Another challenging aspect of theoretical models is their use of structural parameters that cannot be directly measured, such as

tortuosity (path length of the transporting vapor relative to membrane thickness) or pore network grid length(Imdakm and Matsuura, 2004; Khayet et al., 2010; Khayet, 2011). Reliance on non-measurable model parameters yields poor predictive capability for newly-designed membranes. Therefore, there is little ability to forecast or explain the vapor transport performance of novel membranes with fibrous or asymmetric structure.

C) Fabrication challenges have limited exploration of high porosity MD membrane materials. Past efforts to improve MD membranes have focused on varying pore diameter, tortuosity, and thickness.(Khayet et al., 2005; Qtaishat et al., 2009c, 2009a, 2009b; Dumee et al., 2010; Dumée et al., 2011; Drioli et al., 2013; Liao et al., 2013a, 2013b, 2014a, 2014b; Tijing et al., 2014a; Wu et al., 2014) There are very few experimental studies reporting MD performance of membrane materials with low thermal conductivity or high porosity (>90%).(Essalhi and Khayet, 2014; Li et al., 2014b). Studies exploring the effects of parameters specific to novel membranes (such as fiber diameter, pore geometry and selection layer thickness) on vapor transfer are also absent. With more systematic experimental data, vapor transport model predictions could be corroborated, membrane structures can be optimized, and membrane performance forecasts can be made for real MD systems.

1.3 Research Objectives

This work seeks to narrow these knowledge gaps through experimental and modeling work. The primary research objective of this dissertation is to help elucidate how membrane structure affects MD performance. To achieve this objective the work explores:

1. Techniques to adapt existing methods for characterizing heat transfer in the membrane cassette, leading to more reliable calculations of membrane permeability and more valuable reported data;

2. A new MD model which employs dimensional analysis to accurately identify relevant structural parameters for novel membranes and determine their effects on flux performance; and

3. The effects of very high porosity on membrane permeability and thermal efficiency, and how this knowledge can be applied to future membrane development.

1.4 Dissertation Structure

Chapter 1 is this introduction, which summarizes the challenges to wider adoption of MD technology and contributions of this thesis toward that goal. In Chapter 2, theoretical and experimental methods are developed to improve characterization of heat transfer in the membrane cassette, so that better inter-study comparisons of membrane performance can be made. Chapter 3 develops and demonstrates a new MD model that can be generalized for use with unconventional membrane geometries, and shows the effects of fibrous membrane structural parameters on flux. In Chapter 4 a novel membrane is developed and tested to show the effect of maximized porosity on vapor permeability and thermal performance. Chapters 5 and 6 summarize conclusions, present contributions and implications of this research, and make recommendations for future work.

Chapter 2 : REPRODUCTION AND COMPARISON OF MEMBRANE DISTILLATION DATA REQUIRES WELL-CHARACTERIZED NUSSELT NUMBER

2.1 Abstract

Accurate characterization of feed and permeate stream heat transfer is essential for reporting replicable and comparable membrane distillation (MD) data, In this work, we demonstrate the sensitivity of MD experimental results to convective heat transfer within the membrane cassette, and show how cassette channel geometry affects this rate of heat transfer. We provide guidance to select an adequate "baseline" Nusselt number correlation from literature, and then show how to adapt the baseline correlation for a particular MD cassette, so calculated Nusselt numbers accurately describe heat transfer to the membrane surface in the feed and permeate streams. This is accomplished in two steps. First, methods are presented for adjusting an existing Nusselt correlation to an idealized version that describes heat transfer for a given MD cassette geometry. Using this technique, a new idealized Nusselt correlation is formulated for the common case of a flat sheet MD membrane adjacent to laminar flow in rectangular channels. Second, an experimental method is proposed for adjustment of idealized Nusselt correlations to account for flow non-idealities in a real membrane cassette. The experimental method to determine cassette-dependent Nusselt correction factors (NuCF) is preliminarily validated using previously published and newly-collected experimental data. Despite variations in cassette conformation, system conditions, and measured flux, when cassette heat transfer is correctly characterized, experimentally-measured permeabilities for a particular commercial membrane are comparable between labs. It is recommended that MD researchers accompany experimental results with validated cassette heat transfer characteristics. Including experimentally validated cassette heat transfer characteristics in future MD reporting will facilitate cross-study comparison of novel

MD membrane structures and system conformations, enabling the field to converge on ideal membrane and cassette properties that improve MD performance.

2.2 **Introduction**

2.2.1 Typical MD experimental characterization is insufficient to allow inter-study comparison of results

A need for energy efficient separation of high salinity waters has led to a substantial increase in the number of researchers working on membrane distillation (MD) processes. The publication rate for peer-reviewed research with the topic "membrane distillation" nearly quadrupled between 2011 and early 2016.(Web of Science, 2014) A majority of this research is experimental and/or modeling studies describing how membrane, solution, and system characteristics affect MD flux. For the MD community to efficiently leverage information from these studies, results must be reproducible and easily compared. Thus, any MD performance data should be accompanied by process characterization data that accurately describes the mass, heat and momentum transport conditions in the system.

A consistently under-reported MD metric is Nusselt number. Nusselt number is a dimensionless parameter used to characterize the temperature gradient of a moving fluid alongside a solid surface (e.g. a membrane). Research groups use different benchtop system configurations, membrane cassette geometries, flow rates, fluid temperatures, etc. Each of these design choices has an effect on temperature profiles in the feed and permeate channels. A high Nusselt number results from a steep thermal gradient at the membrane surface, signifies efficient heat transfer from/to the feed or permeate stream, and facilitates a high MD driving force. Because driving force is proportional to permeate flux, cassette design choices and operating conditions that

affect Nusselt number also affect flux and process efficiency. Yet Nusselt number is rarely reported. In its absence, commonly published membrane, bulk solution, and bench top system parameters fail to fully characterize the experimental heat transfer characteristics in the feed and permeate streams. There are two primary consequences to poor cassette heat transfer characterization. The first is that, for a particular cassette, MD flux cannot be predicted outside the range of previously-collected experimental data (a new membrane or extreme operating condition necessitates new flux measurements). The second and more significant consequence is the loss of reproducibility and comparability between laboratories. With poor heat transfer characterization, MD results are difficult to compare between studies because flux and process efficiency metrics cannot be conclusively attributed to membrane design, system design, or operating condition.

Flux results have little quantitative value without accurate characterization of cassette heat transfer. To illustrate this, we compile flux data for the identical commercial PVDF phase-inversion membrane (Millipore GVHP) from 16 studies by 7 different research groups, including MD flux data taken from our own DCMD system for this study (Phattaranawik et al., 2003a, 2003b, 2003c; Khayet and Mengual, 2004; Termpiyakul et al., 2005; Yun et al., 2006; Srisurichan et al., 2006; Khayet et al., 2007; Goh et al., 2013; Zuo and Wang, 2013; Yang et al., 2014; Liao et al., 2014a; Silva et al., 2015). Figure 1 plots the wide range of experimental reports of membrane flux versus commonly reported system parameters. Given identical membranes, system conditions, and bulk permeate temperature, theory predicts MD flux will increase exponentially as bulk feed temperature increases (Lawson and Lloyd, 1997; Khayet and Matsuura, 2011). Figure 2.1A shows that bulk temperatures in the feed and permeate streams are not adequate predictors of flux, despite all data collection having occurred with feed and

permeate steams in the laminar flow regime with no turbulence-inducing spacers. Nor is the scatter explained by variations in reported bulk hydrodynamic conditions of the feed and permeate streams. For similar cassette geometries, theory predicts permeate flux to monotonically increase with cassette Reynolds number in the laminar flow regime, and to asymptote to a maximum value in the turbulent flow regime (Phattaranawik et al., 2003c; Izquierdo-Gil et al., 2008). Figure 2.1B reveals a high degree of independence between experimental flux and Reynolds Number, in both the laminar and turbulent flow regimes, when data from multiple labs is aggregated.

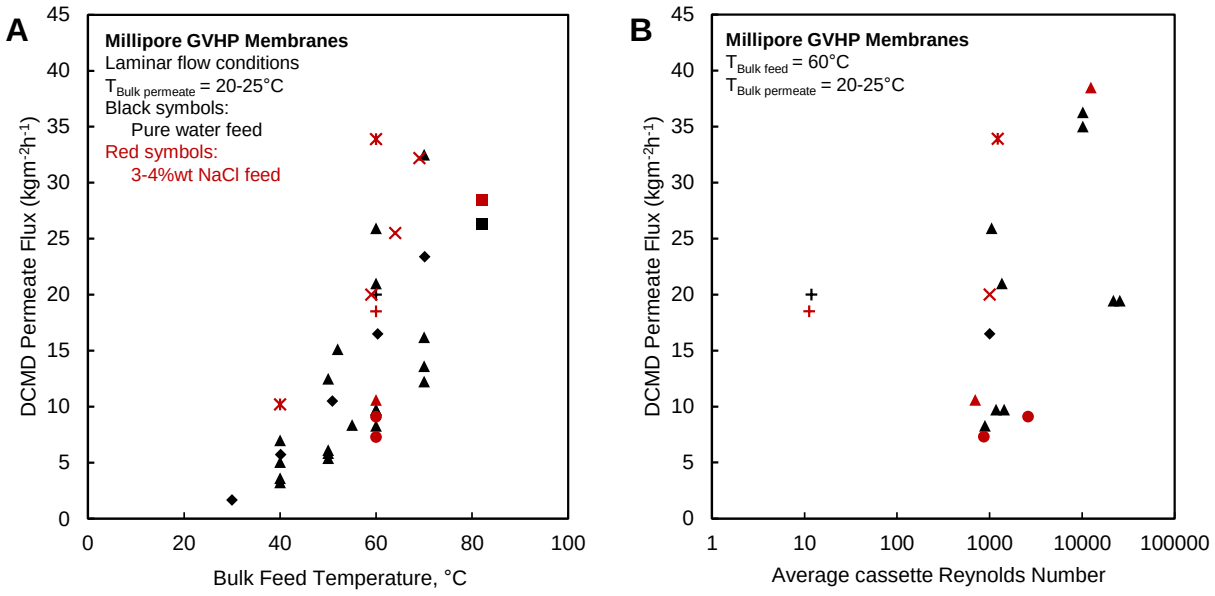

Figure 2.1. DCMD Flux results compiled from the literature. All experiments performed on Millipore phase-inversion PVDF "GVHP" membranes, with no spacers reported. Data symbols index the research group by common authors: ▲ – A. Fane/S. Srisurichan(Phattaranawik et al., 2003a, 2003b, 2003c; Termpiyakul et al., 2005; Srisurichan et al., 2006; Yun et al., 2006; Goh et al., 2013; Liao et al., 2014a), ♦ - M. Khayet(Khayet et al., 2007, 2010), + – H. Shon(Tijing et al., 2016), ■ – A, Silva(Silva et al., 2015) ● – R. Wang(Zuo and Wang, 2013), × – T. He(Yang et al., 2014), ✱ – M. Mauter (this work). A) Shows flux vs bulk feed temperature. Experimental flux varies widely between studies and labs despite similar hydrodynamic conditions and driving force. 2B) Shows experimental GVHP flux for nearly identical bulk temperature driving force, plotted against average Reynolds number in the membrane cassette (including turbulent conditions as well). Feed/permeate Reynolds number cannot fully explain the variation in flux results.

While temperature variation and experimental error can explain a small amount of the data scatter seen in Figure 2.1, inter-lab variance is primarily a result of different thermal profiles in the membrane cassettes. MD researchers can summarize the effects of cassette channel geometry and flow conditions on cassette heat transfer by reporting carefully calculated and experimentally validated Nusselt numbers. Indeed, several research groups have noted the sensitivity of experimental outcomes to Nusselt number or the analogous parameter, convective heat transfer coefficient, *h*.(Gryta and Tomaszewska, 1998; Phattaranawik et al., 2003c; Qtaishat et al., 2008; Hitsov et al., 2015; Gustafson et al., 2016) By addition of feed and permeate Nusselt numbers (or h_f and h_p) to the suite of commonly reported experimental parameters, mass and heat transport in the MD system becomes fully defined. With this information, the intrinsic permeability of novel membrane structures can be accurately characterized and compared across studies, facilitating a fuller understanding of MD vapor transport and assisting in optimization of membrane geometry. Furthermore, cassette heat transfer characterization enables published MD data for any membrane, system design or operating condition to be effectively compared, replicated, and used predictively.

2.2.2 *Contributions of this work:*

The goals of this work are to develop methods for calculating Nusselt numbers in MD systems, with a focus on for laminar, countercurrent feed and permeate streams in rectangular channels. In section 2.3, we introduce the theoretical basis for using Nusselt number to describe the relationship between heat transfer in the cassette and MD flux. In section 2.4, we provide clear guidance on how to select an appropriate baseline Nusselt correlation from the literature. Section 2.5 builds the case for application of theoretical and experimentally-determined correction factors to baseline Nusselt numbers in a laboratory MD cassette. Methods to

determine theoretical correction factors from literature data are presented in section 2.6. Using the correction-factor method, we suggest a new Nusselt correlation appropriate for the common case of a flat sheet membrane with laminar feed and permeate flow in rectangular channels. In section 2.7 we propose and validate an experimental method to correct Nusselt number for flow non-idealities in actual membrane cassettes. We determine correction factors for MD data collected from two different research groups on identical membranes, then apply the correction factors to determine membrane permeability. Despite variations in cassette conformation, system conditions, and measured flux, the (corrected) membrane permeabilities are comparable between labs. We conclude by suggesting guidelines for reporting cassette heat transfer metrics along with MD flux results to allow membranes and system design to be compared across studies.

2.3 Convective heat transfer in MD membrane cassettes: relation to experimental outcomes and the use of Nusselt number for calculation

The objectives of this section are to demonstrate the importance of accurately characterizing convective heat transfer in MD cassettes and the utility of Nusselt number to achieve this. Variables that determine Nusselt number are shown, along with theoretical examples of how small variations in cassette design can change the average Nusselt number, leading to large changes in permeate flux.

2.3.1 *Well-characterized convective heat transfer coefficients are required to calculate heat and mass transport in MD.*

The system of one-dimensional steady-state mass and heat transport equations for membrane distillation, adapted from and described in previous literature(Khayet, 2011; Leitch et al., 2016), are as follows (Eq 1-5):

$$J_w = B_{w,i}\frac{\Delta p_{vap}}{\delta} \quad (1)$$

$$Q_f = Q_m = Q_p \quad (2)$$

$$Q_f = h_f\left(T_{f,b} - T_{f,m}\right) + J_w H_{w,f} \quad (3)$$

$$Q_p = h_p\left(T_{p,m} - T_{p,b}\right) + J_w H_{w,p} \quad (4)$$

$$Q_m = \frac{k_m}{\delta}\left(T_{f,m} - T_{p,m}\right) + J_w H_{w,vap} \quad (5)$$

Here, J_w and Q represent transmembrane mass and heat flux. In direct contact membrane distillation (DCMD), water flux (J_w) is driven by saturation vapor pressure at opposite surfaces of the membrane and is limited by the intrinsic permeability and thickness of the membrane ($B_{w,i}$ and δ). If a difference in vapor pressure exists (Δp_{vap}), solvent at the interface with higher vapor pressure volatilizes, transports through the membrane, then condenses on the opposite side. Vapor pressure of water is a strongly a function of temperature (determined by the Antoine equation), and more weakly a function of mole fraction of solute, and water activity (calculated empirically using osmotic coefficient and temperature (Prausnitz et al., 1999)). Therefore, to determine MD driving force, Δp_{vap}, temperatures at the membrane surface ($T_{f,m}$ and $T_{p,m}$) must be known. Though preliminary research has been conducted to measure MD membrane surface temperature experimentally(Ali et al., 2013; Tamburini, 2013), more research is needed to validate the methods and develop techniques for practical implementation(Hitsov et al., 2015). In the absence of readily available devices to measure temperature at the membrane surface, MD researchers measure and report bulk fluid temperatures. Temperature at the membrane surface is modeled using the heat transport equations (Eq 3-5), where Q_f is heat flux to the membrane surface from the feed stream, Q_m is the sum of conducted and convected heat through the membrane, and Q_p is the heat flux from the fluid at the membrane surface to the permeate

stream. Heat transfer due to transmembrane mass flux is calculated using water enthalpy, H, and heat conducted through the membrane material is quantified using membrane thermal conductivity divided by membrane thickness,$\frac{k_m}{\delta}$. Heat transfer from the bulk feed and permeate streams to the membrane surface is determined by the convective heat transfer coefficients, h_f and h_p.

To use Eq 1-5 to predict MD mass and heat flux, or to explain the effects of experimental system conditions and/or membrane properties on measured fluxes, equations 1-5 are solved simultaneously with a maximum of four unknown variables. $T_{f,m}$ and $T_{p,m}$ are two of the unknowns, so to calculate any one transport metric, such as J_w, Q, or B_w, the either the feed or permeate heat transfer coefficient (h_f or h_p) or both, must be accurately defined. Two hypothetical cases are presented in Figures 2.2 and 2.3 to show the sensitivity of calculated performance metrics to estimated h_f and h_p when solving equations 1-5. Figure 2.2 demonstrates that, for a given set of DCMD system conditions, predicted MD driving force, vapor flux, and heat flux are highly sensitive to estimated cassette heat transfer coefficients. The effect is particularly strong in the laminar regime where average h_f and h_p are expected to be low.

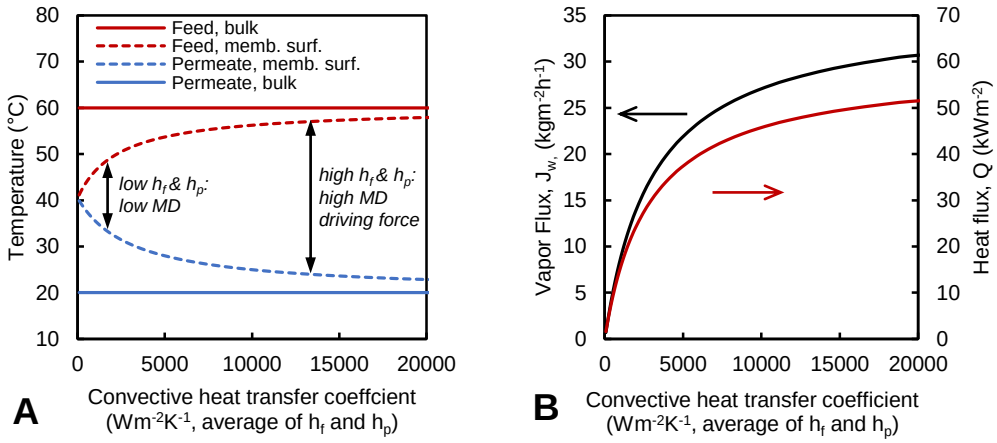

Figure 2.2 The effect of average cassette h_f and h_p on A) modeled average membrane surface temperatures and B) predicted MD vapor flux and heat flux for a commercial phase inversion PVDF membrane (Millipore GVHP) Model inputs: $T_{f,\,avg}$ = 60°C, $T_{p,avg}$ = 20°C, Feed concentration = 35 g/L NaCl, membrane structural and thermal characteristics to calculate theoretical membrane permeability and thermal conductivity, see Table 2.3. Convective heat transfer coefficient (i.e. Nusselt number) determines the temperature gradient between bulk streams and membrane surface, thus MD driving force and flux predictions are sensitive to Nu estimation errors.

Experimental measurements of permeate flux can also be interpreted incorrectly when estimated h_f and h_p are incorrect (Figure 2.3). Experimentally-measured MD thermal efficiency, η ($Q_{m,vapor\ convection}/Q_{m,total}$), or intrinsic membrane permeability, $B_{w,i}$ are often reported to evaluate novel DCMD system configurations or membranes, however calculations of these parameters are highly sensitive to estimated heat transfer coefficients. Figure 2.3B has an important implication for a commonly-applied experimental method in MD literature to determine total membrane permeability, $B_{w,i}/\delta$ (a.k.a. "the membrane coefficient" in some studies). In this method, experimentally measured J_w is plotted vs. Δp_{vap}, and the slope of the line is taken to be $B_{w,i}/\delta$ (Phattaranawik et al., 2003c; Termpiyakul et al., 2005; Gustafson et al., 2016). Accurate calculations of Δp_{vap} (and thus $B_{w,i}/\delta$) are reliant on accurate h_f and h_p inputs. The sensitivity of calculated $B_{w,i}/\delta$ I to cassette heat transfer characterization and potential for misinterpretation of experimental data is discussed further in Appendix A.1.

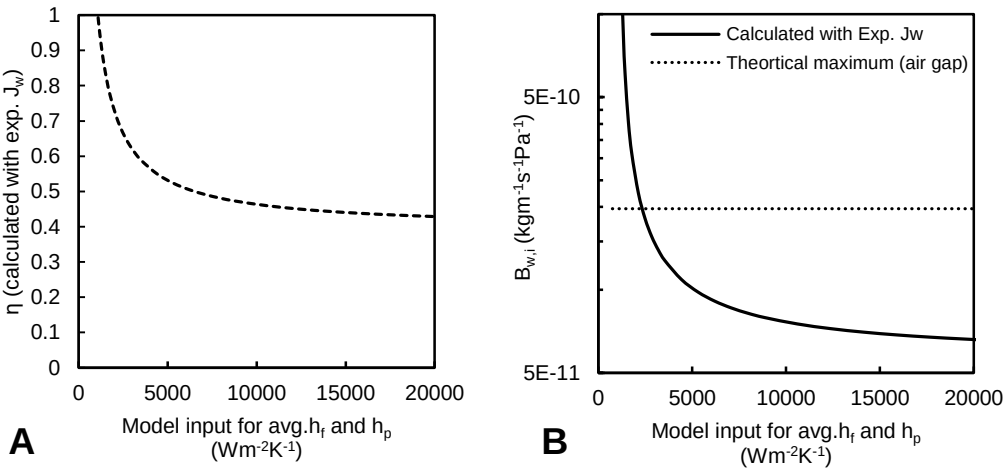

Figure 2.3 The effect of estimated average cassette h_f and h_p on A) modeled thermal efficiency and B) membrane permeability for a given DCMD flux measurement. Model inputs: Experimentally measured flux, J_w = 32 $kgm^{-2}h^{-1}$, $T_{f,avg}$ = 60°C, $T_{p,avg}$ = 20°C, Feed concentration = 35 g/L NaCl, Thermal conductivity of Millipore GVHP membrane estimated theoretically

The modeled parameters in Figures 2.2 and 2.3 demonstrate how correct determination of h_f and h_p is required for meaningful comparison of experimental results between studies, and gives researchers power to predict performance of novel membranes and system designs in un-tested conditions.

Calculation of h_f and h_p is not trivial. There are three methods demonstrated in MD literature: experimental determination, modeling by computational fluid dynamics (CFD), and calculation using a Nusselt correlation(Hitsov et al., 2015). Established methods to determine heat transfer coefficients in MD cassettes are briefly described, along with some strengths and weaknesses of each method.

Experimental values for h_f and h_p can be established for flat-sheet membrane cassettes at specific system conditions. An impermeable barrier is used in place of the membrane; the cassette inlet and outlet temperatures are precisely measured for the desired system conditions, allowing energy balances of the feed and permeate streams to be calculated. Discussion and

demonstration of the method exists in the literature(Gryta and Tomaszewska, 1998; Phattaranawik et al., 2003c). This method to individually calculate h_f and h_p is valuable when thermophysical fluid properties and flow conditions in the membrane cassette are expected to remain static, and when MD system/sensor design supports an accurate energy balance. No author yet has shown a rigorous empirical method to determine cassette h_f and h_p over a range of system conditions or cassette geometries.

Alternatively, h_f and h_p can be solved using CFD to model the feed/permeate thermal profiles. Several authors created CFD models to describe heat and mass transfer in MD feed and permeate channels (Cipollina, 2009; Shakaib et al., 2012; Al-Sharif et al., 2013; Hitsov et al., 2015; Shirazi et al., 2016), however experimental validation of these models has not yet been published. Advantages of CFD are the ability to more accurately model MD channel configuration, including use of turbulence-inducing spacers, and to determine effects on temperature profile when cassette geometry is varied. Disadvantages of CFD are computational intensity and the requirement to model initial conditions and boundary conditions for a particular cassette, which are typically simplified due to uncertainty in real velocity and temperature profiles. These simplifications leave current CFD models unable to forecast non-idealities of experimental flow in the cassette. Experimental calibration of existing models is needed so they can be used practically and predictively.(Hitsov et al., 2015)

The third and most common method to characterize MD cassette heat transfer is to use Nusselt number correlations. For more than a century, engineers in the field of fluid dynamics and heat transfer have developed analytical, numerical, and empirical equations to describe the dimensionless temperature profile, a.k.a., the Nusselt number. Analytical and numerical methods to develop Nusselt number correlations suffer from the same inability to incorporate

complex boundary condition, initial conditions, and cassette non-idealities as CFD. However Nusselt correlations are closed-form expressions and much more simple to use in engineering calculations, hence their popularity in predict heat transfer in MD cassettes. Past research describes how Nusselt number is affected by fluid properties, hydrodynamic conditions, system geometry, boundary conditions, and initial conditions. The following sections define Nusselt number in relation to the convective heat transfer coefficient, and discuss typical variables that affect its magnitude.

2.3.2 *Nusselt number is a universal, dimensionless measure of heat transfer between a fluid and solid surface*

Nusselt number is a dimensionless parameter that describes the thermal profile of fluid adjacent to a wall. Historically, Nusselt number correlations were developed to describe energy transport in heat exchange, automotive, energy generation, and aeronautical applications(Shah and London, 1978). It is defined as follows(Welty et al., 2009):

$$Nu = \frac{\frac{\partial T}{\partial y}\Big|_{y=0}}{(T_{bulk\ fluid} - T_{wall})/d_h} = \frac{h d_h}{k} \qquad (6)$$

Nusselt number can thus be conceptualized as a ratio of slopes: the temperature gradient exactly at the wall surface ($\frac{\partial T}{\partial y}\Big|_{y=0}$) surface divided by macro-scale temperature gradient from the wall to the bulk fluid ($T_{bulk\ fluid} - T_{wall})/d_h$, where d_h is the hydraulic diameter of a channel in which the fluid is flowing. As is evident from the second equality, Nusselt number can also be conceptualized as the ratio of convective to conductive heat transport at a wall, where h is the convective heat transfer coefficient and k is the fluid thermal conductivity. This is the equation

used to directly calculate h_f and h_p after Nusselt number is estimated using an empirical, analytical or numerical correlation.

2.3.3 *Variables that determine Nusselt Number (thermal profile) in the membrane cassette*

Nusselt number is a dimensionless parameter calculated as a function of thermophysical fluid properties, flow dynamics, and system geometry. These input variables are also written as dimensionless parameters, an engineering practice which allows for facile scaling and comparison between similar systems. Parameters commonly used to describe mass and heat transport in channel flow for non-isothermal systems, their physical relevance, and their relation to each other are presented in Table 2.1.

Table 2.1. Dimensionless parameters relevant to heat and mass transport in MD feed and permeate channels

Dimensionless number	Equation	Relation to other dimensionless numbers	Physical relevance	Equation #
Reynolds number, Re	$Re = \frac{vd_h}{\nu}$		Ratio of inertial forces to viscous forces in fluid flow	(7)
Prandtl number, Pr	$\mathrm{Pr} = \frac{\mu c_p}{k}$		Ratio of momentum diffusivity to thermal diffusivity, hydrodynamic to thermal BL development speed	(8)
Dimensionless channel length, x'	$x' = \frac{L}{d_h}$			(9)
Peclet number, Pe	$Pe = \frac{\dot{m}c_p}{k}$	$Pe = RePr$	Ratio of heat transported by convection to heat transported by conduction	(10)
Graetz number, Gz	$Gz = \frac{\dot{m}c_p}{kL}$	$Gz = \frac{RePr}{x'}$	Indicator or thermal development in a conduit: high Graetz signifies low degree of thermal development	(11)
Hydrodynamic inlet distance, x*	$x^* = \frac{kL}{\dot{m}c_p}$	$x^* = \frac{1}{Gz}$		(12)
Duct cross sectional aspect ratio, α*	$\alpha^* = \frac{height}{width}$			(13)
Grashof number, Gr	$Gr = \frac{\beta g \Delta T L^3 \rho^2}{\mu^2}$		Ratio of buoyant to viscous force in fluid. Relevant when natural convection affects heat transfer	(14)
Nusselt Number	$Nu = \frac{hd_h}{k}$	$Nu = f(Re, Pr, x', \alpha^*, \{Gr\})$	Ratio of convective to conductive heat transfer at a wall	
Sherwood number	$Sh = \frac{Kd_h}{D}$		Ratio of convective to diffusive solute mass transfer at a wall (relevant for very high feed salt concentration)	(15)

Nusselt number for solid channel walls adjacent to forced flow is typically correlated as function of Reynolds Number, Prandtl number and dimensionless length. Figure 2.4 shows qualitatively how Nusselt number can be affected by these parameters. The schematic displays development of hydrodynamic and temperature profiles in the feed side of an MD channel. Average Nusselt number along the length of the membrane (and thus average flux recorded by experimenter) is proportional to Reynolds number and Prandtl number, and is inversely proportional to dimensionless channel length. If laminar flow is modeled using uniform velocity and

temperature distributions at the channel entrances, $Nu = \infty$ at the channel entrance, and decreases to a constant non-zero value when hydrodynamic and thermal profiles are fully developed.

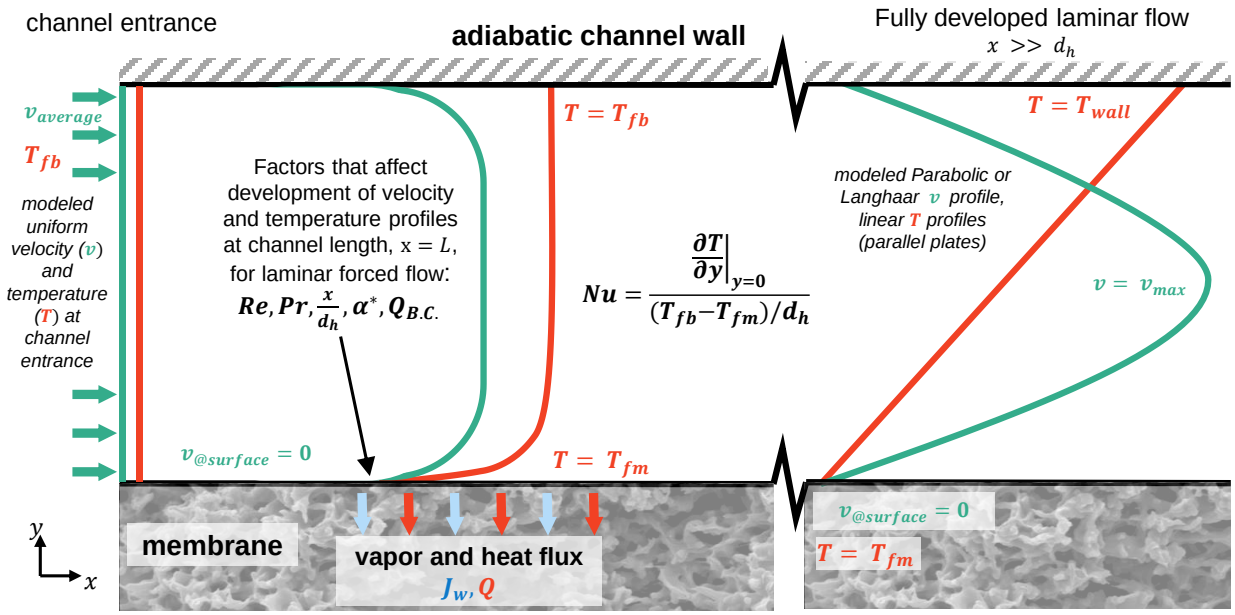

Figure 2.4 Schematic of laminar hydrodynamic and thermal profile development in MD feed channel. For an abrupt channel entrance with uniform hydrodynamic and thermal profiles, Nu = ∞. Nu decreases monotonically and asymptotes to a constant value as flow develops to final hydrodynamic and thermal profile

Other parameters that affect the average thermal profile in a channel (but do not always appear explicitly in Nusselt correlations) are(Shah and London, 1978):

a) Flow regime – Equations for Nusselt that describe laminar flow in an open channel will underestimate heat transfer for transitional or turbulent flow. A Nusselt correlation trained on the proper flow regime must be used.

b) Channel cross-sectional geometry – The thermal profile will vary depending on whether a channel has a circular or rectangular cross-section and depending on the aspect ratio of the cross-section.

c) Heat transfer boundary conditions - Nusselt number is typically higher if heat is transferred on all sides of the membrane channel, as is the case for hollow fiber MD membranes, vs. only one side as in flat sheet configuration.

d) Initial conditions - As can be seen from Figure 2.4, thermal and hydrodynamic profiles at the channel entrance can change the average Nusselt number. If an MD cassette has a hydrodynamic smoothing section prior to membrane exposure, then the thermal profile will develop more quickly, and average Nusselt will be lower.

e. Flow non-idealities – Particularly for flow in the laminar regime, an abrupt channel entrance or, roughness along the channel walls, or channel spacers can cause fluid mixing, changing the thermal profile and likely increasing heat transfer to the membrane surface.

Average Nusselt number in a membrane cassette can vary widely depending on these parameters. Care must be taken to select Nusselt correlations from literature that are trained using relevant geometrical, flow, boundary, and initial conditions. The effects of channel geometry on Nusselt number are particularly apparent in small, bench-scale MD systems where thermal and hydrodynamic boundary layers are never fully developed (Fig 2.4). These developing flow regimes have thinner boundary layers, higher boundary layer thermal gradients, and higher heat flux to the membrane, which act to increase MD driving force and permeate flux.

2.3.4 *Slight variations in cassette design can change the average Nusselt number, leading to large changes in permeate flux*

To demonstrate effects of channel geometry on heat transfer and driving force, DCMD flux through a commercial phase-inversion PVDF membrane (Millipore GVHP) is modeled. Feed

and permeate streams are pure water in laminar flow with bulk temperatures held constant a 60°C and 20°C, respectively. In Figure 2.5A channel cross-sectional aspect ratio is varied, where the channel has a rectangular cross section and flow has become fully developed. In this case, design of the channel height in the cassette substantially influences MD flux. For a hypothetical feed and permeate channel cross section of 4 cm x 5 mm, predicted flux is 2.7 $kgm^{-2}s^{-1}$, but decreasing channel height to 2 mm increases flux to 5.9 $kgm^{-2}s^{-1}$. In Figure 2.5B, the effects of channel length (normalized by hydraulic radius) on membrane flux for thermally developing flow are shown. For the same feed and permeate channel cross-section, 4 cm by 2mm, a membrane length of 10 cm results in 8.6 $kgm^{-2}s^{-1}$ permeate flux, where are for a 5 cm long membrane, flux is 19% higher, at 10.2 $kgm^{-2}s^{-1}$.

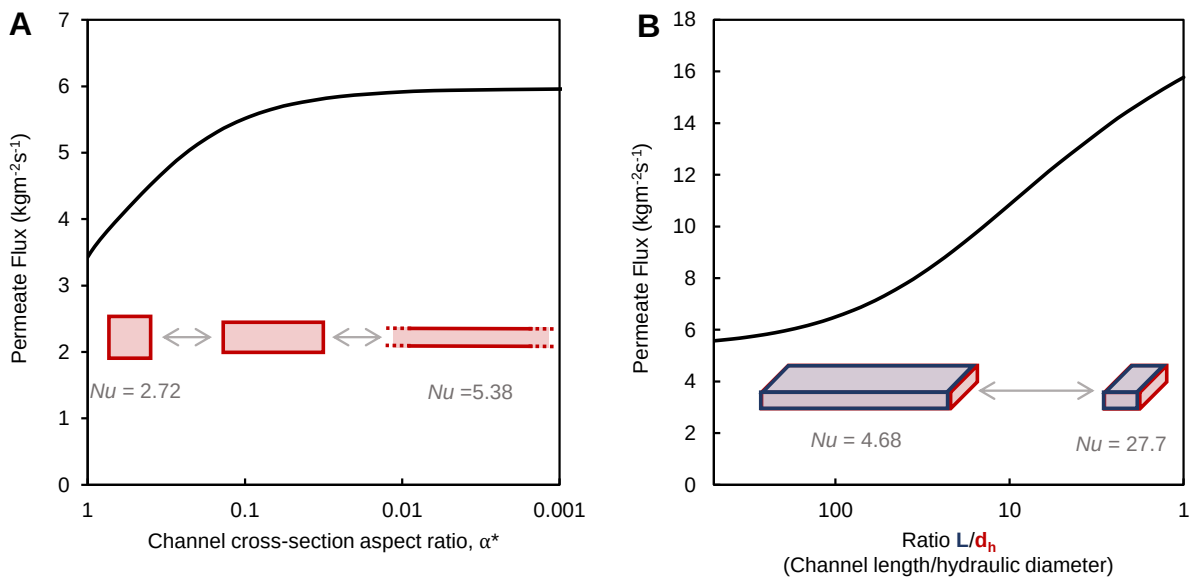

Figure 2.5. Modeled DCMD flux trends for a commercial PVDF membrane with laminar counter-current feed/permeate flow in symmetrical, rectangular channels. Bulk temperatures = 60°C feed, 20°C permeate. Pure water in feed and permeate channels. 5A) Variation of flux with channel cross-section aspect ratio for long feed/permeate channels with fully-developed thermal and hydrodynamic flow. Hydraulic diameter = 0.004 (constant). 5B) Variation of flux with normalized channel length (constant Re and Pr), showing influence of developing hydrodynamic and thermal flow on DCMD performance. Channel cross-section = 0.04 x 0.002 m (constant). For 2B, Hausen correlation was used (simultaneously developing flow, circular cross section, constant Delta T with no adjustments for Pr or aspect ratio (Table 2.1)

Figure 2.5 can partially explain the variability in reported flux by different labs for identical commercial membranes under identical bulk driving force (Figure 2.1B). Simple reporting MD cassette channel dimensions, however, cannot capture the effects of channel entrance configuration and flow non-idealities on MD flux. To fully explain experimental MD measurements, and to make any analysis comparing one lab's results with another, experimentally-validated Nusselt numbers (or convective heat transfer coefficients) must be reported.

In the Section 2.4 a review is given of existing Nusselt correlations applicable to MD along with guidance on how to select an appropriate Nusselt correlation. Following this are discussion of why and how to adjust the baseline Nusselt correlation.

2.4 Existing Nusselt correlations must be carefully selected for application to MD feed and permeate channels

Two primary sources of error in calculating Nusselt number are 1) the choice of an invalid baseline Nusselt correlation for the given MD system geometry and fluid conditions and 2) neglecting to modify the baseline Nusselt correlation to match real membrane cassette geometry and flow conditions.

2.4.1 Nusselt correlation selection methodology

Scores of Nusselt correlations exist in research literature and in textbooks. These empirical correlations are trained using numerical simulation (i.e. fit from CFD models) or experimental data from a variety of flow configuration, some of which are similar to conditions encountered by feed and permeate streams in MD.

To calculate h_f and h_p for use in MD transport equations, an appropriate Nusselt number correlation is selected for given MD cassette geometry and flow conditions, and adjustments to the correlation are appropriate if it was not trained with identical cassette channel geometry, entrance conditions or wall boundary conditions. Unfortunately, in the MD literature, understanding of the source and applicability of existing Nusselt correlations is limited. Some unintentional misuses by MD authors include:

1) Applying a Nu correlation inappropriate for MD channel flow development, e.g. using a correlation designed for fully-developed or thermally developing flow when MD flow

is both thermally and hydrodynamically developing.(Gryta et al., 1997; Srisurichan et al., 2006; Andrjesdóttir et al., 2013)

2) Applying a correlation which calculates the *local* Nusselt number at a point in the cassette when modeling with 1-D mass and heat transport equations, which call for an *average* Nusselt number (i.e. average heat transfer coefficient) for the entire cassette.(Gryta and Tomaszewska, 1998; Phattaranawik et al., 2003c; Andrjesdóttir et al., 2013) The reverse of this mistake can also easily occur: applying a correlation that calculates *average* Nusselt number in a cassette when using a stepwise 2-D mass and heat transport model. In this case, calculation of h_f and h_p is performed for specific locations along the length of the cassette and should be done using correlation that calculates *local* Nusslet number.

3) Using a Nusselt correlation designed with constant temperature as the boundary condition, without adjustment. (Andrjesdóttir et al., 2013) In countercurrent MD, the boundary condition assumption of "constant heat flux" is more physically accurate than a "constant temperature" boundary condition.

4) Using a Nusselt correlations trained on circular channels for external flow across a flat plate without adjustment for rectangular MD channel geometry.(Lawson and Lloyd, 1997; Phattaranawik et al., 2003c; Andrjesdóttir et al., 2013; Leitch et al., 2016)

5) Using correlations that rely on Grashoff number without validating whether natural convection is relevant to the channel(Gryta et al., 1997). Charts exist to make this determination(Kakaç et al., 1983)

6) Selection of a Nusselt correlation because it appears to correctly estimates h_f and h_p for a small set of experimental conditions (as determined using the impermeable

membrane method, described in section 2.3.1), without regard for the correlation's origins or intended use.(Phattaranawik et al., 2003c) The correlation will have little predictive capability for heat transfer in alternate system conditions.

To assist in the search for an applicable Nusselt number correlation, we suggest a set of potentially relevant equations for MD researchers. Figure 2.4 and Tables 2.2 and A2.1-3 provide a methodology to select relevant "baseline" *Nu* correlations and some suggested correlations from the literature. The flow chart in figure 2.4 is used to determine which table of Nusselt correlations is appropriate for the given cassette channel.

Some assumptions and simplifications were made in the compilation of these tables. For all correlations, steady channel flow is assumed through smooth channel walls with no turbulence inducing spacers. The selected correlations each calculate *average* Nusselt number for the length of membrane cassette; average Nusselt is useful to help determine aggregate MD parameters in the cassette, such as average flux and average membrane surface temperatures. If more granularity is desired for 2D or 3D modeling, analogous local Nusselt correlations can be found many of the cited original sources. The boundary condition of constant axial heat flux is assumed to be most relevant to countercurrent MD flow, therefore Nusselt correlations that assume constant heat flux as a boundary condition were selected for this compilation. "H1"annotation signifies constant axial and peripheral heat flux boundary conditions at the channel walls. The cutoffs of dimensionless channel length, $x^* > 0.05$ for developed flow and aspect ratio, $\alpha^* < 0.01$ for use of parallel plate correlations rather than rectangular duct

correlations were estimated from literature data(Thomas, 1993; Shah and Sekulic, 2003).

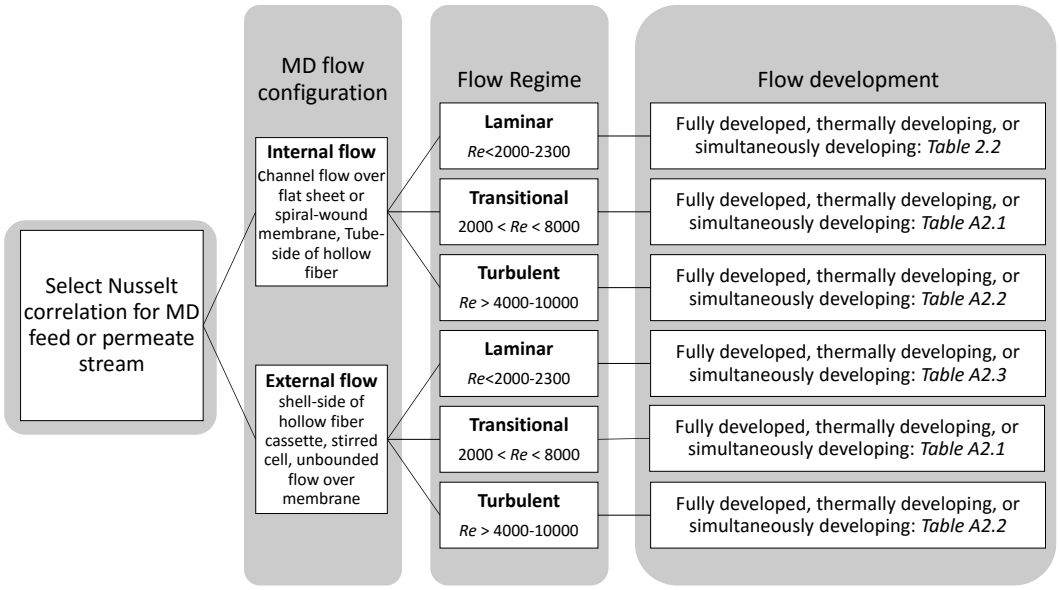

Figure 2.6. Nusselt correlation selection matrix for MD applications

Table 2.2 Nusselt correlations for laminar internal flow

Flow development	Flow cross section	Nusselt# Equation	Source	Derivation method	Thermal boundary conditions	Use in MD papers	Notes
Fully developed hydrodynamic and thermal flow (long channels only) $x^* = \gtrsim 0.05$	Circular	$Nu = \frac{48}{11} = 4.364$	(Shah and London, 1978)	Analytical solution	H1		Most relevant for interior flow in long hollow fiber membranes
	Square	$Nu = 3.608$	(Schmidt and Newell, 1967; Shah and London, 1978)	Analytical solution	H1		
	Square	$Nu = 2.712$	(Schmidt and Newell, 1967; Shah and London, 1978)	Analytical solution	Constant axial heat flux, **heat flux through one channel wall**		(S&LTable 44)
	Rectangular, aspect ratio = α*	$Nu = 8.235(1 - 2.0421\alpha^* + 3.0853\alpha^{*2} - 2.4765\alpha^{*3} + 1.0578\alpha^{*4} - 0.1861\alpha^{*5})$	(Shah and Sekulic, 2003) (Table 7.4)	Correlation of tabular data from analytical solution	H1		
	Rectangular, aspect ratio, α*	Tabular data available for interpolation. Correlation developed in this work, section 4.4.3	(Schmidt and Newell, 1967; Shah and London, 1978)	Analytical solution	Constant axial heat flux, **heat flux through one channel wall**		(S&L Table 44)
	Parallel plates (or α* < 0.01)	$Nu = 8.235$	(Shah and London, 1978)	Analytical solution	H1		
	Parallel plates (or α* < 0.01)	$Nu = 5.385$	(Shah and London, 1978)	Analytical solution	H1		
Hydrodynamically developed, Thermally developing (Short channels with calming entrance section prior to membrane exposure	**Circular**	$\overline{Nu} = 1.86\left(\frac{Re\ Pr\ d_h}{L}\right)^{1/3}\left(\frac{\mu_{bf}}{\mu_{mf}}\right)^{0.14}$	**Sieder-Tate correlation** (Sieder and Tate, 1936)	**Empirical correlation, countercurrent flow**	**Constant heat flux axially & peripherally**	**This work.** (Phattaranawik et al., 2003c; Tun et al., 2005; Song et al., 2007; Izquierdo-Gil et al., 2008; Bui et al., 2010; Leitch et al., 2016)**.**	**Valid only for x* < 0.04** (Thomas, 1993)

$x^* = \lesssim 0.05$	Circular	$\overline{Nu} = 3.66 + \frac{\frac{0.0668 RePrd_h}{L}}{1 + 0.04\left(\frac{RePrd_h}{L}\right)^{2/3}}$	Hausen, 1943 (Kakaç et al., 1983; Thomas, 1993)	Empirical correlation	Constant axial temperature	(Bui et al., 2010)	
	Rectangular	Tabular and graphical data available for interpolation. Correlation developed in this work, section 4.4.1	(Shah and London, 1978; Kakaç et al., 1983; Shah and Sekulic, 2003)	Numerical solutions	H1		
	Parallel plates ($\alpha^* < 0.01$)	$\overline{Nu} = 2.236\left(\frac{RePrd_h}{L}\right)^{\frac{1}{3}} + 0.9$ $for\ 0.001 < x^* < 0.01$	(Shah and London, 1978)	Numerical solution	H1		Solution for local Nusselt number derived by (Wen-Chien and Yi-Hsu, 1986) Shah and London, Table 34.
Hydrodynamically and thermally developing flow (short channels with abrupt entrance)	Circular	$\overline{Nu} = 4.36 + \frac{0.10\frac{RePrd_h}{L}}{1 + 0.016\left(\frac{RePrd_h}{L}\right)^{0.8}}\left(\frac{\mu_{bf}}{\mu_{mf}}\right)^{0.14}$	Hausen 1943 (Kakaç et al., 1983)	Empirical	Constant wall-to-fluid temp difference **Pr = 0.7** (air). For use with water, adjust equation	(Gryta and Tomaszewska, 1998; Andrjesdóttir et al., 2013)	Viscosity correction added here
	Rectangular	Tabular and graphical data available for interpolation. Correlation developed in this work, section 4.4.2	(Shah and London, 1978; Kakaç et al., 1983)	Numerical simulation			
$x^* = \lesssim 0.05$	Parallel plates ($\alpha^* < 0.01$)	$\overline{Nu} = 7.55 + \frac{0.024\left(\frac{PrRed_h}{L}\right)^{1.14}}{1 + \frac{0.0358 Pr^{0.81}}{\left(\frac{L}{d_h Re}\right)^{0.64}}}\left(\frac{\mu_{bf}}{\mu_{mf}}\right)^{0.14}$	(Kakaç et al., 1983) Stephan, 1959	Empirical relation from approximate series solution	Constant wall temperature		Corroborated by a numerical solution provided by Hwang and Fan , 1964
	Parallel plates ($\alpha^* < 0.01$)	$\overline{Nu} = \frac{0.664\left(\frac{PrRed_h}{L}\right)}{Pr^{\frac{1}{6}}}\left[1 + 6.27\left(\frac{L}{d_h Re}\right)^{\frac{4}{9}}\right]^{\frac{1}{2}}$	(Sparrow, 1955)	Analytical solution	Constant axial temperature	(Gryta et al., 1997)	Literature: Mean Nu only available for constant temp. BC, not H1 BC. Though Gryta suggests this equation can be used for Pr>2, Sparrow's equation only claims to be accurate for Pr = 10 and 50.

2.5. To accurately determine heat transfer rate in MD, existing Nusselt correlations should be modified using theoretical and experimental correction factors.

2.5.1 Existing Nusselt equations are not formulated for typical MD cassette geometry

Despite conscientious selection of Nusselt number correlations from literature, the baseline equation is not likely to describe MD channel heat transfer accurately, particularly for laboratory-scale cassettes. The literature lacks correlations to describe developing flow in a flat rectangular channel and heat transfer through one wall, a common configuration for MD cassettes. A literature review revealed numerical analyses, but no closed-form correlations for developing flow in a rectangular channel(Sparrow, 1955; Wibulswas, 1966). No Nusselt correlations exist for developing flow with peripherally varying heat transfer, which is the case for flat-sheet MD, where heat transfer occurs on one side(Incropera et al., 1986).

Nusselt correlations that describe enhanced heat transfer using a rough channel surface or membrane spacer do not exist. Use of membrane spacers in MD can significantly enhance heat transfer for laminar flow, as shown experimentally by Phattaranawik and Fane(Phattaranawik et al., 2003b; Gustafson et al., 2016). General effects of surface roughness on heat transfer is discussed in Kaviany.(Kaviany, 2001) Though typical MD membrane topography is unlikely to influence Nusselt number, the Kaviany reference can be used to determine whether the surface of a novel membrane can influence Nusselt number by inducing turbulence.

It is also likely that theoretically-based Nusselt correlations will underestimate heat transfer for small laboratory-scale MD cassettes. Experimental data is sparse for heat transfer in the entrance region of ducts, particularly for simultaneously developing flow(Sieder and Tate, 1936;

Wibulswas, 1966). Because Nusselt number is asymptotic at low x*, flow non-idealities or small changes in cassette entrance geometry can substantially affect the thermal and hydrodynamic profile development, and alter $h_f and\ h_p$ from the values predicted using standard Nusselt correlations. Limited experimental data suggests that correlations are inaccurate very close to the entrance region(Wibulswas, 1966). Despite this, numerical simulations contain little explanation of how initial conditions affect heat transfer, nor are they experimentally validated at low x*(Shah and London, 1978).

2.5.2 Resolution of potential Nusselt correlation error through application of correction factors.

Given the limitations of existing correlations, we recommend a two-step process to adjust an existing "baseline" Nusselt correlation so it accurately predicts heat transfer coefficients in a real MD cassette under a variety of experimental conditions. First, "theoretical" correction factors applied to the baseline Nusselt correlation to adjust for any incorrect geometrical, flow or boundary conditions. These theoretical correction factors yield an idealized Nusselt correlation specific to the geometry of the MD channel. The process for this is discussed in section 2.6. Then, an "empirical" correction factor is applied to correct heat transfer calculations for flow non-idealities in the particular cassette. The experimental method used to determine these cassette-dependent Nusselt correction factors is given in section 2.7.

2.6 **Application of theoretical correction factors to Nusselt number correlations**

To determine how Nusselt number will vary from a baseline correlation when channel geometry, boundary conditions, or flow development is altered, one can review the literature to find previous studies of these specific effects on a similar heat-exchange systems. Trends seen in

tabular and graphical results of these studies are assumed to hold true for MD cassette channels if the flow regime is the same. Regressions are used to relate the baseline Nusselt numbers to adjusted literature results. In the case of laminar flow, most pertinent studies were published in the decades before 1980 and not all are written in English, so it is not simple to locate, obtain, and understand source data for correlation adjustment. Fortunately, there are a few resources that aggregate data from many of these older studies, provide discussions of experimental/modeling methods and accuracy of results related to other studies. Correction factors found in section 2.6 rely heavily data from on Shah and London's 1978 *Laminar Flow Forced Convection in Ducts*(Shah and London, 1978) and Shah and Sekulic's 2003 *Fundamentals of Heat Exchanger Design*(Shah and Sekulic, 2003) A resource that includes source data for turbulent flow is Kakac, Shah and Aung's, 1987 *Handbook of Single Phase Convective Heat Transfer*(Kakaç et al., 1987)

Calculations of correction factors based on interpolation of tabular data can be done on a case-by-case basis. Here, we provide a few generalized correction factors for rectangular laminar-flow MD channels based on a review of existing literature. Though the correction factors below are specific to laminar flow in rectangular feed and permeate channels alongside a flat sheet membranes, methods to create these correction factors can be extended to other membrane/cassette geometries.

The baseline equation chosen for this analysis is the Sieder-Tate *Nu* correlation (highlighted in Table 2.1). (Sieder and Tate, 1936) Sieder-Tate was chosen because it was trained using experimental heat flux data taken from fluids in a countercurrent flow configuration, which approximates constant heat flux and is similar to most MD cassettes. The Sieder-Tate experiments also used thermally developing flow, which is relevant to most flat-sheet benchtop MD configurations. Despite these strengths, the S-T correlation must be adapted. The channel

used in the original experiments was circular with heat flux occurring symmetrically around the tube circumference, not rectangular with heat flux from one wall as is common in MD. And though the flow was thermally developing, a "calming section" of channel upstream of the experimental region ensured flow was fully hydrodynamically developed. Theoretical corrections are proposed below to render the correlation applicable for hydrodynamically developing flow in a rectangular duct with heat flux at only one wall.

2.6.1 *Correction factor for channel cross-sectional geometry*. The Sieder-Tate Nusselt correlation can be adapted to predict Nusselt for a rectangular channel with a given aspect ratio. This is done by comparison of the baseline Nusselt numbers to those numerically-simulated by Wibulswas(Wibulswas, 1966; Shah and London, 1978) for thermally developing flow in rectangular ducts of varying aspect ratio with constant heat flux at the walls. Inspection of this data reveals Nusselt number for rectangular ducts deviates from circular duct Nusselt numbers as a function of both aspect ratio, α^*, and entry length, x^*. As also shown by Shah and Sekulic (p503), very near the channel entrance ($x^*<0.001$) the Nusselt correction factor for rectangular ducts is solely a function of the aspect ratio. Specifically, it is a linear function of the fully developed channel friction factor for a rectangular duct raised to the 1/3 power, $(f \cdot Re)^{\frac{1}{3}}$.(Shah and Sekulic, 2003) Farther from the channel entrance, $0.001 < x^* < 0.05$, thermal boundary layer development becomes more complex and the circular-to-rectangular duct correction factor is not linear with$(f \cdot Re)^{\frac{1}{3}}$. For this work, we regress the ratios of Wibulswas rectangular-duct Nusselt numbers to Sieder-Tate circular-duct Nusselt numbers to provide an approximate generalized equation for the rectangular duct correction factor (Eq. 17a) that yields < 3% error compared to Wibulswas' tabular data. Note the suggested restrictions on the use of this empirical equation.

For x* > 0.05, correlations for fully developed flow should be used. See Appendix A.3 for correlation calculations and validation against tabular data.

$$To\ estimate\ Nu\ for\ themally\ developing\ flow\ of\ rectangular\ channels\ of\ aspect\ ratio\ \alpha^*\ from\ the\ Seider-Tate\ correlation:$$
$$\overline{Nu_{rect}} = \overline{Nu_{Sieder-Tate}}\left(C(f\cdot Re)^{\frac{1}{3}}\right)$$

$$where\ (f\cdot Re)\ is\ a\ constant\ and\ a\ function\ of\ channel\ aspect\ ratio\ \alpha^*\text{:(Shah and Sekulic, 2003)} \quad (17a)$$
$$(f\cdot Re) = 24\left(1 - 1.3553\alpha^* + 1.9467\alpha^{*2} - 1.7012\alpha^{*3} + 0.9564\alpha^{*4} - 0.2537\alpha^{*5}\right)$$

$$C = 0.392\ for\ x^* < 0.001$$

$$C = 0.392 + x^*\left(-196.07\alpha^{*5} + 441\alpha^{*4} - 360.99\alpha^{*3} + 145.29\alpha^{*2} - 33.734\alpha^* + 5.2873\right)\ for\ 0.001 < x^* < 0.05$$

2.6.2 Correction factor to account for simultaneously developing flow. If the entrance to the feed and permeate channels in the membrane cassette does not contain a smoothing section prior to membrane exposure, the fluid hydrodynamic and thermal profiles will develop *simultaneously* alongside the membrane. This causes *average* Nusselt number (and flux) to be higher than predicted by the Sieder-Tate correlation, or any other correlation trained on thermally developing, but hydrodynamically developed flow. This is because the velocity gradient at the wall near an abrupt channel entrance is very steep and thus the hydrodynamic boundary layer is very thin. Convective heat transfer resistance is proportional to boundary layer thickness, which means h_f, h_p, and Nusselt number are inversely proportional to boundary layer thickness. The magnitude of this increase in average *Nu* is dependent on dimensionless channel length, x*, and on the fluid Prandtl number, the ratio of momentum diffusivity to thermal diffusivity of a fluid. For high Prandtl numbers the hydrodynamic profile develops quickly in comparison to the

thermal profile, and the effect on Nusselt of simultaneously developing flow will be less pronounced than for lower Prandtl numbers. At Pr = ∞, the hydrodynamic profile develops instantaneously and the Nusselt number correlation is the same as the correlation for thermally developing flow.

Literature data exists that compares Nusselt number for simultaneously developing flow in both circular and rectangular channels at different x* and *Pr*. Correction factors for Nu estimated using the Sieder-Tate correlation (or any other Nusselt correlation designed for thermally developing flow) can be made by interpolating tabular data. We use tabular data from Wibulswas to develop general empirical equation to calculate a correction factor for simultaneously developing flow in a rectangular duct. By plotting the ratio of tabular correction factor $\frac{Nu_{sim.devel}}{Nu_{therm.devel}}$ vs x*, we find that for Pr ≥ 0.72, the correction factor is linearly correlated with ln(x*). We also find the correction factor is correlated linearly with $Pr^{-1/3}$. Modeled predictions of $Nu_{sim.devel}$ using the resulting equation, 17b, are valid for simultaneously developing laminar flow with constant axial heat flux at the channel wall. The equations yield a < 2.5% error compared to the Wibulswas tabular data. See Appendix A.4 for calculations and correction factor validation

For estimating simultaneaously developing flow of ***rectangular*** *channels, any Prandtl,*

$$\overline{Nu_{sim.\,devel}} = \overline{Nu_{therm.\,devel}} \left[\left(\frac{-0.0633}{Pr^{\frac{1}{3}}}\right)\ln(x^*) + 1\right] \quad (17b)$$

2.6.3 Correction factor to account for heat flux from only one wall: Nusselt number is highest when heat transfer occurs on all four sides of a rectangular duct. Nusselt numbers for fully-developed laminar flow in rectangular ducts with one or more adiabatic walls and axially

constant heat flux at the non-adiabatic walls were calculated numerically by Schmidt and compared with Nusselt numbers for heat flux at four walls in Shah & London.(Schmidt and Newell, 1967; Shah and London, 1978) The data show that Nusselt number varies as function of duct cross sectional aspect ratio, and the location and number of adiabatic walls. Polynomial correlations can be made of existing tabular data to show the relationship between fully developed *Nu* and rectangular duct aspect ratio. Such a correlation was presented by Shah and Sekulic for Nusselt numbers with constant heat flux at 4-walls of a rectangular duct, is verified in Appendix A.5, and is reproduced as Eq 17c.(Shah and Sekulic, 2003) We derive a similar Nusselt number correlation from the Schmidt data for heat transfer at one long duct wall, the typical geometry for MD using flat sheet membranes (Eq 17d, details in Appendix A3).

Tabulated data for developing flow in rectangular ducts with constant heat flux at one wall was not found. However, experimental and modeled data presented in a figure by Kostic and Hartnett(Kostic and Hartnett, 1986) indicate that the difference between 4-wall heat transfer Nusselt numbers and 1-wall heat transfer Nusselt numbers remains approximately constant regardless of flow development.(Kostic and Hartnett, 1986) Therefore, in the absence of better literature data for the case of heat transfer at one wall, the Nusselt correction factor will be constant for a given duct aspect ratio and should be subtracted from, not multiplied with the Nusselt number for 4-wall heat transfer (Eq 17 e).

$$Nu_{rect,\,fully\,devel.,\,4\,walls\,heat\,flux} = 8.235(1 - 2.0421\alpha^* + 3.0853\alpha^{*2} - 2.4765\alpha^{*3} + 1.0578\alpha^{*4} - 0.861\alpha^{*5}) \tag{17c}$$

$$Nu_{,rect,\,fully\,devel.,\,1\,wall\,heat\,flux} = 5.385\left(1 - 1.0626\alpha^* + 0.933\alpha^{*\,*2} - 0.3662\alpha^{*3}\right) \tag{17d}$$

$$Nu_{rect,\ simul.\ devel\ flow,\ 1\ wall\ heat\ flux} = Nu_{rect,\ simul.\ devel\ flow,\ 4\ walls\ heat\ flux} - (Nu_{rect,\ fully\ devel.\ 4\ walls\ heat\ flux} - Nu_{rect,\ fully\ devel.,\ 4\ walls\ heat\ flux}) \quad (17e)$$

2.6.3 No correction factors are needed to account for mass transport at membrane surface

Mass transport across a membrane can influence Nusselt number for adjacent fluid streams. If fluid "suction" into the membrane occurs, the hydrodynamic boundary layer is compressed and this decreases convective heat transport resistance. The opposite can occur if fluid is "injected" into the stream from the wall; heat transport resistance increases and Nusselt number decreases. The magnitude of this effect has been studied extensively in heat transfer literature(Kaviany, 2001) and for laminar flow, boundary layer deformation is dependent on rate of fluid suction/injection into the interface quantified by the dimensionless blowing parameter, *B*. (Eq 18)

$$B = \frac{v_{x,bulk}}{v_{wall}} Re_{x,bulk}^{\frac{1}{2}} \quad (18)$$

B compares the velocity and Reynolds number of the bulk stream parallel to the wall with the velocity of the injected/suctioned fluid normal to the wall. If *B* less than ~0.1, then the effect of mass transport across the membrane on the laminar boundary layer is negligible.(Kaviany, 2015) In MD, liquid velocities normal to membrane range from approximately $10^{-6.5}$ - $10^{-4.1}$ m/s, so *B* is more than an order of magnitude lower than the threshold value of 0.1. Therefore no correction factor is needed for Nusselt number correlation as a result of mass transfer across the MD membrane. This conclusion is supported by previous MD research.(Qtaishat et al., 2008)

2.6.4 *Modified Sieder-Tate Nusselt equation for flat-sheet membranes in rectangular MD channels undergoing simultaneous hydrodynamic and thermal laminar flow development.* If MD system design and operating conditions indicate a need for all of correction factors from equations 17a-e, Eq (19) may be used to estimate Nusselt number in the feed and permeate channels.

$$Nu_{rect,\ simul.\ devel\ flow,\ 1\ wall\ heat\ flux} = \tag{19}$$

$$1.86(x^*)^{-1/3}\left(\frac{\mu_{bf}}{\mu_{mf}}\right)^{0.14}\ \left(C(fRe)^{\frac{1}{3}}\right)\ \left[\left(\frac{-0.0633}{Pr^{\frac{1}{3}}}\right)\ln(x^*)+1\right]\ -$$

$$(Nu_{rect,\ fully\ devel.\ 4\ walls\ heat\ flux}\ -\ Nu_{rect,\ fully\ devel.,\ 4\ walls\ heat\ flux})$$

The aggregate effect of all correction factors with respect to dimensionless channel length and rectangular duct aspect ratio is displayed in Figure 2.7. For short channels, Nusselt number is predicted to be substantially higher than the Sieder-Tate baseline. The effect increases for wide, flat cassette channels because thinner channels require the hydrodynamic and thermal gradient between the bulk fluid and the channel wall to be steeper, therefore heat transfer is more efficient. Comparison of Figure 2.5A and 2.5B reveals the feed side of the MD cassette is predicted to deviate more from the Sieder-Tate correlation than the permeate side. This is due to the difference in Prandtl number between warm and cold water. For warmer feed water, Prandtl number is lower, so the hydrodynamic profile in the channel develops more slowly and convective heat transfer resistance is lower in short channels.

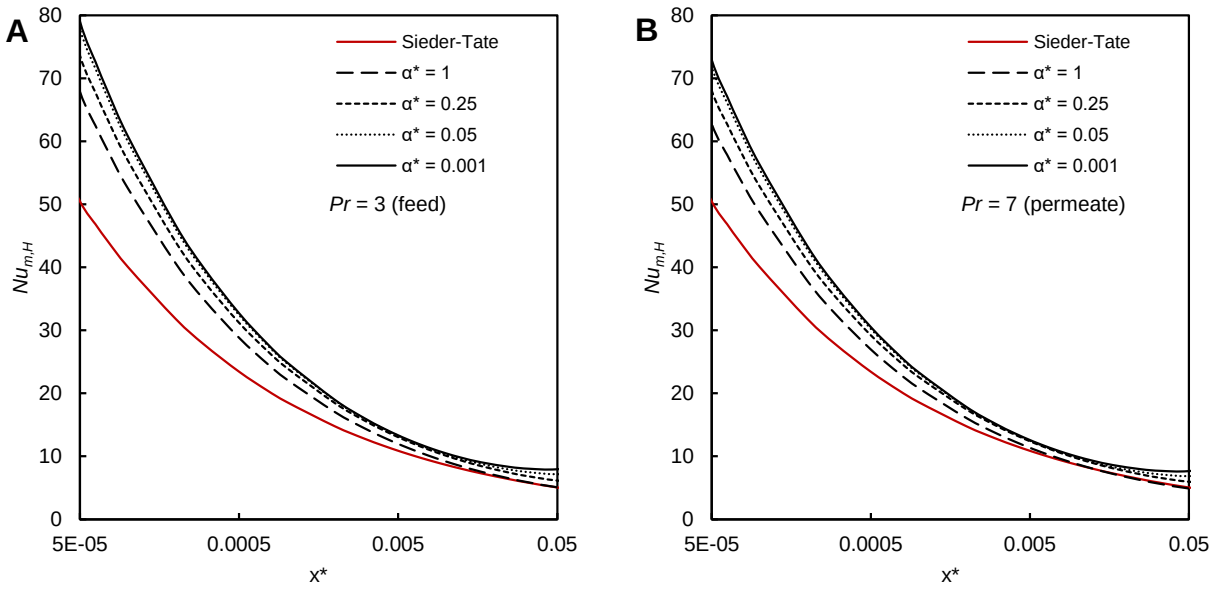

Figure 2.7 Combined effect of correction factors on Nusselt prediction in MD channels. A) Permeate channel (Bulk temperature = ~20°C) and B) Feed channel (Bulk temperature = ~60°C)

As discussed in section 2.5, modification of existing Nusselt correlations using theoretical correction factors is important but not sufficient to accurately characterize thermal profiles in feed and permeate streams of real membrane cassettes. Experimental validation of Nusselt number is particularly important for newly-designed membrane cassettes and small bench-top cassettes (with low x*), where channel entrance configuration and flow non-idealities may cause Nusselt to deviate from theoretical predictions.

2.7 EXPERIMENTAL method to determine cassette-dependent Nusselt correction factor (NuCF)

The following section describes a novel experimental method that uses membrane permeability as a benchmark to determine true feed and permeate stream heat transfer rates. First, the theoretical background for the method is explained. Then the method is demonstrated for a small benchtop DCMD cassette with abrupt channel entrance configuration, and preliminarily

validated by performing the same analysis on published experimental data collected for the same membrane from a different cassette used by a different research group.

2.7.1 Background: Calculation of theoretical MD membrane permeability

Vapor transport through an MD membrane is modeled using the kinetic theory of gases. There are four potential transport mechanisms for vapor molecules in a porous medium: viscous transport, ordinary molecular diffusion (OMD), Knudsen diffusion and surface diffusion. Viscous transport is driven by total pressure gradient in the pores, ∇P_{tot}. DCMD systems are designed such that head pressure on feed and permeate sides of the membrane are approximately equal, so viscous transport is negligible. The remaining transport mechanisms are diffusive and driven by species concentration gradient, though this driving force is expressed as the vapor pressure gradient ∇p_{vap} (analogous to the concentration gradient by the ideal gas law). The three diffusive transport mechanisms are distinguished by the different resistive forces vapor molecules are likely to encounter in the porous material. For OMD transport, progress of vapor molecules through the pores is limited by collisions with other molecules in the pore space. In Knudsen diffusion, transport resistance is due vapor molecule collisions with the membrane material. Sorption of vapor molecules to the membrane surface and subsequent diffusion along the pore walls is limited by the chemical affinity of the vapor molecule for the membrane material. In MD processes, interaction between the lyophobic membrane material and transporting vapor is low by design. Therefore surface diffusion is considered negligible for most MD processes.

For very small membrane pores, Knudsen diffusion dominates and for large pores, OMD dominates. The dimensionless Knudsen number, Kn, is used to determine whether vapor

molecules in a given membrane primarily undergo Knudsen diffusion, OMD, or both. Kn is defined as mean molecule path length, λ, divided by characteristic pore diameter, d_{pore}. The pore size range in which both transport mechanisms are relevant is approximately $0.01 \lesssim Kn \lesssim 10$. For a membrane at ambient pressure with $T_{avg} = 40°C$, this corresponds to $13nm \lesssim d_{pore} \lesssim 13\ \mu m$, a range which encompasses the mean pore sizes of MD membranes.

Original and updated versions of the Dusty Gas Model (DGM) provide a framework for calculating the contributions of OMD and Knudsen diffusion in the membrane(Mason and Malinauskas, 1983; Lawson and Lloyd, 1997; Khayet, 2011; Field et al., 2013). According to the DGM, MD mass flux, $\boldsymbol{J_w}$, is a function of driving force, ∇p_{vap} multiplied by the sum of the diffusive resistances. These resistances are inversely proportional to the effective vapor diffusivity, $D_{i,e}$ and are a function of thermophysical vapor characteristics and membrane structure. Effective Knudsen and OMD diffusivity of water vapor in the membrane are given as equations 20 and 21:

$$D_{w,e}^{knudsen} = \frac{2r_{pore}\varepsilon}{3\tau}\bar{u} = \frac{8r_{pore}\varepsilon}{3\tau}\sqrt{\frac{RT}{2\pi M_w}} \tag{20}$$

$$D_{wa,e}^{OMD} = \frac{\varepsilon}{\tau}P_{tot}D_{wa} \tag{21}$$

The variable $\bar{u}$ is the mean speed of vapor molecules and D_{wa} is the diffusivity of water in air, calculated using an empirical formula. M_w is the molecular weight of water, P_{tot} is the total pressure in the pores, and the remaining variables describe membrane structure: r_{pore} is the average pore radius, ε is the porosity and τ the tortuosity of the membrane. For this research, the

empirical correlation developed by Mason and Marrero(Marrero and Mason, 1972) is used (equation 21):

$$D_{wa} = 1.87 * 10^{-10} T_{avg}^{2.072} \ [\frac{m^2}{s} @ 1\ atm] \quad (22)$$

Equations 23 and 25 present the classic DGM equation for mass transport and the updated form suggested recently by Field et.al (Field et al., 2013). Field argues that the effective OMD diffusivity should increase proportionally with the Knudsen number because, at any given moment, molecules undergoing Knudsen diffusion are not experiencing molecule-molecule collisions. This reduces the effective total pressure in the membrane pores therefore will decrease resistance to OMD.

If the vapor flux equations are simplified by substitution of $\Delta p_{vap}/\delta$ for ∇p_{vap}, then a term for the theoretical intrinsic membrane permeability, $B_{w,i,theo}$ can be defined as: $J_w = B_{w,i,theo}\Delta p_{vap}/\delta$. Equations 24 and 26 display DGM expressions for $B_{w,i,theo}$.

Classic Dusty Gas Model

$$J_{w,DGM} = -\frac{1}{RT}\nabla p_{vap}\left(\frac{1}{D_{w,e}^{knudsen}} + \frac{p_a}{D_{w,a,e}^{OMD}}\right)^{-1} \approx \frac{\Delta p_{vap}}{RT\delta}\left(\frac{1}{D_{w,e}^{knudsen}} + \frac{p_a}{D_{wa,e}^{OMD}}\right)^{-1} \quad (23)$$

$$B_{w,i,DGM} = \frac{1}{RT}\left(\frac{1}{D_{w,e}^{knudsen}} + \frac{p_a}{D_{wa,e}^{OMD}}\right)^{-1} \quad (24)$$

Modified DGM (Field)

$$J_{w,DGM-Field} = -\frac{1}{RT}\nabla p_{vap}\left(\frac{1}{D_{w,e}^{knudsen}} + \frac{p_a}{(\mathbf{1}+\boldsymbol{Kn})D_{w,a,e}^{OMD}}\right)^{-1} \approx \frac{\Delta p_{vap}}{RT\delta}\left(\frac{1}{D_{w,e}^{knudsen}} + \frac{p_a}{(\mathbf{1}+\boldsymbol{Kn})D_{wa,e}^{OMD}}\right)^{-1} \quad (25)$$

$$B_{w,i,DGM-Field} = \frac{1}{RT}\left(\frac{1}{D_{w,e}^{knudsen}} + \frac{p_a}{(\mathbf{1}+\boldsymbol{Kn})D_{wa,e}^{OMD}}\right)^{-1} \quad (26)$$

Here $p_a$represents the partial pressure of air in the membrane pores. Using these expressions, one can model the theoretical variation in membrane permeability with membrane structural properties and MD system conditions. For a given membrane structure, only modest $B_{w,i}$ variation is projected to occur under the range of typical MD conditions. Inspection of equations 24 and 26 reveal the primary system parameter controlling $B_{w,i,theo}$ is the temperature in the membrane pores on an absolute scale (K) (Average membrane temperature ($T_{avg,m}$) is used to calculate $B_{w,i,theo}$.) Figure 2.8 illustrates the theoretical relationship of $T_{avg,m}$ to $B_{w,i}$ for two different commercial membranes. Individual contributions of OMD and Knudsen diffusion to membrane $B_{w,i}$ are dependent on pore size, therefore the relationship between T_{avg} and total permeability will vary between membranes. As pore size increases, DGM estimations of total permeability approach $B_{w,i,OMD\ only}$. Figure 2.8 also plots the theoretical maximum intrinsic permeability of a membrane at atmospheric pressure, calculated using structural parameters r = ∞ and ε = τ = 1 in the diffusivity equations 20 and 21, and is analogous to an air gap.

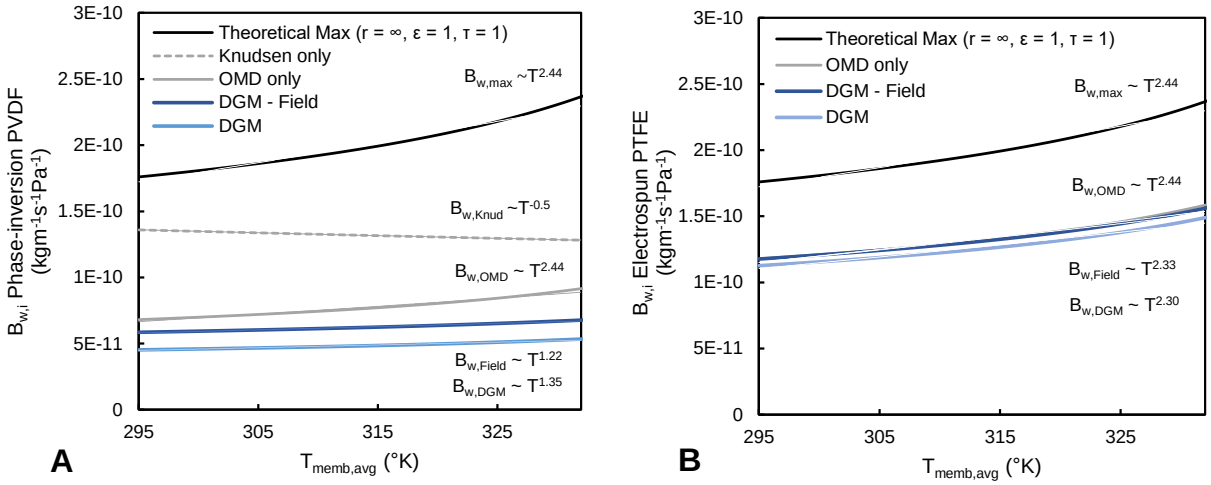

Figure 2.8 The relation of theoretical membrane permeability, $B_{w,i,}$ to average membrane temperature for two different commercial membranes. A) Phase inversion PVDF (Millipore GVHP) with r = 0.12 μm , ε = 0.62, τ = 1/ε and B) Electrospun PTFE membrane (Zeus Filtriq) with r ≈ 1.37 μm, ε= 0.81, τ = 1/ε

Therefore, any experimental parameter that affects $T_{avg,m}$, such as bulk stream temperatures, $T_{f,b}$ and $T_{p,b}$, will affect $B_{w,i}$. Conversely, if an experimental parameter does not significantly effect $T_{avg,m}$, $B_{w,i}$ should not be affected. For example, in a countercurrent membrane cassette with symmetrical channels and identical feed and permeate flow rates, variation in these flow rates (i.e. Reynolds number), should not have a significant influence on T_{avg}.

2.7.2 Experimental method of determining MD membrane permeability

As discussed in section 2.3.2, membrane $B_{w,i,}$ (and Q, T_{fm}, T_{pm}) can also be determined experimentally by inputting measured vapor flux, MD system conditions, and select membrane parameters into a system of mass and heat transport equations (Eq 1-5). Advantages of experimental determination of membrane permeability over theoretical methods (section 2.7.1), are that it does not require extensive in(i.e. no error is introduced by simplifying assumptions implicit in DGM equations, such as that the membrane is symmetrical and the pores are uniform, cylindrical and isolated).

However, if cassette h_f *and* h_p are calculated inaccurately by use of an inappropriate *Nu* correlation or because flow non-idealities exist in the cassette, then calculated $B_{w,i,\,experimental}$ may have several flaws. For example, if estimated *Nu* is too low, $B_{w,i,\,experimental}$ will be overestimated and highly variable with T_{avg}. This effect can be seen in Figure 2.9. Additionally, $B_{w,i,\,experimental}$ may appear to be dependent on irrelevant system variables, such as average cassette Reynolds number if incorrect *Nu* correlations are used. *Comparison of* $B_{w,i,\,theoretical}$ *with* $B_{w,i,\,experimental}$ *is the premise for the following method to determine true heat transfer coefficients in a membrane cassette.*

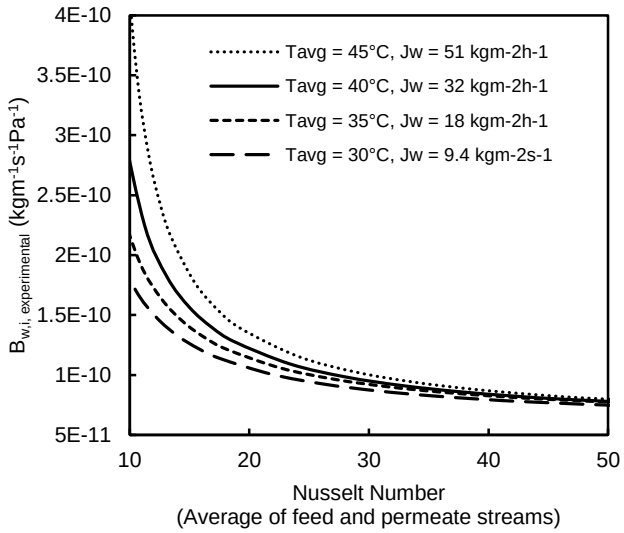

Figure 2.9 Model of $B_{w,i,experimental}$ of commercial membrane (Millipore GVHP) vs average Nusselt Number, given a measured experimental flux at four different average membrane temperatures. Calculated $B_{w,i}$ will change significantly based on Nusselt number

2.7.3 Method overview: Determining cassette-dependent Nusselt correction factor (NuCF)

Idealized Nusselt correlations can be "calibrated" to a specific membrane cassette by the following three steps:

1. **Compare DCMD flux data across temperature and cassette flow rates for a single, well-characterized membrane.** In the first series of collected DCMD data, average membrane temperature, T_{avg}, is varied, and in the second series, feed and permeate flow rates are varied. The analysis is performed on a membrane with experimentally characterized thickness, porosity, pore size, and tortuosity so these metrics can be used to calculate $B_{w,i,theoretical}$. This analysis assumes flow configuration is counter-current with identical feed and permeate channel dimensions, and that data points are collected within a single feed/permeate flow regime (laminar, turbulent, or transitional).

2. **Solve for experimental membrane permeability, $B_{w,i,\,experimental}$, and $B_{w,i,theoretical}$ then regress these vs. T_{avg} and vs. Re_{avg}.** Comparison of power regression exponents between $B_{w,i,\,experimental}$ and $B_{w,i,theoretical}$ curves will reveal whether theoretical Nusselt correlations used to calculate $B_{w,i,\,experimental}$ have adequately quantified heat transfer in the feed and permeate streams. If one or both of the $B_{w,i,\,experimental}$ curves deviate from theoretical predictions, a Nusselt correlation correction factor (NuCF) is required to accurately account for non-idealities in the cassette.

3. **Determine the cassette-dependent NuCF for multiplication with theoretical Nusselt correlations.** If a NuCF is required, it may be a constant, C_1, or factor that depends on other system variables, such as $C_1 Re^{C_2}$. Mass and heat transport equations should be re-solved with systematic variation of C_1 and C_2 until $B_{w,i,\,experimental}$ follows theoretical trends.

Determining and applying a cassette-dependent NuCF will allow experimental MD data from a given cassette to be analyzed and reported accurately, regardless of membrane type or feed/permeate flow rates (provided the flow rates fall within the same laminar or turbulent regime in which NuCF was characterized). Sections 2.7.4-6 discuss the method in detail and provides example NuCF calculations for a cassette with abrupt entrance and exit configuration. For comparison and preliminary validation, a NuCF analysis is also performed using published data collected by a different research group.(Srisurichan et al., 2006)

2.7.4 NuCF data collection: methods and results

Membrane selection and characterization: An ideal membrane for the NuCF analysis has a symmetrical cross-section, uniform physical or chemical attributes between membrane coupons,

and no change in morphology when DCMD conditions are varied. Membranes must be well-characterized so that $B_{w,i,theoretical}$ and $B_{w,i,experimental}$ can be computed. Membrane structural attributes needed to calculate effective diffusivities (Eq. 20 and 21) for input into $B_{w,i,theoretical}$ equations (Eq. 24 or 26) are thickness (δ), pore radius (r), and porosity (ε), tortuosity (τ). Membrane bulk thermal conductivity (k_m) and δ are needed to solve the system of mass and heat transport equations for $B_{w,i,experimental}$.

NuCF analyses were conducted using two different commercial membrane types. A phase inversion PVDF membrane (Millipore GVHP) was used both in this work and in the previously-published work by Srisurichan. New DCMD data was also collected using an electrospun PTFE membrane (Zeus Filtriq), so NuCF could be compared for two membrane types on the same cassette. Theoretically, the NuCF is a function of the cassette geometry and should be the same (or very similar) for flat sheet membranes regardless of the membrane type. Membranes were characterized using scanning electron microscopy, gravimetric measurements, capillary flow porometry and contact angle goniometry. Evaluation methods for δ, r, ε, τ, and k_m are described in detail in Chapter 4 of this dissertation. Characterization of pore radius for the electrospun membrane was made using an empirical correlation with fiber diameter and porosity as inputs, described in Chapter 3. Table 2.3 displays relevant membrane properties:

Table 2.3. Characterization of commercial phase inversion PVDF membrane (Millipore GVHP) and electrospun PTFE membrane (Zeus Filtriq). Refer to Chapter3 of this dissertation for details on membrane fabrication

	Phase-inversion PVDF	**Electrospun PTFE**
thickness[a] (μm)	109 ± 5	62 ± 6
porosity[b] (%)	62.2 ± 3.1	81.8 ± 4.9
fiber diameter[a] (μm)	N/A	0.94 ± 0.66
avg pore diameter,[c,d] (nm)	244	2730
SD pore diameter[c,d] (nm)	387	314
thermal conductivity[e] ($Wm^{-1}K^{-1}$)	0.096	0.065
tortuosity[e]	1.61	1.22
contact angle[g]	147 ± 2.8°	151 ± 1.3°

a) SEM
b) gravimetric analysis
c) capillary flow porometry, GalwickTM fluid (phase inversion membrane)
d) Pore-size estimated from literature based on fiber characteristics. See appendix B.3
e)Theoretical calculation

DCMD experiments: To show the effectiveness of theoretical (and adjusted) Nusselt correlations in a range of DCMD operational conditions, two series of DCMD flux data should be collected. In one series, $T_{avg,memb}$ is varied and channel flow rates are held constant. In the second series, feed and permeate flow rates are varied with constant $T_{f,b}$ and $T_{p,b}$ (to approximate constant average $T_{avg,memb}$). Each series should have at least four distinct data points, and experimental replicates are recommended for confidence in $B_{w,i,experimental}$ calculations. Experimental parameters required for calculation of $B_{w,i,theoretical}$ and $B_{w,i,experimental}$ are:

permeate flux, J_w, average bulk feed and bulk permeate temperature, $T_{f,b}$ and $T_{p,b}$ (in-cassette: requires pre- and post- cassette sensors on feed and permeate sides), feed and permeate flow rates, $\dot{q}_f \; and \; \dot{q}_p$, feed stream solute concentration, cassette channel dimensions and exposed membrane dimensions. To ensure transport model inputs are valid, membrane salt rejection should be close to 100% and feed/permeate stream pressure differential should be close to zero. Periodic permeate conductivity readings and measurements from in-stream pressure transducers can validate these assumptions.

In this work we performed DCMD experiments using a small cassette with abrupt entrance and exit configuration and 0.01 x 0.04 x 0.002 m feed and permeate channels. Appendix C.3 contains an image and design schematics of the membrane cassette, along with a detailed description of the bench-top DCMD system. The following system conditions were chosen for the DCMD experiments:

Series 1: $T_{p,b}$ =20°C (constant), $T_{f,b}$ = 40, 50, 60, 70°C. Feed and perm velocity = 0.25 m/s

Series 2: Feed and perm flow rates = 0.11, 0.15, 0.21, 0.25 m/s, $T_{p,b}$ =20°C, $T_{f,b}$ = 60°C

For all experiments, feed concentration was 35 g/L NaCl. Salt rejection for all membranes was greater than 99.9%, and total pressure differential between feed and permeate streams was < 10 mbar.

Using their own benchtop DCMD system and membrane cassette with 0.04 x 0.1 x 0.0025 m feed and permeate channels, Srisurichan et. al. collected and reported flux data for an identical phase inversion PVDF membrane (Millipore GVHP) under system condition similar to Series 1 in this study. Reported $T_{p,b}$ and $T_{f,b}$ settings are the same, whereas feed and perm velocity = 0.23 m/s and pure water was used in both the feed and permeate solutions. Pressure differential

between feed and permeate streams was not reported by Srisurichan, but is assumed negligible for the purposes of this analysis. The DCMD flux results for each experiment series are presented in Figure 2.10.

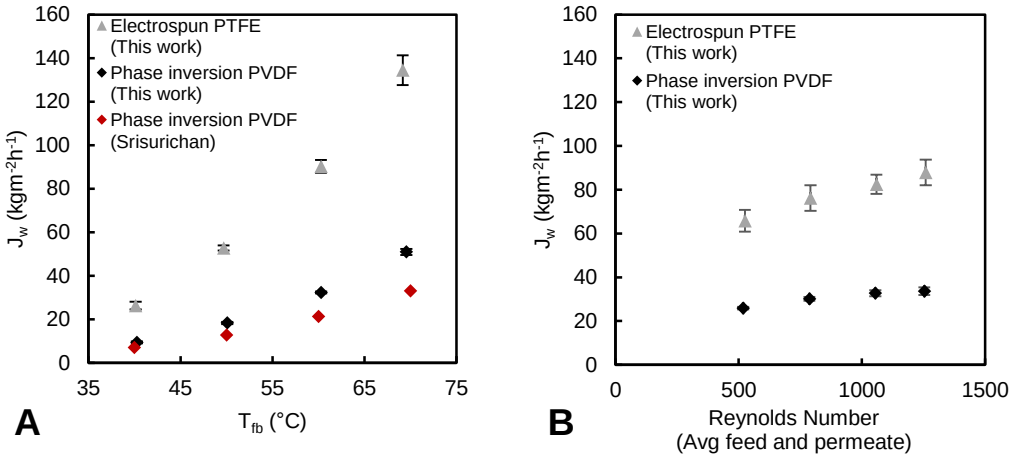

Figure 2.10 Flux results for two membrane types with A) varying bulk feed temperature. B) varying cassette flow rate. Note that flux vs. Re is not included for Srisurichan because these data were not reported. For all experiments, $T_{p,b}$ = 20°C. For Series A experiment feed and permeate flow rates = 0.3 LPM ($Re_{avg} \approx 1200$). For Series B experiments, $T_{p,b}$ = 60°C

As expected, permeate flux for both membranes increases as bulk feed temperature and cassette flow rate increases. Collected experimental and membrane characterization data are now used to model $B_{w,i,theoretical}$ and $B_{w,i,experimental}$.

2.7.5 Comparison of $B_{w,i,theoretical}$ and $B_{w,i,experimental}$: Evaluation of theoretically-based Nusselt correlations

To determine whether theoretical Nusselt correlations adequately describe heat transfer for a given cassette, $B_{w,i,experimental}$ *and* $B_{w,i,theoretical}$ values are calculated for each experimental run. It is not expected that calculated $B_{w,i,experimental}$ *and* $B_{w,i,theoretical}$ will be equal, because the membrane structural parameters used in DGM modeling are simplified (*r*) or

difficult to characterize accurately (τ). Also, the DGM diffusivity equations are formulated based on cylindrical, isolated pore geometry, which is not the case for most real membranes tested in MD. Instead, we rely on the validity of the kinetic gas theory used in $B_{w,i,\,theoretical}$ calculations to determine whether the series of $B_{w,i,\,experimental}$ values are behaving according to theory. $B_{w,i,\,experimental}$ and $B_{w,i,\,theoretical}$ are regressed separately versus $T_{avg.membrane}$ and versus Re_{avg}. Power regressions are used compare the relationships of $B_{w,i,\,experimental}$ and $B_{w,i,\,theoretical}$ with the dependent variables, as theory typically predicts a non-linear relationship of $B_{w,i}$ with $T_{avg.membrane}$ (Fig 2.8). No significant relationship is expected between membrane permeability and Re_{avg}. In cassettes with countercurrent flow and equal feed and permeate velocities, average vapor properties in the membrane pores are not predicted to vary significantly with flow rate, as long as average bulk temperatures are not varied. If the computed exponents for $B_{w,i,\,experimental}$ regressions match those for $B_{w,i,\,theoretical}$ regressions, then the Nusselt correlations model heat transfer consistently well for all experimental conditions, and do not need to be modified.

In this work, $B_{w,i,theoretical}$ is solved using Eq. 26, the DGM method modified by Field. $B_{w,i,\,experimental}$ is modeled using mass and heat transport equations (Eq 1-5) with h_f and h_p derived from theoretical Nusselt correlations. We examine the effectiveness of the Sieder-Tate Nusselt correlation (Table 2.1), the modified-Sieder-Tate correlation (Eq 19) and an equation recommended by Phattaranawik for laminar flow(Phattaranawik et al., 2003c), that was developed by Hausen in 1945 (Eq 27).

$$Nu_{Hausen} = 4.36 + \frac{\frac{0.036 Re Prd_h}{L}}{1+0.0011\left(\frac{RePrd_h}{L}\right)^{0.8}} \qquad (27)$$

Figure 2.11 shows calculated $B_{w,i}$ values and regression curves for membranes in each experimental data series.

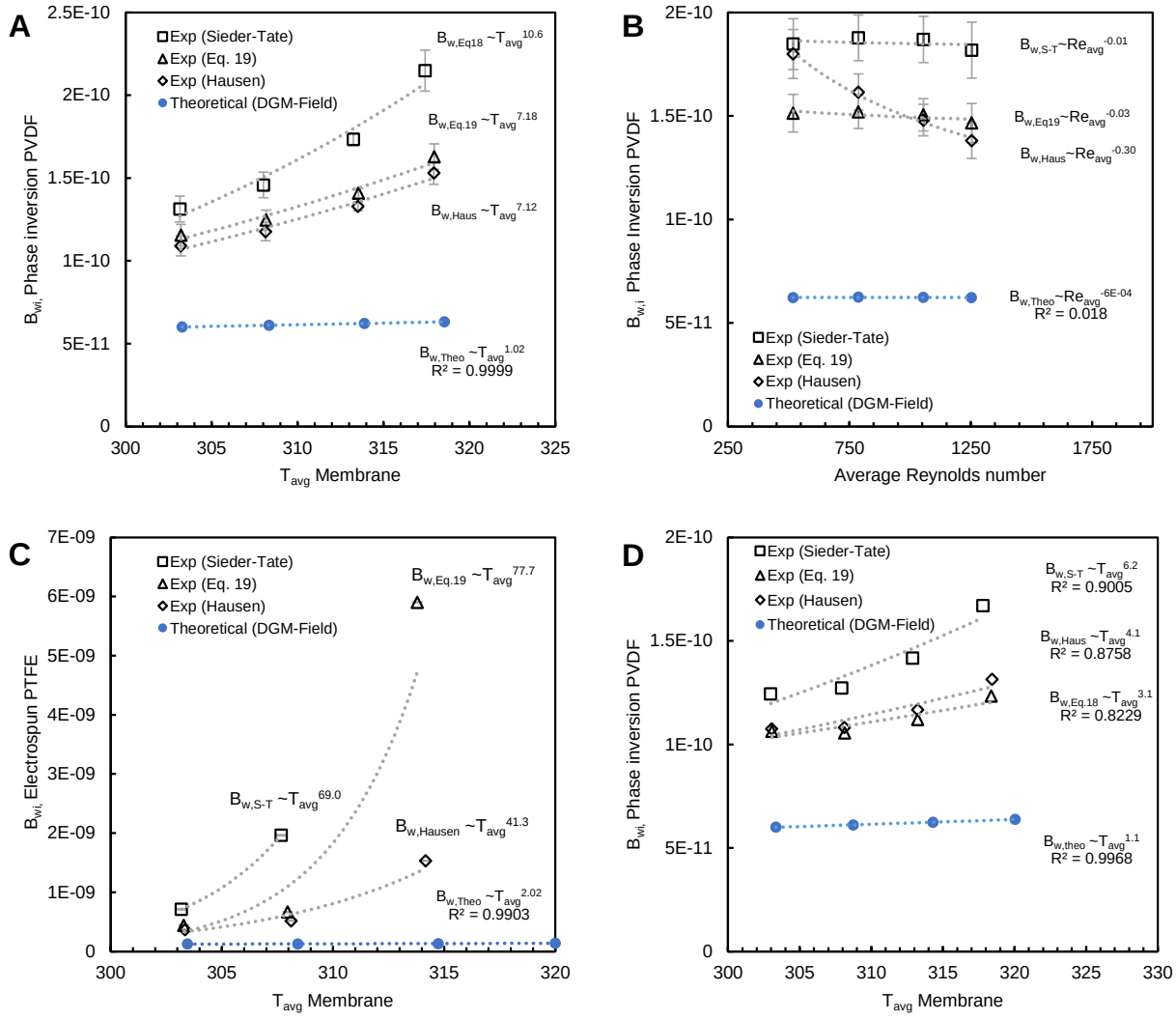

Figure 2.11 Power regressions of $B_{w.i,experimental}$ and $B_{w,i,theoretical}$ for different DCMD experiment series. $B_{w.i,experimental}$ calculated using three separate Nusselt correlations for comparison A) $B_{w,i}$ vs T_{avg} for phase inversion PVDF membranes B) $B_{w,i}$ vs Re_{avg} for phase inversion PVDF membranes. C) $B_{w,i}$ vs T_{avg} for electrospun PTFE membranes. D) $B_{w,i}$ vs T_{avg} for phase inversion PVDF membranes (data collected by Srisurichan et al)

Regarding all plots, 2.11a-d, $B_{w,i,\,experimental}$ values calculated using theoretical Nusselt correlations were far higher than the theoretical values, even exceeding the theoretical maximum

intrinsic permeability for MD (shown in Fig 2.8) in the case of the electrospun membrane. This suggests the h_f and h_p calculated using theoretical Nu correlations are lower than real heat transfer coefficients in the cassettes. The regressed relationship of $B_{w,i,\,experimental}$ to the dependent variables provides further evidence for the inadequacy of the theoretical Nusselt correlations in these cassettes. In the case where T_{avg} is varied, PVDF membrane permeability should be approximately linear with absolute temperature, but the experimental curves for both cassettes have higher exponents. For the electrospun membranes, theory predicts $B_{w,i}$ will be proportional to ~T^2, but the exponents far exceed this value. In general, for the experiments where T_{avg} was varied, the original S-T correlation performed the most poorly and the Hausen correlation performed similarly to the modified Sieder-Tate correlation, Eq.19 formulated in this work.

No trend is expected when $B_{w,i,\,experimental}$ is plotted vs average cassette Reynolds number (Fig 2.11b, data from Series 2 experiments). By this criteria, the Sieder-Tate correlation and Eq. 19 performed as expected. Use of the Hausen correlation to calculate *Nu* caused $B_{w,i,\,experimental}$ to vary substantially with Reynolds number. This variation is attributable to the design of the Hausen correlation, which was intended for use calculating local Nusselt number, not average Nusselt number. When channel length, L, is used as a parameter, the Hausen correlation estimates the Nusselt number at the channel exit, where the flow is most developed, rather than then average Nusselt number along the entire length of the cassette. Because local Nusselt number drops steeply as flow develops, and low Reynolds number is associated with quicker flow development, the Hausen correlation will underestimate Nusselt number proportionally more at low *Re*. The Hausen correlation underestimation of *Nu* at low Re causes

the negative trend in $B_{w,i,\,experimental}$. $B_{w,i,\,experimental}$ vs. *Re* was not plotted for the PTFE membrane experiments because the permeate flux measurements were too high and boundary layer heat transfer coefficients were too low for the transport model to converge. In other words, attempting to calculate membrane permeability using DCMD flux measurements and substantially underestimated feed/permeate heat transfer coefficients can cause the transport-model to output unrealistically large temperature gradients in the feed and permeate channels, resulting in non-physical negative driving force between the feed and permeate sides of the membrane.

From these observations we conclude that a Nusselt correlation correction factor (NuCF) is required for both membrane cassettes. The Srisurichan paper did not explicitly mention a hydrodynamic calming section in the cassette prior to membrane exposure, so it is assumed the feed and permeate flows were simultaneously developing. Therefore, equation 19, the modified Sieder-Tate correlation, is chosen as the best theoretical baseline equation for both cassettes.

2.7.6 3. Determination of the cassette-dependent Nusselt correction factor (NuCF) for multiplication with theoretical Nusselt correlations

There are two hypothesized reasons experimental NuCF are needed. The first is potential inaccuracy of theoretical equations near a channel entrance; little experimental data exists in the literature to validate analytical and numerically modeled Nusselt correlations for simultaneously developing flow. Since Nusselt number is asymptotic near a channel entrance, inaccuracy in the theoretical prediction may have a significant effect on predicted *Nu* for a small MD cassette. Feed and permeate flow non-idealities in the cassette may also drive the need for a NuCF

correction factor. Membrane cassette channels with abrupt 90° entrances and exits, for example, may lead to more fluid mixing than predicted by theory.

These two hypotheses suggest NuCF takes the form,

$$\text{NuCF} = C_1 Re^{C_2} \quad (27)$$

for laminar flow, in which a non-zero positive exponent means the effect of flow non-idealities increases with flow rate. NuCF is multiplied with the theoretical Nusselt correlation, yielding new values for h_f and h_p, and new $B_{w,i,\,experimental}$. The objective is to find a combination $\boldsymbol{C_1}$ and $\boldsymbol{C_2}$ in which $B_{w,i,\,experimental}$ has the same relationship to T_{avg} as $B_{w,i,\,theoretical}$, while $B_{w,i,\,experimental}$ has no correlation with Re_{avg}

The set of potentially correct values for NuCF (and thus, potentially correct pairs of C_1 and C_2) can be bounded using $B_{w,i,\,experimental}$. NuCF is too low if resulting $B_{w,i,\,experimental}$ is higher than the theoretical maximum. NuCF is too high if $B_{w,i,\,experimental}$ has a negative slope when plotted against T_{avg} (if modeled heat transfer coefficients are too high, MD driving force will be overestimated and membrane permeability will appear to decrease as ΔT_{bulk}increases). Once ranges of potentially correct C_1 and C_2 pairs are identified, values within these ranges are tested to achieve the correct slopes of $B_{w,i,\,experimental}$ vs. T_{avg} and vs. Re_{avg}. This can be done by design of an optimization function, but for this study, model runs were simply repeated systematically until a suitable pair was found. C_1 was varied between 0.05 and 6, and C_2 was varied from 0 to 0.33 based on the initial bounding analysis for these variables.

Precision of the NuCF calculation was limited by variability in experimentally measured flux, represented by standard error bars plotted on each graph. However, for the cassette in this study,

a single NuCF was identified that caused $B_{w,i,\,experimental}$ to behave similarly to $B_{w,i,theo,Field}$ for both tested membrane types in both experiment series: **NuCF = 0.5$Re^{\frac{1}{4}}$** See figure 2.12 A-D. Consistency of NuCF between membrane types is as expected; the correction factor should be dependent only on non-idealities in the feed and permeate fluid flow, not on membrane characteristics. The small discrepancy between the experimental and the theoretical electrospun membrane $B_{w,i}$ regression exponents in Fig 2.12C can be attributed to experimental uncertainty or uncertainty in membrane characterization data.

Use of this correction factor causes the adjusted Eq. 19 Nusselt correlation to be proportional to $Re^{1/3} * \ln(Re) * Re^{\frac{1}{4}} \approx Re^{0.74}$. This exponent is similar to those found in transitional flow Nusselt correlations (see Table A2.1), suggesting feed and permeate streams behave more like transitional than laminar flow, even at Reynolds numbers < 2000. This is likely due to the abrupt entrance and exit configuration of the cassette and resulting flow non-idealities.

A very slight negative trend in theoretical and experimental $B_{w,i}$ for the PTFE membranes in Fig 2.12D is the result of a minor system pressure increase (~ 13 mbar) as pump speed was increased. This effect was unintentionally induced, observed for this series of experiments only, and has little effect on the NuCF calculations. However the Fig 2.12D trends give insight into the detectability of total system pressure effects on MD membrane permeability. With well-characterized cassette heat transfer and well-controlled MD system conditions, these effects could be used to explore the validity of effective diffusivity equations in classic and Field DGM formulas.

For the cassette used in the Srisurichan paper, a single C_1 and C_2 pair could not be estimated without a second series of MD data where cassette flow rate was varied. Also, an absence of

granular $T_{f,b}$ and $T_{p,b}$ measurements in the published data limited the accuracy of the $B_{w,i,\,experimental}$ regression, see figure 2.12E. Authors reported that variation from published bulk temperatures was within +/- 0.5°C however an increase in driving force by this amount could be reason for the slightly anomalous location of $B_{w,i,\,experimental}$ at $T_{avg,m}$ = 30°C (303 K). A "window" of likely NuCF values was identified by regressing Srisurichan data with and without the $T_{avg,m}$ = 30°C data point, and finding NuCF values which cause each regression to match the $B_{w,i,\,theoretical}$ curve. Averaging these two NuCF values, gives an estimate **NuCF ≈ 1.5** for the Srisurichan cassette.

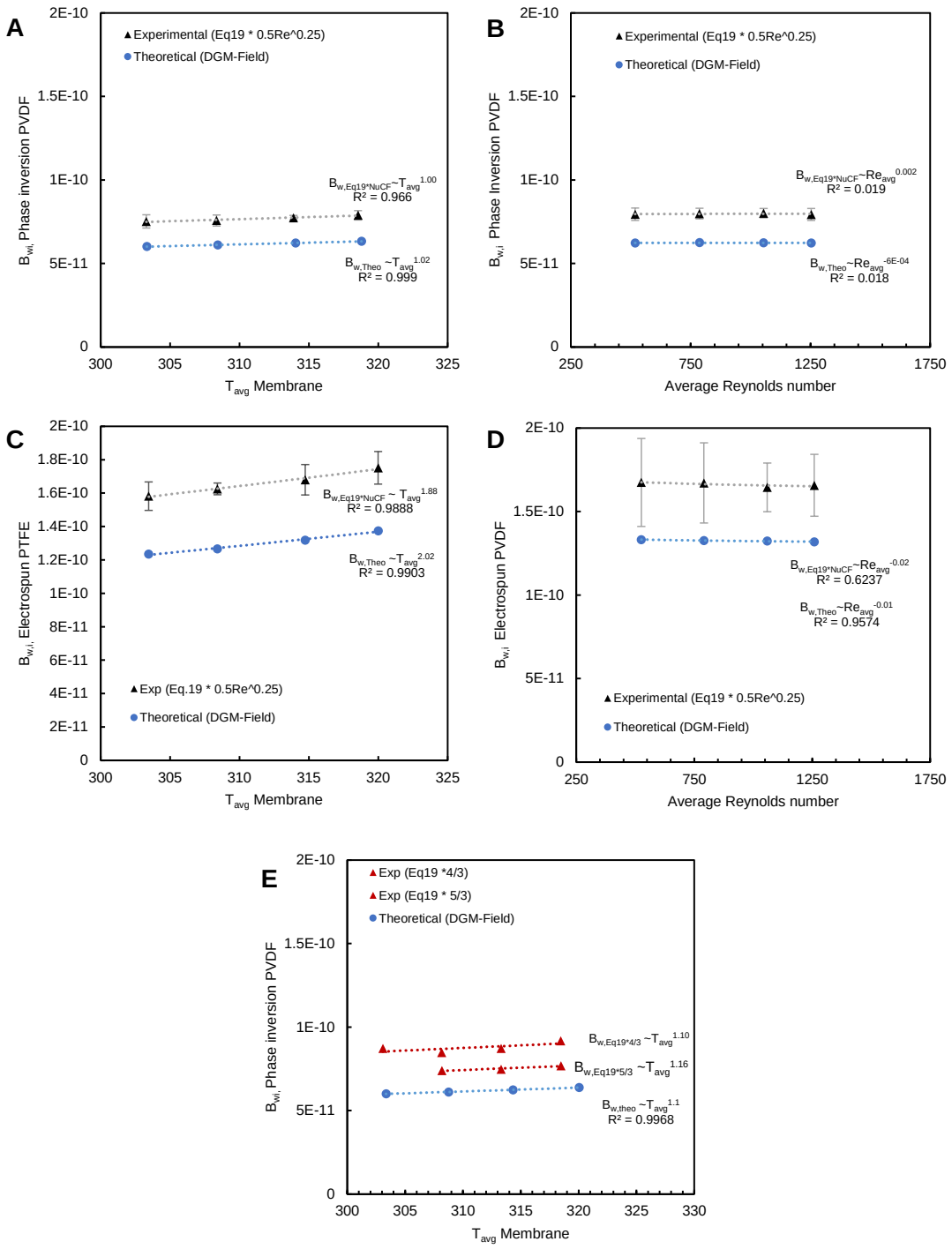

Figure 2.12 Power regressions of $B_{w.i,experimental}$ and $B_{w,i,theoretical}$ for different DCMD experiment series. $B_{w.i,experimental}$ calculated using Eq19*NuCF. A) $B_{w,i}$ vs T_{avg} for phase inversion PVDF membranes B) $B_{w,i}$ vs Re_{avg} for phase inversion PVDF membranes. C) $B_{w,i}$ vs T_{avg} for electrospun PTFE membranes. D) $B_{w,i}$ vs Re_{avg} for phase inversion PVDF membranes. E) $B_{w,i}$ vs T_{avg} for phase inversion PVDF membranes (data collected by Srisurichan et al)

To improve confidence in the $B_{w,i,\,experimental}$ values (or any derived metric, such as η) from Srisurichan MD cassette data, a more precise NuCF would be needed. However, there is some value to the rough NuCF estimation made here. First, the analysis shows a Nusselt correction factor is indeed necessary to describe channel heat transfer in the Srisurichan cassette, which has feed and permeate channels 10x larger than the cassette channels used in this study. This suggests that experimental determination of NuCF may be prudent for all benchtop membrane cassettes used in MD research.

A second benefit of estimating Srisurichan cassette NuCF is it provides preliminary validation of the $B_{w,i,\,experimental}$ values calculated for the PVDF and PTFE membranes. Table 2.4 gives $B_{w,i}$ values calculated for both membranes types using the Field-modified DGM theory, experimentally when the Equation 19 Nusselt correlation is used, and experimentally when the Eq 19 Nusselt correlation is modified by NuCF. For both membrane types and for both cassettes, experimentally-found membrane permeability is substantially higher than theoretical permeability. When NuCF is not used, $B_{w,i,\,experimental}$ is particularly high compared to the DGM prediction. Additionally, if cassette heat transfer is not corrected, DCMD experiments on the same commercial PVDF membrane using different cassettes lead to different estimations of $B_{w,i,\,experimental}$. When NuCF are used, however, $B_{w,i,\,experimental}$ seem to converge.

Table 2.4 Calculations of intrinsic membrane permeability, $B_{w,i}$ $[kgm^{-1}s^{-1}Pa^{-1}] \times 10^{11}$ at $40°C$ for two commercial membranes. When cassette heat transfer coefficients are corrected using a NuCF, experimental measurements of permeability converge for the same commercial PVDF membrane using two different cassettes.

	Phase inversion PVDF	**Commercial electrospun PTFE**
$\boldsymbol{B_{w,i,theoretical} \times 10^{11}}$	6.23 ± 0.004	13.2 ± 0.02
This work		
$\boldsymbol{B_{w,i,exp} \times 10^{11} - Eq.19\ only}$	14.9 ± 0.31	590 ± 235
$\boldsymbol{B_{w,i,exp} \times 10^{11} - Eq\ 19 * NuCF}$	$\mathbf{7.94 \pm 0.12}$	16.5 ± 0.68
Literature data		
$\boldsymbol{B_{w,i,exp} \times 10^{11} - Eq\ 19\ only}$	11.2	---
$\boldsymbol{B_{w,i,exp} \times 10^{11} - Eq.19 * NuCF}$	$\mathbf{8.0 \pm 0.6}$	---

The convergence of GVHP permeability measurements for separate datasets suggests the cassette-dependent NuCF method sufficiently characterizes feed and permeate channel heat transfer. If this characterization is indeed accurate, methods presented in this study can be used to conclusively compare permeability of different membranes tested in different cassettes. This method to relate experimental permeability with theoretical permeability may also allow researchers to study and tune diffusivity contributions in MD membrane transport models. Collaborative research between multiple laboratories is needed to examine the accuracy of membrane permeability calculations made using the NuCF method, as discussed in section 2.9.

2.8 Heat transfer reporting recommendations for MD experimental work

We recommend researchers report experimentally-validated Nusselt numbers (Nu_f and Nu_p) or heat transfer coefficients (h_f and h_p) with any MD flux measurement. Methods used to calculate and validate these parameters should also be detailed in any peer-reviewed publication.

For MD experimental results to be valuable to other researchers and engineers, characteristics of the system must be fully defined. Otherwise, intra-study comparisons cannot be made; attributing differences in MD flux and thermal performance to any one factor is impossible. Review of 1-D heat and mass transport equations (Eq 1-5) provides guidance for the minimum information required by researchers to understand membrane flux results, compare experimental results across studies, and predict membrane performance under un-tested conditions. (See discussion in Section 2.3.1). As evidenced by the comparative analysis in section 2.7, determination and reporting of experimentally-validated heat transfer characteristics in an MD membrane cassettes can significantly increase the accuracy of membrane permeability calculations and provide meaning to reported MD flux.

2.9 Conclusions and Future Work

Conclusions

For the MD technology to achieve wider adoption, process and reliability and efficiency must be demonstrated. Progress toward these goals depends on the ability of MD researchers and engineers to build on previous work. This chapter provides guidance and tools to improve reporting of experimental results, facilitating inter-study comparison by more accurate characterization of system mass and heat transport.

In this study, we provide the MD community with a clear methodology for predicting heat transfer rate in feed and permeate streams using Nusselt numbers. First, we outlined the process for selecting a Nusselt number correlation from literature. Then we demonstrate *theoretical* methods to modify a pre-existing Nusselt number correlation for conditions specific to a MD

cassette. We apply these methods specifically to suggest a modified Nusselt correlation for MD cassettes with rectangular feed and permeate channels undergoing laminar flow. Next, we develop an *experimental* method to correct the heat transfer coefficients predicted by the Nusselt number correlation. Through review of published MD data and experiments on our own MD cassette, we show flow non-idealities can substantially increase the heat transfer coefficients predicted by theoretical Nusselt correlations. A test case comparing MD data collected on identical membranes under different system conditions in different laboratories indicated that application of experimental Nusselt correction factors is required for the studies' calculations of membrane permeability to converge. This suggests feed and permeate channel heat transfer in the MD membrane cassette is more accurately characterized using experimentally-validated Nusselt numbers. The research also suggests that methods presented in this study can be used to conclusively compare the MD permeability of novel membrane structures. Based on these observations, we recommend MD researchers experimentally validate and report heat transfer characteristics of the cassette feed and permeate channels along with any measured flux result.

Future work

An experimental cassette-dependent Nusselt correction factor (NuCF) is useful to the MD community if it can accurately compare novel membrane permeability between research groups for a range of experimental conditions and if it can be used to study contributions of individual vapor transport mechanisms on total membrane flux. A few research questions therefore stem from the development of the NuCF method in this dissertation:

a) Does the NuCF method identify "true" permeability of MD membranes? In essence, can Bwi calculated for a given membrane in a particular cassette be used by other research groups to predict flux in their own cassettes, or to quickly calculate NuCF for their own cassette? These

questions can be answered by a collaborative study between two or three laboratories in which DCMD data is compared for identical membranes collected by different operators using different DCMD systems.

b) Can the relationships between membrane structure and individual contribution of diffusive vapor transport mechanisms be identified by examining $B_{w,i,Experimental}$ and $B_{w,i,Theoretical}$ vs $T_{avg,membrane}$? Furthermore, can the interaction between diffusive and viscous transport mechanisms be identified in MD membranes operated under a pressure differential (as is the case for vacuum membrane distillation)? According to the Dusty Gas Model (DGM) each transport mechanism has a distinct dependence on driving force, thermodynamic vapor properties and on membrane structure. By design of experiments that vary these factors individually while hold others constant, then examining the apparent effect on $B_{w,i,Experimental}$, classic models for MD vapor transport can be validated and updated.

c) Is the NuCF method valid for a variety of cassette geometries (hollow fiber, spiral wound), flow regimes (turbulent, laminar with spacers) and MD permeate-side configurations (Air gap membrane distillation, vacuum membrane distillation, sweeping gas membrane distillation)? Validation of the NuCF method for a variety of MD cassettes and operating conditions is needed to determine whether it can be used practically and widely. Much work remains to facilitate inter-system and inter-membrane comparison of MD performance.

Chapter 3 : PREDICTION OF MEMBRANE DISTILLATION FLUX FOR FIBROUS MEMBRANES USING BUCKINGHAM-PI DIMENSIONAL ANALYSIS

3.1 Abstract

We developed a dimensional-analysis-based empirical modeling method for membrane distillation (MD) flux that is adaptable for novel membrane structures. The method makes fewer simplifying assumptions about membrane pore geometry than existing theoretical (i.e. mechanistic) models, and allows selection of simple, easily-measureable membrane characteristics as structural parameters. Furthermore, effects of feed and permeate heat transfer are easily incorporated without the need for iterative fitting of mass and heat transfer equations.

The Buckingham-Pi dimensional analysis method is tested for direct contact membrane distillation (DCMD) using non-woven/fibrous structures as the model membrane material. Twelve easily-measured variables to describe DCMD operating conditions, fluid properties, membrane structures, and flux were identified and combined into eight dimensionless parameters. These parameters were regressed using experimentally-collected data for a multiple electrospun membrane types and DCMD system conditions, achieving R^2 values >95%. We found that vapor flux through isotropic electrospun membranes can be estimated using only membrane thickness, solid fraction, and fiber diameter as structural parameters. Buckingham-Pi model DCMD flux predictions compare favorably with previously-developed empirical and theoretical models, and suggest this simple yet theoretically-grounded empirical modeling method can be used practically in the MD field.

3.2 Introduction

Research Motivation and Background

A variety of theoretical and empirical models have been developed to describe and predict vapor transport through membrane distillation (MD) membrane materials. Pursuit of such models in the MD research community yields both scientific and practical insights. Theoretically-based (i.e. mechanistic) models can elucidate the contributions of and interactions between different mass transport mechanisms depending on membrane structure, membrane chemistry, and the thermodynamic properties of the pore fluid. A model that accurately predicts flux has practical value as well. It can be used to optimize internal membrane structure for low mass transport resistance, and high thermal efficiency. Accurate predictions of mass transport are also desired as inputs for process-level models to reveal the suitability of MD for commercial and industrial applications.

Existing modeling methods, however, exhibit some weaknesses when applied to unconventional membrane structures, such as fibrous or asymmetric membranes. These weaknesses are primarily due to structural parameters used and assumptions made regarding pore-geometryDetailed reviews of MD modeling techniques exist in the literature, (Khayet, 2011; Alkhudhiri et al., 2012; Hitsov et al., 2015). Here, theoretical and empirical models are briefly summarized with a focus on the applicability of common structural parameters and inherent pore geometry assumptions to novel membranes.

Theoretical techniques to model mass transport in MD membranes include the Dusty Gas Model (and variations thereof) (Mason and Malinauskas, 1983; Lawson et al., 1995; Lawson and Lloyd, 1997; Martínez et al., 2003; Phattaranawik et al., 2003a; Khayet et al., 2004; Khayet, 2011; Field

et al., 2013), Schofield's model(Schofield et al., 1987, 1990), structural network models(Imdakm and Matsuura, 2004; Khayet et al., 2010), a ballistic transport model(Soukane et al., 2014), and computational fluid dynamics (CFD) models(Xu et al., 2009; Charfi et al., 2010; Hwang et al., 2011). Theoretical models are based on the kinetic theory of gases, in which vapor transport occurs as a result of ordinary molecular diffusion, Knudsen diffusion, viscous flow and/or surface diffusion depending on fluid characteristics, pore geometry, driving force and membrane surface chemistry. Each model assumes one or more of these transport mechanisms occur in the MD membrane, though there is little consensus on the contributions of individual mechanisms to total vapor flux. In particular, recent work has explored the relationship between membrane structural characteristics and the combined effects of Knudsen and ordinary molecular diffusion, however precise experimental validation has not been demonstrated.(Essalhi and Khayet, 2013b; Field et al., 2013) More research is needed to determine the presence and proportion of predicted vapor transport mechanisms in MD, and how these mechanisms are influenced by operating conditions and pore structure.

Most theoretical MD models assume a simple, symmetrical membrane geometry of uniform, cylindrical, isolated pores. Structural parameters used to predict membrane permeability are pore radius (r), pore tortuosity (τ), membrane porosity (ε), and membrane thickness (δ). Some authors have adapted the DGM to improve accuracy of predicted MD membrane permeability by incorporating statistical parameters of pore size distribution (Martínez et al., 2003; Phattaranawik et al., 2003a; Khayet et al., 2004), or by weighting individual contributions of transport mechanisms based on Knudsen number (i.e. pore size) (Field et al., 2013). Imdakm's pore network model assumes an interconnected cubic grid of cylindrical pores (Imdakm and

Matsuura, 2004; Khayet et al., 2010) and also accounts for pore size distribution. The dimension of the cubic grid is a uniform a parameter set by the modeler.

Thus, when applying theoretical vapor transport modeling techniques to novel MD membranes, there are a few possible sources of error. Theoretical models employ structural assumptions that are problematic for novel membranes. Often pore geometry is highly simplified (e.g. cylindrical, non-interconnected pores, uniform characteristics throughout membrane) so models are not sensitive to mass transport benefits of interconnected or asymmetrical pore networks. Shirazi et. al. notes the inadequacy of MD-CFD models to describe complex membrane geometries. He reviews general CFD literature and suggests porous transport models that can potentially be adapted for MD(Shirazi et al., 2016). Another problematic aspect of existing theoretical models is their use of structural parameters that are difficult to measure accurately, such as tortuosity, pore network grid length, or pore size distribution. Reliance on non-measurable model parameters yields poor predictive capability for new membranes. Finally, given the lack of consensus on how to calculate contribution of individual vapor transport mechanisms to total MD flux, certainty in flux predictions for novel membrane types with unusual pore geometries will be particularly low.

Empirical MD transport models fare no better. Empirical models employing Response Surface Methodology (RSM) (Khayet et al., 2007; Onsekizoglu et al., 2010) and Artificial neural networks (ANN) (Khayet and Cojocaru, 2012, 2013) have been used to predict MD transport. Existing formulations do not use membrane structural parameters to predict flux; only system parameters were correlated with MD performance. A model recently published by Rao and Childress develops a membrane structural parameter to predict MD flux(Rao et al., 2014). This is done by measuring DCMD performance for a sets of supported and unsupported phase inversion

membranes then agnostically combining membrane structural properties (pore size, porosity, membrane thickness, tortuosity, thermal conductivity, liquid entry pressure) to find good correlations with the flux data. Ultimately, a structural parameter is chosen, $\frac{1}{\delta(1-\varepsilon)}$, that provides an adequate fit ($R^2 = 0.71$) for flux data and the can be calculated using minimal membrane characterization experiments. The final flux model presented in the Rao-Childress is difficult to apply as-is to new experimental work because it contains only the aforementioned structural parameter, and no additional adjustable parameters to describe scale of intrinsic membrane features or to describe MD operating conditions. In summary, existing empirical models have been trained exclusively on conventional phase inversion membranes (supported and unsupported) and either ignore membrane structure entirely or contain an incomplete set of structural parameters in the final model correlation. These models are not expected to accurately predict flux for novel membranes.

To describe MD mass transport for membranes for highly-interconnected, non-cylindrical and/or asymmetric pore networks, existing models must be adapted or new models must be developed. Ideally, these models would a) be capable of predicting MD flux for a wide range of membrane characteristics and experimental conditions, b) use simple, easily-measured membrane structural parameters, and c) be easy to replicate and validate across different laboratories.

Modeling MD transport for fibrous membranes

The need for a scalable, thermally efficient and highly permeable separation material has led to the development of fibrous, electrospun polymer membranes. Several research groups demonstrate excellent flux and salt rejection of as-spun, heat-pressed, and surface-modified electrospun membranes as compared to conventional phase inversion membranes.(Tijing et al.,

2007, 2014b, 2016; Essalhi and Khayet, 2013b, 2014; Liao et al., 2014b; Su et al., 2016; Yao et al., 2016) An MD group has yet to successfully adapt or develop a mass transport model specific to the fibrous membrane structure. (In a 2013 publication, Essalhi and Khayet proposed a DGM model adaptation for electrospun membranes.(Essalhi and Khayet, 2013b) However, the model equation for total effective diffusivity of vapor contained a coefficient which a caused the calculated vapor diffusivity in the membrane to exceed vapor diffusivity in open air, the theoretical maximum at ambient pressure. Thus, the model calculations overestimated electrospun membrane permeability.) Development of vapor transport models for fibrous MD membranes will allow optimization of membrane structure for particular chemical and system conditions, prediction of pertinent transport metrics such as thermal efficiency, and facilitate a better understanding of theoretical vapor transport mechanism relevant to fibrous matrices.

Applied to fibrous membrane materials, existing theoretical and empirical MD transport models are particularly flawed. Structural characteristics and simplifying assumptions used to model pore space of dense polymeric membranes or track-etched membranes are not adequate to describe pore space in fibrous membranes. In a fibrous matrix, pore space is neither cylindrical nor isolated; isotropic arrangement of fibers means there are no continuous pores walls, and pore space is highly interconnected. This suggests traditional models will poorly predict flux in fibrous membranes.

Additionally, membrane thickness and pore size characterization methods introduce error when modeling vapor transport through fibrous membranes. Commonly used methods to measure pore size, such as capillary flow porometry, liquid-liquid displacement porometry, mercury porosimetry, evapoporometry, and BJH nitrogen adsorption/desorption are based on Young-Laplace or Kelvin equations, theories which assume cylindrical pore geometry. Not only will

assumptions of cylindrical pore geometry tend to over-estimate average inter-fiber space, these methods often induce significant hydrostatic- or capillary- pressures that can alter the sample structure of highly-porous membranes comprised of sub-micron diameter fibers. Microscopy-based pore-size characterization methods are inaccurate for layered fibrous materials because pore-edge selection is arbitrary (pore size is inversely proportional to the number of layers of stacked fibers chosen for image analysis). Typical methods to measure membrane thickness also are difficult to implement accurately for soft fibrous membranes. Pressure-based profilometers may compress highly-porous as-spun membranes, and freeze-fracturing for cross-section imaging requires the membrane to be pre-soaked in a supporting fluid, such as isopropyl alcohol, (otherwise the fibrous network will bend, not break.) Soaking and later evaporation of the supporting fluid from the fiber network causes capillary stress, and may lead to undetected aggregation of fibers and a thinner apparent cross-section. This phenomenon is well-documented for other soft materials such as sol-gels.(Hench and West, 1990; Jin et al., 2011) A vapor flux model that incorporates easily and precisely measurable structural parameters will predict flux more accurately than one relying on parameters with high-uncertainty.

3.2.2 Research Objectives

The objective of this work is to develop a modeling method for MD flux that is adaptable for novel membrane structures. The method will make fewer simplifying assumptions about membrane pore geometry than existing theoretical models, and will allow selection of simple, easily-measureable membrane characteristics as structural parameters. Furthermore, effects of feed and permeate heat transfer will be easily incorporated without the need for iterative fitting of mass and heat transfer equations. We hypothesize a dimensional-analysis-based empirical

DCMD model can meet these objectives and more accurately predict flux for fibrous membranes than existing theoretical or empirical MD models.

To test this hypothesis, dimensional analysis of the MD process is performed using the Buckingham-Pi method, with non-woven/fibrous structures as the model membrane material. Structural parameters relevant to an isotropic fibrous network are used and flux is predicted using only easily-measurable membrane characteristics. Experimental MD flux measurements are compared with flux predicted by the new Buckingham-Pi model, the Rao-Childress empirical model and classic and Field/Wu-modified Dusty Gas Models

3.3 Methods and Materials

3.3.1 Background: Dimensional analysis and The Buckingham-Pi method

In the field of fluid dynamics and heat transfer, the complexity of molecular-level mass, heat, and momentum transport often prevents evaluation of bulk system behavior using fundamental differential transport equations. Analytical solutions to transport equations are impossible in all but the simplest geometries, boundary conditions, and flow regimes. Numerical methods such as CFD are computationally expensive and also require simplifying assumptions for system geometry, boundary conditions and initial conditions. As an alternative, engineers and scientists often employ dimensional analysis to help explain and predict bulk system behavior. For a given physical system, derivation of dimensionless parameters via dimensional analysis provides the general relationships between system variables. Once relevant fluid properties and system conditions are summarized in this way, empirical correlations of the parameters can be developed. Correlations of dimensionless parameters are useful to show relationships between

similar systems, to reduce work by simplifying the number of controlling variables defining an outcome and for scale modeling.

In 1914, Edgar Buckingham adapted a systematic method for selecting the relevant system variables and arranging them into dimensionless “Pi” parameters (Buckingham, 1914). The method is taught in undergraduate-level fluid dynamics and chemical engineering courses (Sonin, 2001; Welty et al., 2009). Despite the effective application of Buckingham-Pi (B-P) in fluid dynamics and heat transport applications, no published studies have evaluated its use to describe transport in membrane distillation. We explore the usefulness of dimensional analysis to model direct contact membrane distillation (DCMD) by developing and experimentally evaluating B-P parameters for the case of water vapor transport through fibrous membranes.

3.3.2 Model development: Use of B-P to describe MD transport through fibrous membranes.

The first step in dimensional analysis is selection of a complete and independent set of variables that describe the physical system. To ensure the model is simple to use, we add a requirement that variables are obtainable by direct experimental measurement or by calculation using a closed form expression. Variables were ruled out if their characterization methods are approximate (e.g. membrane tortuosity) or their calculation requires iterative solution to mass and heat transport equations (e.g. membrane surface temperature). In this way, a master list of 82 potential variables gathered from MD theoretical transport models was reduced to 12. Appendix B.1 contains the master list of considered variables and Table 3.1, summarizes the chosen variables.

Table 3.1 Summary of Buckingham-Pi variable selection

Selected variables:	Reason for selection	Calculation method
$\boldsymbol{Permeate\ Flux}, \boldsymbol{J_w}, \left[\frac{kg}{m^2 s}\right], \left[\frac{M}{L^2 T}\right]$	Dependent variable	Direct measurement
$\boldsymbol{Bulk\ Driving\ Force}, \Delta \boldsymbol{T_{bulk}}, [\boldsymbol{K}, \boldsymbol{\theta}]$	Standard DCMD measurement	Direct measurement
$\boldsymbol{Membrane\ Fiber\ diameter}, \boldsymbol{d_f}\ [\boldsymbol{L}]$	More easily and accurately measured than pore diameter	Direct measurement
$\boldsymbol{Membrane\ Thickness}, \boldsymbol{\delta}, [\boldsymbol{L}]$	Standard parameter to describe mass and heat transport resistance	Direct measurement
$\boldsymbol{Diffusivity\ of\ water\ in\ air}, \boldsymbol{D_{w,a}}, \left[\frac{m^2}{s}, \frac{L^2}{T}\right]$	Standard parameter to quantify molecular diffusion	Empirical correlation (average temp, pressure) (Marrero and Mason, 1972)
$\boldsymbol{Water\ vapor\ viscosity}, \boldsymbol{\mu}, [\boldsymbol{Pa} * \boldsymbol{s}], [\frac{M}{LT}]$	Standard parameter to measure viscous transport resistance	Empirical correlation (average temperature, pressure) (Morvay and Gvozdenac, 2008)
$\boldsymbol{Average\ pore\ vapor\ density}, \boldsymbol{\rho_{v,pore}}, \left[\frac{M}{L^3}\right]$ ($\boldsymbol{scales\ with\ average\ T}$)	Related by the ideal gas law to vapor pressure, and has simpler dimensions	Empirical Antoine equation (saturation vapor pressure, temperature)(NIST Chemistry WebBook, 2016)
$\boldsymbol{Polymer\ thermal\ conductivity}, \boldsymbol{k_p}, \left[\frac{W}{mK}\right], \left[\frac{LM}{T^3 \theta}\right]$	Standard parameter in MD heat flux equations. Bulk thermal conductivity not used because it is not independent of porosity	Standard reference (Wypych, 2012)
$\boldsymbol{Membrane\ porosity}, \boldsymbol{\varepsilon}$, $\boldsymbol{or\ solid\ fraction}\ (\mathbf{1} - \boldsymbol{\varepsilon})\ [\boldsymbol{Dimensionless}]$	Standard parameter used to calculate membrane permeability and bulk thermal conductivity	Direct measurement
$\boldsymbol{Activity\ of\ bulk\ feed\ water}, \boldsymbol{a_w}, [\boldsymbol{mole\ fraction}: \boldsymbol{di}$	Accounts for vapor pressure depression	Empirical correlation (Pitzer et al., 1984)
$\boldsymbol{Feed\ Nusselt\ number}, \boldsymbol{Nu_{feed}}, [\boldsymbol{dimensionless}]$	Accounts for feed stream temperature and concentration profiles	Empirical and experimental correlation [Chapter 2]
$\boldsymbol{Permeate\ Nusselt\ number}, \boldsymbol{Nu_{perm}}, [\boldsymbol{dimensionles}$	Accounts for feed stream temperature and concentration profiles	Empirical and experimental correlation [Chapter 2]

The 12 variables are comprised of four dimensions, $[L, T, M, \theta]$. Four "repeating variables" are chosen, based on typical criteria (Sonin, 2001), for use in calculating each dimensionless parameter: d_f, $\Delta T_{bulk}, \mu,\ and\ \rho_{vap}$. The model therefore contains eight independent non-dimensional numbers: $\Pi_1, \Pi_2, \Pi_3, \Pi_4, \varepsilon, a_{w,bulk}, Nu_{feed}$, and Nu_{perm} to describe the MD process. The Pi functions are as follows (Eq.1-5):

$$\Pi_1 = f\left(\Pi_2, \Pi_3, \Pi_4, \varepsilon, a_{w,bulk}, Nu_{feed}, Nu_{perm}\right) \quad (1)$$

$$\Pi_1 = \Pi_1\left(d_f, \Delta T_{bulk}, \mu, \rho_{vap}, J_w\right) \text{ (Dependent variable)} \quad (2)$$

$$\Pi_2 = \Pi_2\left(d_f, \Delta T_{bulk}, \mu, \rho_{vap}, \delta\right) \quad (3)$$

$$\Pi_3 = \Pi_3\left(d_f, \Delta T_{bulk}, \mu, \rho_{vap}, k_p\right) \quad (4)$$

$$\Pi_4 = \Pi_4\left(d_f, \Delta T_{bulk}, \mu, \rho_{vap}, D_{w,a}\right) \quad (5)$$

Calculation of the dimensionless parameters is shown in Appendix B.1. The set of dimensionless numbers used for empirical correlation, presented as ratios that positively correlate with permeate flux, are as follows (Eq 6-10):

$$\Pi_1 = \frac{d_f J_w}{\mu} \quad (6)$$

$$\Pi_2 = \frac{\Delta T_{bulk} d_f^2 \rho_{vap}^2 k_p}{\mu^3} \quad (7)$$

$$\Pi_3 = \frac{d_f}{\delta} \quad (8)$$

$$\Pi_4 = \frac{D_{w,a}\rho_{vap}}{\mu} \quad (9)$$

$$\frac{d_f J_w}{\mu} = f\left(\frac{\Delta T_{bulk} d_f^2 \rho_{vap}^2 k_p}{\mu^3}, \frac{d_f}{\delta}\frac{D_{w,a}\rho_{vap}}{\mu}, (1-\varepsilon)^{-1}, a_w, Nu_{feed}, Nu_{perm}\right) \quad (10)$$

Dimensionless parameters have physical relevance that provide the researcher intuition on how alteration of one system parameter will affect others. A classic example is Reynolds Number, *Re*, which is defined as $\frac{vL\rho}{\mu}$. If bulk fluid velocity (v), length scale (L) and fluid density (ρ) are large in relation to the dynamic viscosity (μ), inertial forces dominate over viscous forces in given flowing fluid.

The derived parameters Π_1, Π_2, Π_3, and Π_4 have a physical significance specific to the MD process, and are analogous to well-known dimensionless numbers used to describe transport. The significances of Π_1, Π_3, and Π_4 are relatively intuitive. The dependent variable, Π_1, is the Reynolds number for vapor transporting through the membrane, where permeate flux, J_w, represents the inertial force and $\frac{\mu}{d_f}$ the viscous force. Π_3 is the dimensionless membrane geometry, and can be conceptualized as the ratio of pore diameter to pore length (Fiber diameter in isotropically arranged networks has been related to pore diameter mathematically and experimentally(Ryu et al., 2003; Eichhorn and Sampson, 2005; Szentivanyi et al., 2011)). Mass transport resistance will decrease as Π_3 increases. Π_4 is the ratio of mass diffusivity to momentum diffusivity in the membrane pores, analogous to the inverse of the Schmidt number, *Sc*. Therefore, Π_4 compares the rate of ordinary molecular diffusion to viscous transport resistance and its magnitude is controlled by average membrane temperature. As temperature increases, water vapor diffusivity increases and viscosity decreases, leading to an increase in flux.

Π_2 is the least intuitive dimensionless parameter, but manipulation using kinetic vapor theory equations allows Π_2 to be disaggregated into a set of smaller, easily-interpreted dimensionless

numbers. Equations 11-14 are common approximations used for a pure gas comprised of rigid, non-attracting spheres(Bird et al., 2007):

$$\mu = \frac{1}{3}\rho_{tot}\bar{u}\lambda \tag{11}$$

$$\bar{u} = \sqrt{\frac{RT_{avg}}{2\pi M_w}} \tag{12}$$

$$\lambda = \frac{1}{\sqrt{2}\pi d_{mol}^2 n} \tag{13}$$

$$k_g = \frac{15}{4}\frac{R}{M_w}\mu \tag{14}$$

Here, ρ_{tot} is the total density of the gas, $\bar{u}$ is the mean molecular speed, λ is the molecular mean free path, R is the gas constant, M_w is the average molecular weight of the gas, d_{mol} is the molecule diameters, and n is molecular number density. k_g is the thermal conductivity of a gas. Using these equations, the following substitutions can be made:

$$\Pi_2 = \frac{\Delta T_{bulk} d_f^2 \rho_{vap}^2 k_p}{\mu^3} = \frac{\Delta T_{bulk} d_f^2 \rho_{vap}^2 k_p}{\mu\left(\frac{1}{9}\rho_{tot}^2 \bar{u}^2 \lambda^2\right)} = \frac{9\Delta T_{bulk} k_p}{\mu \bar{u}^2} * \frac{\rho_{vap}^2}{\rho_{tot}^2} * \frac{d_f^2}{\lambda^2} =$$

$$= \frac{135\pi}{2} * \frac{\Delta T_{bulk}}{T_{avg}} * \frac{k_p}{k_g} * \frac{\rho_{vap}^2}{\rho_{tot}^2} * \frac{d_f^2}{\lambda^2} \tag{15}$$

Now the significance of Π_2 parameters and their relationship to vapor flux is clearer. MD vapor flux will increase with driving force ($\frac{\Delta T_{bulk}}{T_{avg}}$) and increase with the mass fraction of vapor in the pores ($\frac{\rho_{vap}^2}{\rho_{tot}^2}$). Given a particular membrane material, these effects will be somewhat tempered by gas thermal conductivity, k_g, which increases with temperature; faster heat transfer through the membrane pores will reduce the overall MD driving force and reduce flux.

Lastly, the presence of parameter $\frac{d_f^2}{\lambda^2}$ imbedded in the Π_2 parameter is particularly interesting, as it reveals potential opportunities to study mass transport mechanism using this simple Buckingham Pi model. The fraction is similar to the squared inverse of the Knudsen number,

$$Kn = Knudsen\ number = \frac{\lambda}{d_{pore}} \tag{16}$$

Kn, introduced in Chapter 2 of this dissertation, is the ratio of molecular path length (λ) to the characteristic pore dimension (d_{pore}). In the case of an isotropically-arranged fiber network, fiber diameter is considered to be proportional to pore dimension, therefore $\frac{d_f^2}{\lambda^2}$ is proportional to Kn^{-2}. The approximate relationship of Knudsen number to diffusion mechanisms can be expressed as follows (eq 17):

$$D_{OMD} \propto \bar{u}\,\lambda \tag{17}$$

$$D_{Knudsen} \propto \bar{u}\,d_f \ \ and \ \ (d_f \propto d_{pore}) \tag{18}$$

$$\frac{d_f^2}{\lambda^2} \propto \frac{D_{Knudsen}^2}{D_{OMD}^2} \tag{19}$$

D_{OMD} and $D_{Knudsen}$ are the ordinary molecular and Knudsen diffusivities in the pores, so these parameters suggest Π_2 will be correlated with Knudsen diffusivity. Since Π_4 is a function of ordinary molecular diffusivity, an opportunity may exist to study the relative influence of each parameter on MD flux, and from this infer the relative contributions of each transport mechanism on vapor flux. This experimental design is left for future work.

A second manipulation of the Buckingham-pi parameters reveals an opportunity simplify membrane characterization. In the empirical model, Π_1 values will be correlated with the rest of

the dimensionless parameters multiplied together. When Π_3 is multiplied with the solid-fraction parameter, it is shown to be a function of the Rao-Childress "structural parameter," C_m. (Eq 20)

$$\Pi_3(1-\varepsilon)^{-1} = \frac{d_f}{\delta(1-\varepsilon)} = d_f C_m \tag{20}$$

As demonstrated in the Rao-Childress paper, C_m can be computed using only the length, width, mass, and pure polymer density of a membrane sample, eliminated the need for thickness measurements. Computation of $\Pi_3(1-\varepsilon)^{-1}$ using this structural parameter therefore has a potential benefit of reducing parameter uncertainty due to inaccurate thickness measurements.

To determine an empirical relationship between the dependent B-P model parameter (Π_1) and the remaining dimensionless parameters, a series of isotropic fibrous membranes were structurally characterized and the tested in direct contact membrane distillation (DCMD). The following methods describe the collection of data to validate the Buckingham Pi model.

3.3.3 Data collection

Membrane Fabrication/Selection: We used six electrospun membrane geometries for development Buckingham Pi correlation. Five membranes were electrospun in-house, and one membrane was commercially obtained.

Materials: Polyvinylidene fluoride (PVDF) Kynar HSV 900 was provided by Arkema Inc., (King of Prussia, PA). N,N- dimethylformamide (DMF) and Acetone were purchased from Sigma Aldrich (St. Louis, MO). The commercial membrane was symmetrical unsupported isotropic fibrous PTFE, trade name "Filtriq" from ZeusInc.

Electrospinning of PVDF nanofibers: PVDF nanofibers were prepared using a custom-built electrospinning setup. Details of the electrospinning system have been described elsewhere [1].

Solution of PVDF in DMF/Acetone solvent mixture with ratio 60/40 % was prepared by continuously stirring the polymer in the solvent for 24 h at 60oC. Prior to electrospinning, the polymer solution was degassed overnight at room temperature. Polymer solutions were prepared with different concentrations of 7, 8, 9 and 10%. The amount of the dissolved polymer was kept constant at 2 gm for all solutions. The as-prepared polymeric solution was electrospun at a flow rate of 4mL/hr onto a polypropylene backing layer which is peeled of prior to using the membrane in DCMD test. The time of electrospinning varied with the concentration of the polymer. It ranged from 5-7 hours to keep the total amount of polymer spun at 2 gm. Electrospinning was conducted at ambient temperature and at an applied voltage of 20-24 kV. Relative humidity inside the electrospinning chamber was kept between 60-70%.
Heat press post-treatment was applied for the 10% PVDF membrane sample. This was done by heat press machine (Model QX-A1, Anhui, China) for 1 min at 140^{o}C.

Characterization of Electrospun membranes: We use a Quanta 600 FEG Scanning Electron Microscope (SEM) to evaluate thickness of as-spun membranes and post-DCMD membrane samples. Thickness measurements are taken by IPA-freeze-fracturing small membrane coupons from a larger electrospun sheet, then mounting the fractured face on a vertical stub. Thickness was analyzed for as-spun and post-DCMD membrane samples. Fiber diameter is measured using SEM Images of the feed and permeate face of the membrane and are analyzed using ImageJ with the plug-in DiameterJ.(Schneider et al., 2012; Hotaling et al., 2015). We calculate the membrane porosity (ε) gravimetrically using a microbalance and dimensional measurements, Equation 21.

$$\varepsilon = \left(1 - \frac{\rho_{membrane}}{\rho_{pure\ PVDF}}\right) \ \ where \ \ \rho_{membrane} = \frac{m_{membrane}}{V_{membrane}} \qquad (21)$$

The "membrane structural parameter," C_m, as described by Rao(Rao et al., 2014) was determined using the same tools:

$$C_m = \frac{\rho_p l_m w_m}{m} = \frac{1}{\delta(1-\varepsilon)} \quad (22)$$

Advancing contact angles were measured using a Rame-hart Contact Angle Goniometer(Korhonen et al., 2013) to assess membrane hydrophobicity. Bulk thermal conductivity (k_m) of the membranes was calculated theoretically (Eq. 23).

$$k_m = k_g\varepsilon + k_{pol}(1-\varepsilon) \quad (23)$$

Here, k_g is the thermal conductivity of dry air in membrane pores (evaluated at the average temperature inside the membrane(Kadoya et al., 1985)) and k_{pol} is the thermal conductivity of the pure polymer. Pore size for DGM modeling was estimated using an empirical correlation between fiber diameter, porosity and pore size as described in Appendix B.2. Fiber diameter in isotropically arranged networks has been related to pore diameter mathematically and experimentally. Solid fraction and fiber diameter are the primary structural parameters used to model viscous and gas transport in isotropic fibrous membranes. (Ryu et al., 2003; Eichhorn and Sampson, 2005; Szentivanyi et al., 2011)

Direct Contact Membrane Distillation Experiments: The bench-scale system used to conduct DCMD experiments is described in Appendix C.3. The membrane cassette has rectangular feed and permeate channels of dimension 0.01 x 0.04 x 0.002 m, with no spacers. Feed and permeate streams are counter-current and under laminar flow conditions. Feed and permeate flow rates were 0.3 LPM. Bulk feed concentration was 3.5wt% NaCl.

Two series of DCMD experiments were performed with multiple trials for each set of conditions. In the first series, each membrane type was tested at the same the driving force, ΔT_{bulk} = 40°C (60°C average bulk feed and 20°C average bulk permeate temperature). In the second series, ΔT_{bulk} was varied; permeate temperature was held at 20°C, and the electrospun PTFE membranes were tested at bulk permeate temperatures of 40°C, 50°C, 60°C and 70°C. The 8% PVDF membranes were also evaluated at higher driving forces (T_{fb} = 73-76°C)

Throughout each experiment, average temperatures in the feed and permeate streams, conductivity of the permeate reservoir, pressure in the feed and permeate streams, laboratory humidity, and mass of permeate were monitored and recorded.

Determination of Nusselt Number: We determined experimental Nusselt numbers by selecting an empirical correlation from literature, then modifying the equation using theoretical and empirical correction factors as discussed in Chapter 2. The Sieder-Tate Nusselt correlation was modified to account for theoretical effects of channel cross-sectional geometry, simultaneous development of laminar flow, and for the 1-wall heat flux boundary condition as described in previous work (Ch2, Eq 19). The experimentally validated correction-factor specific to the bench-top cassette was $0.5Re^{\frac{1}{4}}$.

3.3.4 B-P model regression analysis, validation, and comparison with other models:

B-P regression and internal validation. Structural characteristics and DCMD experimental data for each membrane were used to calculate dimensionless parameters, with measurement uncertainty propagated. Relationships of dimensionless parameters to the dependent variable, Π_1, were explored by regressing individual parameters and combinations of them against Π_1. To

determine a range of likely exponents for each dimensionless variable, a log-linear regression was performed (Eq 24):

$$\Pi_1 = \log\left[\Pi_2^a * \left(\frac{\Pi_3}{1-\varepsilon}\right)^b * \Pi_4^c * a_{w,bulk}^d * \left(Nu_{feed}Nu_{perm}\right)^e\right]$$

$$= a\log(\Pi_2) + b\log\left(\frac{\Pi_3}{1-\varepsilon}\right) + c\log(\Pi_4) + d\log\left(a_{w,bulk}\right) + e\log\left(Nu_{feed}Nu_{perm}\right) \quad (24)$$

Given the scatter associated experimental data collection, a multivariate linear regression will output point estimates and confidence intervals for the regression coefficients, *a*-*e*. Instead of directly using these irrational values as exponents in the log-linear regression, a simpler and more intuitive set of exponents was derived using the ratios of these regression coefficients to each other. Fractions that provide a good fit for the data were chosen for *a*-*e*.

Regressions using porosity as the fifth parameter were compared with regressions using solid fraction. Regressions with $\frac{\Pi_3}{1-\varepsilon}$ calculated using measured SEM thickness (both as-spun and post-DCMD measurements) were compared to those calculated using the Rao-Childress method (Eqs, 20, 22). The model was validated for both series of experimental data by comparison of full-data-set regression parameters to regression parameters calculated when data points from particular experimental conditions are withheld.

Comparison of B-P model performance to variations of the Dusty Gas Model and the Rao-Childress empirical model. Two theoretical models and one empirical model were chosen for comparison with the B-P model.

<u>Dusty Gas Model – Classic and Field/Wu diffusivity:</u> The DGM was chosen because it calculates membrane permeability using the two most likely vapor transport mechanisms for DCMD; Knudsen diffusion and ordinary molecular diffusion (OMD). Surface diffusion of vapor is

unlikely due to the hydrophobic nature of the membrane polymer, and viscous transport is unlikely because feed and permeate streams are maintained at the same, atmospheric pressure. Another reason to compare the B-P model with DGM is it is the most common model employed by MD researchers. As mentioned in section 3.1, the DGM and has been modified by a few research groups to attempt to improve membrane flux predictions. Field and Wu proposed a modification in which effective OMD diffusivity increases proportionally to (1+*Kn*), as vapor molecules undergoing Knudsen diffusion would not contribute to the transport resistance experienced by molecules undergoing OMD.(Field et al., 2013)

Electrospun membrane flux for each experimental run was predicted using both the classic and Field-modified DGM. This requires simultaneous solution of one dimensional mass and heat transport equations, as described in Chapter 2 and reproduced below (Eq. 25-29) with experimentally-measured system and membrane characteristics as inputs.

$$J_w = B_{w,i} \frac{\Delta p_{vap}}{\delta} \quad (25)$$

$$Q_f = Q_m = Q_p \quad (26)$$

$$Q_f = h_f\left(T_{f,b} - T_{f,m}\right) + J_w H_{w,f} \quad (27)$$

$$Q_p = h_p\left(T_{p,m} - T_{p,b}\right) + J_w H_{w,p} \quad (28)$$

$$Q_m = \frac{k_m}{\delta}\left(T_{f,m} - T_{p,m}\right) + J_w H_{w,vap} \quad (29)$$

The two versions of the DGM models differ only in the calculation of intrinsic membrane permeability, $B_{w,i}$, estimated by taking the resistance associated with ordinary molecular diffusion and Knudsen diffusion in series (Lawson and Lloyd, 1997; Khayet and Matsuura, 2011). (Eq 30, 31):

$$B_{w,i,DGM} = \frac{1}{RT}\left(\frac{1}{D_{w,e}^{knudsen}} + \frac{p_a}{D_{wa,e}^{OMD}}\right)^{-1} \quad (30)$$

$$B_{w,i,DGM-Field} = \frac{1}{RT}\left(\frac{1}{D_{w,e}^{knudsen}} + \frac{p_a}{(\mathbf{1}+\boldsymbol{Kn})D_{wa,e}^{OMD}}\right)^{-1} \quad (31)$$

The effects of Field's modification to calculated membrane permeability are explored in Chapter 2. To calculate $B_{w,i}$ for electrospun membranes, pore radius (r) and tortuosity (τ) of the electrospun membranes were estimated. Tortuosity is estimated as $1/\varepsilon$, as explained previously(Leitch et al., 2016). An empirical correlation was developed from published characterization data of electrospun membranes that relates fiber diameter and membrane porosity with average pore radius (Prince et al., 2012; Essalhi and Khayet, 2013b, 2014; Liao et al., 2013a, 2013b, 2014a, 2014b; Wu et al., 2014; Li et al., 2014a; Tijing et al., 2014a; Leitch et al., 2016). The correlation is published in Appendix B.2.

Rao-Childress Model (Empirical): This model was the only other empirical model in the literature that relates membrane structural parameters to MD performance.(Rao et al., 2014) The model correlation is as follows:

$$J_w = 10.1 + 318\, C_m = 10.1 + 318\frac{1}{\delta(1-\varepsilon)} \quad (32)$$

Units for J_w and δ are [$Lm^{-2}h^{-1}$] and [μm], respectively. Despite the similarity of Rao-Childress structural parameter to the dimensionless parameters $\Pi_3(1-\varepsilon)^{-1}$, the model is not expected to perform well quantitatively on the electrospun membrane dataset. Though the model was developed using the same bulk feed and permeate temperature as this study (60°C and 20°C), there are no parameters to describe cassette heat transfer or feed composition. Also the model was trained using a combination of supported and unsupported phase inversion membranes, a geometry dissimilar to the electrospun membranes.

Qualitative and quantitative performance of the models were evaluated. Experimental flux was compared with modeled flux predictions for all three models. A Student's T-test was made to show whether average modeled flux for a given membrane type differed statistically from average experimental flux. Model predictions and experimental results for individual membranes are plotted to show qualitative performance of the models.

3.4 Results and Discussion

3.4.1 Membrane characterization and DCMD performance. Figure 3.1 shows morphology of electrospun membrane fibers magnified at 5000x. Fibers are isotropically arranged in the x-y plane, and increase in fiber diameter is apparent as PVDF solution concentration increases. Hot-pressing did not visibly change membrane surface morphology. Fiber surfaces exhibit nanoscale roughness, similar to previous observations of PVDF spun from a DMF/Acetone solvent mixture(Liao et al., 2013b). The hierarchical roughness of the PVDF and PTFE membranes causes higher apparent hydrophobicity than a smooth polymer surface(Doshi et al., 2005), which is favorable for process salt rejection. Advancing contact angle (ACA) for DI water on the electrospun PVDF membrane was 143.5 +/- 1.3° as compared to an expected ACA of 80° for a smooth PVDF surface(Wypych, 2012) . Contact angle did not differ significantly between the PVDF membrane types. For the commercial electrospun PTFE, advancing contact angle was 150.7 +/- 0.8° as compared to a literature value of 122° for smooth PTFE.(Wypych, 2012) High contact angle of the membranes facilitated high salt rejection.

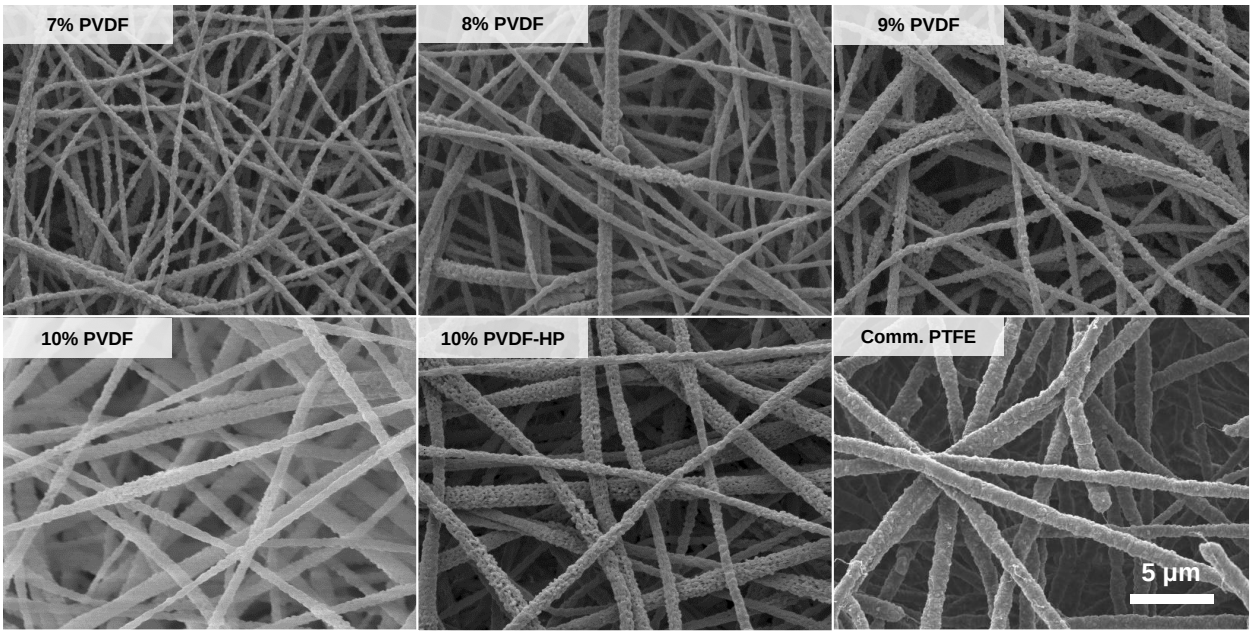

Figure 3.1 Representative images of electrospun membranes

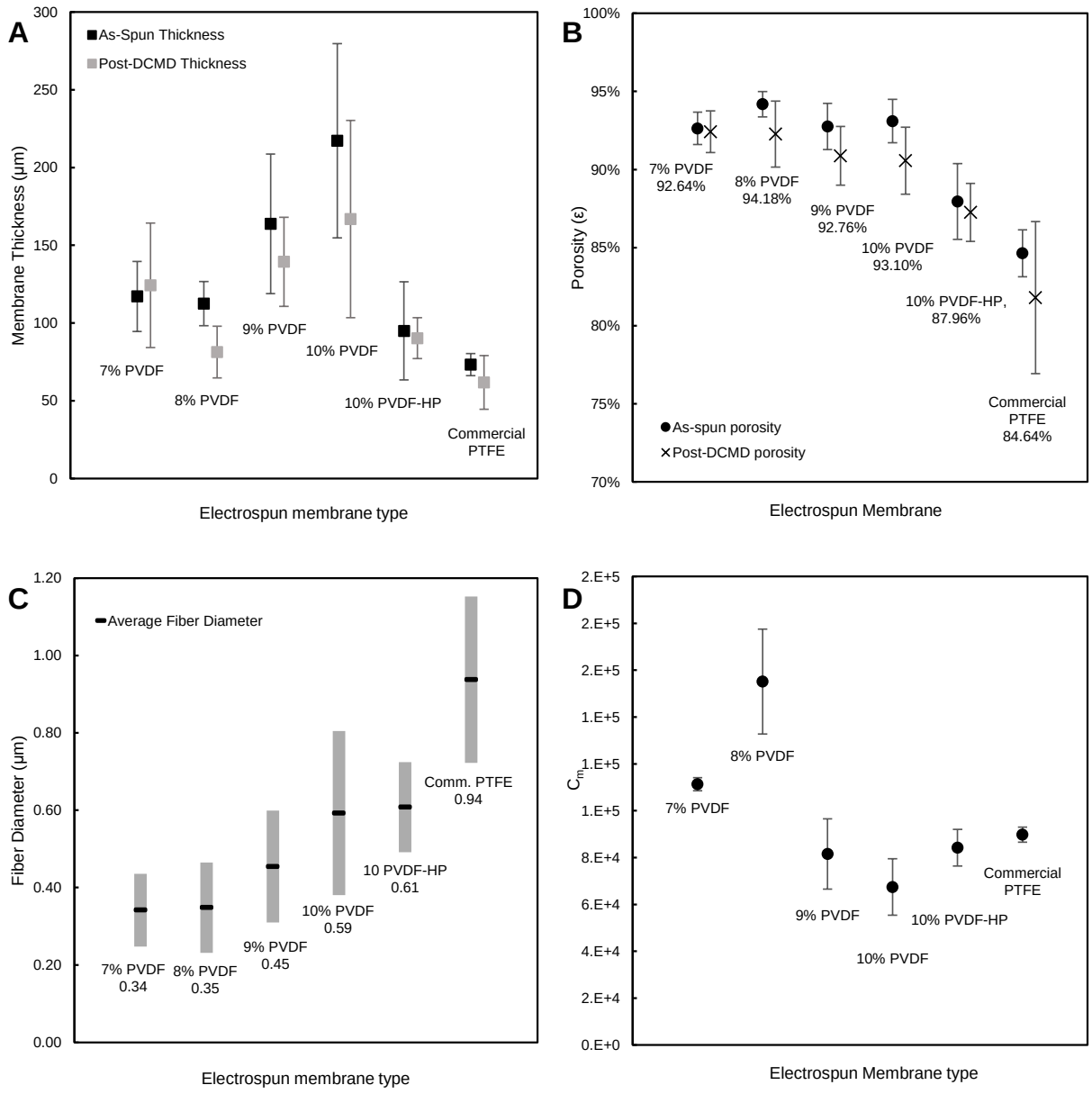

Figure 3.2 Structural characterization of isotropic fibrous membranes. A) Pre- and Post DCMD membrane thickness. B) Gravimetric porosity calculated using pre- and post-DCMD membrane thickness. C) Fiber diameter distribution (Gaussian mean and standard deviation) D) Membrane structural parameter, Cm, measured gravimetrically

Membrane characterization results are shown in Figure 3.2. Raw membrane characterization data and DCMD performance data are also tabulated in Appendix B.3, including feed and permeate Nusselt number, and DCMD flux for all membranes in each experiment.

Intra-sheet membrane thickness was highly variable for the as-spun PVDF membranes, possibly a result of charge asymmetry on the electrospinning collector plate. The hot-pressed and commercial membranes had more uniform thickness. Average thickness of the post-DCMD membrane coupons are typically lower than thicknesses measured for the pristine membrane. This deviation can be attributed to intra-sheet thickness variability and slight compression of the membrane under DCMD conditions(Leitch et al., 2016).

Average porosity of PVDF membranes were very high and appeared to decrease slightly under DCMD conditions due to the decrease in membrane thickness. Porosity of the 10% PVDF membrane decreases when subjected to hot-pressing, however still exhibits higher porosity than the commercial PTFE membrane.

As predicted by theory and previous experimental work, fiber diameter increases when PVDF concentration in the electrospinning solution increases.(Nasir et al., 2006; Essalhi and Khayet, 2014) Fiber diameter distribution did not vary between the feed and permeate faces of the membrane, nor did hot-pressing alter the mean fiber diameter of the 10% PVDF membranes.

Gravimetric measurements of structural parameter, C_m, show intra-membrane variability between coupons, particularly for the 8%, 9% and 10% PVDF membranes. This corroborates the thickness variability seen in the SEM cross-section measurements, however the gravimetric-only C_m characterization method ($\frac{\rho_{pol} l_m w_m}{m}$) results in lower parameter uncertainty as compared to C_m calculated using measured SEM thickness and solid fraction $\frac{1}{\delta(1-\varepsilon)}$, as shown by error bars in Fig 3.3

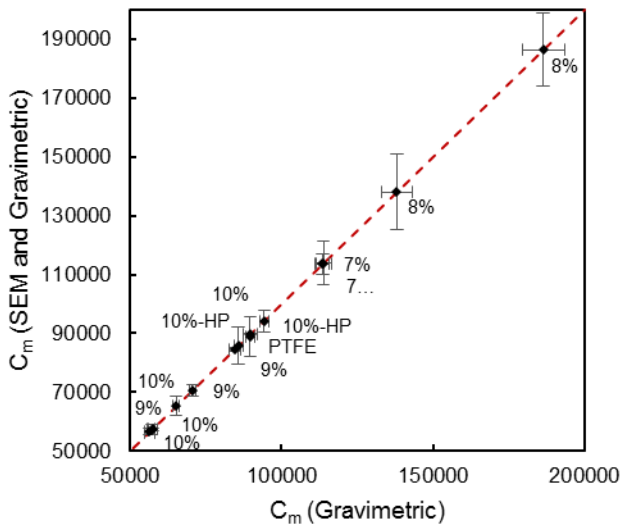

Figure 3.3 Membrane structural parameter, C_m, calculated for individual membranes using SEM thickness and gravimetric measurements vs gravimetric measurements only

Membranes exhibited excellent vapor flux as compared to previously reported flux for electrospun membranes (Fig. 3.5).(Tijing et al., 2014b) This is in part due to cassette design, which facilitates efficient heat transfer between the bulk feed and permeate streams (a evidenced by high Nusselt numbers, Appendix B.3). Structural attributes that contribute to membrane performance are evaluated using the Buckingham-Pi model.

3.4.2 B-P model regression and flux prediction

DCMD flux was measured and structure characterized for a total of 42 individual membrane coupons. Figure 3.4 presents the regression of experimental data (flux and characterization for individual membranes) using B-P dimensionless parameters. Plot 3.4A shows the "raw" regression model with independent parameters inversely proportional to the dependent parameter, Π_1. Plot 3.4B shows the total least squares regression with exponents applied as discussed in section 3.3.4, in the log-linear form used for model validation.

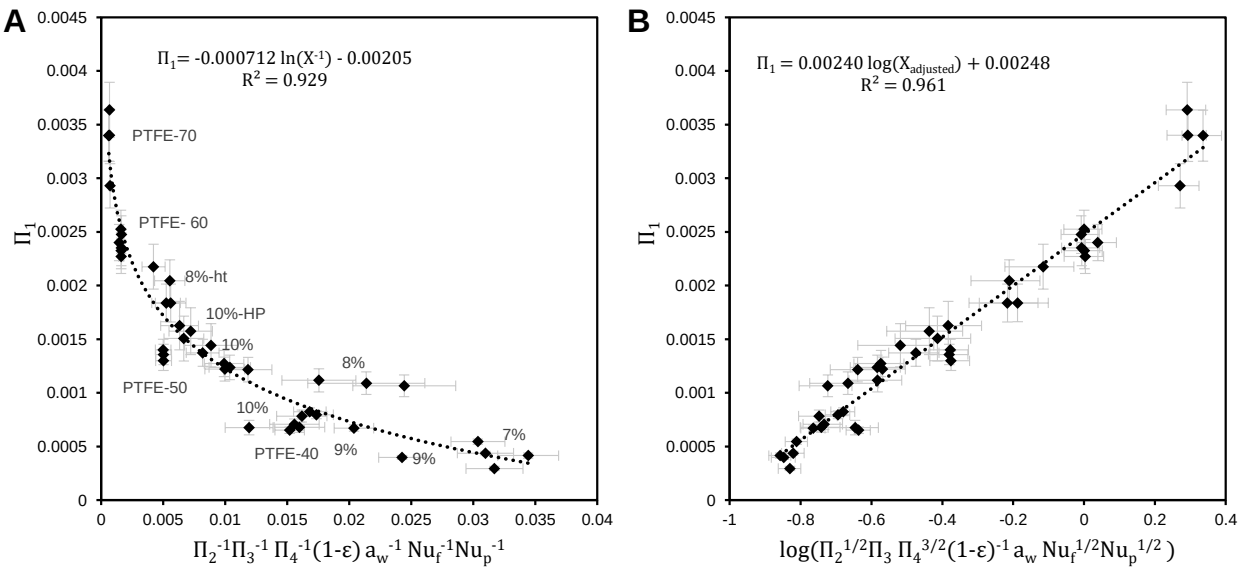

Figure 3.4 Buckingham-Pi regressions model. 3A) All parameters inversely proportional to flux, showing uncertainty for each experimental data point. 3B) Log-Linear plot with adjusted exponents used for flux prediction and model validation

Choice of model parameters: Figure 3.4 B-P regressions use gravimetric measurements of C_m to compute $\frac{\Pi_3}{1-\varepsilon}$, because this decreased propagated uncertainty for individual data points. Calculation of $\frac{\Pi_3}{1-\varepsilon}$, using SEM thickness measurements made no significant difference to the regression model output. Regressions were examined using porosity, ε, as an alternative structural parameter to solid fraction $(1-\varepsilon)$ as the fifth parameter. Model fits using solid fraction were superior to those that used porosity as the parameter, evidenced by a 0.12 increase in R^2. (The porosity correlation is displayed in Appendix B4). We postulate this is an effect of the membranes used to train the model. For sparse structural networks, porosity is not sensitive enough as a parameter to differentiate transport characteristics between similar membranes. For example, the difference between multiplying by a factor of 0.94 or 0.96 is not particularly significant on a dependent outcome variable. On the other hand, multipliers 0.06 and 0.04 scale a dependent variable much differently from each other (The dependent variable scaled with 0.06

will be 50% larger than the variable scaled with 0.04). For highly-porous membranes, a solid fraction parameter exerts more of an influence than porosity parameter on the dependent variable, Π_1. Because the B-P model fits were superior with the use of solid fraction, we can conclude $(1-\varepsilon)$ is an appropriate parameter to predict MD flux in fibrous, highly porous membranes.

Significance of model parameters: An analysis was performed to determine the significance of each dimensionless parameter to the regression model. The model was designed to be generalizable for a variety of feed solution conditions and feed/permeate cassette configurations, which is why $a_w, Nu_f, and\ \ Nu_p$ were included, however the data collected in this study does not require all seven parameters to produce a good fit. Because this study focuses on the effects of electrospun membrane structure on flux, only Π_2, $\frac{\Pi_3}{(1-\varepsilon)}$, and Π_4 were systematically varied. In the log-linear regression (Eq 24), p-values for Π_2, $\frac{\Pi_3}{(1-\varepsilon)}$, and Π_4 coefficients ranged from 10^{-10} to 10^{-14}, highly significant. Plots given in Appendix B.4 show some specific effects of these structural parameters on the model fit; for this dataset, good correlation to Π_1 can be achieved with only Π_2, $\frac{\Pi_3}{(1-\varepsilon)}$, and Π_4 ($R^2 = 0.959$). Regressing Π_1 against single dimensionless parameters shows Π_2, has the best fit ($R^2 = 0.818$), because it incorporates the driving force for vapor transport. Addition of both $\frac{\Pi_3}{(1-\varepsilon)}$, and Π_4 is required for any improvement to the model regression. The significance of the parameter $\frac{\Pi_3}{(1-\varepsilon)}$ to this regression shows that membrane structural parameters should certainly be included in empirical MD flux models, but that for the case of isotropic fibrous membranes, membrane characterization can be done without measuring pore size distribution or membrane thickness.

Regarding the remaining parameters, a_w was not correlated with Π_1 and p-values for Nu_f Nu_p could not be determined precisely because variations in bulk feed temperature caused Nu_f to be collinear with Π_4. We expect Nu_f, Nu_p and a_w will influence model fit if they are varied independently of other parameters. Effects of these parameters can be explored in future work.

3.4.3 Model validation. Table 3.2 presents repeated regression analyses showing how the model changes when subsets of experiments are withheld. We find the regression is stable for a variety of membrane geometries and experimental conditions. Most change in the regression analysis occurs when data from all 60°C or 70°C feed temperature experiments were withheld. Removal of all 60°C experiments from the dataset excludes all but 14 data points and eliminates all 7% and 9% PVDF membrane data at the low end of the regression curve. Likewise, withholding high-temperature data removes all data points from the high end of the regressions curve. This suggests the regression model should be trained with a large number of data points, and model flux predictions will not be accurate for high or low Π_1 values outside the trained regression. B-P model performance for each subset of membranes is analyzed using the "withheld data" regressions found in Table 3.2. This allows predictive capabilities of the B-P model to be fairly compared with the DGM and Rao-Childress models.

Table 3.2 – Regression analysis repeated by removing subsets of experimental results. Green text signifies 95% confidence intervals of log-linear regression parameters with all experimental data. Red text signifies model parameters fall outside the confidence interval when data is withheld.

	Log-linear equation slope	**Log-linear equation intercept**	**R^2**
Withheld membranes			
None	**0.00240 ± 6.4%**	**0.00248 ± 3.3%**	**0.961**
7% PVDF	0.00237	0.00248	0.956
8% PVDF	0.00245	0.00249	0.967
9% PVDF	0.00238	0.00248	0.959
10% PVDF	0.00242	0.00247	0.967
10%-HP	0.00241	0.00247	0.964
Comm. PTFE	0.00239	0.00249	0.916
Withheld driving force experiments			
40 °C feed	0.00241	0.00248	0.959
50 °C feed	0.00240	0.00250	0.967
60 °C feed	0.0025 (+7.0%)	0.00248	0.965
70+ °C feed	0.00225	0.00239 (-3.5%)	0.945

3.4.4 Comparison of modeled flux predictions with experimental flux

Figure 3.5 compares DGM, Rao-Childress and B-P model predictions with experimental data. In Figure 3.5A and B, average experimental flux for each membrane type is compared with average modeled flux for each experimental series. A Student's T-test is performed to determine whether differences between average model predictions and experimental results are statistically significant at the $\alpha = 0.05$ level. This method, and a qualitative assessment of model predictions for individual experiments (Figure 3.4C), confirms the B-P model predicts DCMD flux more accurately for electrospun membranes than either the classic DGM or Rao-Childress model.

The B-P model slightly over-predicts experimental flux for PTFE membranes at 50°C and 60°C feed temperature. Observation of Fig. 3.4a shows experimental flux for PTFE membrane at

40°C feed also falls below the unadjusted regression curve. This could be the result of inexact membrane characterization. For example, polymer thermal conductivity and polymer density For PVDF and PTFE were both estimated using literature values(Wypych, 2012). Another plausible reason for the overestimation of MD flux for the PTFE membranes is that the B-P parameter exponents *(a-e)* are not static, but variable with experimental conditions or membrane type. In section 3.2.2., we show that Π_2 is proportional to $\frac{D_{Knudsen}^2}{D_{OMD}^2}$ and Π_4 is proportional to $D_{w,a(OMD)}$. Theoretical MD models postulate the contribution of each diffusion mechanism to total MD flux is variable with pore size and properties of the pore-fluid. This would cause the ratio of the exponents of Π_2 and Π_4 to also vary with these experimental conditions. The data collected in this exploratory study is not rich enough to explore this hypothesis. However, statistical methods, such as factorial design or response surface methodology, can be used to design experimental training sets that yield correlations with predictive accuracy for a wide range of membrane structural parameters and/or experimental conditions. (Khayet et al., 2007; Khayet and Cojocaru, 2012)

The R-C empirical model was not formulated for quantitatively accurate flux predictions; it does not contain parameters to account for system conditions such as bulk driving force or cassette Nusselt number (See Fig3.5B). However, the empirical model also did not qualitatively predict which membrane types would perform better than others.(Fig 3.5A). The model's lack of a dimensional parameter to account for membrane interior structure, such as pore size or fiber diameter, resulted in an inability to predict how electrospun membranes would perform in relation to each other. Conversely, both the DGM, Field-DGM, and B-P models had good qualitative agreement of which electrospun membrane structures should lead to higher flux, except for the 7% PVDF membrane. A hypothesis for the substandard model performance for

the 7% membrane is the presence of slight beading in the fibers. See Appendix B.5 for comparison of the membrane surfaces. Finally, it is noted that model predictions using the Field-DGM model were higher than classic DGM model predictions yet still generally under-predict electrospun membrane flux. This suggests the DGM models underestimate membrane permeability, caused by the inherent structural assumption of isolated pores.

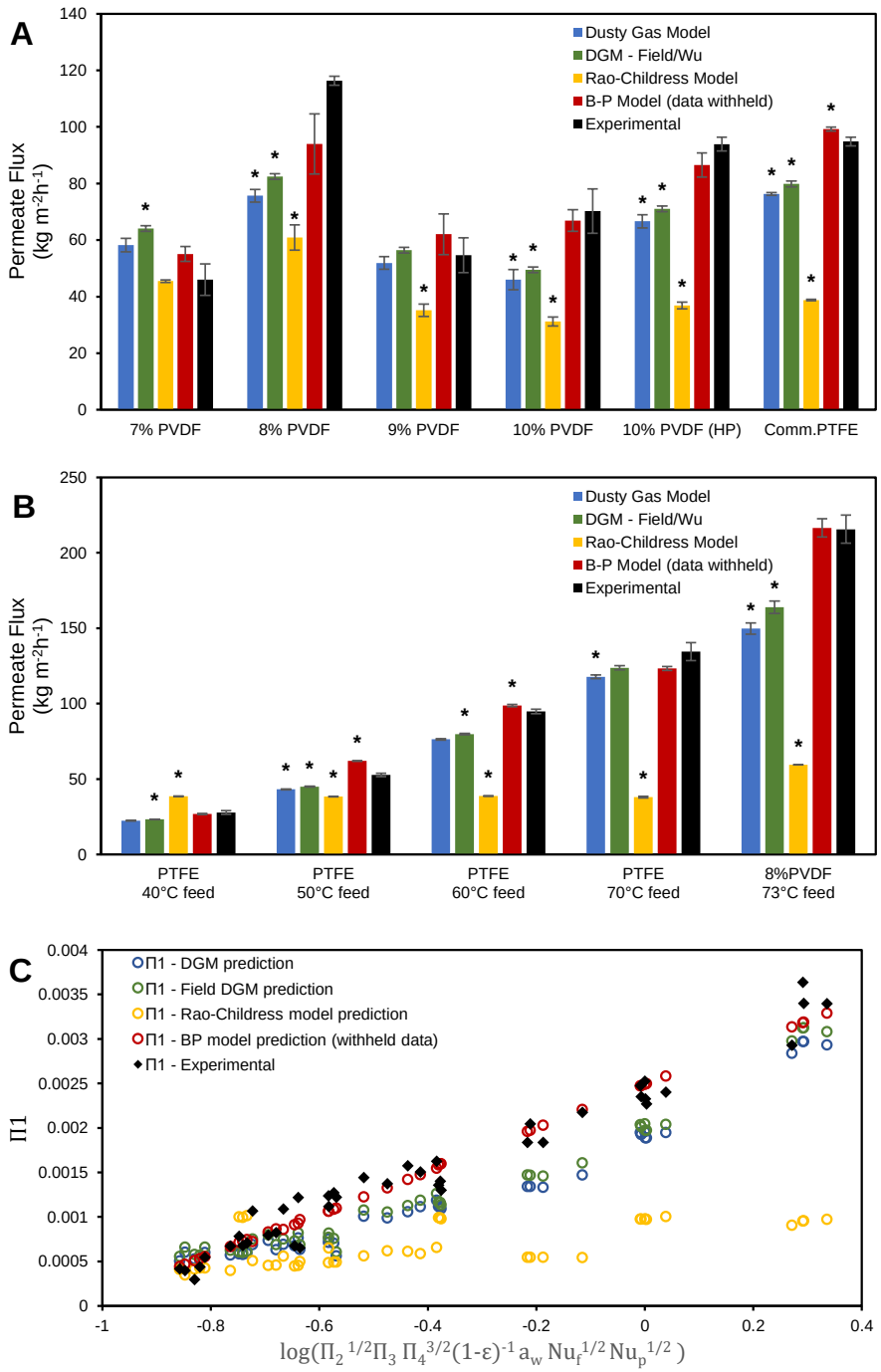

Figure 3.5 Comparison of modeled predictions with experimental data. A) Average modeled and experimental flux. Asterisk shows model results differ from experimental results at the α = 0.05 level. B) Data plotted for individual membranes on the B-P regression axes. Show qualitative differences in model performance.

The power of any theoretical and empirical MD flux model is limited by uncertainty in characterization techniques. If characterization of DCMD conditions or membrane structure for

input data is uncertain, this uncertainty propagates to uncertainty in model correlation coefficients and model predictions. The value of structural characterization data typically collected for fibrous membranes is limited by inaccurate methods to calculate pore size and tortuosity as well as uncertainty in membrane thickness characterization. Specific limitations of SEM thickness characterization are its inability to a) non-destructively measure thickness of a membrane sample before and after DCMD testing and b) to efficiently characterize membrane thickness variability by analyzing large cross-sections in multiple planes throughout the membrane. The B-P model proposed in this work therefore contributes two primary improvements to the MD literature: a set of easily and accurately measurable structural characteristics to determine fibrous membrane performance in DCMD, and an empirical method to predict MD flux for fibrous membranes.

3.5 Conclusions and Future work

3.5.1 Conclusions: Buckingham-Pi dimensional analysis was applied to formulate a new empirical model for MD transport through fibrous membrane structures. Improvements of this model over existing *theoretical* transport models are its use of easily-measurable structural parameters specific to the geometry of fibrous membranes, and an absence of simplifying assumptions about pore structure. Improvements over existing *empirical* models are its inclusion of both membrane and channel parameters to predict flux, and the physical meaning that can be attributed to each model parameter. Agnostically-determined dimensionless parameters corroborate vapor transport theory by showing a dependence of flux on Knudsen diffusion and ordinary molecular diffusion. Using empirical correlations, we show the derived dimensionless parameters are more effective at predicting MD flux for fibrous membranes than commonly-used theoretical models and an empirical model.

The B-P model holds practical appeal due to its simple membrane characterization requirements and its use of a closed-form expression to predict MD permeate flux, however more work is needed to determine its applicability for wider ranges of membrane types and system conditions. Future work should expand of the correlation to a wider array of experimental conditions, focusing particularly on varying feed water activity, and cassette Nusselt Numbers. Furthermore, the dependence of parameter exponents on vapor properties and membrane pore size should be explored to determine whether they vary based on contributions from different diffusive transport mechanisms. Validation of the correlation across different DCMD bench-scale systems can give insight into the model's predictive capabilities.

Finally, future work can address the generalizability of the empirical B-P model for membrane distillation flux prediction. By adapting the parameters for membrane structural characteristics or transport mechanism, the method could be extended to other emergent MD membrane geometries (e.g. asymmetric or hollow fiber membrane) or permeate-side configurations (e.g. vacuum membrane distillation or air gap membrane distillation). Valid B-P correlations of MD flux for a range of membrane types and operating conditions could facilitate a better qualitative understanding of the influence of system and membrane parameters on MD performance as well as easier back-of-the-envelope computations of specific effects of design choices on MD flux.

ACKNOWLEDGEMENTS: We thank Zeus incorporated for providing samples of the Filtriq electrospun PTFE membranes for use in this study.

Chapter 4 : BACTERIAL NANOCELLULOSE AEROGEL MEMBRANES: NOVEL HIGH-POROSITY MATERIALS FOR MEMBRANE DISTILLATION(Leitch et al., 2016)

4.1 ABSTRACT

We developed, characterized, and tested novel fibrous aerogel membranes in direct contact membrane distillation (MD) to elucidate the effects of a model high-porosity membrane material on MD performance. Unsupported bacterial nanocellulose aerogels exhibit higher porosity, thinner fibers, and lower bulk thermal conductivity than any previously reported MD material. We demonstrate through modeling and experiments that these material properties translate to significant improvements in intrinsic membrane permeability and thermal efficiency over a symmetric PVDF phase inversion membrane with lower porosity. Development of macroporous fibrous membranes with aerogel-like porosity and thermal conductivity (>98% and <0.03 $Wm^{-1}K^{-1}$, respectively) in thinner-film formats may further improve MD flux.

4.2 INTRODUCTION AND BACKGROUND

Membrane distillation (MD) is a thermally-driven separation process in which a solvent volatilizes from a warm feed solution, transports through a lyophobic membrane, and condenses in a cool permeate stream. The weak dependence of vapor pressure on ionic strength makes this technology attractive for desalinating high salinity feed streams (>100,000 Total Dissolved Solids (TDS)), including brines from carbon capture and storage operations,(Burant et al., 2013) reverse osmosis (RO) concentrate, and industrial wastewaters. Use of low-grade heat as the energy input has the potential to significantly reduce the energy intensity of MD relative to other thermal and membrane treatment technologies. Despite these process advantages, the

commercial implementation of MD has been limited by the low permeability and high conductive heat loss of current MD membranes.(Khayet, 2011)

Large pore diameter, low pore tortuosity, high porosity, low thermal conductivity, and optimized thickness of MD membrane materials are correlated with high vapor permeability and thermal efficiency, regardless of MD process conditions.(Khayet, 2011; Tijing et al., 2014b) Optimized thickness refers to the balance between minimizing mass transfer resistance to flow of vapor while maximizing the thermal gradient. Past efforts to improve MD performance have focused almost entirely on varying pore diameter, tortuosity, and thickness.(Khayet et al., 2005; Qtaishat et al., 2009c, 2009a, 2009b; Dumee et al., 2010; Dumée et al., 2011; Drioli et al., 2013; Liao et al., 2013a, 2013b, 2014a, 2014b; Tijing et al., 2014a; Wu et al., 2014) There are very few experimental(Essalhi and Khayet, 2014; Li et al., 2014b) or theoretical studies reporting MD performance of membrane materials with low thermal conductivity or high porosity (>90%).

One relevant class of materials is aerogels, which exhibit porosities up to 99.9% and ambient-pressure thermal conductivity as low as 0.012 $Wm^{-1}K^{-1}$.(Lu et al., 1992; Kugland et al., 2008; Sun et al., 2013) These materials may be composed of silica or other metal-oxides,(Kistler, 1931; Teichner et al., 1976; Gash et al., 2001; Clapsaddle et al., 2004) polymers,(Pekala, 1989) hybrid organic/inorganic materials,(Nguyen et al., 2010; Randall et al., 2011) or nano-carbon,(Bryning et al., 2007; Lin et al., 2011; Kim et al., 2012) and are created by replacement of liquid with gas in a network obtained by the sol-gel process. Unfortunately, traditional aerogels are difficult to process into uniform thin-films, require a rigid support to compensate for their brittleness, tend to form small pores of only 10-20 nm,(Suh and Park, 1996; Dorcheh and Abbasi, 2008) and may be difficult to hydrophobize.

An alternative to traditional organic and polymeric aerogels are fibrous nanocellulose aerogels. The high aspect ratio of nanocellulose fibers confer processability, flexibility, and tunable pore sizes ranging between 0.47 nm and 500 μm.(Zaborowska et al., 2010; Lavoine et al., 2012) Past work on nanocellulose aerogels has demonstrated that cellulose source, processing, drying method, and surface functionalization can be adapted to achieve a wide range of structural and surface characteristics.(Pääkkö et al., 2008; Klemm et al., 2011; Wang et al., 2013)

The nanocellulose matrix material may originate from plant matter or may be produced as a biofilm by select aerobic mesophilic heterotrophs.(Klemm et al., 2011) The characteristics of bacterial nanocellulose (BNC) vary depending on the bacteria sub-species and growth conditions, but it most often comes in the form of a highly-entangled web of highly-crystalline cellulose-I nanofibers, bound together by hydrogen bonds where the fibers intersect. The fibers can be rod or ribbon-shaped, are 5 to 100 nm in diameter, and are often over 100 μm in length.(Haigler et al., 1982; Ross et al., 1991; Zhang, 2013) When grown in static liquid media, pure cultures of *Gluconacetobacter xylinus, Gluconacetobacter medellinensis* or other cellulose-producing species will form a uniform gel mat of ~1% cellulose fibers and ~99% liquid at the air-media interface.(Klemm et al., 2011) The ultra-high-porosity fibrillar structure, the facile chemical surface modification of cellulose fibers, and their mechanical stability and flexibility in hydrogel form has motivated the use of BNC gels for applications in medicine, electronics, and textiles.(Iguchi et al., 2000; Klemm et al., 2001, 2011; Moon et al., 2011; Petersen and Gatenholm, 2011) Supercritical drying or lyophilization of the BNC matrix prevents collapse of the cellulose gel network and transforms nanocellulosic biofilms into a thin BNC aerogel (BNCA) membrane.(Pääkkö et al., 2008)

The present research introduces flexible, unsupported bacterial nanocellulose aerogels as a model material for investigating the influence of porosity and thermal conductivity on MD flux. We fabricate and characterize hydrophobic BNCAs for porosity, pore size, fiber diameter, thickness and thermal conductivity prior to evaluating membrane flux in direct contact membrane distillation (DCMD) mode. We compare experimentally-obtained intrinsic permeability and thermal efficiency against a lower-porosity commercial symmetric phase-inversion polyvinylidene fluoride (PVDF) membrane. Finally, we discuss commercially viable analogs to BNCA membranes that may form the basis for next-generation MD membrane materials.

4.3 MATERIALS AND METHODS

Fabrication of hydrophobic BNCA membranes: We grow BNC gels from pure *Gluconacetobacter medellinensis* cultures. Gels are cleaned and supercritically dried as described in the Supporting Information (SI-1). This process yields a hydrophilic nanocellulose aerogel that is hydrophobized via the "bottle-in-bottle" chemical vapor deposition method described in Jin, 2011.(Jin et al., 2011) BNCA reacts with (tridecafluoro-1,1,2,2-tetrahydrooctyl)trichlorosilane vapor at 70°C for 3 hours, resulting in dense monolayer coverage of the cellulose fibers with hydrophobic silane.(Jin et al., 2011)

Characterization of BNCA and benchmark polymer membranes: We use a Quanta 600 FEG Scanning Electron Microscope to determine membrane morphology, thickness, and fiber diameter. Images are analyzed using ImageJ with the plug-in DiameterJ.(Schneider et al., 2012; Hotaling et al., 2015) We calculate the membrane porosity (ε) gravimetrically as described in SI-2. Pore size distribution is measured with a PMI CFP-1500-AE capillary flow porometer using

Galwick^{TM} commercial wetting fluid. To determine effectiveness of silane hydrophobization, we obtain FTIR spectra of hydrophilic and hydrophobic gels with a Thermo Nicolet Avatar 380 FT-IR Spectrometer and measure advancing contact angles of the hydrophobic gels using a Rame-hart Contact Angle Goniometer as described in Korhonen, 2013.(Korhonen et al., 2013) Bulk thermal conductivity (k_m) of the membranes was calculated theoretically (Eq. 1).

$$k_m = k_g\varepsilon + k_{pol}(1-\varepsilon) \quad (1)$$

Here, k_g is the thermal conductivity of dry air in membrane pores (evaluated at the average temperature inside the membrane(Kadoya et al., 1985)) and k_{pol} is the thermal conductivity of the pure polymer.

DCMD experiments: We compare flux performance of BCNAs to PVDF membranes (Millipore© GVHP, 0.22 μm nominal pore diameter) using a bench-top DCMD system. A schematic depicting the design of the bench top unit is provided in SI-3. Experimental permeate temperature is held at 20°C, while feed temperatures are chosen to simulate low-grade heat sources. In one set of experiments, membranes were tested with a 40°C feed, representative of heat rejected in the condenser streams of US power plants.(Gingerich and Mauter, 2015) Another set of membranes were tested with a 60°C feed to simulate a higher-grade flue gas exhaust,(Gingerich and Mauter, 2015) geothermal, or solar heat driving force. We subjected each membrane to DCMD conditions for three to six hours such that the error in salt rejection calculations averaged below 0.02%.

Membrane morphology change during DCMD: We infer structural and chemical stability of BNCA and PVDF membranes using theory, modeling, and experimental evidence. A complete discussion is provided in SI-4. We assess membrane compressibility under the ~6.2 KPa of transverse head pressure in the DCMD system by performing static tests on representative

membrane samples and analyzing changes in cross-sectional thickness. We evaluate any changes in surface morphology via SEM of membranes before and after DCMD, and we compliment this work with modeling to assess any potential implications of fiber aggregation on flux. We examine chemical stability of the hydrophobic silane coating by performing contact angle measurements before and after exposure to high temperature feed streams.

Determination of membrane permeability and thermal performance: To evaluate the intrinsic permeability ($B_{w,i}$) and thermal performance of the tested membranes, we solve mass and heat transport equations (Eq. 2 – 6), adapted from Khayet,(Khayet, 2011) simultaneously.

$$J_w = B_{w,i}\frac{\Delta p_w}{\delta} \quad (2)$$

$$Q_f = Q_m = Q_p \quad (3)$$

$$Q_f = h_f\left(T_{f,b} - T_{f,m}\right) + J_w H_{w,f} \quad (4)$$

$$Q_p = h_p\left(T_{p,m} - T_{p,b}\right) + J_w H_{w,p} \quad (5)$$

$$Q_m = \frac{k_m}{\delta}\left(T_{f,m} - T_{p,m}\right) + J_w H_{w,vap} \quad (6)$$

As illustrated in Figure 1, J_w is the mass (vapor) flux through the membrane, $B_{w,i}$ is the intrinsic membrane permeability, and Δp_w is the difference in saturation vapor pressure between the feed and permeate side, and δ is the membrane thickness. Q_f, Q_m and Q_p are the combined convective and conductive heat flux through the feed boundary layer, the membrane, and the permeate boundary layer, respectively. $T_{f,b}$, $T_{f,m}$, $T_{p,m}$, and $T_{p,b}$ are average in-cassette temperatures of the bulk feed stream, the feed-side membrane surface, the permeate-side membrane surface, and the bulk permeate stream, respectively. The boundary layer heat transfer coefficients are h_f and h_p,

and k_m is the thermal conductivity of the membrane. Enthalpies of the distillate convecting through the feed boundary layer, the membrane, and the permeate boundary layer are $H_{w,f}$, $H_{w,vap}$ *and* $H_{w,p}$, respectively. In these equations, J_w, $T_{f,b}$, $T_{p,b}$ are measured directly during DCMD experiments, k_m and δ are found by characterizing each membrane. All other parameters are calculated using experimental data, as described in SI-5.

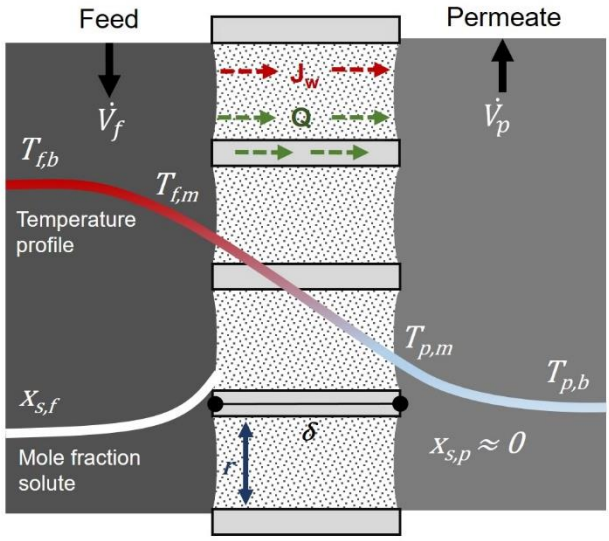

Figure 4.1 Schematic of membrane cross-section in DCMD

Expressions for thermal efficiency (η) and the average temperature polarization coefficient (TPC) are provided in Eq. 7 and Eq. 8, respectively.

$$\eta = \frac{Q_{m,vap}}{Q_{m,total}} \tag{7}$$

$$TPC = \frac{T_{f,m} - T_{p,m}}{T_{f,b} - T_{p,b}} \tag{8}$$

The parameter $Q_{m,vap}$ equals $J_w H_{w,vap}$, the heat flux through the membrane due to vapor convection, therefore η is the ratio of 'productive' heat to total heat transported in the MD process. Under

identical DCMD system conditions, the TPC compares how effectively different membranes insulate the feed from the permeate stream and maintain the driving force along the length of a membrane module.

Finally, specific heat duty (β, i.e. the thermal energy used per mass of permeate produced) can be compared between the BNCA membranes and commercial PVDF membranes by taking the reciprocal of the ratio of their thermal efficiencies (Eq. 9).

$$\frac{\eta_{GVHP}}{\eta_{BNCA}} = \frac{Q_{GVHP,vap} * Q_{BNCA,total}}{Q_{BNCA,vap} * Q_{GVHP,total}} = \frac{J_{w,GVHP} H_{w,vap} * Q_{BNCA,total}}{J_{w,BNCA} H_{w,vap} * Q_{GVHP,total}} = \frac{\beta_{BNCA}}{\beta_{GVHP}} \quad (9)$$

4.4 Results and Discussion

Characteristics of nanofibrous BNCA membranes. BNCA membranes are formed from thin and uniform cellulose fibers with isotropic orientation in the x-y plane (Figure 2). There is evidence of layering in the z-direction (Figure 2F), as well as slight cross-sectional asymmetry that is likely due to evaporative aggregation of surface-fibers during biofilm growth and processing. This morphology is consistent with lyophilized and supercritically dried BNCA described elsewhere.(Klemm et al., 2009; Liebner et al., 2010; Moon et al., 2011; Zeng et al., 2014) On average, the BCNA membranes are 2.3 times thicker than the commercial PVDF membrane (Figure 2F, 2I) and have a more open and interconnected pore network (Figure 2E, 2H). Gravimetric measurements confirm that BNCAs have much higher porosity (98.0%) than the PVDF membrane (62.2%). Skeletal conductivity of PVDF and cellulose polymer are comparable (PVDF: 0.17-0.25 $Wm^{-1}K^{-1}$ and cellulose: 0.054- 0.13 $Wm^{-1}K^{-1}$),(Brandrup et al., 1999) but the high porosity of the BNCA membrane results in a much lower effective bulk thermal conductivity. Table 1 summarizes quantitative characterization results.

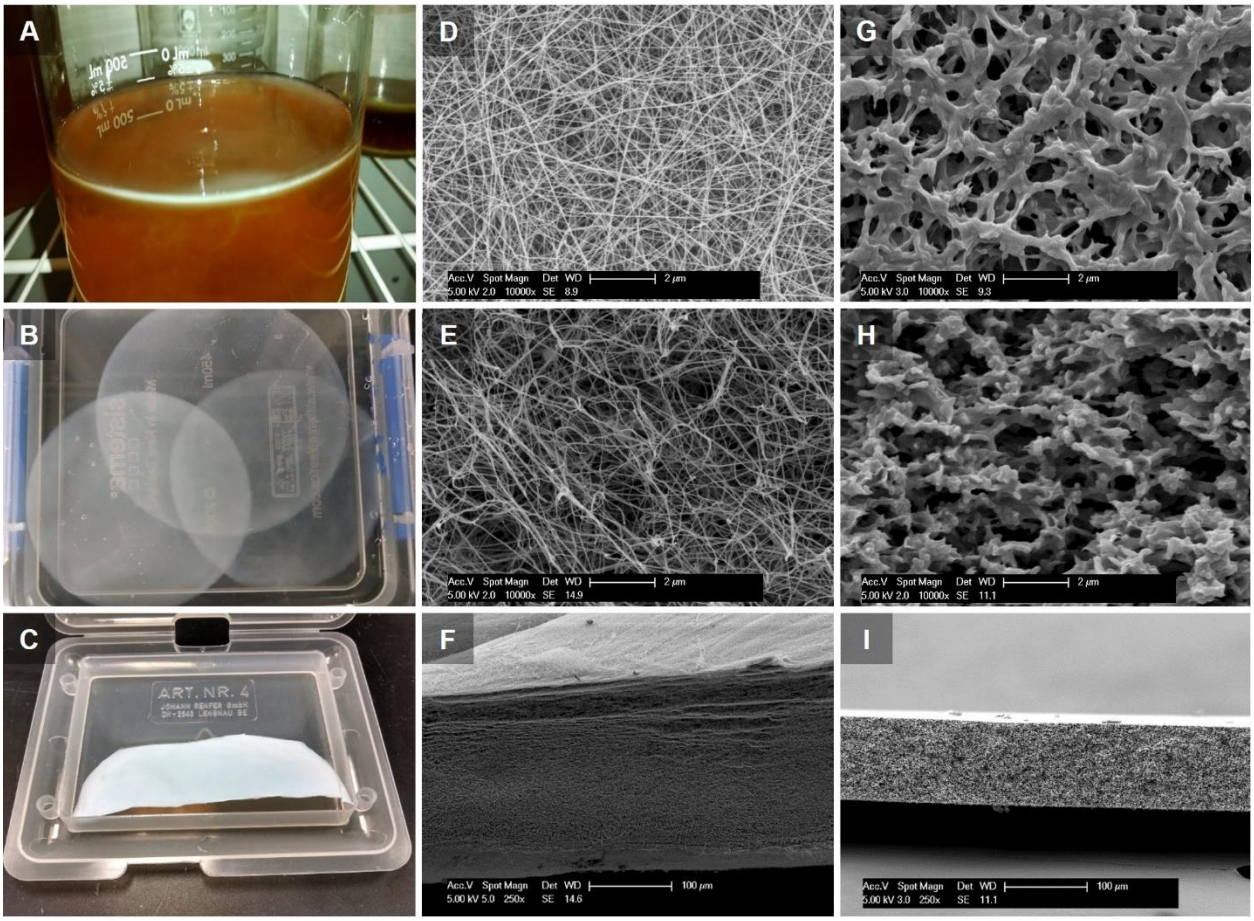

Figure 4.2. Images of typical BNCA and PVDF membrane samples. A) BC biofilm growth in media; B) Three cleaned BC gels in DI water; C) Supercritically dried BNCA; D) BNCA membrane surface, 10,000x; E) BNCA cross section, 10,000x; F) BNCA cross section, 250x; G) PVDF membrane surface, 10,000x; H) PVDF cross section, 10,000x; I) PVDF cross section, 250x.

Table 4.1. Characterization of polymer benchmark and BNCA membranes. Uncertainty represents variations between samples. There is significant variation in the BNCA membrane thickness from sample to sample. Similarly-sized samples were used for each temperature experiment, which minimized intra-experiment variability.

	PVDF	**BNCA**
thickness[a] (μm)	109 ± 5	257 ± 45
thickness reduction, static compression (%)	8.9±4.1	13±3.7
thickness reduction, surface fiber aggr. (%)	N/A	0 - 10
porosity[b] (%)	62.2 ± 3.1	98.0 ± 0.5
fiber diameter[a] (nm)	N/A	32 ± 15
bubble point[c] (MPa)	0.033	0.266
max pore diameter[c] (nm)	1,390	171
avg pore diameter[c] (nm)	244	115
SD pore diameter[c] (nm)	387	38
thermal conductivity[d] ($Wm^{-1}K^{-1}$)	0.089	0.027
contact angle[e]	147 ± 2.8°	156 ± 5.5°

a) SEM
b) gravimetric analysis
c) capillary flow porometry, Galwick™ fluid
d) theoretical calculation
e) contact angle goniometry

FTIR spectra indicate the appearance of new infrared Si-OR stretching absorption bands at wavenumbers 1145 cm^{-1} and 897 cm^{-1}, as well as CF_2-CF_2 stretching absorption at 1238 cm^{-1} and 1206 cm^{-1} after silane functionalization of the BCNA membranes. FTIR spectra and advancing contact angle images are presented in Section SI-6, Figures S10 and S11. Porometry data indicate that aerogels have a smaller average pore diameter and narrower pore size distribution than the commercial PVDF membranes (CFP data reported in SI-7).

Post-DCMD micrographs reveal aggregation of a thin layer of BNCA fibers on the feed side of the membrane, but experimental and modeling evidence suggest that this aggregation does not significantly affect membrane permeability or thermal efficiency (SI-4). Subsequent analysis of membrane permeability and thermal efficiency incorporate uncertainty related to *in situ* membrane thicknesses and surface morphology. Beyond this thin layer of fiber aggregation in the BNCA membranes, and approximately 10% compression in both BNCA and PVDF membranes due to DCMD head pressure, there is no evidence for significant structural or chemical change during membrane testing (Table 1, SI-4).

High intrinsic permeability and thermal performance of BNCA Membranes: The metric of merit for symmetric membrane materials is intrinsic permeability, or the experimental permeability (B_w) normalized by thickness ($B_w \cdot \delta$) (Figure 3A). Figure 3B compares membrane thermal efficiencies, and Table 2 reports permeate flux, salt rejection, and TPC. BNCA and PVDF flux are comparable because the BNCA membranes are substantially thicker. BNCA flux and salt rejection remained constant throughout each 3 - 6 hour DCMD experiment, indicating stability of BNCA morphology and chemistry under the experimental conditions. Future work should explore the limits of BNCA durability under more extreme operating conditions, including performance in the presence of foulants and stability during chemical cleaning.

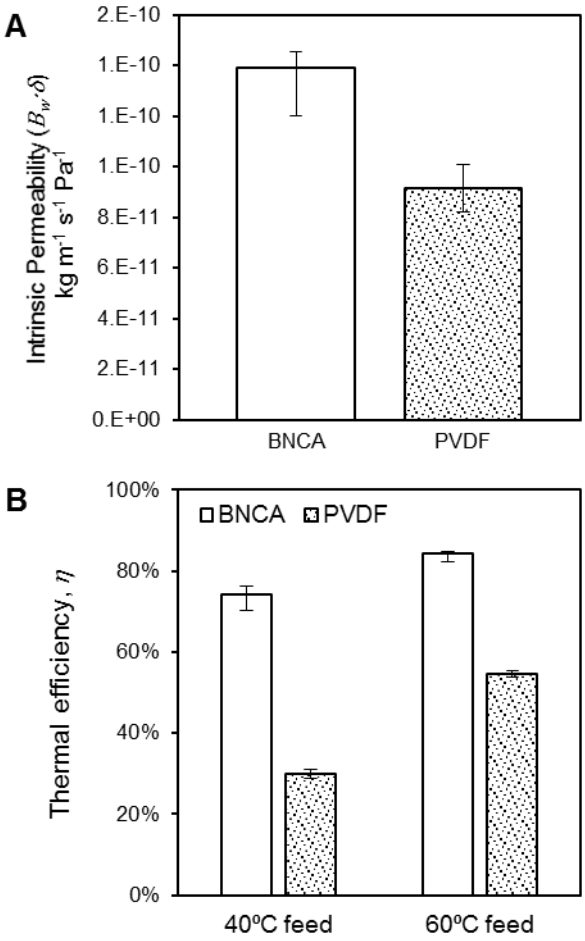

Figure 4.3. Experimentally-measured intrinsic (thickness-normalized) membrane permeability and thermal efficiency. Membrane permeability comparison (A) shows enhanced morphological suitability of BC aerogel structure over commercial phase-inversion PVDF membranes. High thermal efficiency (B) observed for BNCA compared to the benchmark indicates high-porosity fibrous membranes could be advantageous under conditions where the quality or quantity of the thermal energy for desalination is limited, or where there is demand for very high recovery rates. For all experiments, feed TDS = 35 g/l NaCl, permeate temperature = 20ºC, feed and permeate Velocities = 0.25 m/s. Error bars represent the Standard Error of the Mean for multiple experiments. N ≥ 8 for all experimental results

Intrinsic permeabilities of both BNCA and commercial PVDF membranes are higher than the theoretical permeability calculated with the Dusty Gas Model,(Mason and Malinauskas, 1983; Lawson and Lloyd, 1997; Khayet and Matsuura, 2011) which assumes cylindrical non-connected pores (see data presented in SI-8, Figure S13). In membranes with pore size regimes between 1 and 100 times the mean free path of water vapor (14-1400 nm pore diameter at 50^0C), ordinary

molecular diffusion (OMD) and Knudsen vapor diffusion are relevant transport mechanisms.(Lawson and Lloyd, 1997; Field et al., 2013) Greater pore interconnectivity, which produces an apparent increase in pore size, favors the OMD transport mechanism. We hypothesize that preferential OMD transport though interconnected pore space in fibrous aerogel materials is responsible for the 52% higher intrinsic permeability of BNCAs compared to the phase-inversion PVDF membrane.

The high void fraction of BNCA reduces conducted heat flux from the feed to the permeate stream, resulting in improved TPC (Table 2) and thermal efficiency (η) (Figure 3A) compared to the PVDF membranes. The specific heat duty (β) performance ratio is 2.47 for the 40°C experiments, meaning the BNCA prototypes produced 2.47 times the freshwater permeate of the commercial benchmark membranes per kilojoule of heat energy. The ratio was 1.54 for the 60°C experiments. Because thermal efficiency and specific heat duty of a membrane are largely independent of membrane thickness,(Field et al., 2013) these results can be ascribed to the high porosity and low thermal conductivity of the aerogel structure.

Table 4.2 Comparison of flux, salt rejection, Temperature Polarization Coefficient (TPC) between membrane-types (error expressed as standard error of the mean for multiple experiments). There is significant variation in the BNCA membrane thickness from sample to sample. Similarly-sized samples were used for each temperature experiment, which minimized intra-experiment variability.

	Thickness (μm)	**$T_{f,b}$ (°C)**	**flux (kg m^{-2} hr^{-1})**	**rejection (%)**	**TPC**
PVDF	109 ± 5	**40**	5.79 ± 0.27	99.53 ± 0.08	0.500 ± 0.004
	109 ± 5	**60**	25.80 ± 0.61	99.97 ± 0.04	0.402 ± 0.004
BNCA	218 ± 30	**40**	8.42 ± 0.21	99.87 ± 0.05	0.711 ± 0.012
	280 ± 36	**60**	22.92 ± 0.96	99.95 ± 0.04	0.662 ± 0.018

Increasing pore size, while maintaining high porosity, may further reduce mass transport resistance of the fibrous aerogel materials. This can be accomplished by manipulating fiber diameter, as pore radius is directly proportional to fiber diameter when porosity is held

constant.(Eichhorn and Sampson, 2005) One approach for achieving this material structure may be to adapt nanocellulose drying methods to induce partial aggregation of the 32 nm *Gluconacetobacter medellinensis* fibers. Unfortunately aggregation is not easily controlled, and earlier attempts have yielded a non-isotropic hierarchical structure.(Pääkkö et al., 2008)

A simpler solution for increasing pore size while maintaining high porosity might be to mimic the BNCA structure using alternative materials and fabrication methods, for example by electrospinning polymer membranes. Bacterial nanocellulose biofilms are a natural analog to electrospun polymers, with similar isotropic fibrous structure yet tunable fiber diameter, between 15 nm and 7 μm.(Wang et al., 2011) Though electrospun materials have been explored for use as MD membranes,(Feng et al., 2008; Essalhi and Khayet, 2013a; Liao et al., 2013a; Li et al., 2014a; Tijing et al., 2014b; Wu et al., 2014) no published studies have maximized porosity (>93.3%)(Essalhi and Khayet, 2014) of electrospun membranes in MD. Our research suggests it would be beneficial to minimize bulk density of electrospun polymer membranes while optimizing fiber diameter/pore size to yield improved flux, thermal efficiency, and salt rejection performance in MD.

We have fabricated BNCA membranes with >98% porosity and shown them to be functional in MD. These experiments provide MD performance results for materials with significantly higher porosity than the benchmark PVDF membrane used in this study or other membranes tested in the literature. BNCA membranes exhibit substantial improvements in intrinsic permeability and thermal efficiency, suggesting that there is an opportunity to advance MD process viability through improved membrane design. Future membrane materials may benefit from mimicking the aerogel-like porosity and pore-interconnectivity of BNCA, but could further

reduce mass transport resistance by increasing the pore size and optimizing the membrane thickness.

ACKNOWLEDGMENT

This work would not have been possible without the Molecular Materials research group led by Dr Olli Ikkla from Aalto University, who generously hosted Ms. Leitch for a three-month collaboration as part of the NSF GROW Travel Grant

AUTHOR'S NOTE:

Chapter 4 appears as-published in Environmental Science & Technology Letters. The analyses of membrane permeability, thermal efficiency, and TPC herein pre-date the Chapter 2 Nusselt study. The models were re-run to determine how alteration of cassette convective heat transfer coefficients by the NuCF method would quantitatively and qualitatively change the metrics reported in this study. Modified results are reported in Appendix C.9. The outcomes to not alter the conclusions communicated in the published study.

Chapter 5 : CONCLUSIONS, RESEARCH CONTRIBUTIONS & IMPLICATIONS

The research objective of this dissertation is the elucidation of membrane structural effects on performance in membrane distillation. The work presented here narrows knowledge gaps in the field by identifying opportunities for MD researchers to improve data collection and reporting, by development of a novel transport model generalizable for novel membrane structures, and by development and testing of novel high-porosity membrane materials including bacterial nanocellulose.

5.1 Conclusions

In Chapter 2, techniques to improve characterization of heat transfer in the membrane cassette were developed, facilitating better estimation of membrane properties from measured flux data, as well as inter-study reproducibility and comparison of experimental results. A systematic theoretical and experimental methodology for determining Nusselt number in MD cassettes was proposed: selecting a Nusselt number correlation from literature, adapting the baseline correlation to an "idealized" form that accounts for specific MD cassette geometry and flow conditions, then determining an experimental correction factor that adjusts the idealized Nusselt correlation for flow non-idealities in benchtop cassette. These methods are applied specifically to suggest an idealized Nusselt correlation for MD cassettes with rectangular feed and permeate channels undergoing laminar flow (the most commonly used configuration for MD research). Review of published MD data and newly collected experimental data suggest flow non-idealities can substantially increase the heat transfer coefficients predicted by baseline and/or idealized Nusselt correlations. A test case comparing MD data collected on identical membranes under different system conditions in different laboratories suggests application of experimental Nusselt correction factors will allow studies' calculations of membrane permeability to converge.

Universal reporting of experimentally-validated heat transfer coefficients when published MD flux results is recommended.

In chapter 3, Buckingham-Pi dimensional analysis is applied to formulate a new empirical model for MD transport through non-woven electrospun fibrous membrane structures. Improvements of this model over existing theoretical (mechanistic) transport models are its use of easily-measurable structural parameters specific to the geometry of fibrous membranes, and an absence of simplifying assumptions about pore structure. Improvements over existing empirical models are its inclusion of both membrane and channel parameters to predict flux, and mathematical rigor in the determination of relationships between structural and system parameters. Agnostically-determined model parameters corroborate vapor transport theory by showing a dependence of flux on both Knudsen diffusion and ordinary molecular diffusion. Applied to a trial set of electrospun fibrous membranes, the model shows promise for systematically determining effects of membrane structures on flux performance. Empirical correlations of the dimensionless parameters are shown to be more effective for predicting MD flux through electrospun fibrous membranes than the Dusty Gas Model and the empirical model recently proposed by Rao and Childress(Rao et al., 2014).

Chapter 4 explores the effects of very high porosity on membrane permeability and thermal efficiency, and how this knowledge can be applied to future membrane development. Bacterial nanocellulose aerogel (BNCA) membranes with >98% porosity were successful fabricated and shown to be functional in MD. The experiments provide MD performance results for materials with significantly higher porosity than a benchmark commercial phase-inversion polymer membranes or other fibrous membranes tested in the literature. BNCA membranes exhibit substantial improvements in intrinsic permeability and thermal efficiency, suggesting that there is an opportunity to advance MD process

viability through improved membrane design. Future membrane materials may benefit from mimicking the aerogel-like porosity and pore-interconnectivity of BNCA, but could further reduce mass transport resistance by increasing the pore size and optimizing the membrane thickness.

5.2 Research Contributions and Implications

This dissertation contributes experimental data and modeling techniques to improve knowledge of membrane structural effect on MD performance. These contributions have implications for the wider adoption of MD technology through better reproducibility of published experimental results, enhanced transport modeling to optimize membrane structure, and demonstrated thermal efficiency of a highly porous materials.

This work identifies inadequate cassette heat transport characterization in the MD literature. A survey is made of published flux measurements, and convective heat transport theory is used to identify un-characterized cassette geometry and flow non-idealities as reasons for disparities between measurements made on identical commercial membranes. Knowledge of the inadequate characterization of MD cassette heat transfer in the literature indicates it is unproductive to make direct comparisons of reported fluxes measured for novel membranes. This research reveals the importance for the MD researchers to accurately estimate and experimentally validate cassette heat transfer when reporting MD membrane performance. Collaborative inter-laboratory studies are needed to validate that membrane permeabilities identified using the corrected Nusselt correlations can be used predictively in a variety of MD system conditions and configurations. These methods will lead to greater comparability and reproducibility of experimental results, facilitating meaningful research and more rapid development of MD technology.

This research establishes theoretical reasons for poor mass transport characterization by traditional MD models when applied to novel membrane structures. To rectify existing models' inability to accurately characterize structure in novel membranes, this dissertation contributes a new empirical model. The use of dimensional analysis to form flux model parameters is novel to the MD field. Dimensional analysis gives the parameters physical meaning and allows the model to comprehensively incorporate system conditions, vapor properties, and membrane structural parameters in its predictions. Development and preliminary validation of this modeling method has implication for future MD research. Model parameter dependence on vapor transport mechanisms suggest the model might be used to empirically determine dominant mass transport processes for given membrane structures. With this knowledge it would be possible to optimize structural parameters of novel membranes for MD vapor transport. Finally, demonstration of improved model predictive capability for fibrous membranes suggests dimensional analysis modeling might also be applied to other novel membrane structures that are poorly described by traditional theoretical models.

Finally, this dissertation identifies an absence of experimental work demonstrating MD performance for membranes at the upper limits of porosity. By developing a novel aerogel membrane and evaluating it in DCMD, this research contributes to the literature unique MD mass and heat transport results for ultra-high porosity materials. Demonstration of unprecedented thermal efficiency by these membranes has implications for the improved viability of MD technology. If scalable fabrication methods can be used to develop similarly-structured high-porosity fibrous membranes, these membranes have the potential to lower overall specific heat duty (i.e. energy inputs) of water desalinated by MD.

Chapter 6 : FUTURE WORK

Future research ideas stemming from this dissertation explore the wider applicability and relevance of the membrane characterization methods developed herein. For the cassette-dependent Nusselt correction factor method or the Buckingham-Pi model to be of value to the MD research community, they should be validated in multiple laboratories under range of experimental conditions. Furthermore, given the significant efforts by MD researchers to improve membrane permeability, there has been comparatively little research on the process-level impacts to improved membrane structure. Modeling of the effects of membrane performance on flux, specific energy consumption, and capital cost in a multi-stage MD system is an important step to determine how membrane design affects MD process viability.

6.1 Use of computational fluid dynamics to develop idealized Nusselt correlations specific to MD cassette conformations and operating conditions

The method used in this study to determine the idealized Nusselt correlation (for MD heat transfer with developing laminar flow in a rectangular cassette channel – Eq. 2.19) relies on the adaptation of an existing Nusselt correlation by regressing and interpolating previously published data. There are a couple weaknesses in this approach. First, reliance on other researchers' low-granularity published tabular data constrains the accuracy of any correction factor. Second, the method uses multiple corrections to the baseline Nusselt correlation, but there is no opportunity to determine the interaction between correction factors. For example, in this study, it is assumed correction factors for aspect ratio and flow development act independently to control convective heat transfer rate, but this cannot be verified without specific exploration using computational fluid dynamics (CFD) or experimental studies.

Therefore, a useful research topic would be the creation of a series of Nusselt correlations using CFD, specifically designed for common MD cassette configurations and flow conditions. Nusselt correlations specifically designed for MD will likely be more accurate over a wider range of temperatures and flow conditions, and will require less adjustment for experimental non-idealities. Additionally, it would be interesting to validate (or invalidate) the correction factor methods used to create the idealized Nusselt equation determined in this study (Eq 19). The following paragraphs outline a method to develop a Nusselt correlation using CFD.

To create a simple Nusselt correlation for laminar, simultaneously developing flow in a rectangular MD channel, one can create a CFD model of water flowing in a 3-D rectangular channel. The initial conditions for the flow are a uniform temperature and velocity profile at the channel inlet. The boundary conditions are three adiabatic walls and one wall with constant heat flux (i.e. a membrane with counter-current flow on the opposite side), with no-slip at the walls. Mass transfer through the membrane can be included but it is not expected to significantly change the temperature profiles relevant to Nusselt number calculations (See Section 2.6.3 of this dissertation). Using the CFD model software, steady-state temperature and velocity profiles are calculated for the length and width of the channel. Nusselt Number at any given point on the membrane surface is calculated using Equation 2.6. To determine a full correlation for the channel, a series of model runs should vary:

- *Reynolds Number* (~100 - 2300 by varying fluid velocity)

- *Prandtl Number* (~2 - 10, by varying temperature)

- $\alpha^*, channel\ aspect\ ratio$ (~0.002 – 1)

- Heat flux direction (into the membrane for feed, and into the channel for permeate), and

- Dimensionless length $\left(\frac{x}{d_h}\right)$ However, if one is building an idealized Nusselt correlation and not concerned with the effects of channel exit configuration on convective heat transfer, it might be more efficient to model a single long channel (such that Nusselt asymptotes to a constant fully –developed value by the end of the channel). Effect of channel length and/or flow development on average *Nu* can then be determined by just evaluating average Nu for subsets of the channel)

In each of these CFD runs, to account for feed TDS and temperature polarization, the software must allow viscosity, density, thermal conductivity and heat capacity of the fluid stream to vary with temperature and salt concentration (a more complex version of the model would also account for concentration polarization by adding mass flux through the membrane wall)

Given the large matrix of potential model runs (~1000 x two heat flux directions if all variables are modeled at 10 discrete values), speed of data collection is a limiting factor in the creating of the correlation. There are statistical methods to reduce the number of data points needed for multivariate regressions, such as Response Surface Methodology, discussed in Chapter 3, which can be explored to reduce the burden of data collection and analysis. Once CFD model runs are complete, the following method can be used to determine a Nusselt correlation

To create a "local" Nu correlation:

1) For each model run, find how *Nu* (calculated using Eq. 2.6) varies along the length of the cassette by regressing *Nu* vs. $\left(\frac{x}{d_h}\right)$. This requires integration of *Nu* values across the width of the cassette – these integrated values should logarithmically or exponentially decay to a constant value once the velocity and temperature profile in the channel is fully-developed.

2) Take as the dependent variables the *Nu* vs. $\left(\frac{x}{d_h}\right)$ regression coefficients for each model run. Regress these dependent variables vs the remaining parameters (*Re, Pr,* α^*,heat flux direction, represented by $\left(\frac{\mu_{bulk}}{\mu_{wall}}\right)$.

To create an "average" Nu correlation (practical for prediction of average heat transfer coefficient for an entire channel):

a) Integrate the local *Nu* correlation with respect to $\left(\frac{x}{d_h}\right)$, or

b) For each model run of a particular long channel and fluid flow configuration, create copies of the data simulating various channel lengths. Calculate average *Nu* for each channel length for each model run and regress these values vs. all other parameters.

The result will be empirical local and average Nusselt correlations with similar format to the Buckingham Pi correlation developed in Chapter 3. Once a correlation is developed it should be experimentally validated using multiple MD cassettes and series of flow conditions. Due to flow non-idealities in membrane cassettes, it is likely the correlation will have variable accuracy depending on the cassette. Determination of experimental cassette-dependent correction factors will still be needed.

6.2 Multi-laboratory collaborative studies to examine MD membrane permeability using the NuCF method.

An experimental cassette-dependent Nusselt correction factor (NuCF) is useful to the MD community if it can accurately compare novel membrane permeability between research groups

for a range of experimental conditions and if it can be used to study contributions of individual vapor transport mechanisms on total membrane flux. A few research questions therefore stem from the development of the NuCF method in this dissertation:

a) Does the NuCF method identify "true" permeability of MD membranes? In essence, can B_{wi} calculated for a given membrane in a particular cassette be used by other research groups to predict flux in their own cassettes, or to quickly calculate NuCF for their own cassette? These questions can be answered by a collaborative study between a few laboratories in which cassette-dependent NuCFs are calculated for each DCMD bench-top system, then DCMD data is compared for identical membranes collected by different operators using different DCMD systems. An example step-by step method is outlined below:

1. Three to five types of commercial flat sheet hydrophobic membranes are selected and characterized, and coupons of each membrane type are distributed to three laboratories with different benchtop DCMD systems. The benchtop systems have different cassette dimensions, but similarly configured sensor systems capable of precisely controlling and measuring feed/permeate flow rates and average temperature in the membrane cassette. System sensors should also measure pressure on the feed and permeate sides of the membrane. For the first round of experiments, the flat-sheet membrane cassettes will be operated in counter-current configuration and in the same flow regime (e.g. laminar, laminar-with-spacers, or turbulent)

2. Each laboratory selects a different membrane and uses the methods outlined in Chapter 2 to determine a $Nu_{experimental}$ correlation. Once these cassette-dependent Nusselt correlations are determined, heat transfer coefficients in the cassettes can be estimated for a variety of MD operating conditions within the flow regime.

3. Each laboratory performs series of DCMD experiments on each of the remaining membranes varying experimental T_{avg} and Re_{avg}. Then the system of 1-D mass and heat transport equations (with heat transfer coefficients determined by $Nu_{experimental}$) are solved to find $B_{w,i,experimental}$ values for each membrane type under each experimental condition.

4. $B_{w,i,experimental}$ values calculated for each membrane type are checked for internal consistency in each lab (they should be approximately the same regardless of experimental conditions and any variations should be attributable to relationships of $B_{w,i,theoretical}$ with T_{avg} and Re_{avg}.

5. $B_{w,i,experimental}$ values are compared between laboratories for identical membranes at identical T_{avg}. We hypothesize that, with well-characterized heat transfer coefficients, membrane permeabilities measured by different benchtop DCMD systems should be nearly identical. Any differences between $B_{w,i,experimental}$ values for identical membranes should be attributable to differences in system and/or atmospheric pressure.

b) By comparing the phase inversion PVDF and electrospun PTFE membrane regressions of permeabilities vs $T_{avg,membrane}$, we see that pore size has an effect on the slope of the regression. The theoretical permeability equations indicate this slope is a function of individual contributions of Knudsen and Ordinary Molecular diffusive transport mechanisms. The research question that follows is: Can the relationships between membrane structure and individual contribution of diffusive vapor transport mechanisms be identified by examining $B_{w,i,Experimental}$ and $B_{w,i,Theoretical}$ vs $T_{avg,membrane}$? Furthermore, can the interaction between diffusive and viscous transport mechanisms be identified in MD membranes operated

under a pressure differential (as is the case for vacuum membrane distillation)? According to the Dusty Gas Model (DGM) each transport mechanism has a distinct dependence on driving force, thermodynamic vapor properties and on membrane structure. By design of experiments that vary these factors individually while hold others constant, then examining the apparent affect on $B_{w,i,Experimental}$, classic models for MD vapor transport can be validated and updated. Table 6.1 describes some-experimental series which could shed light on the relationships between membrane structure, experimental conditions, and transport mechanism.

Table 6.1 Experimental series using NuCF method to determine relationships between membrane structure, experimental conditions, and transport mechanism

Independent variable 1	Independent variable 2	Dependent variables (determined by MD experiments)	Potential transport mechanism insight
Membrane pore size / fiber diameter	T_{avg}	$B_{w,i,Experimental}$ $B_{w,i,theoretical}$	T_{avg} affects Knudsen and OM diffusivity differently (increases in temperature increase OMD proportionally more than Knudsen diffusivity). Because contribution of OMD should increase as pore size increases. the relationship between $B_{w,i}$ and T_{avg} should be stronger at larger pore sizes. Comparison of theoretical predictions of $B_{w,i}$ to experimental $B_{w,i}$ values at various pore sizes can show how well theoretical contributions of OMD and Knudsen diffusion represent real contributrions
Membrane structure (phase-inversion/fibrous/ track-etched/asymmetric)	T_{avg}	$B_{w,i,Experimental}$ $B_{w,i,theoretical}$	To determine whether pore interconnectivity increases the contribution of OMD proportional to Knudsen diffusion, one can compare $B_{w,i}$ vs T_{avg} for membranes of similar nominal pore size. Interconnectivity may lead to a stronger dependence of $B_{w,i}$ on T_{avg} than would be expected for the nominal pore size.
$\boldsymbol{P_{avg,\ total}}$	T_{avg}	$B_{w,i,Experimental}$ $B_{w,i,theoretical}$	Decrease in average total pressure in membrane pores should decrease OMD transport resistance, but have little effect on Knudsen transport resistance, thus increasing $B_{w,i}$ for a given membrane. Comparison of experimental $B_{w,i}$ with theoretical predictions for a range of temperatures and pressures could provide richer data to validate the theoretical contributions of each transport mechanism, as proposed by the Field-modified DGM.
$\boldsymbol{\Delta P_{avg,\ total}}$ **(viscous driving force)**	$P_{avg,\ total}$ and/or Membrane pore size / fiber diameter	$B_{w,i,Experimental}$ $B_{w,i,theoretical}$	This set of experiments is relevant to determine how membrane permeability is changed under vacuum MD conditions. Theoretical contributions of viscous transport mechanism predicted by the DGM can be validated by comparing $B_{w,i,Experimental}$ with $B_{w,i,theoretical}$ for a variety of driving forces and membrane types.
Membrane material hydrophobicity	T_{avg}	$B_{w,i,Experimental}$ $B_{w,i,theoretical}$	Surface diffusion is typically considered negligible in the MD process due to low interactions between the hydrophobic membrane material and the water vapor, but this has not been explored experimentally. Membranes with a variety of surface chemistries but similar structure could be evaluated in DCMD to determine whether there is any effect of surface chemistry on permeability.

c) Is the NuCF method valid for a variety of cassette geometries (hollow fiber, spiral wound), flow regimes (turbulent, laminar with spacers) and MD permeate-side configurations (Air gap membrane distillation, vacuum membrane distillation, sweeping gas membrane distillation)? Validation of the NuCF method for a variety of MD cassettes and operating conditions is needed

to determine whether it can be used practically and widely. Much work remains to facilitate inter-system and inter-membrane comparison of MD performance.

6.3 Exploration of Buckingham Pi method generalizability and usefulness in determining dominant vapor transport mechanisms

The B-P model holds practical appeal due to its simple membrane characterization requirements and its use of a closed-form expression to predict MD permeate flux, however more work is needed to determine its applicability for wider ranges of membrane types and system conditions. To increase the utility of the method, future work should expand of the correlation to a wider array of experimental conditions. Experimental design should focus on varying each of the seven "independent" dimensionless parameters independently of the others to determine their effects on Π_1. This will allow more rigorous statistical determination of parameter exponents using log-linear regression. Additionally, a large experimental matrix can provide insight as to whether a single universal correlation can be used to estimate DCMD flux for isotropic fibrous membranes, or if more accurate predictions can be obtained when correlation coefficients/exponents are allowed to vary depending on structural characteristics or experimental conditions. Validation of the correlation(s) across different DCMD bench-scale systems can also give insight into the model's predictive capabilities. Table 6.2 presents a matrix of potential experiments to independently vary each dimensionless parameter. Similar to the series of experiments proposed in section 6.1, it would be prudent to use a statistical method to reduce the total number of experiments required to obtain dimensionless correlation.

Table 6.2 Matrix of potential experiments to independently vary each B-P dimensionless parameter

Independent dimensionless variable	Experimental variable(s)	Notes
$\mathbf{\Pi_2}$	k_p T_{fb} T_{pb}	Variation of electrospun polymer type will vary polymer thermal conductivity, k_p, however an experimental method to measure fiber k_p may need to be developed to reduce uncertainty. It ΔT_{bulk} and ρ_{vap} can be varied using bulk feed and permeate temperature, however $\mathbf{\Pi_4}$, $\mathbf{Nu_f}$, and $\mathbf{Nu_p}$ will co-vary, so careful selection of a variety of experimental temperatures will be needed to account for collinearity and allow independent determination of log-linear exponents.
$\mathbf{\Pi_3}$	d_f δ	Fiber diameter can be varied using electrospinning conditions or solution characteristics Thickness can be varied using hot-pressing, but this will cause porosity, ε, to co-vary
$\mathbf{\Pi_4}$	$T_{avg,memb}$ P_{tot}	ρ_{vap} can be varied using the bulk feed and permeate temperatures, however $\mathbf{\Pi_2}$, $\mathbf{Nu_f}$, and $\mathbf{Nu_p}$ will co-vary. Perhaps an interesting way to independently vary $\mathbf{\Pi_4}$ is to vary the average head pressure, P_{tot}, in the DCMD system, which should be inversely proportional to D_{wa}
$(\mathbf{1-\varepsilon})$	ε	Solid fraction can be varied using hot-pressing or by varying fiber diameter, but this will cause $\mathbf{\Pi_3}$, to co-vary. It may be prudent to calculate just one log-linear regression coefficient for $\mathbf{\Pi_3(1-\varepsilon)^{-1}}$
$\mathbf{a_w}$	TDS_{feed}	Changing salt concentration will change activity coefficient, but any parameter containing μ may also co-vary. Therefore a series of experiments should be designed varying both the concentration and the composition of the feed waters, such that μ is constant but a_w varies.
$\mathbf{Nu_f}$, $\mathbf{Nu_p}$	v_{avg} *cassette channel dimensions*	Regression coefficients can be found independently for $\mathbf{Nu_f}$ and $\mathbf{Nu_p}$ by varying average feed or permeate velocity or the average flow development.

Furthermore, the dependence of parameter exponents on vapor properties and membrane pore size should be explored to determine whether they vary based on contributions from different diffusive transport mechanisms. Chapter 3 postulates the B-P parameter exponents *(a-e)* are not static, but variable with experimental conditions and membrane type. In section 3.2.2., Π_2 is shown to be proportional to the ratio of two vapor diffusion mechanisms: $\frac{D_{Knudsen}^2}{D_{OMD}^2}$ and Π_4 is

proportional to D_{OMD}. Theoretically, the contributions of each diffusion mechanism to total MD flux are variable with pore size and properties of the pore-fluid. This would cause the ratio of the exponents of Π_2 and Π_4 to vary detectably with experimental conditions and membrane structure. If this hypothesis is true, transport mechanisms can be studied using a carefully selected matrix of experiments that individually vary Π_2 and Π_4 annot be proven using the data collected in this exploratory study. Statistical methods, such as factorial design or response surface methodology, can be used to design experimental training sets that yield correlations with predictive accuracy for a wide range of membrane structural parameters and/or experimental conditions. (Khayet et al., 2007; Khayet and Cojocaru, 2012). Using statistical methods to design experimental work could lead to a better mechanistic understanding of how structural characteristics can be optimized for minimum vapor transport resistance.

Finally, future work can address the generalizability of the empirical B-P model for membrane distillation flux prediction. By adapting the parameters for membrane structural characteristics or transport mechanism, the method could be extended to other emergent MD membrane geometries (e.g. asymmetric or hollow fiber membrane) or permeate-side configurations (e.g. vacuum membrane distillation or air gap membrane distillation). Valid B-P correlations of MD flux for a range of membrane types and operating conditions could facilitate a better qualitative understanding of the influence of system and membrane parameters on MD performance as well as easier back-of-the-envelope computations of specific effects of design choices on MD flux.

6.4 Process modeling to show sensitivity of system-level MD performance and cost to membrane structural parameters.

Modeling is needed to show process-level effects of membrane mass and heat transport characteristics on energy efficiency for a variety of membrane, cassette, and permeate-side conformations. This can quantify the influence of membrane structural optimization on volumetric energy use and on MD process viability for a variety of permeate-side conformations (Direct contact, Vacuum, Air Gap, sweeping gas, etc). Process-level modeling will also identify tradeoffs between membrane production expense, longevity of the membrane (associated with mechanical strength and surface chemistry), thermal efficiency of the membrane and permeability of the membrane. This information will allow MD researchers to focus efforts on the most important inefficiencies and engineering uncertainties currently limiting wider adoption of MD as a desalination technology.

APPENDICES

A. APPENDIX A

A.1 Experimentally-measured membrane permeability is dependent on heat transfer coefficient

A commonly used method to estimate permeability for a membrane, a.k.a. the membrane coefficient, is to plot experimentally-measured flux vs. modeled Δp_{vap} between the membrane surfaces. This method is highly sensitive to the model inputs for convective heat transfer coefficient, see Figure A.1

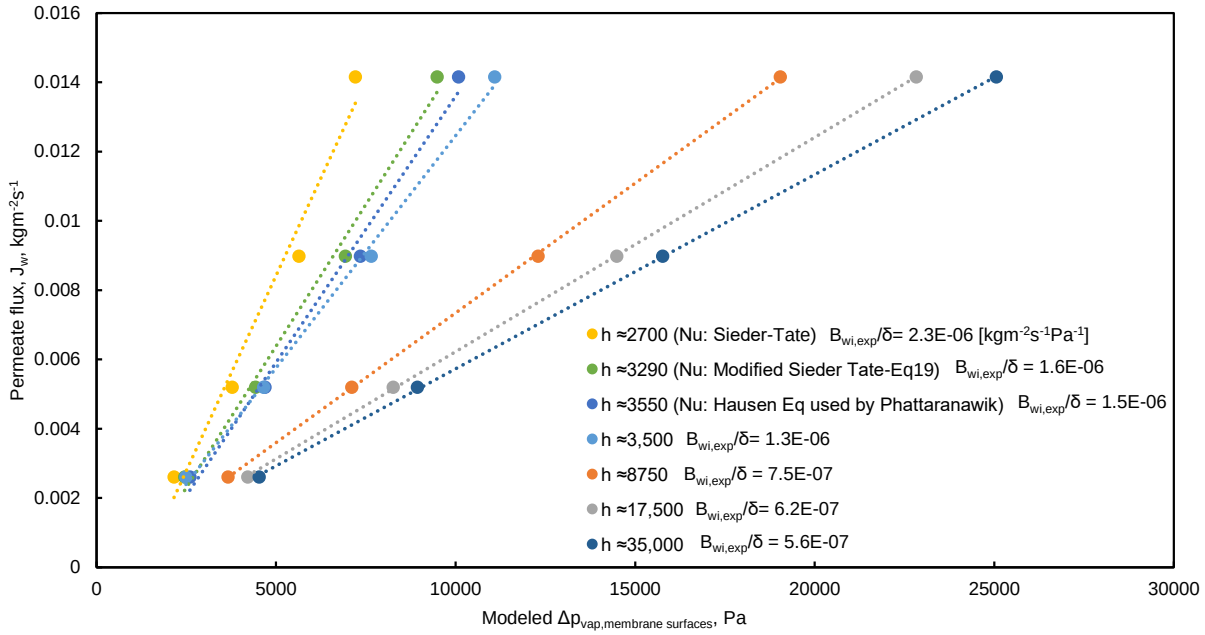

Figure A.1 Experimental permeate flux for a phase inversion PVDF membrane (Millipore GVHP) versus modeled Δp_{vap} between membrane surfaces. Slope of linear regression is the estimated total membrane permeability, or membrane coefficient, B_{wi}/δ. For a given set of experimental flux results, estimated convective heat transfer coefficients, *h*, can have a substantial effect on calculated B_{wi}/δ. The flux vs. Δp_{vap} curve is linear for a wide range of estimated Nusselt numbers/convective heat transfer coefficients, so linearity is not an indicator of the validity of the *Nu / h* estimation method

A.2 Nusselt correlations

Table A.1 Nusselt correlations for transitional *internal* or *external* flow

Flow development	Flow cross section	Nusselt# Equation	Source	Derivation method	Thermal boundary conditions	Use in MD papers	Notes
Fully developed hydrodynamic and thermal flow (long channels only) $x^* = \gtrsim 0.05$	Circular	$Nu = 0.0395\, Re^{0.75} Pr^{n}$ $where\ n = 0.5\ for\ feed\ (liquid\ cooling)$ $n = \frac{1}{3}\ for\ liquid\ heating\ (permeate)$	(Thomas, 1980)	Empirical	Constant axial heat or constant axial temperature		
Any	Any internal cross-section	$Nu = \left(1.33 - \frac{Re}{6000}\right) Nu_{L@2000} + (-0.33 + \frac{Re}{6000}) Nu_{T@8000}$	Taborek,1990 (Thomas, 1993; Shah and Sekulic, 2003)	Empirical	Any		2000 < *Re* < 8000 May be useful for spacer-filled MD channels at lower flow rates

Table A.2 Nusselt correlations for turbulent *internal* or *external* flow

Flow development	Flow cross section	Nusselt# Equation	Source	Derivation method	Thermal boundary conditions	Use in MD papers	Notes
Fully developed hydrodynamic and thermal flow (long channels only) $x^* = \gtrsim 0.05$	Any	$Nu = 0.023 Re^{0.8} Pr^{n} \left(\frac{\mu_{bulk}}{\mu_{memb}}\right)^{m}\ where\ (n, m) = (0.3,\ 0.25)\ for\ feed\ (liquid\ cooling)$ $(n, m) = (0.4,\ 0.11)\ for\ permeate\ (liquid\ heating)$	(Holman; Dittus and Boelter, 1930; Sieder and Tate, 1936; McAdams et al., 1942; Petukhov, 1970; Thomas, 1993)	Empirical	Any	(Kimura et al., 1987; Schofield et al., 1987; Phattaranawik et al., 2003c; Srisurichan et al., 2006; Qtaishat et al., 2008; Andrjesdóttir et al., 2013; Gustafson et al., 2016)	Dittus-Boelter, 1930 (original format) Constant modified by McAdams (1942) Viscosity correction added by Seider-Tate, m = 0.14 (1936) Viscosity exponents valid for liquid flow suggested by Petukhov (1970), reproduced in Thomas (1992) and Holman(2002)

	Any	$Nu = \frac{\left(\frac{f}{2}\right) RePr}{C + 12.7\left(\frac{f}{2}\right)^{\frac{1}{2}}\left(Pr^{\frac{2}{3}} - 1\right)}\left(\frac{\mu_{bulk}}{\mu_{memb}}\right)^{m}$ $C = 1.07 + \frac{900}{Re} - \frac{0.63}{1 - 10Pr}$ $f = 0.00128 + 0.1143Re^{-0.311}$ $m = 0.25\ for\ feed\ (liquid\ cooling)$ $m = 0.11\ for\ permeate\ (liquid\ heating)$	(Petukhov and Popov, 1963; Bhatti and Shah, 1987; Shah and Sekulic, 2003)	Empirical	Any		*Re* > 4000, 0.5 < *Pr* < 10.6 Original correlation by Petukhov&Popov (1963) Fanning friction factor by Bhatti and Shah, 1987 Reproduced in Shaw and Sekulic. Gnielinski (1976) equation is very similar, but has lower accuracy than this correlation, according to Shah&Sekulic
	Any	$Nu = 0.036Re^{0.8}Pr^{\frac{1}{3}}\left(\frac{d_h}{L}\right)^{0.055}\left(\frac{\mu_{bulk}}{\mu_{memb}}\right)^{m}$	(Nusselt, 1931)	**Empirical**	**Any**	(Qtaishat et al., 2008)	**$10 < L/d_h < 400$ Correlation proposed by Nusselt**
Hydrodynamically developed, Thermally developing (Short channels with calming entrance section prior to membrane exposure $Y = \frac{x}{d_h Re Pr} \leq 0.05$	Any	$Nu = \frac{\left(\frac{f}{2}\right) RePr}{C + 12.7\left(\frac{f}{2}\right)^{\frac{1}{2}}\left(Pr^{\frac{2}{3}} - 1\right)}\left(\frac{\mu_{bulk}}{\mu_{memb}}\right)^{m}\left(\mathbf{1} + \frac{\mathbf{1.4}\boldsymbol{d_h}}{\boldsymbol{L}}\right)$ $C = 1.07 + \frac{900}{Re} - \frac{0.63}{1 - 10Pr}$ $f = 0.00128 + 0.1143Re^{-0.311}$ $m = 0.25\ for\ feed\ (liquid\ cooling)$ $m = 0.11\ for\ permeate\ (liquid\ heating)$	(Petukhov and Popov, 1963; Bhatti and Shah, 1987; Shah and Sekulic, 2003)	Empirical	Any		*Re* > 4000, 0.5 < *Pr* < 10.6 Original correlation by Petukhov&Popov (1963) Fanning friction factor by Bhatti and Shah, 1987 Reproduced in Shaw and Sekulic.
	Any	$Nu = 0.023Re^{0.8}Pr^{n}\left(\frac{\mu_{bulk}}{\mu_{memb}}\right)^{m}\left(\mathbf{1} + \frac{\mathbf{1.4}\boldsymbol{d_h}}{\boldsymbol{L}}\right)\ where$ $(n, m) = (0.3, 0.25)\ for\ feed\ (liquid\ cooling)$ $(n, m) = (0.4, 0.11)\ for\ permeate\ (liquid\ heating)$	(Hartnett and Rohsenow, 1973; Thomas, 1993)	Any	Any		Presented in Thomas (1992), quoted from Rohsenow and Hartnett text (1973)

Hydrodynamically and thermally developing flow (short channels with abrupt entrance) $x^* = \lesssim 0.05$	Any	$Nu = \frac{\left(\frac{f}{2}\right) RePr}{C + 12.7\left(\frac{f}{2}\right)^{\frac{1}{2}}\left(Pr^{\frac{2}{3}} - 1\right)}\left(\frac{\mu_{bulk}}{\mu_{memb}}\right)^{m}(\mathbf{1} + \frac{\boldsymbol{6d_h}}{\boldsymbol{L}})$ $C = 1.07 + \frac{900}{Re} - \frac{0.63}{1 - 10Pr}$ $f = 0.00128 + 0.1143Re^{-0.311}$ $m = 0.25\ for\ feed\ (liquid\ cooling)$ $m = 0.11\ for\ permeate\ (liquid\ heating)$	(Petukhov and Popov, 1963; Bhatti and Shah, 1987; Shah and Sekulic, 2003)	Empirical	Any	$Re > 4000$, $0.5 < Pr < 10.6$ Original correlation by Petukhov&Popov (1963) Fanning friction factor by Bhatti and Shah, 1987 Reproduced in Shaw and Sekulic
	Any	$Nu = 0.023Re^{0.8}Pr^{n}\left(\frac{\mu_{bulk}}{\mu_{memb}}\right)^{m}(\mathbf{1} + \frac{\boldsymbol{6d_h}}{\boldsymbol{L}})\ where$ $(n, m) = (0.3,\ 0.25)\ for\ feed\ (liquid\ cooling)$ $(n, m) =$ $(0.4,\ 0.11)\ for\ permeate\ (liquid\ heating)$	(Hartnett and Rohsenow, 1973; Thomas, 1993)	Any	Any	Presented in Thomas (1992), quoted from Rohsenow and Hartnett text (1973)

Table A.3 Nusselt correlations for laminar external flow

Flow development	Membrane geometry	Nusselt# Equation	Source	Derivation method	Thermal boundary conditions	Use in MD papers	Notes
Fully developed hydrodynamic and thermal flow (long channels only) $x^* = \gtrsim 0.05$	Flat, unbounded plate	$Nu = 0.332\ Re^{1/2}Pr^{1/3}$	(Pohlhausen, 1921; Bird et al., 2007)	Analytical	Constant temperature		
Fully developed hydrodynamic and thermal flow (long channels only) $x^* = \gtrsim 0.05$	Irregularly-shaped objects	$\overline{Nu} = 0.6\ Re^{1/2}Pr^{1/3} + \overline{Nu_0}$ $where\ \overline{Nu_0}\ is\ the\ experimentally\ found\ mean\ Nusselt\ number\ at\ Re = 0$	(Bird et al., 2007)	Empirical	Constant temperature		

A.3 Calculation of Nusselt correction factor for rectangular duct

Table A.4 Raw data, reproduced from Wibulswas thesis data (Shah&London table 51)(Wibulswas, 1966; Shah and London, 1978) Mean Nu,H1 for thermally developing flow in rectangular ducts vs aspect ratio (peripherally constant heat transfer)

1/x*	**Nusselt for various duct aspect ratios, α***				**Nusslet for circular duct (Sieder-Tate correlation)**
	α = 1*	*α* = 0.5*	*α* = 1/3*	*α* = 0.25*	
0	3.6	4.11	4.77	5.35	~0
10	4.48	4.94	5.45	6.03	4.01
20	5.19	5.6	6.06	6.57	5.05
30	5.76	6.16	6.6	7.07	5.78
40	6.24	6.64	7.09	7.51	6.36
60	7.02	7.45	7.85	8.25	7.28
80	7.66	8.1	8.48	8.87	8.01
100	8.22	8.66	9.02	9.39	8.63
120	8.69	9.13	9.52	9.83	9.17
140	9.09	9.57	9.93	10.24	9.66
160	9.5	9.96	10.31	10.61	10.10
180	9.85	10.31	10.67	10.92	10.50
200	10.18	10.64	10.97	11.23	10.88

(Note: Sieder-Tate correlation is not valid for fully developed flow because it asymptotes to 0 as x* increases… this data is not used in the following correlations)

Table A.5 Tabular correction factors: Ratio of rectangular duct Nusselt # to circular duct Nusselt #

x*	$\boldsymbol{CF_{rect,\alpha*} = Nu_{rect}/Nu_{circ,S-T}}$ vs. aspect ratio, α*			
	α = 1*	*α* = 0.5*	*α* = 1/3*	*α* = 0.25*
0.1	1.118	1.233	1.360	1.505
0.05	1.028	1.109	1.200	1.301
0.033333	0.997	1.066	1.142	1.223
0.025	0.981	1.044	1.115	1.181
0.016667	0.964	1.023	1.078	1.133
0.0125	0.956	1.011	1.058	1.107
0.01	0.952	1.003	1.045	1.088
0.008333	0.947	0.995	1.038	1.071
0.007143	0.941	0.991	1.028	1.060
0.00625	0.941	0.986	1.021	1.051
0.005556	0.938	0.982	1.016	1.040
0.005	0.936	0.978	1.009	1.032

We desire an equation that can predict these correction factors. Shah and Sekulic (Shah and Sekulic, 2003) show that, very near the thermal duct entrance, Nusselt number of rectangular ducts are a solely a function of x* and the fully-developed friction factor constant (which is a function of duct aspect ratio). We thus calculate relation between fully developed friction in rectangular channels vs aspect ratio (correlation from Shaw and Sekulic)(Shah and Sekulic, 2003), as displayed in Table A.6, and then scale the tabular correction factors by this factor to see if, at low x*, the correction factor for all rectangular ducts approach a constant value:

$$(f \cdot Re)_{rect} = 24\left(1 - 1.3553\alpha^* + 1.9467\alpha^{*2} - 1.7012\alpha^{*3} + 0.9564\alpha^{*4} - 0.2537\alpha^{*5}\right)$$

$$Note: (f \cdot Re)_{circle} = 16$$

Table A.6 Channel aspect ratio vs *f*Re*

α^*	$f \cdot Re$	$(f \cdot Re)^{\frac{1}{3}}$
1	14.23	2.42
0.5	15.56	2.50
0.333333	17.09	2.58
0.25	18.23	2.63
0.125	20.59	2.74
0.01	23.68	2.87
0	24	2.88

Table A.7 Find Correction factor constant, "C" (Divide Tabular correction factors by $(f \cdot Re)_{rect}$)

x*	$(Nu_{rect}/Nu_{circ,S-T})/(f \cdot Re)^{\frac{1}{3}}$			
	α = 1*	*α* = 0.5*	*α* = 1/3*	*α* = 0.25*
0.1	0.461	0.494	0.528	0.572
0.05	0.424	0.444	0.466	0.494
0.033333	0.411	0.427	0.443	0.465
0.025	0.405	0.418	0.433	0.449
0.016667	0.398	0.410	0.418	0.430
0.0125	0.394	0.405	0.411	0.420
0.01	0.393	0.402	0.406	0.413
0.008333	0.391	0.399	0.403	0.407
0.007143	0.388	0.397	0.399	0.403
0.00625	0.388	0.395	0.396	0.399
0.005556	0.387	0.393	0.394	0.395
0.005	0.386	0.392	0.391	0.392

Plot the data:

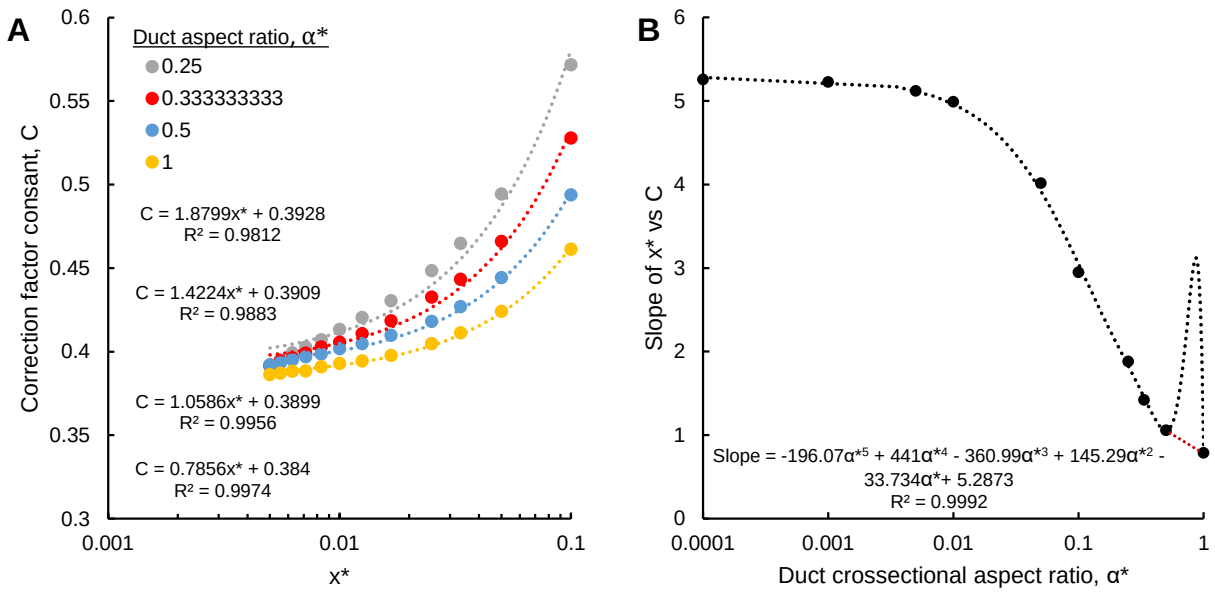

Figure A.1.2 A) Plot Data from Table A.4, Find correlations, B) Correlation for constant "C" slope in with respect to aspect ratio

Division of tabular correction factors by $(\boldsymbol{f} \cdot \boldsymbol{Re})^{\frac{1}{3}}$ then plotting show curves all duct aspect ratios approach a constant value ~ 0.39 as x* approaches 0. Next, we plot the slopes of each correction factor curve. To ensure the correlation is applicable outside the narrow range of α* given in the Wibulswas data (particularly because we expect aspect ratio to be relatively low for MD channels), on the same curve we plot expected values of the slope at x* = 0.05 ("developed flow") for narrower channels (smaller α*). Predictions for C were made using Nu values for fully-developed flow inserted in Equation 17a. This data plotted in Figure A.1.2B and the polynomial correlation (in the style of Shaw and Sekulic) gives the effect of aspect ratio on the Nusselt correction factor outside the asymptotic entrance region for Figure A.1.1, at 0.001 < x* < 0.05. The polynomial correlation is not valid for aspect ratios between 1 and 0.5 but square duct geometries are not expected in MD. In the case of the aspect ratio = 0.5 – 1, the slope of C should be determined by linear interpolation as shown by the dotted red line in Fig A.1,2B.

Now the proposed equation is as follows:

$$For\ estimating\ Nu\ for\ themally\ developing\ flow\ of\ rectangular\ channels\ 0.01 < \alpha^* < 0.5$$
$$from\ the\ Seider - Tate\ correlation\ ,$$
$$\overline{Nu_{rect}} = \overline{Nu_{Sieder-Tate}} \left(C(f \cdot Re)^{\frac{1}{3}}\right)$$

where $(f \cdot Re)$ *is a constant and a function of channel aspect ratio* α^*:(Shah and Sekulic, 2003)

$$(f \cdot Re) = 24\left(1 - 1.3553\alpha^* + 1.9467\alpha^{*2} - 1.7012\alpha^{*3} + 0.9564\alpha^{*4} - 0.2537\alpha^{*5}\right)$$
$$C = 0.392\ for\ low\ values\ of\ x*$$
$$C = 0.392 + x^*\left(-196.07\alpha^{*5} + 441\alpha^{*4} - 360.99\alpha^{*3} + 145.29\alpha^{*2} - 33.734\alpha^* + 5.2873\right)\ for\ higher\ values\ of\ x*$$

Next, validation is needed to show the how the correction factor affects Nusslet number at a variety of aspect ratios and entrance lengths, and to show correction factor accuracy with respect to the tabular data provided by Wibulswas. Plots in Figure A.2 validates the cutoff of x* < 0.001 for the use of C = 0.392, particularly when ducts are thin.

$$\overline{Nu_{rect}} = \overline{Nu_{Sieder-Tate}}\left(C(f \cdot Re)^{\frac{1}{3}}\right)$$

$$C = 0.392 + x^*\left(-196.07\alpha^{*5} + 441\alpha^{*4} - 360.99\alpha^{*3} + 145.29\alpha^{*2} - 33.734\alpha^* + 5.2873\right)$$

$$C = 0.392$$

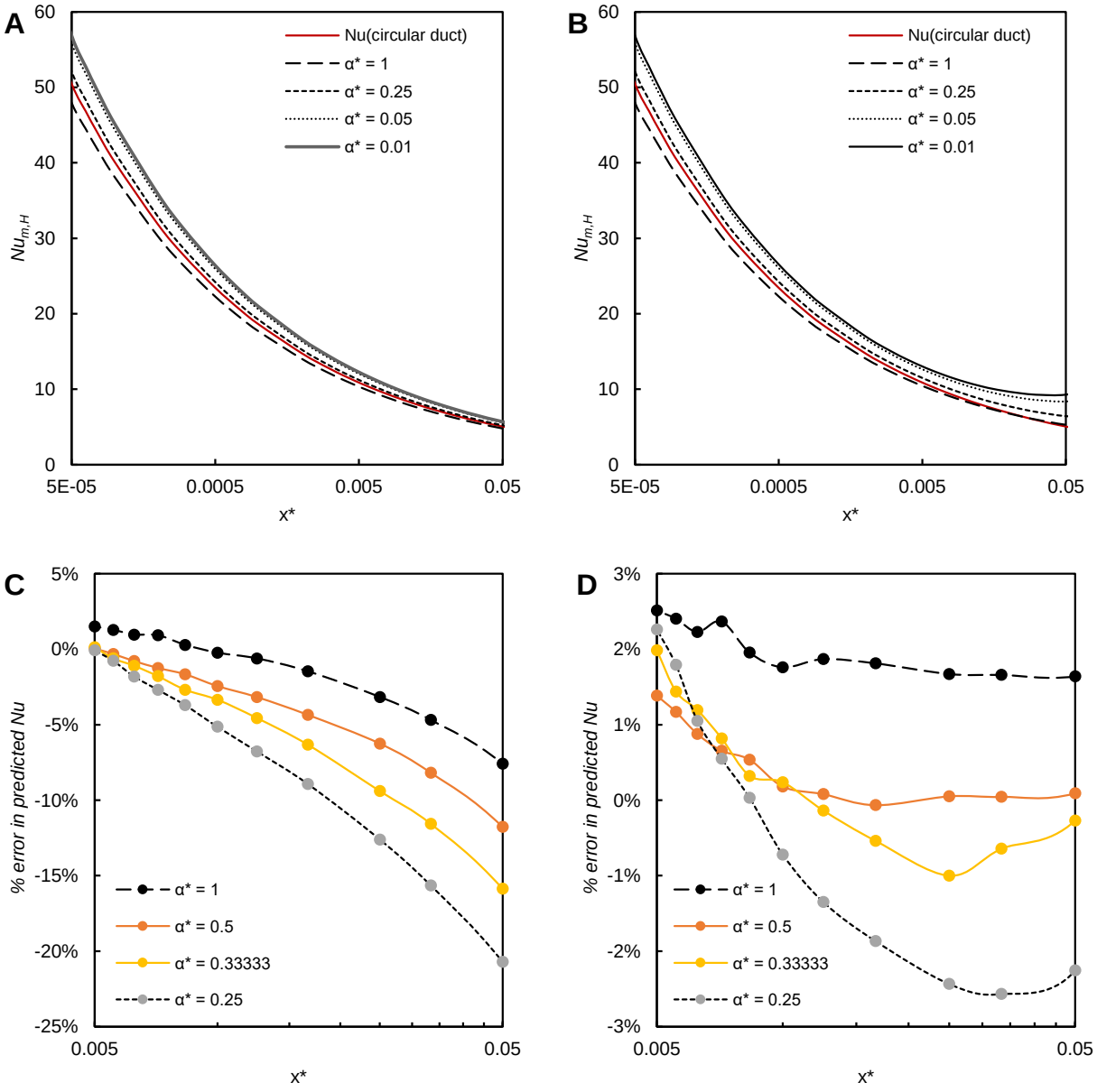

Figure A.2 Evaluation of Nusselt prediction using duct geometry correction factors. A) Nusselt numbers vs x* calculated using C = Constant, and b) Nusselt numbers vs x* calculated using polynomial C. C) Percent error in Nu correlation calculation compared to Wibulswas data when C = constant. D) percent error in Nu Calculation compared to Wibulswas data when polynomical C is used in correction factor. The plots show that C = constant leads to significant error as x* and aspect ratio increases. Polynomial correlation for C yields < 3% error for Wibulswas data and should be used when x* > 0.001

A.4 Calculation of Nusselt correction factor for simultaneously developing flow

Table A.8 Mean Nusselt number, "H1" constant heat flux boundary condition for simultaneously developing flow in a rectangular duct, α* = 0.5. Raw data, reproduced from Wibulswas PhD Thesis(Wibulswas, 1966; Shah and London, 1978). Range of interest for flow of water in MD channels: $Pr \approx 2 - 10$

Mean Nusselt # at various Prandtl #				
x*	**Pr = 0 (slug flow)**	**Pr = 0.72**	**Pr = 10**	**Pr = ∞ (hydrodynamically developed flow)**
0.05	8.65	6.94	6.15	5.6
0.025	10.4	8.54	7.5	6.64
0.016667	11.65	9.77	8.4	7.45
0.0125	12.65	10.83	9.2	8.1
0.01	13.5	11.7	9.9	8.66
0.007143	14.95	13.15	11.05	9.57
0.005556	16.15	14.35	11.95	10.31
0.004545	17.2	15.35	12.75	10.95
0.003846	18.1	16.25	13.45	11.5
0.003333	18.9	17	14.05	12
0.002857	19.8	17.75	14.75	12.55
0.0025	20.65	18.5	15.4	13

Table A.9 Tabular correction factors: Ratio of Nusselt# for simultaneously developing flow to Nusselt # for Pr = ∞ (hydrodynamically developed, thermally developing flow)

$CF_{Simul.development} = \frac{Nu_{Pr \neq \infty}}{Nu_{Pr=\infty}}$				
x*	**Pr = 0**	**Pr = 0.72**	**Pr = 10**	**Pr = ∞**
0.05	1.545	1.239	1.098	1.000
0.025	1.566	1.286	1.130	1.000
0.016667	1.564	1.311	1.128	1.000
0.0125	1.562	1.337	1.136	1.000
0.01	1.559	1.351	1.143	1.000
0.007143	1.562	1.374	1.155	1.000
0.005556	1.566	1.392	1.159	1.000
0.004545	1.571	1.402	1.164	1.000
0.003846	1.574	1.413	1.170	1.000
0.003333	1.575	1.417	1.171	1.000
0.002857	1.578	1.414	1.175	1.000
0.0025	1.588	1.423	1.185	1.000

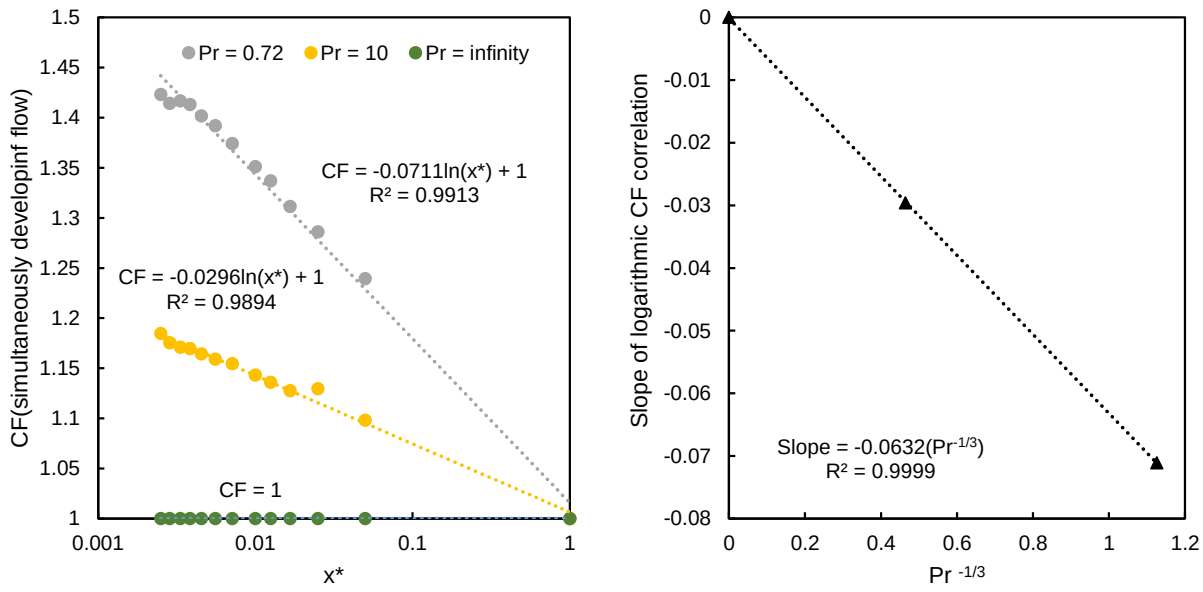

Figure A.3 A) Regression of tabular correction factors for simultaneously developing flow vs x* B) Regression of slopes from A

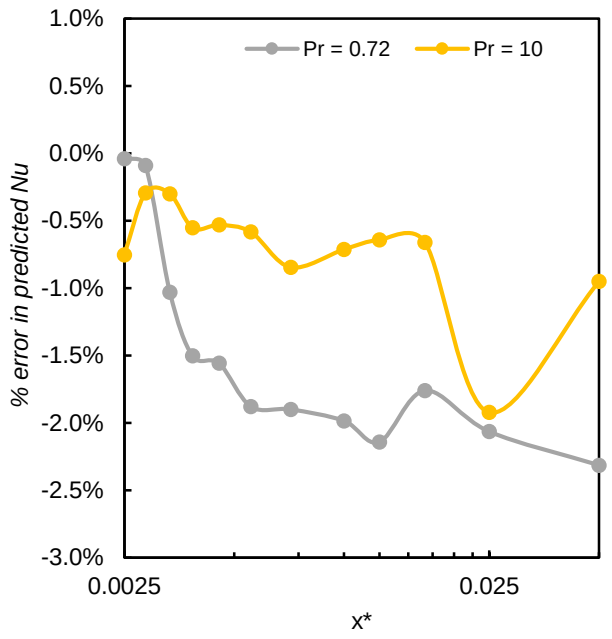

Figure A.4 Percent error in Nusselt calculations compared to Wibulswas thesis data

A.5 Calculation of Nusselt correction factor for heat flux from one wall

Table A.10 Fully developed Nusselt numbers for flow in rectangular ducts with constant axial heat flux. Tabular results compiled by Schmidt (Schmidt and Newell, 1967) and reproduced from Shah& London (Shah and London, 1978)

α*	$Nu_{H,4\ walls}$	$Nu_{H,1\ long\ wall}$
1	3.608	2.712
0.699301	3.75	3.149
0.5	4.123	3.539
0.4	4.472	3.777
0.3	4.99	4.06
0.2	5.738	4.411
0.1	6.785	4.851
0.0001	8.235	5.385

In Figure A.5 we plot tabular data from Table A.10, the Nusselt polynomial correlation for peripherally constant (4-wall) heat flux given by Shah and Sekulic(Shah and Sekulic, 2003), and a polynomial correlation for 1-wall heat transfer, calculated from the tabular data.

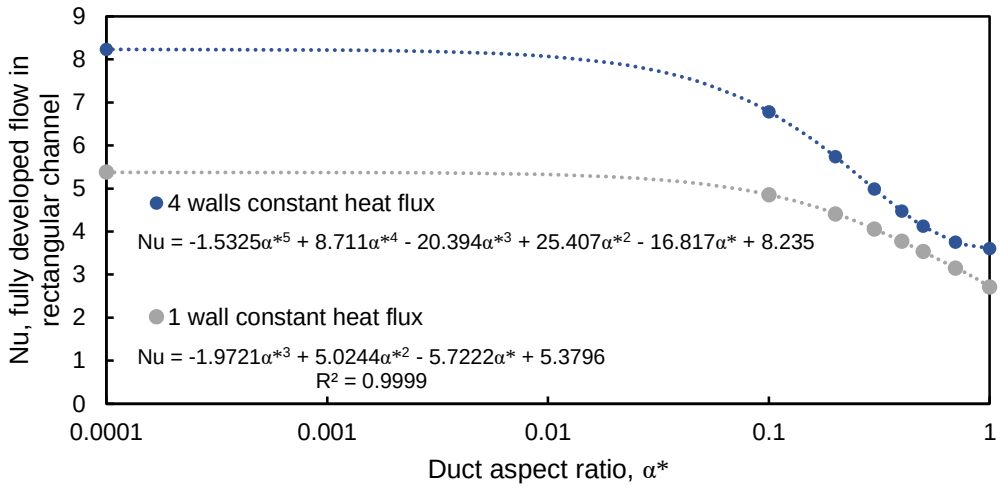

Figure A.5 Tabular data plotted along with polynomial correlations of fully developed Nusselt number in a rectangular duct

B. APPENDIX B

B.1: Solution for B-P dimensionless coefficients

Variables considered for B-P analysis:

MD Performance
J_w, $[kgm^{-2}s^{-1}]$, vapor flux
$v_{avg,memb}$, $[ms^{-2}]$, average vapor velocity
Q, $[Wm^{-2}]$, heat flux
η, $[dimensionless]$, thermal efficiency
TPC, $[dimensionless]$, temperature polarization coefficient
β, $[dimensionless]$, specific heat duty

Membrane Structure/chemistry parameters
δ, $[m]$, thickness
ε, $[dimensionless]$, porosity
d_f, $[m]$, average fiber diameter
d_{pore}, $[m]$, average pore diameter
C_m, $[m^{-1}]$, structural coefficient
τ, $[dimensionless]$, tortuosity
k_p, $[Wm^{-1}K^{-1}]$, Thermal conductivity of polymer
k_m, $[Wm^{-1}K^{-1}]$, Bulk membrane thermal conductivity
LEP, $[Pa]$, liquid entry pressure
$\theta_{adv}, \theta_{rec}$, [°], advancing/receding contact angle
cross-sectional asymmetry
fiber isotropy

Vapor Characteristics (Average in membrane)
ρ_{vap}, $[kgm^{-3}]$ density
p_{vap}, $[Pa]$, saturation vapor pressure (average)
υ, $[m^2s^{-1}]$, kinematic viscosity
μ, $[kgm^{-1}s^{-1}]$, dynamic viscosity
D_{wa}, $[m^2s^{-1}]$ ordinary molecular diffusion coefficient
λ, $[m]$, vapor mean path length
T_{avg}, $[K]$, average membrane temperature
ΔH_{vap}, $[Jkg^{-1}]$, enthalpy/heat of vaporization
c_p, $[Jkg^{-1}K^{-1}]$, specific heat of vapor
k_a, $[Wm^{-1}K^{-1}]$, thermal conductivity of air/vapor mixture
k_m, $[Wm^{-1}K^{-1}]$, bulk membrane thermal conductivity

Liquid Solution conditions
T_{fb}, T_{pb}, $[K]$, bulk feed/permeate temperatures
T_{fm}, T_{pm}, $[K]$, membrane surface temperatures

$\Delta T_{bulk}, [K]$, bulk temperature driving force
$\Delta T_{membrane}, [K]$, membrane surface temperature driving force
$p_{vap,fb}$, $p_{vap,pb}, [Pa]$, bulk vapor pressures
$p_{vap,fm}$, $p_{vap,pm}, [Pa]$, membrane surface vapor pressures
$\Delta p_{vap,bulk}, [Pa]$, bulk vapor pressure driving force
$\Delta p_{vap,memb}, [Pa]$, membrane surface vapor pressure driving force
$\varphi_{fb}, [dimensionless]$ feed osmotic coefficient (bulk)
$\varphi_{fm}, [dimensionless]$feed osmotic coefficient (membrane surface)
$a_w, [dimensionless]$ bulk water activity
$a_{w,m}$ $[dimensionless]$, membrane surface water activity
$\rho_{fb}, \rho_{pb}, [kgm^{-3}]$, bulk feed/permeate density
$\rho_{fm}, \rho_{pm}, [kgm^{-3}]$, membrane surface feed/permeate density
$\mu_{fb}, \mu_{pb}, [kgm^{-1}s^{-1}]$, bulk viscosity of feed/permeate streams
$\mu_{fm}, \mu_{pm}, [kgm^{-1}s^{-1}]$, viscosity of feed/permeate (membrane surface)
$H_{fb}, H_{pb}, [Jkg^{-1}]$, liquid enthalpy (bulk)
$H_{fm}, H_{pm}, [Jkg^{-1}]$, liquid enthalpy (membrane surface)
$c_{p,fb}, c_{p,pb}, [Jkg^{-1}K^{-1}]$, Specific heat (bulk)
$c_{p,fm}, c_{p,pm}, [Jkg^{-1}K^{-1}]$, Specific heat (surface)

System conditions
$v_f, v_p, [ms^{-1}]$, average velocity of feed/permeate streams
$k_{feed}, k_{perm}, [Wm^{-1}K^{-1}]$, thermal conductivity of feed/permeate solution
l, $[m]$, feed/permeate channel length
w, $[m]$, feed/permeate channel width
h, $[m]$, feed/permeate channel width
$h_f, h_p, [Wm^{-2}K^{-1}]$, feed/permeate convective heat transfer coefficient
$Re_f, Re_p, [dimensionless]$, feed/permeate Reynolds number
$Pr_f, Pr_p, [dimensionless]$, feed/permeate Prandtl Number
$Nu_f, Nu_p, [dimensionless]$, Feed/permeate Nusselt number
flow regime/development/non-idealities

Development of dimensionless parameters

Define functions (the four repeating variables chosen are $d_f, \Delta T_{bulk}, \mu, \rho_{vap}$):

$$\Pi_1 = f(\Pi_2, \Pi_3, \Pi_4, \varepsilon, \mathrm{a}_{w,bulk}, Nu_{feed}, Nu_{perm})$$

$$\Pi_1 = \Pi_1(d_f, \Delta T_{bulk}, \mu, \rho_{vap}, J_w)$$
$$\Pi_2 = \Pi_2(d_f, \Delta T_{bulk}, \mu, \rho_{vap}, k_p)$$
$$\Pi_3 = \Pi_3(d_f, \Delta T_{bulk}, \mu, \rho_{vap}, \delta)$$
$$\Pi_4 = \Pi_4(d_f, \Delta T_{bulk}, \mu, \rho_{vap}, D)$$

Solve for dimensionless parameters:

Step 1 – Set up equations with unknown exponents

$$\Pi_1 = {d_f}^a {\Delta T_{bulk}}^b \, \mu^c \rho_{vap}^d \, J_w$$
$$\Pi_2 = {d_f}^i {\Delta T_{bulk}}^j \, \mu^k \rho_{vap}^l \; k_p$$
$$\Pi_3 = {d_f}^e {\Delta T_{bulk}}^f \, \mu^g \rho_{vap}^h \; \delta$$
$$\Pi_4 = {d_f}^m {\Delta T_{bulk}}^n \, \mu^o \rho_{vap}^p \, D$$

Step 2 – Substitute Dimensions of variables

$$\Pi_1 = \; [L]^a \, [\theta]^b \; [ML^{-1}T^{-1}]^c \, [ML^{-3}]^d \, [ML^{-2}T^{-1}]$$
$$\Pi_2 = \; [L]^e \, [\theta]^f \; [ML^{-1}T^{-1}]^g \, [ML^{-3}]^h \, [L]$$
$$\Pi_3 = \; [L]^i \, [\theta]^j \; [ML^{-1}T^{-1}]^k \, [ML^{-3}]^l \, [MLT^{-3}\theta^{-1}]$$
$$\Pi_4 = \; [L]^m \, [\theta]^n \; [ML^{-1}T^{-1}]^o \, [ML^{-3}]^p \, [L^2T^{-1}]$$

Step 3 – Consolidate primary dimensions

$$\Pi_1 = L^{a-c-3d-2} T^{-c-1} M^{c+d+1} \theta^b$$
$$\Pi_2 = L^{i-k-3l+1} T^{-k-3} M^{k+l+1} \theta^{j-1}$$
$$\Pi_3 = L^{e-g-3h+1} T^{-g} M^{g+h} \theta^f$$
$$\Pi_4 = L^{m-o-3p+2} T^{-o-1} M^{o+p} \theta^n$$

Step 4 – Solve for exponents

$a-c-3d-2=0$ $-c-1=0$ $c+d+1=0$ $b=0$	Therefore:	$d=0$ $b=0$ $c=-1$ $a=1$	And:	$\Pi_1 = \frac{d_f \, J_w}{\mu}$

$i-k-3l+2=0$ $-k-3=0$ $k+l+1=0$ $j-1=0$	Therefore:	$j=1$ $l=2$ $k=-3$ $i=1$	And:	$\Pi_2 = \frac{\Delta T_{bulk} d_f^2 \rho_{vap}^2 k_p}{\mu^3}$ *or the inverse*
$e-g-3h+1=0$ $-g=0$ $g+h=0$ $f=0$	Therefore:	$f=0$ $h=0$ $g=0$ $e=-1$	And:	$\Pi_3 = \frac{\delta}{d_f}$ *or the inverse*

$m-o-3p+2=0$ $-o-1=0$ $o+p=0$ $n=0$	Therefore:	$n=0$ $p=1$ $o=-1$ $m=0$	And:	$\Pi_4 = \frac{\rho_{vap} D_{w,a}}{\mu}$ *or the inverse*

The final form is therefore

$$\boldsymbol{\Pi_1 = f(\Pi_2, \Pi_3, \Pi_4, \varepsilon, a_w, Nu_{feed}, Nu_{perm})}$$

$$\frac{d_f \, J_w}{\mu} = f\left(\frac{\Delta T_{bulk} d_f^2 \rho_{vap}^2 k_p}{\mu^3}, \frac{d_f}{\delta}, \frac{D_{w,a} \rho_{vap}}{\mu} \; \varepsilon, a_w, Nu_{feed}, Nu_{perm}\right)$$

B.2 Correlation to estimate pore diameter for fibrous membranes

Figure B.1 presents a correlation of electrospun membrane characterization data from the literature. Pore diameter, obtained using capillary flow porometry, is plotted versus the ratio of fiber diameter to membrane solid fraction. The dependence of fibrous membrane pore diameter on fiber diameter and porosity are mathematically established in previous works(Eichhorn and Sampson, 2010; Szentivanyi et al., 2011). Rather than use a theoretical model to estimate pore size of electrospun membranes, this empirical data from membrane distillation papers was correlated instead. This allows a closer qualitative comparison of fibrous membranes produced for this work with fibrous membrane tested previously in MD.

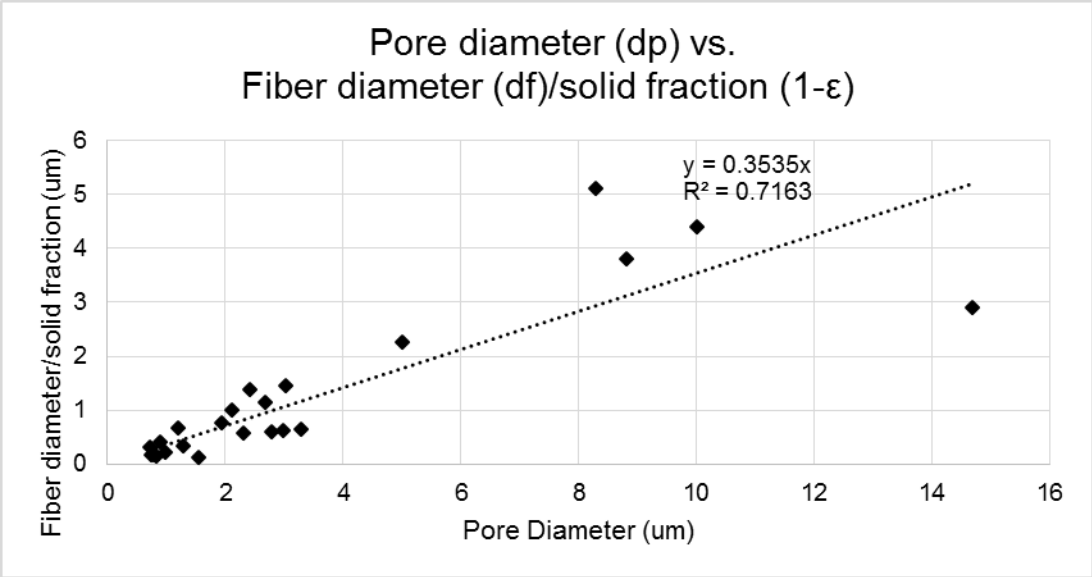

Figure B.1 Correlation of electrospun membrane characterization data from literature. (Prince et al., 2012; Essalhi and Khayet, 2013b, 2014; Liao et al., 2013a, 2013b, 2014a, 2014b; Wu et al., 2014; Li et al., 2014a; Tijing et al., 2014a; Leitch et al., 2016)

B.3 Tabulated experimental results

Table B.1 Structural, Flux, Nusselt Number, and Salt rejection data for Series A and Series B experiments

Membrane	$D_{f,avg}$ (µm)	C_m (m^{-1})	DCMD Series	T_{fb} (K)	T_{fm} (K)	Nu_{feed}	Nu_{perm}	J_w ($kgm^{-2}h^{-1}$)	Salt rejection (%)
7% PVDF-1	0.342	1.09E+05	A	332.4	293.0	56.12	47.14	45.09	99.959
7% PVDF-2	0.342	1.09E+05	A	333.3	292.9	56.36	47.00	32.05	99.987
7% PVDF-3	0.342	1.14E+05	A	333.1	293.2	56.22	47.36	59.28	99.995
7% PVDF-8	0.342	1.14E+05	A	333.3	292.5	56.32	47.03	47.59	99.966
8% PVDF-2	0.348	1.38E+05	A	332.8	292.9	55.97	47.75	113.65	99.995
8% PVDF-3	0.348	1.55E+05	A	333.0	293.0	56.00	47.77	116.24	99.990
8% PVDF-4	0.348	1.86E+05	A	333.2	292.9	56.03	47.77	119.10	99.967
9% PVDF-1	0.454	7.07E+04	A	333.4	293.0	56.34	47.21	54.91	99.962
9% PVDF-2	0.454	8.56E+04	A	333.3	293.2	56.26	47.40	67.41	99.996
9% PVDF-4	0.454	9.65E+04	A	333.3	292.8	56.32	47.16	53.30	99.896
9% PVDF-5	0.454	5.73E+04	A	334.2	292.2	56.58	46.81	32.50	99.955
9% PVDF-6	0.454	8.46E+04	A	333.4	292.6	56.27	47.25	65.09	99.996
10% PVDF-1	0.592	8.98E+04	A	332.5	292.3	55.97	47.35	85.89	99.987
10% PVDF-2	0.592	5.65E+04	A	333.4	292.3	56.41	46.81	42.34	99.993
10% PVDF-5	0.592	5.74E+04	A	332.9	293.0	56.13	47.43	76.25	99.990
10% PVDF-6	0.592	6.37E+04	A	333.1	293.2	56.20	47.45	77.58	99.947
10% PVDF-7	0.592	6.53E+04	A	333.3	293.0	56.30	47.35	76.60	99.996
10% PVDF-8	0.592	6.54E+04	A	332.7	293.1	57.93	48.93	79.73	99.993
10% PVDF-HP-1	0.608	9.43E+04	A	333.4	293.0	56.13	47.70	99.37	99.993
10% PVDF-HP-2	0.608	8.57E+04	A	333.0	293.1	56.06	47.65	96.15	99.995
10% PVDF-HP-3	0.608	7.60E+04	A	332.3	292.8	55.89	47.55	88.03	99.994
10% PVDF-HP-4	0.608	8.09E+04	A	334.2	293.6	56.34	47.78	92.23	99.942
comm. PTFE-1	0.937	8.97E+04	A	333.1	293.3	55.97	47.83	93.21	99.643
comm. PTFE-2	0.937	8.97E+04	A	332.8	294.0	55.91	48.02	92.23	99.994
comm. PTFE-3	0.937	8.97E+04	A	333.2	292.9	55.99	47.78	98.12	99.998
comm. PTFE-4	0.937	8.97E+04	A	333.4	293.1	56.02	47.83	100.08	99.995
comm. PTFE-40A	0.937	9.09E+04	B	313.2	293.2	51.34	47.06	27.24	99.996
comm. PTFE-40B	0.937	8.85E+04	B	313.1	293.5	51.33	47.16	26.16	99.997
comm. PTFE-40C	0.937	8.93E+04	B	313.1	293.1	51.29	47.08	30.14	99.998
comm. PTFE-50A	0.937	8.84E+04	B	322.6	293.4	53.55	47.43	50.69	99.998
comm. PTFE-50B	0.937	8.97E+04	B	322.7	292.6	53.58	47.23	52.95	99.998
comm. PTFE-50C	0.937	8.93E+04	B	322.8	292.8	53.58	47.30	54.66	99.994
comm. PTFE-60A	0.937	8.96E+04	B	332.8	294.2	55.92	48.03	90.09	99.997
comm. PTFE-60B	0.937	9.36E+04	B	333.4	294.0	56.05	48.02	95.33	99.997
comm. PTFE-70A	0.937	8.28E+04	B	341.6	295.1	57.97	48.57	117.95	99.994
comm. PTFE-70B	0.937	9.13E+04	B	342.3	295.1	58.12	48.68	136.91	99.998
comm. PTFE-70C	0.937	8.88E+04	B	342.3	293.6	58.10	48.36	146.26	99.998
comm. PTFE-70D	0.937	8.90E+04	B	342.4	293.6	58.11	48.31	136.78	99.998
8%PVDF-70A	0.348	1.55E+05	B	349.3	295.2	59.83	49.28	238.60	N/A (0% feed TDS)
8%PVDF-70B	0.348	1.55E+05	B	346.5	293.9	59.89	48.83	222.84	N/A (0% feed TDS)
8%PVDF-70C	0.348	1.55E+05	B	346.5	293.7	59.92	48.63	200.26	N/A (0% feed TDS)
8%PVDF-70D	0.348	1.55E+05	B	346.5	295.1	59.92	48.97	200.70	99.986

B.4 B-P regressions for alternate parameter sets

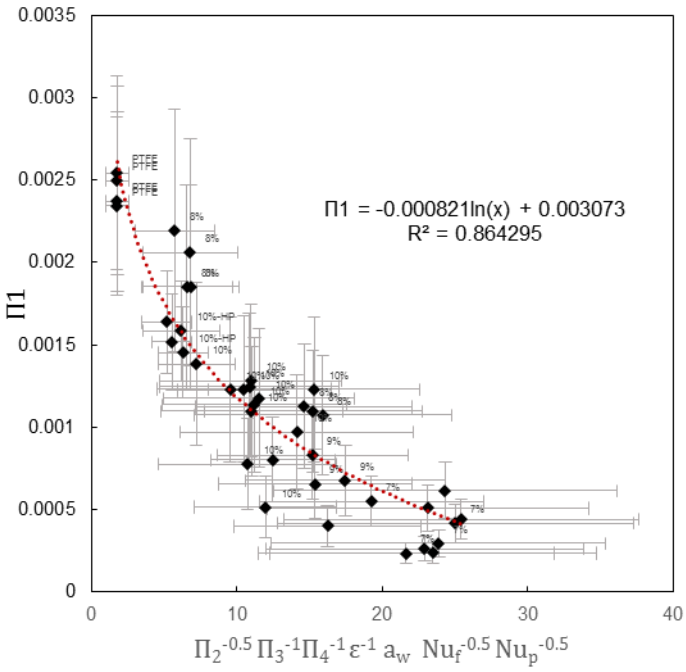

Figure B.2 B-P model correlation fit is poorer when porosity is used as a parameter instead of solid fraction

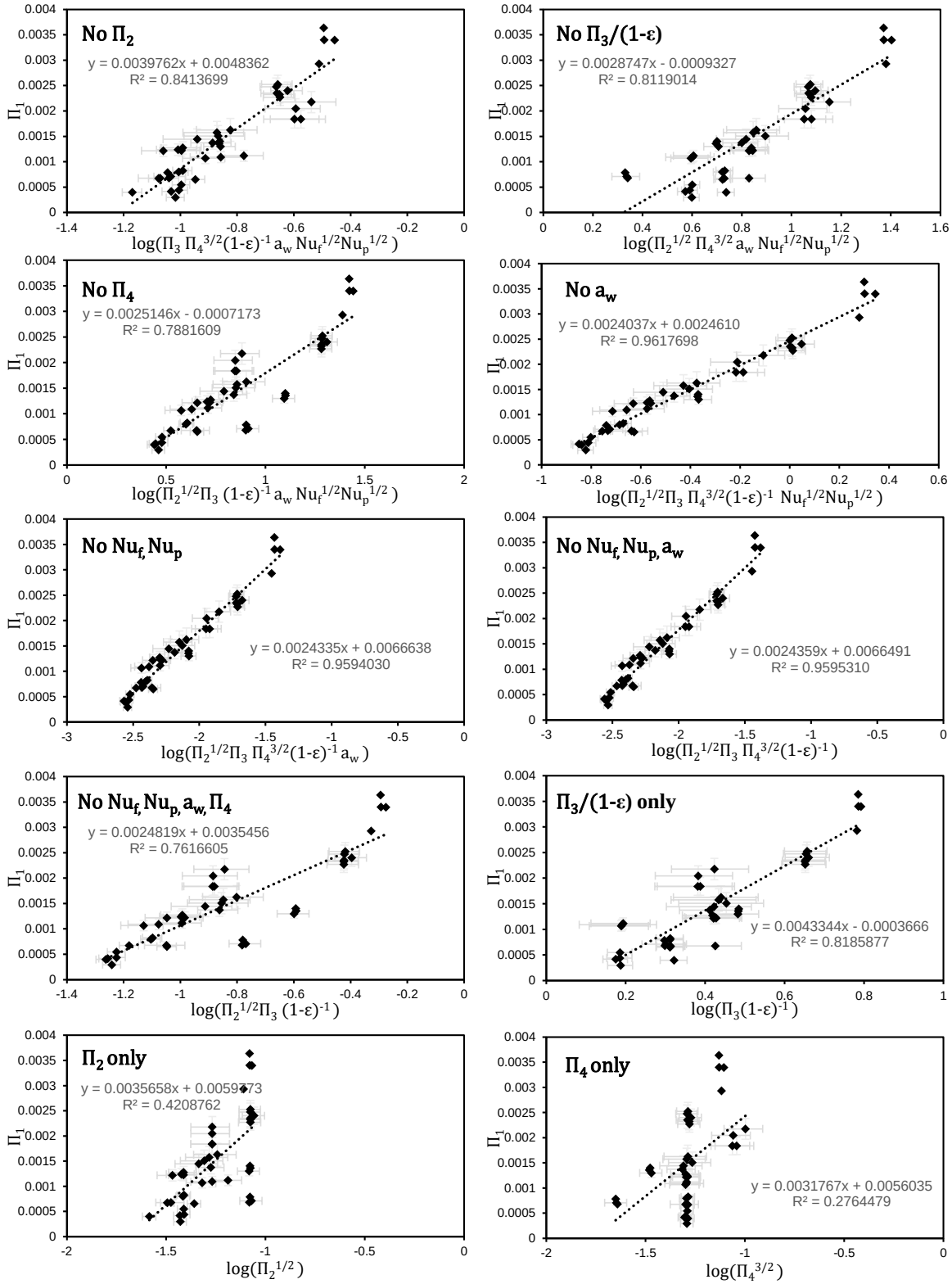

Figure B.3 Experimental data regressed for limited parameter sets. Shows full correlation is not a result of over-fitting: The correlation is valid for multiple combinations of structural parameters. $\Pi_3/(1-\varepsilon)$ is the most important parameter for correlation, revealing the strong relationship of MD flux to electrospun membrane structure

B.5 Supplemental SEM images for fibrous membranes

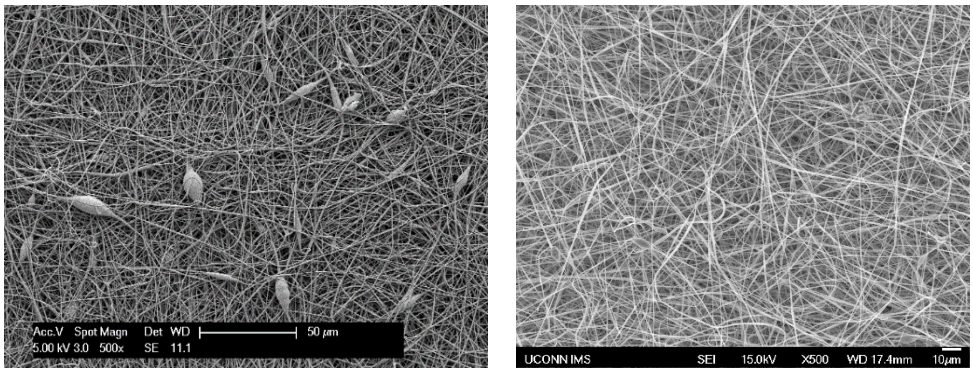

7% PVDF membrane, 500x 10% PVDF membrane, 500x

Figure B.4 Presence of beading in 7% PVDF electrospun membrane samples

C. APPENDIX C

C.1. Detailed methods for fabricating BNCA membranes and discussion of various bacterial strains tested for this research

We prepare modified Hestrin-Schramm media (2 wt% Glucose, 0.5 wt% Acros 61180-1110 Yeast extract, 0.5 wt% Peptone, 0.27 wt% Na_2HPO_4 in DI water, brought to pH 5 by addition of citric acid ~0.23 wt%, then autoclaved), then seed the sterile media with *Gluconacetobacter medellinensis* and incubate at 28°C. Every 36 hours, we harvest thin, translucent sheets of nanocellulose growing at the air-media interface. The cellulose sheets are rinsed in deionized (DI) water, cleaned in 0.5 M NaOH overnight, then transferred back to DI water. After a gradual (8-step) solvent exchange from DI to 200-proof ethanol, then to liquid CO_2, the BC is dried supercritically.

The following is a list of bacterial strains grown in this research with a qualitative assessment of their growth in modified Hestrin-Schramm media. Both ATCC 53582 and *G. medellinensis* produced cellulose pellicles suitable for use as DCMD membranes under the growth conditions specified above. *G. medellinensis* was chosen because it was the fastest producer of cellulose sheets

Bacterial Strain	**Source**	**Cellulose Pellicle Characteristics**
G.xylinus NRRL/USDA B-1034	NRRL ARS culture collection	Non-viable
G.xylinus NRRL/USDA B-43	NRRL ARS culture collection	Non-cohesive fibers
G.xylinus NRRL/USDA B-758	NRRL ARS culture collection	Non-cohesive fibers
G.xylinus ATCC 11142	NRRL ARS culture collection	Non-cohesive fibers
G.xylinus ATCC 10245	NRRL ARS culture collection	Slow growth, variable density/thickness
G.hansenii ATCC 53582	ATCC	Fast growth, good uniformity
G.medellinensis	Aalto University, Helsinki	Fastest growth, good uniformity

C.2 Gravimetric calculation of porosity

We calculate porosity (ε) gravimetrically by measuring membrane mass (m) and dimensions to determine aerogel volume (V) and density (ρ), both before and after hydrophobization, then apply the following formulas:

$$\rho_{cellulose\ in\ aerogel} = \frac{m_{hydrophilic\ aerogel}}{V_{hydrophobic\ aerogel}} \quad \text{(S1.1)}$$

$$\rho_{silane\ in\ aerogel} = \frac{(m_{hydrophobic\ aerogel} - m_{hydrophilic\ aerogel})}{V_{hydrophobic\ aerogel}} \quad \text{(S.2.2)}$$

$$\varepsilon_{BNCA} = \left(1 - \frac{\rho_{cellulose\ in\ aerogel}}{\rho_{pure\ BNC\ fiber}} - \frac{\rho_{silane\ in\ aerogel}}{\rho_{pure\ silane}}\right) * 100 \quad \text{(S2.3)}$$

C.3 Characteristics and Schematic of Benchtop DCMD system

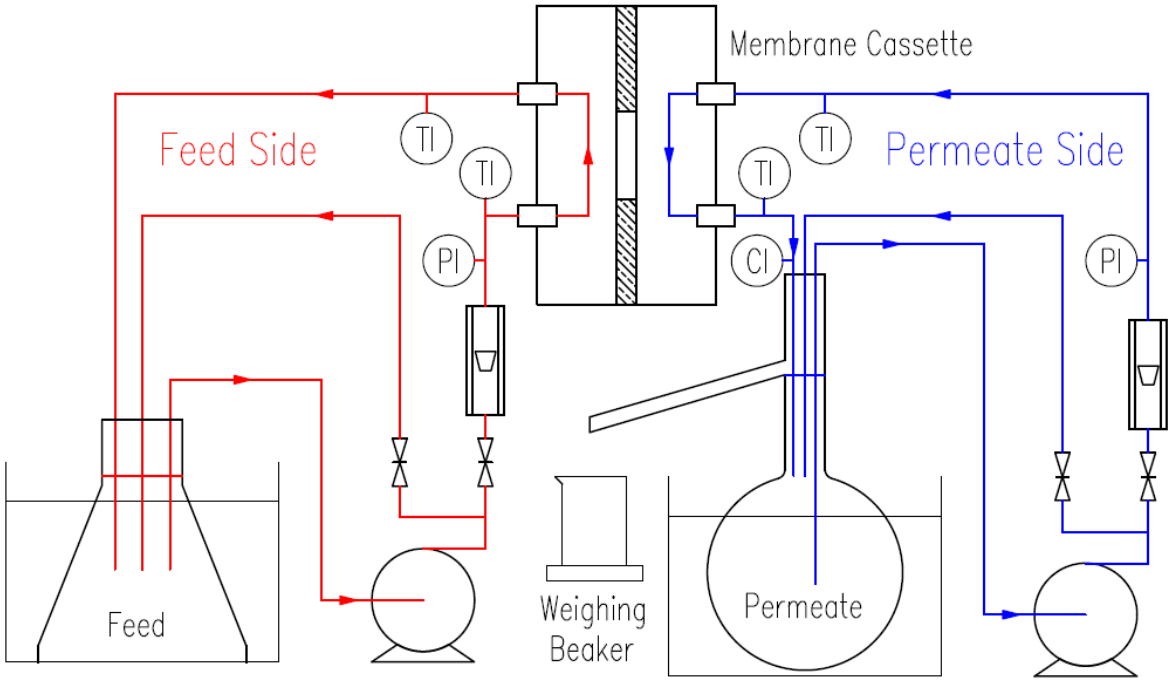

Figure C.1 Benchtop DCMD Schematic

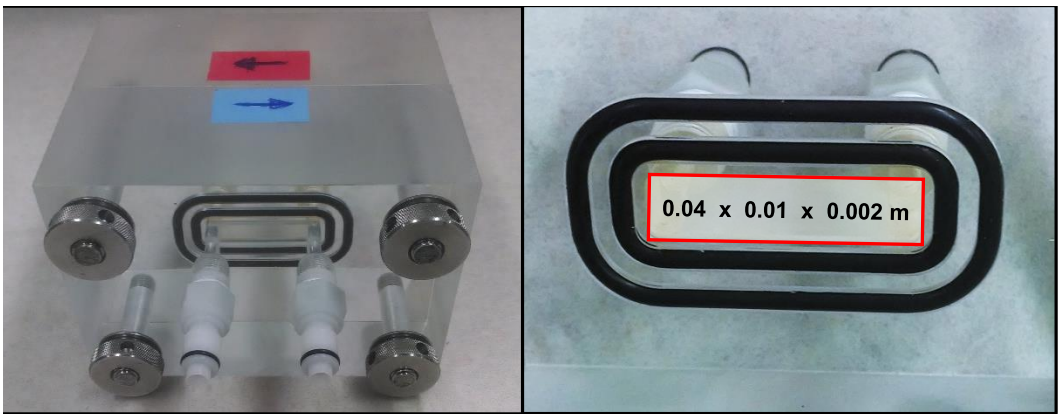

Figure C.2 Images of DCMD cassette used for data collection.Feed and permeate flow counter-current with no spacers. Channel entrance and exit are abrupt

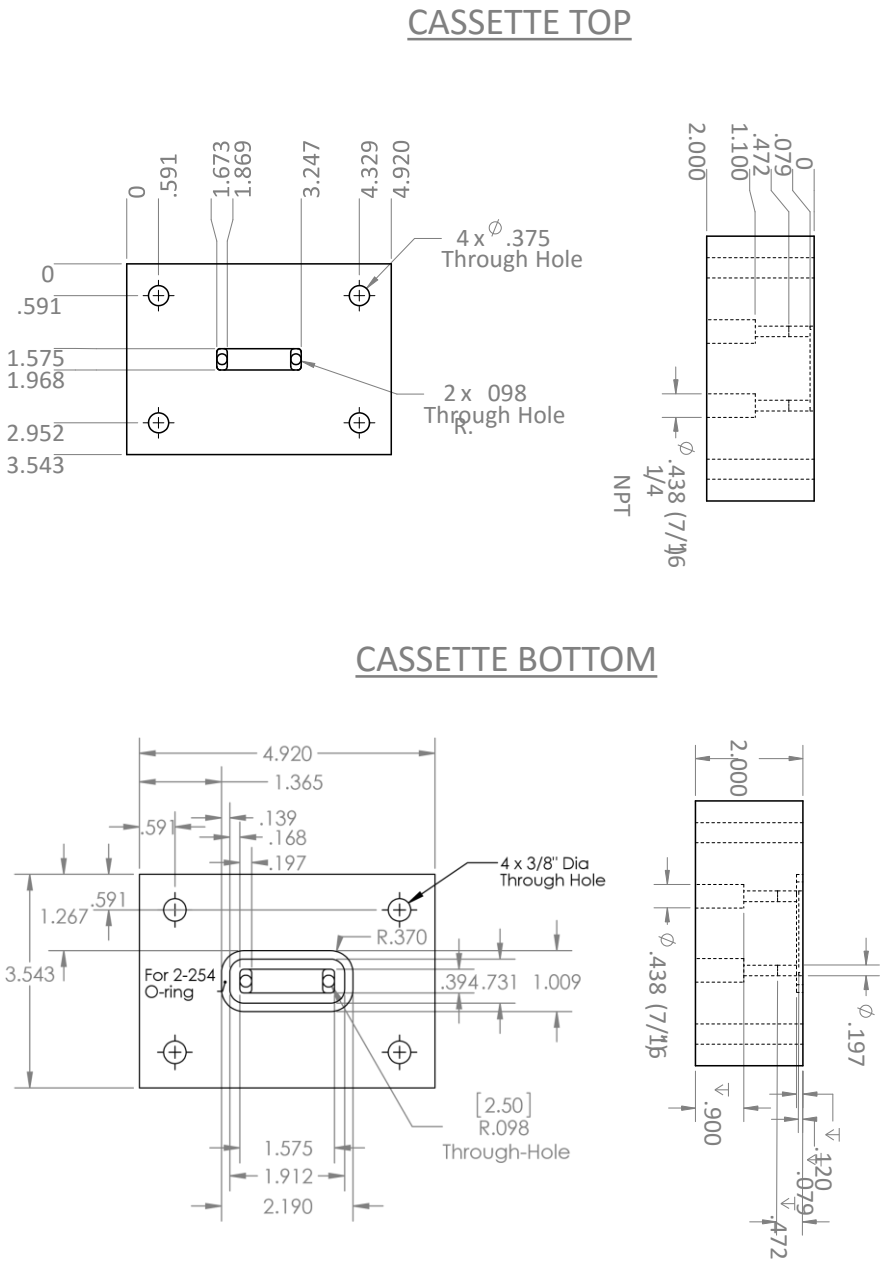

Figure C.3 Schematic of MD cassette

The membrane cassette holds a flat-sheet membrane with an effective area of 0.01 x 0.04 m, designed for counter-current flow with no support or spacers. We monitor system conditions such as cassette inlet and outlet temperatures, inlet pressures, flow rates, and permeate conductivity

using digital and analog sensors. Feed water with 35,000 ppm NaCl and de-ionized permeate are circulated by pumps at a rate of 0.3 L/min (mean velocity of 0.25 m/s in the cassette, flow channel dimensions: 0.002 m height x 0.01 m width x 0.04 m length). Vapor flux through the membrane is calculated by measuring the mass of permeate reservoir overflow over 3-6 hours. Experiment length is set to ensure the uncertainty in calculated permeate flux was less than 4% and the uncertainty in calculated salt rejection is less than 0.02%. National Instruments LabView software is programmed to automatically collect temperature, pressure and balance readings. Raw data was is subsequently processed and analyzed by a MATLAB program.

Model numbers for DCMD components:

- Balance: Scout Pro with Square Platform, Ohaus
- Flow meter: 7510/7511 Series, King Instrument Company
- Temperature sensor: NI 9219, Universal Analog Input, 24-Bit, 100 S/s/ch, 4 Ch Module, National Instruments
- Pressure sensor: Pressure switch w/display, Standard, 29 PSI , G1/4", 4-20 mA, (1) PNP, Balluff
- Conductivity meter: S470 SevenExcellence™ pH/Conductivity, Mettler Toledo
- Conductivity sensor: InLab® 731-ISM, 4-electrode graphite conductivity sensor, ATC

C.4 Theoretical, Modeling and Experimental Discussion of BNCA matrix stability under DCMD conditions

In situ measurements of morphological and chemical changes to membrane characteristics during DCMD are difficult. Instead, we use theoretical, modeling and experimental evidence to infer the chemical and structural stability of the BNCA matrix at both feed temperatures. Both BNCA and PVDF membranes undergo slight compression in DCMD due to transverse head pressure. In addition, we observe very slight aggregation of surface fibers at the feed-side interface. **The modeling analysis presented below demonstrates that neither have a detectable impact on experimental flux.** Furthermore, the literature review, modeling analysis, and experimental evidence below suggests that there is little additional chemical or structural change to the aerogels attributable to water exposure or temperature in the 40^0C and 60^0C DCMD flux experiments

Chemically, three potential mechanisms exist that could disrupt fiber/pore morphology under DCMD conditions: polymer conformation change, weakening of H-bonds, and loss of silane modification. None of these are likely to occur for the BNCA membrane for the reasons outlined below.

1) Polymer melt/conformation change. Experiments were conducted well below the glass-transition or melt temperatures of the cellulose fibers which is 220-245°C according to the Handbook of Polymers(Wypych, 2012), Thus, it is unlikely that the 60 C temperature alone caused the polymeric nanofibers to deform.

2) Weakening of hydrogen bonding between fibers. Previous research indicates that the hydrogen-bond based modulus in cellulose changes only slightly in the regime between 40° and 60°C.(Yano et al., 1976) No morphological changes are noted between 40 and 60^0C water exposure experiments. Thus, it is unlikely that the 60 C temperature caused weakening of H-bonding between fibers.

3) Hydrolytic instability of the silane modification. We do not find any evidence for silane instability in our experimental data (e.g. changes in flux with time or decreased salt rejection). However, long-term hydrolytic stability of the hydrophobic silane coatings is a design issue that should be considered in future

work, as higher temperatures are known to decrease hydrolytic stability of any silane,(Plueddemann, 2013) and there is evidence that dipodal silanes may be more stable than the monopodal silanes used here.(Arkles et al., 2014) We could not find any literature discussing the limits of hydrolytic stability for the particular silane used in this research, but Geerken et. al. demonstrated the hydrolytic stability of perfluorinated octyltrichlorosilane coatings (very similar in structure) were unaffected over 180 hours stored at pH 5-8 at 50°, 65°, and 80°C.(Geerken et al., 2004)

Structurally, two mechanisms exist that that could change the BNCA membrane morphology under DCMD conditions:

4. **BNCA network compression/collapse due to trans-membrane pressure.** As with most membrane materials, both BNCA and PVDF undergo a small amount (<13%) of compression when exposed to ~0.9 PSI (6.2 KPa) static compressive head pressure in the benchtop DCMD system. More significant compression of the BNCA membranes is inconsistent with our experimental and modeling results. Gradual compression of the BNCA membranes under DCMD conditions would have ramifications for flux, which stayed constant during our experiments.

5. **Fiber aggregation & matrix compression due to ambient evaporation of water in contact with nanofibers.** We observe a small degree of aggregation of the surface layer of BNCA fibers during or after the DCMD experiment. This morphological change is too slight to affect membrane flux, permeability, or thermal efficiency, as demonstrated in modeling work shown below. We attribute fiber aggregation to capillary forces at the air-liquid interface, either during DCMD or after removing the water-exposed membrane from the DCMD cassette. Previous research has shown that skeletal nanofibrous structures are susceptible to aggregation while drying, which is why lyophilization or critical point drying is required in the fabrication process.(Kettunen et al., 2011) Partial compression/aggregation of membrane fibers would result in a hierarchical structure that increases average pore size,(Pääkkö et al., 2008) whereas complete ambient drying of the wetted structure (post DCMD) leads to more dense mat

with porosity 60-94%.(Zeng et al., 2014) Effects of both (hypothetical) aggregation-induced morphologies on membrane flux are modeled below.

A sixth mechanism, couples chemical and structural modification:

6. **Water infiltration into membrane pores.** As with scenario 3, constant flux and salt rejection over the course of the experiments do not support the infiltration of water into membrane pores.

The hypothetical loss of BNCA membrane stability (described in scenarios 1-6 above) would lead to changes in bulk membrane characteristics, such as thickness, average porosity, and average pore size. The effects on DCMD flux of these bulk morphological changes during DCMD process were modeled to determine whether gradual or immediate change in BNCA membrane structure are consistent with experimental behavior of the membranes in DCMD.

In Figure C.4 we model the effects of scenarios 2, 3, 4, and 6 on DCMD flux. If a BNCA membrane is gradually compressed or infiltrated throughout the experiment, then an increase in flux should be observed based on the effects of compression on permeability and thermal efficiency. This is inconsistent with our experimental results where flux was stable over the duration of the experiment.

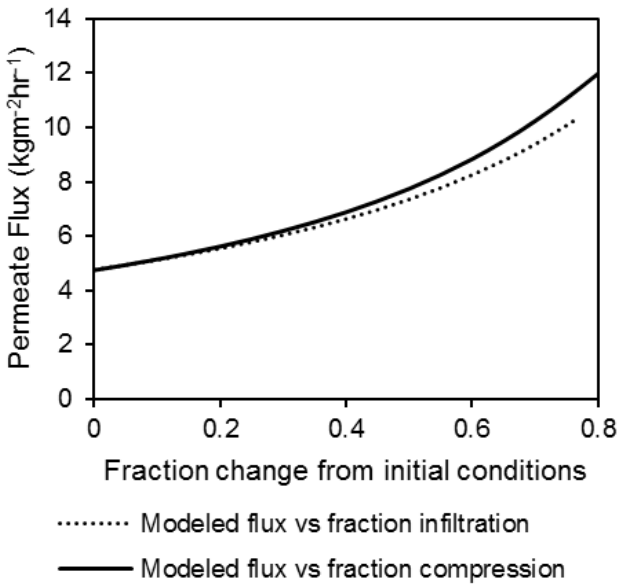

Figure C.4 Variation in modeled DCMD flux of BNCA membrane if membranes are gradually and uniformly compressed (decrease in thickness and porosity, pore size held constant), or if they are slowly infiltrated from the feed and permeate sides with liquid water. In both cases, flux increases over time, which is inconsistent with our experimental results where flux was stable over the duration of the experiment

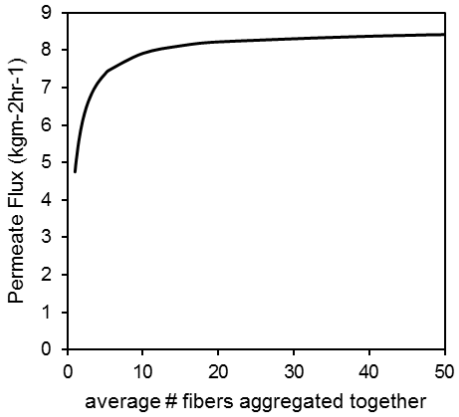

Figure C.5 Variation in modeled DCMD flux of BNCA membrane with uniform evaporative fiber aggregation(assumes thickness and porosity are held constant and pore radius increases)

Figure C.5 models scenario 5, where partial evaporative aggregation of membrane fibers leads to increased average pore size throughout the thickness of the membrane. Increased pore size increases the contributions of Knudsen vapor diffusion and would result in increased flux. Again, this is not observed experimentally.

Figure C.6 models scenarios 4 and 5 for more conservative cases in which only a fraction of the membrane cross section (e.g. the outermost 10%, 30%, 50%, or 70% of fibers) is compressed or experiences evaporative aggregation. We find that if a significant portion of the membrane collapses, then flux will increase, but if only a small cross section of the membrane is affected, then variation in flux, permeability or thermal efficiency would not be significant or detectible in our experimental set-up.

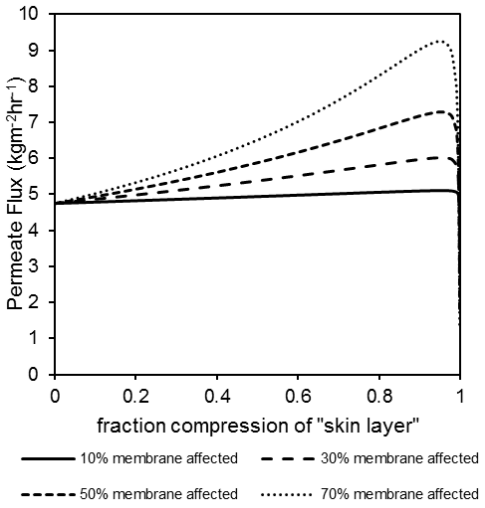

Figure C.6 Variation in modeled DCMD flux with partial compression of membrane, due to evaporative aggregation.In this model, thickness, porosity and pore size of the affected layer decrease

In summary, any significant BNCA (or PVDF) deformation under DCMD conditions would cause experimental flux to increase and salt rejection to decrease over time. We did not observe any changes in flux or salt rejection over the course of 3 or 6 hour experiments (Figures A.17A-D). We also did not observe any immediate deformation of the membrane material in simulated tests exposing the membrane to high temperature water.

17A. BNCA, 40^0 C feed temperature **17B. PVDF, 40^0 C feed temperature**

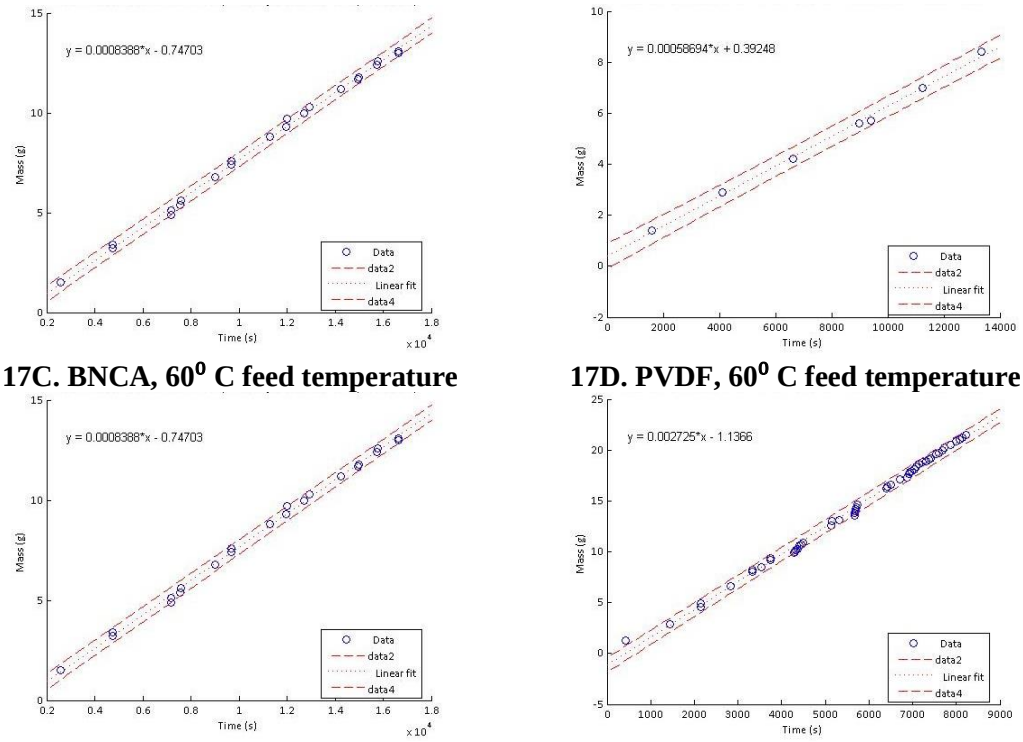

17C. BNCA, 60^0 C feed temperature **17D. PVDF, 60^0 C feed temperature**

Figure C.7 Representative raw data from DCMD experiments

Constant flux exhibited in Figure C.7 also indicates that the BNCA membrane does not infiltrate with liquid water, suggesting the silane modification was stable. This conclusion is further supported by Figure C.8, which demonstrated that salt rejection remains constant in a representative BNCA membrane in DCMD with a 60^{0}C feed.

Similarly, the advancing contact angle data for feed and permeate surfaces of BNCA and PVDF membranes before and after 60^{0}C-feed DCMD testing were relatively unchanged (Table C.1), suggesting good stability of the silane. Small decreases in the average advancing contact angle are observed on the feed and permeate sides, likely due to a decrease surface roughness in the ambiently-dried post-DCMD membranes as depicted in Figure C.9.

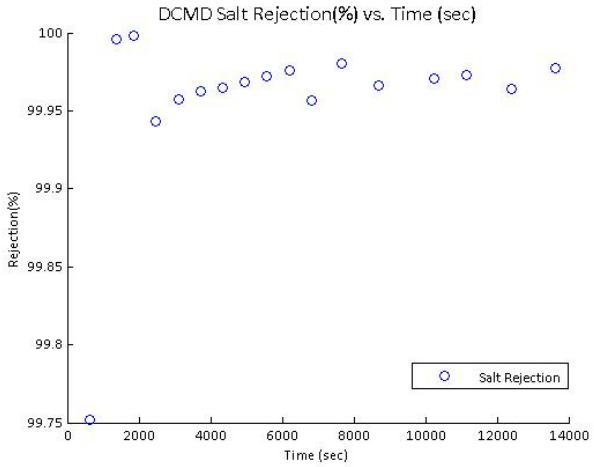

Figure C.8 Representative plot of BNCA salt rejection, 60°C bulk feed

Table C.1 Measurements of advancing contact angle (ACA) of membranes before and after DCMD testing

	Feed-side ACA		**Permeate-side ACA**	
	Pre-DCMD	***Post-DCMD***	***Pre-DCMD***	***Post-DCMD***
PVDF	118 ± 4.2^0	119.3 ± 16.8^0	147 ± 2.8^0	142 ± 2.6^0
BNCA	149.7 ± 4.7^0	136.7 ± 13.3^0	156 ± 5.5^0	148.3 ± 4.9^0

Figure C.9 shows representative morphological change to surface fibers of pre- and post-DCMD BNCA. Surface fiber aggregation is possibly due to capillary forces of evaporating feedwater causing aggregation of a thin layer of surface fibers. **Because rate of flux did not increase throughout the experiment, we deduce the fiber aggregation affected only a small fraction (0-10%) of the membrane cross-section (i.e. the surface).**

Static experiments were also designed in response to reviewer comments, to determine whether BNCA exposure to DCMD head pressure or feed/permeate waters alone could result in morphological change. Figure C.10 presents representative cross-sectional images of a BNCA membrane subjected to pressure, water at ambient temperature, and 3.5 wet% salt at 60^0 C. **Results from these experiments demonstrate the intra-sheet thickness variation of these biofilms and suggest BNCA may undergo as much as a 13% reduction in thickness due to DCMD head pressure, while PVDF membranes undergo 9% compression. Neither membrane material experiences complete pore collapse.**

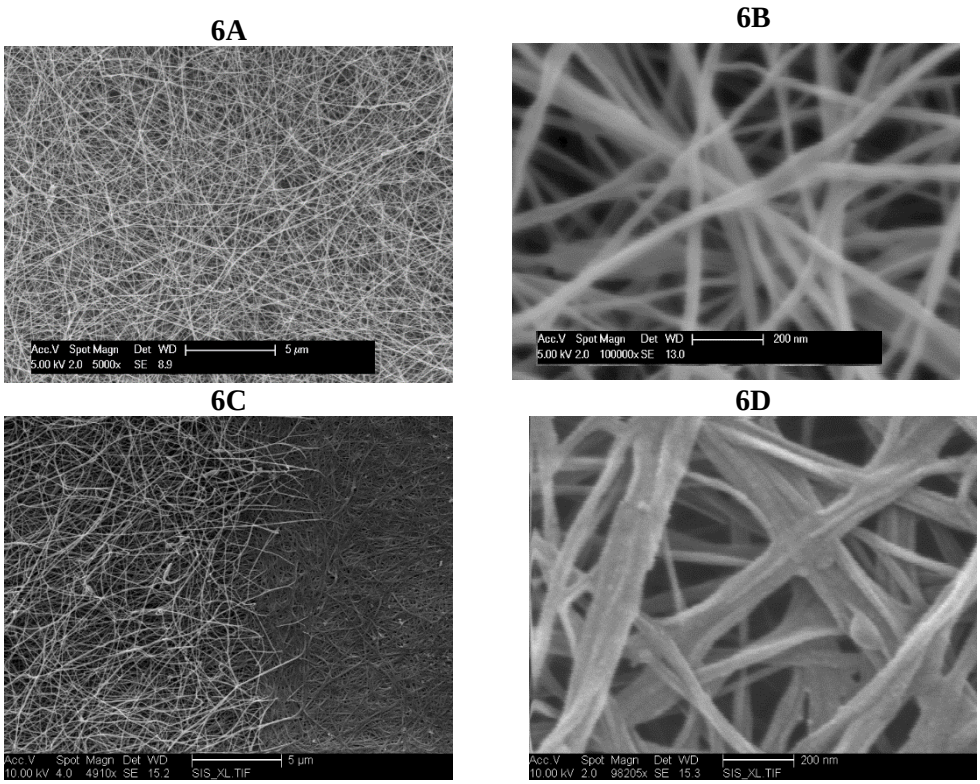

Figure C.9 Feed-side of membrane before and after DCMD testing. A) Pre-DCMD 5000x, B) Pre-DCMD 100,000x, c) post-DCMD (60^0C feed), 5000x, interface between membrane exposed to feed flow and not exposed to feed flow. d) post-DCMD (60^0C feed), 100,000x

7A. Control: hydrophobic BNCA	**7B.** 1.0 PSI compression (1 min)	**7C.** 3 hr, room temp, deionized water exposure	**7D**. 3 hr, 60^0C water, 3.5%wt NaCl exposure
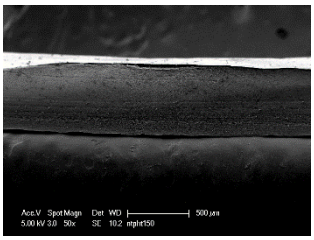	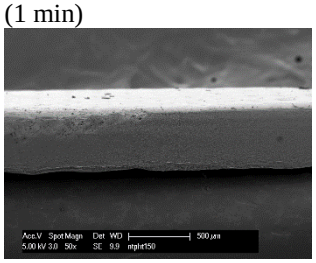	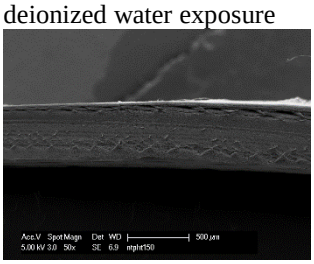	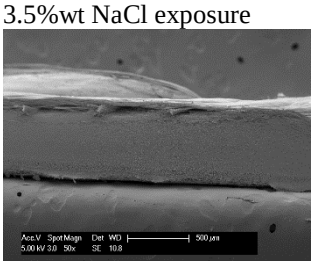
504 ± 22 μm	439 ± 19 μm	499 ± 28 μm	622 ± 29 μm

Figure C.10 Representative cross sectional images of a BNCA membrane subjected to static pressure, heat, water, and salt exposures to evaluate individual effects of DCMD stresses on membrane thickness/morphology

C.5 Calculation of parameters for DCMD mass and heat transport

S5.1 Experimentally-Measured Parameters:

$T_{f,b}$ = Bulk Temperature of the Feed [°K] - Experimental average of the feed-flow temperature readings by thermocouples placed just before and just after membrane

$T_{p,b}$ = Bulk Temperature of the Permeate [°K] - Experimental average of the permeate-flow temperature readings by thermocouples placed just before and just after membrane

$P_{f,b}$ = Bulk feed Pressure [Pa] – Atmospheric pressure + differential pressure of feed stream as measured by a transducer just prior to the membrane

$P_{p,b}$ = Bulk permeate Pressure [Pa] – Atmospheric pressure + differential pressure of feed stream as measured by a transducer just prior to the membrane

$C_{NaCl,b}$ = Bulk Concentration of NaCl in the Feed [mg/L] – Always 35,000 mg/L for this study

$\dot{V}_f$ = Volumetric flow rate of the Feed stream [L/min] – measured by an in-line flowmeter, always 0.3 L/min for this study

$\dot{V}_p$ = Volumetric flow rate of the Permeate stream [L/min] – measured by an in-line flowmeter, always 0.3 L/min for this study

w = Width of exposed membrane in membrane cassette [m] – always 0.01 m for this study

l = length of exposed membrane in membrane cassette [m] – always 0.04 m for this study

h = Channel height in membrane cassette [m] – always 0.002 for this study

ε = membrane porosity [%] – measured gravimetrically

r = average membrane pore radius [m] – measured using Capillary Flow Porometry

δ = membrane cross-sectional thickness [m] – measured using SEM

k_p = thermal conductivity of the pure polymer[W m^{-1} K^{-1}] – estimated from ranges provided in the 2012 Handbook of Polymers.

k_m = bulk thermal conductivity of the membrane [W m^{-1} K^{-1}] – estimated using equation (1) from manuscript

J_w = Experimental Vapor Flux [g/s] – measured by collecting permeate reservoir overflow on analytical balance, corrected for evaporation using temperature and relative humidity readings. (converted to $molm^{-2}s^{-1}$ to solve calculated parameters)

C5.2 Calculated Parameters (System of non-linear equations):

To calculate the permeability and thermal performance for each membrane under DCMD conditions, equations 1-5 from the manuscript must be solved simultaneously. On first inspection, it appears there are ten unknowns ($\boldsymbol{B_w}$, $\boldsymbol{\Delta p_w}$, $\boldsymbol{Q}$, $\boldsymbol{T_{f,m}}$, $\boldsymbol{T_{p,m}}$, $\boldsymbol{h_f}$, $\boldsymbol{h_p}$, $\boldsymbol{H_{w,f}}$, $\boldsymbol{H_{w,p}}$, $\boldsymbol{H_{w,vap}}$) for just four equations. Several of the unknowns, however, can be defined as functions of the experimentally measured system and membrane parameters (S4.1), of $\boldsymbol{T_{f,m}}$, and of $\boldsymbol{T_{p,m}}$. The full system of non-linear equations is presented here. In this study, they were solved iteratively (using an Excel model) to find $\boldsymbol{B_w}$, $\boldsymbol{Q}$, $\boldsymbol{T_{f,m}}$, and $\boldsymbol{T_{p,m}}$ for each membrane in each DCMD experiment.

$$\boldsymbol{J_w} = \boldsymbol{B_w}\,\Delta\boldsymbol{p_w} \quad \textbf{(2)}$$

$$\Delta\boldsymbol{p_w} = p_{w,f} - p_{w,p} \quad \text{(S2.1)}$$

$$p_{w,f} = vapor\ pressure\ of\ feed\ water\ at\ membrane\ surface\ [Pascal],\ calculated\ using\ relation\ between\ osmotic\ coefficient\ and\ water\ activity\ (thus, vapor\ pressure)\ pp\ 512\ to\ 517\ of\ Prausnitz\text{(Prausnitz et al., 1999):}\ p^o_{w,f}\exp\left(-\phi_{w,f}M_{H_2O}m_{NaCl}\nu_{NaCl}\right) \quad \text{(S2.2)}$$

$$p^o_{w,f} = saturated\ vapor\ pressure\ of\ pure\ water\ at\ membrane\ surface\ in\ feed, solved\ by\ Antoine\ equation\ (304-333^oK\ from\ NIST):\ 10^{5.20389-\left(\frac{1733.926}{T_{f,m}-39.485}\right)} * 100000 \quad \text{(S2.3)}$$

$$\phi_{w,f} = Osmotic\ Coefficient\ for\ feed\ at\ membrane, empirical\ fit\ calculated\ from\ Pitzer\ et\ al, 1984\ \text{(Pitzer et al., 1984):}$$
$$0.9209 - 0.02983m_{NaCl} + 0.0002632T_{f,m\,(^oC)} + 0.02957m^2_{NaCl} + 0.001026m_{NaCl}T_{f,m\,(^oC)} - 0.00001133T^2_{f,m\,(^oC)} - 0.004153m^3_{NaCl} - 0.0001337m^2_{NaCl}T_{f,m\,(^oC)} - 0.0000077m_{NaCl}T^2_{f,m\,(^oC)} + 0.0000001143T^3_{f,m\,(^oC)} + 0.0002678m^4_{NaCl} - 0.000001318m^3_{NaCl}T_{f,m\,(^oC)} + 0.00000074m^2_{NaCl}T^2_{f,m\,(^oC)} + 0.000000009754m_{NaCl}T^3_{f,m\,(^oC)} - 0.00000000004058T^4_{f,m\,(^oC)} \quad \text{(S2.4)}$$

$$M_{H_2O} = molar\ mass\ of\ water = 0.018015\,\frac{kg}{mol} \quad \text{(S2.5)}$$

$$m_{NaCl} = molality\ of\ salt\ in\ feed\ water = 0.59998\,\frac{mol}{kg} \quad \text{(S2.6)}$$
(model uses bulk concentration, does not account for concentration polarization at membrane surface)

ν_{NaCl} = $ions\ per\ molecule\ of\ salt = 2$ (S2.7)

$p_{w,p}$ = $saturated\ vapor\ pressure\ of\ (pure)\ permeate\ water\ at\ membrane\ surface\ solved\ by\ Antoine\ equation, (273 - 303^{o}K, from\ NIST)$: (S2.8)

$$10^{5.40221-\left(\frac{1838.675}{T_{f,m}-31.737}\right)} * 100000$$

$\boldsymbol{Q}$ = $\boldsymbol{Q_f = Q_m = Q_p}$ **(3)**

$\boldsymbol{Q_f}$ = $\boldsymbol{h_f(T_{f,b} - T_{f,m}) + J_w H_{w,f}}$ **(4)**

$\boldsymbol{h_f}$ = $Feed\ boundary\ layer\ heat\ transfer\ coefficient\ \left[\frac{W}{m^2 * K}\right] : \frac{Nu_f k_f}{d_h}$ (S4.1)

d_h = $Hydraulic\ radius\ in\ cassette\ [m]: \frac{4lw}{2(l+w)}$ (S4.2)

k_f = $Thermal\ conductivity\ of\ water\ \left[\frac{W}{m * K}\right].\ Calculated\ from\ NIST\ correlations\ using\ average\ temperature\ between\ bulk\ and\ membrane$: (S4.3)

$$0.6065\left(-1.48445 + 4.12292\left(\frac{\frac{T_{f,b}+T_{f,m}}{2}}{298.15}\right) - 1.63866\left(\frac{\frac{T_{f,b}+T_{f,m}}{2}}{298.15}\right)^2\right)$$

Nu_f = $Nusslet\ Number\ evaluated\ for\ laminar\ feed\ flow$ (Re = 900 for permeate, 1500 for feed), and Gz > 100 (Gz = 480 for permeate and 450 for feed) as detailed in McCabe, 2001(McCabe et al., 2001): (S4.4)

$$1.86 * Gz_f^{\frac{1}{3}} * \left(\frac{\mu_{f,b}}{\mu_{f,m}}\right)^{0.14}$$

$\mu_{f,b} \& \mu_{f,m}$ = $dynamic\ fluid\ viscosity\ (bulk\ \&\ membrane\ surface)\left[\frac{kg}{m * s}\right]$

$Calculated\ from\ equations\ in\ El\ Dessouky,$ 2002(El-Dessouky, Hisham T., Ettouney, 2002): (S.4.5)

$$exp\left(-3.79418 + \frac{604.129}{139.18 + T_{f,x,^{o}C}}\right) * (1 + \left(0.001474 + 0.000015\, T_{f,x,^{o}C} - 0.00000003927\, T_{f,x,^{o}C}^2\right)\left(\frac{C_{NaCl,b}}{\rho_{w,room\ temp}}\right) + (0.000010734 - 0.000000085\, T_{f,x,^{o}C} + 0.000000000223\, T_{f,x,^{o}C}^2)\left(\frac{C_{NaCl,b}}{\rho_{w,room\ temp}}\right)^2)/1000$$

$\rho_{w,room\ temp}$ = $density\ of\ water\ at\ room\ temperature(NaCl\ solution\ prep\ conditions)\ calculated\ from\ correlation\ in Handbook\ of\ Hydrology$(Maidment, 1993) (S.4.6)

$$999.842594 + 0.06793952(T_{room,°C}) - 0.00909529(T_{room,°C})^2 + 0.0001001685(T_{room,°C})^3 - 0.000001120083(T_{room,°C})^4 + 0.000000006536332(T_{room,°C})^5$$

Gz_f = $Graetz\ number\ for\ feed\ flow$: $\frac{d_h}{l} * Re_f * Pr_f$ (S4.7)

Re_f, Pr_f = $Reynolds\ and\ Prandtl\ numbers\ for\ feed\ in\ cassette,$ $calculated\ as\ customary\ using\ \dot{V}_f, d_h, T_{f,b}, T_{f,m}, \mu_{f,b}, \mu_{f,m}, k_f\ and\ c_{p,f}$ $(c_{p,f}\ is\ feed\ specific\ heat\ from\ Shomate\ equation)$ (S4.8)

$\boldsymbol{H_{w,f}}$ = $Enthalpy\ of\ liquid\ feed\ [\frac{J}{mol}], correlation$ $from\ CRC\ handbook, (does\ not\ account\ for\ NaCl\ concentration)$ (Lemmon, 2013)**:** $\left(4.18867 * \left(\frac{T_{f,b} + T_{f,m}}{2}\right) - 1143.48\right) * M_{H_2O} * 1000$ (S4.9)

$\boldsymbol{Q_p}$ = $\boldsymbol{h_p(T_{p,m} - T_{p,b}) + J_w H_{w,p}}$ **(5)**

$\boldsymbol{h_p}$ = $Permeate\ boundary\ layer\ heat\ transfer\ coefficient\ \left[\frac{W}{m^2 * K}\right]$: $\frac{Nu_p k_p}{d_h}$ (S5.1)

d_h = $(same\ as\ feed - side)$ (S5.2)

k_p = $Thermal\ conductivity\ of\ water\ \left[\frac{W}{m * K}\right].\ Calculated\ from\ NIST$ $correlations\ using\ average\ temperature\ between\ bulk\ and\ membrane$: $0.6065\left(-1.48445 + 4.12292\left(\frac{\frac{T_{p,b}+T_{p,m}}{2}}{298.15}\right) - 1.63866\left(\frac{\frac{T_{p,b}+T_{p,m}}{2}}{298.15}\right)^2\right)$ (S5.3)

Nu_p = $Nusslet\ Number\ evaluated\ for\ laminar\ permeate\ flow$ (Re = 900 for permeate, 1500 for feed), and Gz > 100 (Gz = 480 for permeate and 450 for feed) as detailed in McCabe, 2001(McCabe et al., 2001): $1.86 * Gz_p^{\frac{1}{3}} * \left(\frac{\mu_{p,b}}{\mu_{p,m}}\right)^{0.14}$ (S5.4)

$\mu_{p,b}$ & $\mu_{p,m}$ = $dynamic\ fluid\ viscosity\ (bulk\ \&\ membrane\ surface)\ \left[\frac{kg}{m * s}\right]$ $Calculated\ from\ equations\ in\ El\ Dessouky,$ 2002(El-Dessouky, Hisham T., Ettouney, 2002) (same as feed-side but solute concentration = 0): $exp\left(-3.79418 + \frac{604.129}{139.18 + T_{p,x,°C}}\right) * \left(\frac{1}{1000}\right)$ (S.5.5)

Gz_f = $Graetz\ number\ for\ feed\ flow$: $\frac{d_h}{l} * Re_p * Pr_p$ (S5.6)

Re_f, Pr_f = $Reynolds\ and\ Prandtl\ numbers\ for\ feed\ in\ cassette,$
$calculated\ as\ customary\ using\ \dot{V}_p, d_h, T_{p,b}, T_{p,m}, \mu_{p,b}, \mu_{p,m}, k_p\ and\ c_{p,f}$
$(c_{p,f}\ is\ feed\ specific\ heat\ from\ Shomate\ equation)$ (S5.7)

$\boldsymbol{H_{w,p}}$ = $Enthalpy\ of\ liquid\ permeate\ [\frac{J}{mol}], correlation\ from\ CRC\ handbook$ (Lemmon, 2013):

$$\left(4.18867 * \left(\frac{T_{p.b} + T_{p,m}}{2}\right) - 1143.48\right) * M_{H_2O} * 1000 \quad \text{(S5.8)}$$

$$\boldsymbol{Q_m} = \boldsymbol{Q_{m,conduct} + Q_{m,vap} = \frac{k_m}{\delta}(T_{f,m} - T_{p,m}) + J_w H_{w,vap}} \quad \textbf{(6)}$$

$\boldsymbol{H_{w,vap}}$ = $Enthalpy\ of\ transported\ liquid\ feed\ \left[\frac{J}{mol}\right], correl.\ from\ CRC\ handbook$(Lemmon, 2013) (S6.1)

$$(1.75231 * \frac{T_{f.m} + T_{p,m}}{2} + 2024.09395) * M_{H_2O} * 1000$$

Solution method: All equations and constants are inserted into a spreadsheet with two sets of cells reporting $T_{f,m}$ and $T_{p,m}$ (the temperatures at the membrane surface). For one set of cells an initial guess is made for $T_{f,m}$ and $T_{p,m}$, and for the second set of cells $T_{f,m}$ and $T_{p,m}$ are solved using equations (4) and (5). The spreadsheet replaces the initial guess with the calculated guess and recalculates: this process is iterated until the guessed and calculated values for $T_{f,m}$ and $T_{p,m}$ converge within 0.001°K.

C5.3. Normalization of experimentally calculated membrane permeability with membrane thickness:

Membrane permeability $\boldsymbol{B_w}$ calculated in equation (2) by the system of equations has units [mol s kg^{-1} m^{-1}]. When multiplied by $\boldsymbol{\Delta p_w}$ (difference in vapor pressure from one membrane surface to the other [Pa = kg m^{-1} s^{-2}], the flux, $\boldsymbol{J_w}$ is obtained [mol m^{-2} s^{-1}]. We simplify permeability units by the following equation:

$$B_{w,normalized}[s] = B_w * M_{H_2O} * \delta$$

C5.4 Calculation of Theoretical Membrane permeability coefficient, $\mathbf{B_{w,\ theoretical}}$ *(uses DGM theory)*

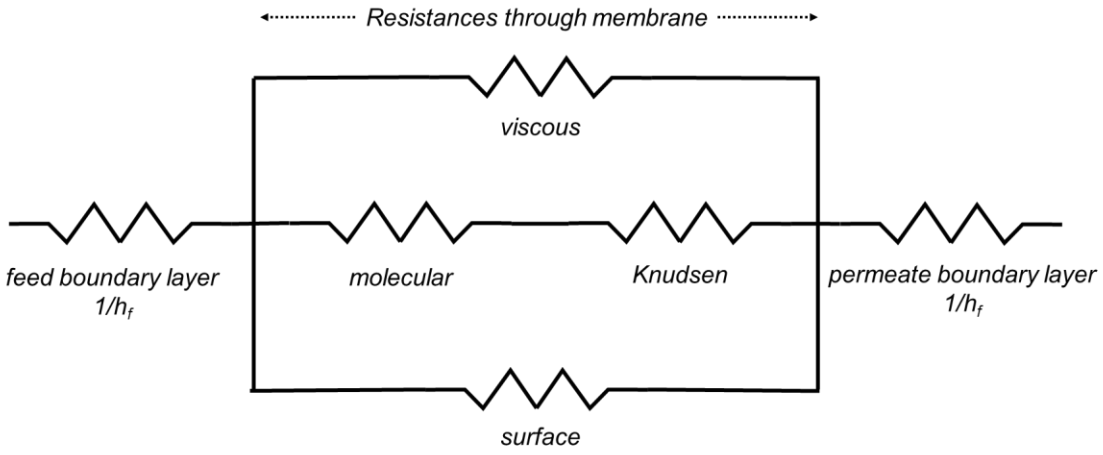

Figure C.11 Electrical analogue of mass transfer resistances in MD. Adapted with permission from(Lawson and Lloyd, 1997). Copyright 1997 Elsevier. h = BL heat transfer coefficient

Transport of water molecules from the bulk feed solution to the bulk permeate solution may be conceptualized using a simple electrical circuit model, as drawn by K.W. Lawson (Lawson and Lloyd, 1997) and reproduced in Figure C.11. Here, the "current" represents permeate flux, J_w, the "voltage" drop is the difference between saturated vapor pressures of feed and permeate streams, Δp_w, and the "resistors" represent various mass transport resistances between the bulk solutions and the membrane surface, as well as the resistances inside the membrane itself. The resistors in the parallel circuits represent four different potential transport mechanisms through the membrane as designated by the widely-used "Dusty Gas Model" (DGM,), developed by Mason and Malinauskas in 1983(Mason and Malinauskas, 1983) to describe generalized transport through porous media. Because this research proposal concerns the influence of membrane characteristics on MD performance, this theory section will focus on the relationship between permeate flux and membrane resistance (viscous, Knudsen, molecular, and surface resistance). Mass transport in boundary layers of the "circuit" is determined by system parameters and is described in Khayet, 2011. (Khayet, 2011)

Continuing the parallel circuit analogy, vapor flux (current) through the membrane is calculated by dividing the driving force (voltage) by the total membrane mass transport resistance, R_w:

$$J_w = \Delta p_w / R_w \qquad \text{(S7.1)}$$

The convention for membrane systems, however, is to express R_w in terms of its reciprocal, the membrane permeability coefficient, B_w. The full modified expression (Darcy's Law) is:

$$J_w = B_w \Delta p_w = B_w \left(p^0_{w,f} \gamma_{w,f} x_{w,f} - p^0_{w,p} \gamma_{w,p} x_{w,p}\right) \quad \text{(S7.2)}$$

Simply put, maximization of MD permeate flux, J_w, requires system conditions that maximize transmembrane vapor pressure and membranes that maximize permeability (Ref: **Table S1** for nomenclature box for a full description of parameters). To evaluate the total theoretical permeability, B_w, individual permeability coefficients of each transport mechanism are summed. Given the hydrophobic nature of the membrane in MD, surface diffusion of water vapor along membrane pores is considered negligible, and since the "resistance" is so high, the bottom branch of the parallel circuit is ignored. If feed water contains hydrophobic contaminants, surface diffusion of these molecules may be relevant. The following modified DGM permeability equations take into account all three of the remaining flow mechanisms:

$$B_w = B^v_w + B^D_w = B^v_w + \frac{B^K_w * B^o_w}{B^K_w + B^o_w} \quad \text{Where:} \quad \text{(S7.3)}$$

$$B^v_w = \frac{1}{8RT} * \frac{\varepsilon r^2 P_{avg}}{\tau \delta \mu} \qquad B^K_w = \frac{1}{RT} * \frac{2\varepsilon r}{3\tau\delta} * \left(\frac{8RT}{\pi M}\right)^{1/2} \qquad B^o_w = \frac{1}{RT} * \frac{\varepsilon}{\tau\delta} * \frac{PD}{p_a} \quad \text{(S7.4, 5, 6)}$$

The relative importance of viscous (Poiseuille) flux and diffusive flux (Knudsen and ordinary molecular), are debated in current MD modeling papers. Viscous flux is driven by the total (air + vapor) pressure gradient across the membrane; some researchers include it in calculations,(Chen et al., 2009) and some drop it unless Knudsen diffusion is irrelevant (e.g. the pore are large, a permeate-side vacuum is applied or if the feed, permeate, and pores are de-*gassed).*(Andrjesdóttir et al., 2013; Field et al., 2013) Diffusive flux mechanisms are driven by the vapor pressure gradient alone. Knudsen and Ordinary Molecular diffusion occur simultaneously when the membrane pore diameter is between 1 and 100 times the length of the mean free path of water vapor (a pore-size range of 0.014 to 1.4 μm at 1 atm and 50 C); at smaller pore sizes, Knudsen diffusion dominates and at larger pore sizes, ordinary diffusion dominates.

Since pore tortuosity (τ) is estimated as the inverse of porosity (1/ε),(Iversen et al., 1997) analysis of total theoretical MD permeability is reduced to a few key relationships. Membrane permeability is: (1) proportional to the square of porosity, meaning an aerogel with 97% porosity would have more than twice the permeability as a commercial membrane with 65% porosity, (2) inversely proportional to membrane thickness, δ and (3) either proportional to the pore radius squared, proportional to the pore radius, or independent of the pore radius, depending on the dominant transport mechanism.

C.6 Hydrophobization characterization

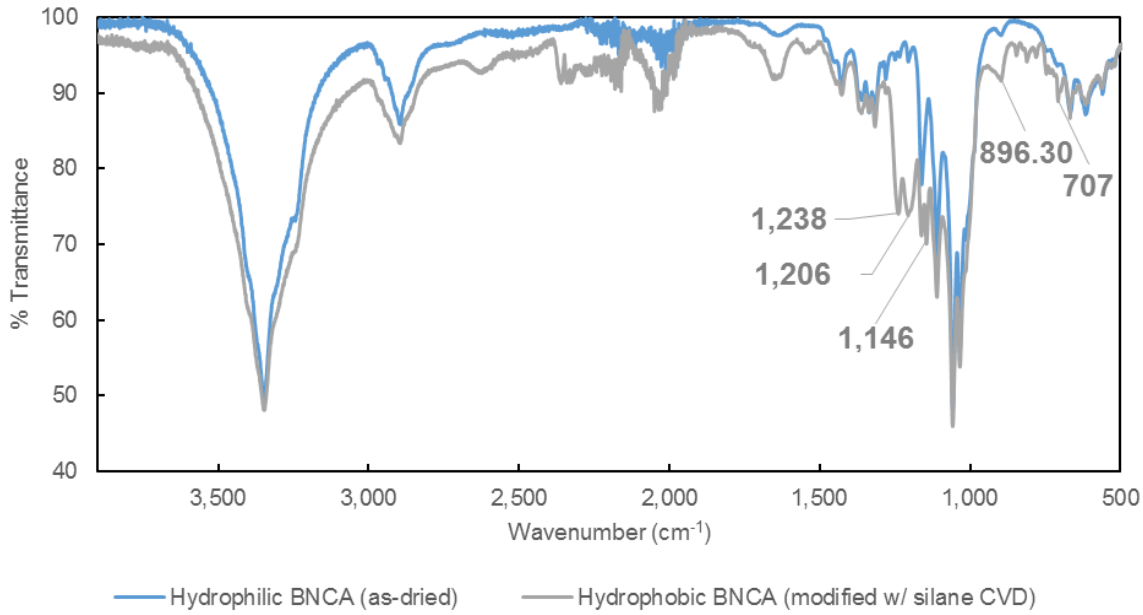

Figure C.12 Representative FTIR spctra verifying silane modificaion of BNCA membranes

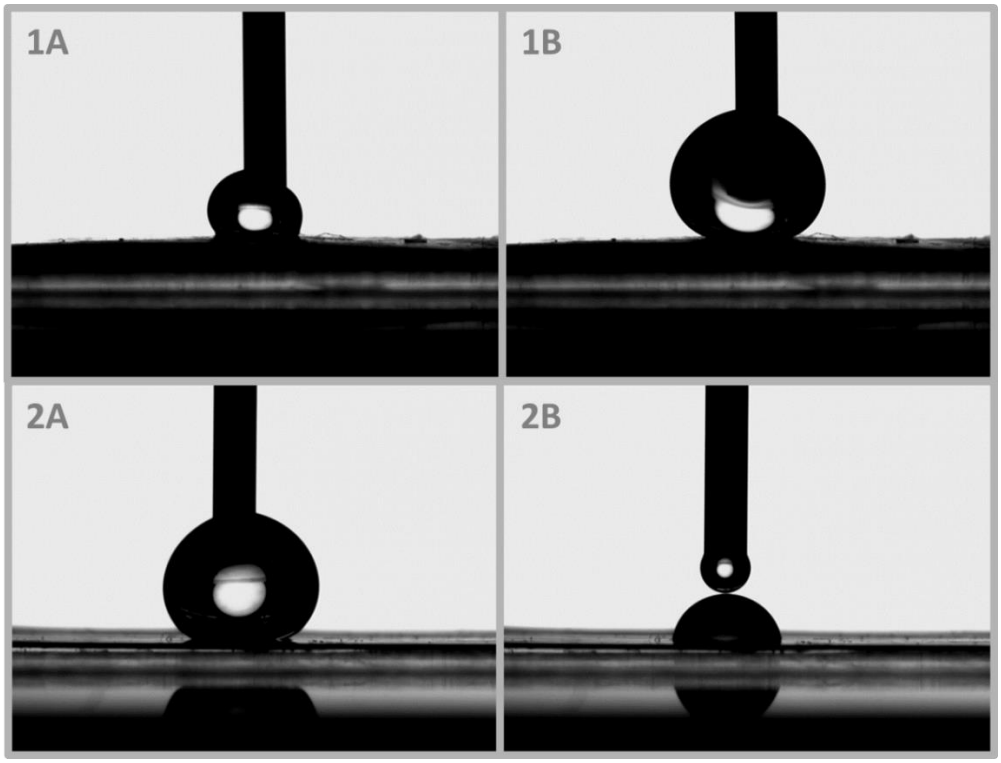

Figure C.13 Typical BNCA advancing contact angle measurement images. 1A) Initial droplet (2 µL) before testing advancing contact angle on BC membrane surface 1B) Final droplet (10 µL) after testing advancing contact angle on BC membrane surface 2A) Initial droplet (12 µL) before testing receding contact angle on BC membrane surface 2B) Final droplet after testing receding contact angle on BC membrane surface. Note: Prior to silane modification, BNCA ACA ≈0° - water was immediately adsorbed into the membrane

C.7 Capillary Flow Porometry Data and discussion of Liquid Entry Pressure

Pore size distributions taken at Porous Materials, Inc. Analytical Services Division 20 Dutch Mill Rd. Ithaca, NY 14850

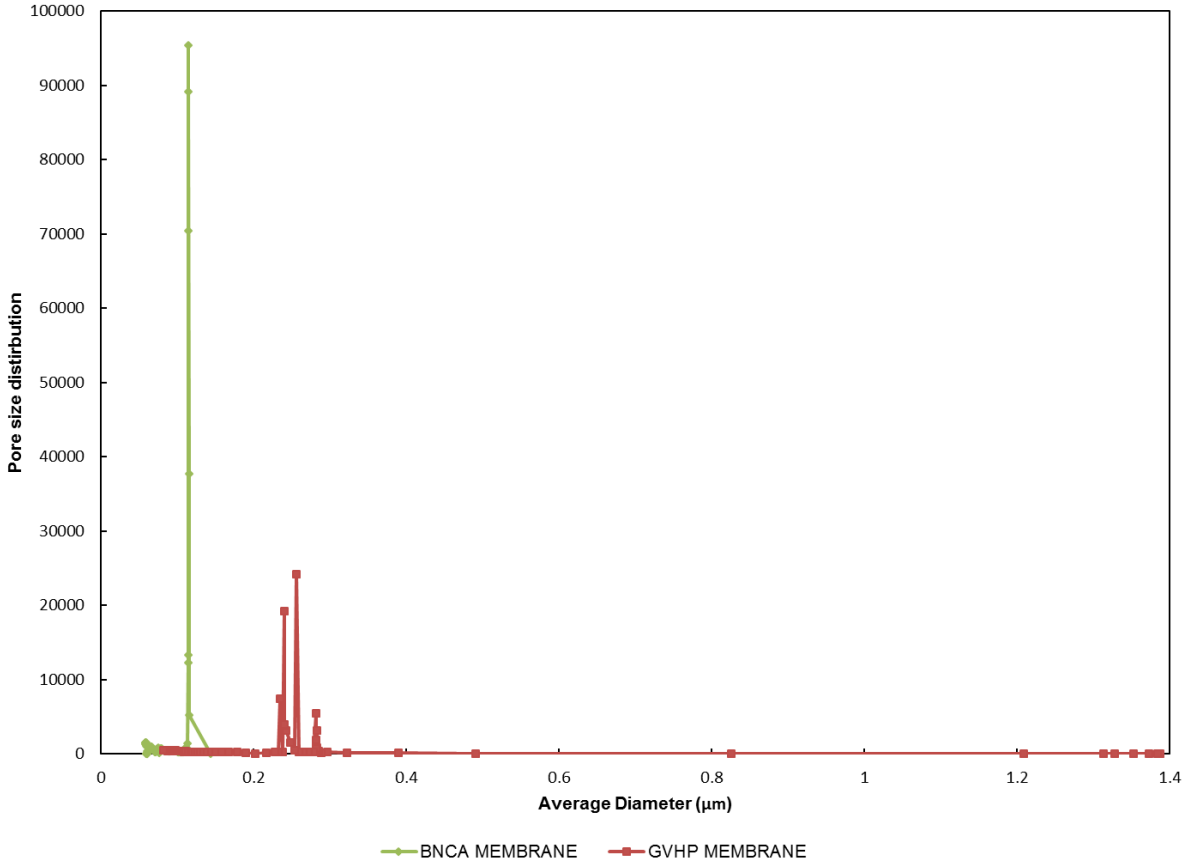

Figure C.14 CFP pore size distribution for a hydrophobic BCNA membrane (36 hour growth) and Millipore GVHP membrane

Note: It is probable that both soaking in the Galwick fluid and applying normal pressures required to obtain CFP data alter the BNCA and GVHP membrane structures. Also, pore size calculated from CFP data generally assume a cylindrical geometry, which can result in over-estimation of pore diameter in fibrous membranes (air will infiltrate at lower pressures than expected for a cylindrical pore due to acute fiber intersection angles). These are general weaknesses of the CFP Pore size characterization method, but unfortunately other pore size distribution characterization methods (e.g. BET/BJH Nitrogen adsorption/desorption,

evapoporometry, mercury porosimetry, liquid-liquid displacement porometry, SEM Image Analysis, AFM image analysis, X-ray computed tomography, etc) have similar faults. CFP was chosen because it is the most common method used to characterize MD membranes

Discussion of Liquid Entry Pressure (LEP): It is typical for MD research papers to report the LEP of tested membranes; this provides perspective on ability of the membrane pores to resist infiltration by the feed solvent solution during MD operation. Unfortunately, our lab was unable to collect valid data of the water LEP for BNCA membranes because of the extreme resistance to wetting coupled with relatively low mechanical strength; the membrane deformed and ruptured prior to liquid entry. Instead we report CFP bubble point and advancing contact angle for both membranes, which suggest the BNCA has a higher water LEP than the GVHP membrane.

C.8 Experimental vs. Theoretical permeability of tested membranes

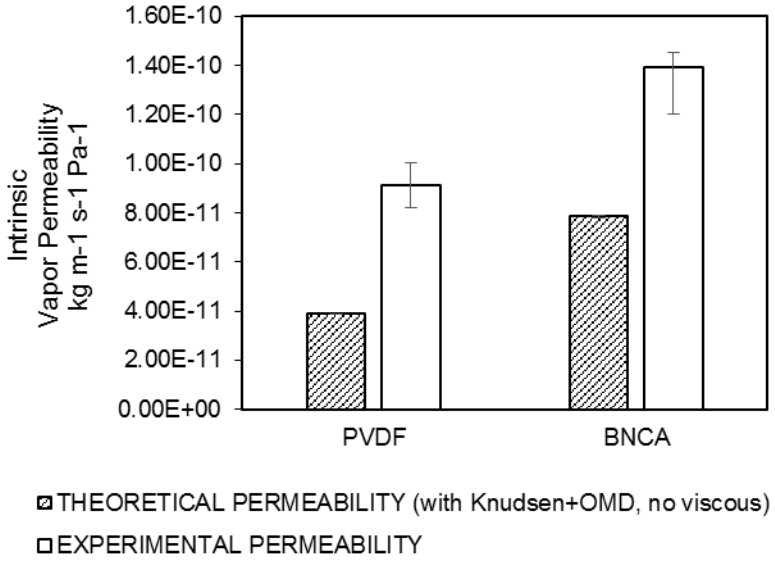

Figure C.15 Comparison of experimental to modeled membrane permeability for characterized and tested membranes. Membrane permeability modeled using DGM is typically lower than experimentally-measured permeability. TDS = 35 g/L NaCl,, Permeate Temp = 20°C

C.9 Revised data for BNCA study: DCMD metrics re-modeled using Ch2 Nusselt number correction factors

Using the cassette-dependent Nusselt correction factor, BNCA and PVDF membrane permeability, thermal efficiency and TPC were modeled again and the revised figures are presented below. While resulting metrics were quantitatively different from published values, qualitative comparisons between the PVDF and BNCA membranes remain the same.

Table C.2 Updated temperature polarization coefficients using NuCF to model heat transfer coefficients

	Thickness (μm)	$T_{f,b}$ **(°C)**	**flux (kg m^{-2} hr^{-1})**	**rejection (%)**	**TPC**
PVDF	109 ± 5	**40**	5.79 ± 0.27	99.53 ± 0.08	0.790 ± 0.002
	109 ± 5	**60**	25.80 ± 0.61	99.97 ± 0.04	0.759 ± 0.002
BNCA	218 ± 30	**40**	8.42 ± 0.21	99.87 ± 0.05	0.908 ± 0.002
	280 ± 36	**60**	22.92 ± 0.96	99.95 ± 0.04	0.895 ± 0.004

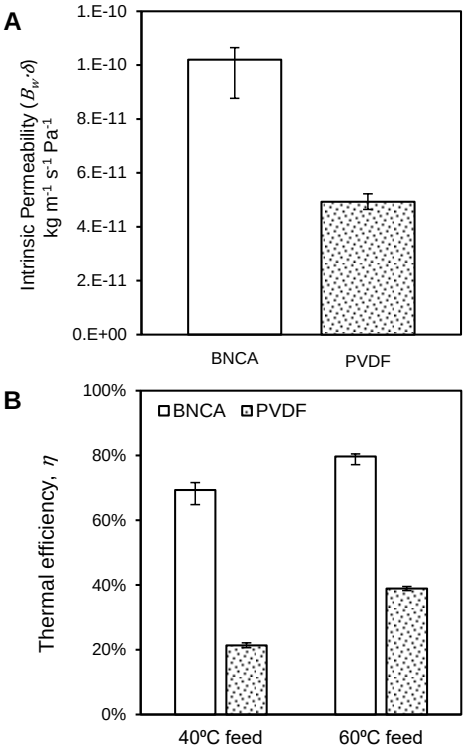

Figure C.16 Updated Permeability and thermal efficiency comparisons between BNCA and PVDF membranes. Use of cassette-dependent NuCF to calculate convective heat transfer coefficients causes calculated permeability and thermal efficiency of membranes to decrease, but the effect is greater for the PVDF membrane

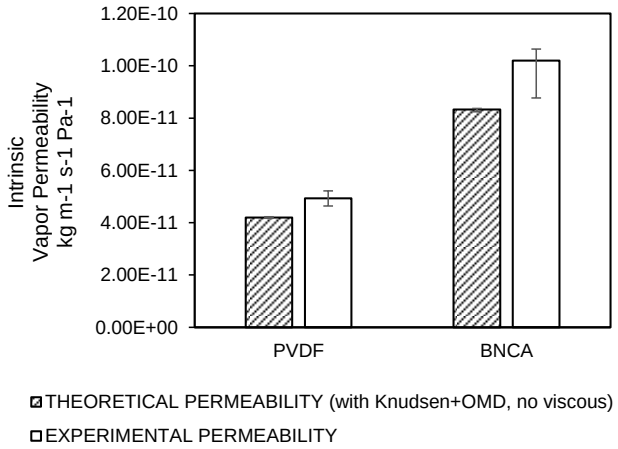

Figure C.17 Updated comparison of theoretical vs experimental permeability of BNCA and PVDF membranes using NuCF method to calculate the heat transfer coefficient. Better characterization of Nusselt number causes experimental membrane permeability measurements to more closely match theoretical measurements

NOMENCLATURE

$\alpha^* = duct\ cross\ sectional\ aspect\ ratio$

$a_w = water\ activity\ [dimensionless]$

$B_w = total\ membrane\ permeability, or\ membrane\ coefficient\ [kgm^{-2}s^{-1}Pa^{-1}]$

$B_{w,i} = intrinsic\ membrane\ permeability\ [kgm^{-1}s^{-1}Pa^{-1}]$

$c_p = Specific\ heat\ \ [Jkg^{-1}K^{-1}]$

$C_m = membrane\ structural\ parameter, defined\ in\ Ch.3\ [m^{-1}]$

$d_h = hydraulic\ diameter\ [m]$

$D = diffusivity\ [m^2s^{-1}]$

$f = friction\ factor\ [dimensionless]$

$Gz = Graetz\ number\ [dimensionless]$

$Gr = Grashoff\ number\ [dimensionless]$

$h = Boundary\ layer\ heat\ transfer\ coefficient\ [Wm^{-2}K^{-1}]$

$H = Enthalpy\ of\ distillate\ transporting\ from\ feed\ to\ permeate\ streams\ [J\ kg^{-1}]$

$J = Mass\ flux\ [kg\ m^{-2}h^{-1}]$

$k = \ Thermal\ conductivity\ [Wm^{-1}K^{-1}]$

$K = Mass\ transfer\ coefficient\ [ms^{-1}]$

$Kn = Knudsen\ number\ [dimensionless]$

$L = conduit\ length\ [m]$

$\dot{m} = mass\ flow\ rate\ [kgs^{-1}]$

$M_w = molecular\ weight\ [g\ mol^{-1}]$

$Nu = Nusselt\ number\ [dimensionless]$

$p = partial\ pressure\ [Pa]$

$p_w^0 = saturation\ vapor\ pressure\ of\ pure\ water\ [Pa]$

$P = total\ pressure\ [Pa]$

$Pe = Peclet\ number\ [dimensionless]$

$Pr = Prandtl\ number\ [dimensionless]$

$Q = Heat\ Flux\ [W\ m^{-2}]$

$r = average\ pore\ radius\ [m]$

$R = gas\ constant\ [JK^{-1}mol^{-1}]$

$Re = Reynolds\ number\ [dimensionless]$

$Sh = Sherwood\ number\ [dimensionless]$

$T = Temperature\ [K]$

$TPC = Temperature\ Polarization\ Coefficient\ [dimensionless]$

$\bar{u} = mean\ molecular\ speed\ [ms^{-1}]$

$v = fluid\ velocity\ [m\ s^{-1}]$

$x = mole\ fraction\ [dimensionless]$

$x' = dimensionless\ channel\ length$

$x^* = hydrodynamic\ inlet\ distance\ [dimensionless]$

$\beta = Specific\ heat\ duty\ [dimensionless]$

$\beta = Coefficient\ of\ thermal\ expansion\ (as\ applied\ to\ Grashof\ number)\ [K^{-1}]$

$\gamma_w = water\ activity\ [dimensionless]$

$\delta = membrane\ thickness\ [m]$

$\varepsilon =\ membrane\ porosity\ [dimensionless]$

$\eta = thermal\ efficiency\ [dimensionless]$

$\lambda = mean\ molecular\ path\ length\ [m]$

$\mu = dynamic\ fluid\ viscosity\ [kgm^{-1}s^{-1}]$

$\nu = kinematic\ fluid\ viscosity, \frac{\mu}{\rho}\ , [m^2s^{-1}]$

$\Pi = Derived\ variable\ in\ Buckingham\ Pi\ analysis\ [dimensionless]$

$\rho =\ density\ [kgm^{-3}]$

$\tau = tortuosity\ [dimensionless]$

Subscripts:
$\boldsymbol{a} = \ air$
$\boldsymbol{b} = \ bulk$
$\boldsymbol{DGM} = \ Dusty\ Gas\ Model$
$\boldsymbol{e} = \ effective$
$\boldsymbol{f} = \ feed$
$\boldsymbol{g} = \ gas$
$\boldsymbol{i} = \ intrinsic$
$\boldsymbol{m} = membrane$
$\boldsymbol{OMD} = \ Ordinary\ Molecular\ Diffusion$
$\boldsymbol{p} = permeate$
$\boldsymbol{pol} = \ polymer$
$\boldsymbol{pore} = \ pore$
$\boldsymbol{s} = \ solute$
$\boldsymbol{tot} = \ total$
$\boldsymbol{vap} = \ vapor$
$\boldsymbol{w} = \ water$

REFERENCES

Ali, A.; Macedonio, F.; Drioli, E.; Aljlil, S.; Alharbi, O. A. Experimental and Theoretical Evaluation of Temperature Polarization Phenomenon in Direct Contact Membrane Distillation. *Chem. Eng. Res. Des.* **2013**, *91* (10), 1966–1977.

Alkhudhiri, A.; Darwish, N.; Hilal, N. Membrane Distillation: A Comprehensive Review. *Desalination* **2012**, *287*, 2–18.

Al-Sharif, S.; Albeirutty, M.; Cipollina, A.; Micale, G. Modelling Flow and Heat Transfer in Spacer-Filled Membrane Distillation Channels Using Open Source CFD Code. *Desalination* **2013**, *311*, 103–112.

Andrjesdóttir, Ó.; Ong, C. L.; Nabavi, M.; Paredes, S.; Khalil, A. S. G.; Michel, B.; Poulikakos, D. An Experimentally Optimized Model for Heat and Mass Transfer in Direct Contact Membrane Distillation. *Int. J. Heat Mass Transf.* **2013**, *66*, 855–867.

Arkles, B.; Pan, Y.; Larson, G. L.; Singh, M. Enhanced Hydrolytic Stability of Siliceous Surfaces Modified with Pendant Dipodal Silanes. *Chemistry* **2014**, *20* (30), 9442–9450.

Bhatti, M. S.; Shah, R. K. Turbulent and Transition Flow Convective Heat Transfer in Ducts. *Handb. single-phase Convect. heat Transf.* **1987**, 1–4.

Bird, B.; Stewart, W.; Lightfoot, E. *Transport Phenomena*, 2nd ed.; John Wiley & Sons, Inc: New York, 2007.

Bryning, B. M. B.; Milkie, D. E.; Islam, M. F.; Hough, L. A.; Kikkawa, J. M.; Yodh, A. G. Carbon Nanotube Aerogels. *Adv. Mater.* **2007**, *20020*, 661–664.

Buckingham, E. On Physically Similar Systems: Illustrations of the Use of Dimensional Equations. *Phys. Rev.* **1914**, *4* (4), 345.

Bui, V. A.; Vu, L. T. T.; Nguyen, M. H. Modelling the Simultaneous Heat and Mass Transfer of Direct Contact Membrane Distillation in Hollow Fibre Modules. *J. Membr. Sci.* **2010**, *353*, 85–93.

Burant, A.; Lowry, G. V; Karamalidis, A. K. Partitioning Behavior of Organic Contaminants in Carbon Storage Environments: A Critical Review. *Environ. Sci. Technol.* **2013**, *47* (1), 37–54.

Charfi, K.; Khayet, M.; Safi, M. J. Numerical Simulation and Experimental Studies on Heat and Mass Transfer Using Sweeping Gas Membrane Distillation. *Desalination* **2010**, *259*, 84–96 ST – Numerical simulation and experimental .

Chen, T.-C.; Ho, C.-D.; Yeh, H.-M. Theoretical Modeling and Experimental Analysis of Direct Contact Membrane Distillation. *J. Membr. Sci.* **2009**, *330* (1-2), 279–287.

Chung, H. W.; Swaminathan, J.; Warsinger, D. M.; Lienhard V, J. H. Multistage Vacuum Membrane Distillation (MSVMD) Systems for High Salinity Applications. *J. Memb. Sci.* **2016**, *497*, 128–141.

Cipollina, A. CFD Simulation of a Membrane Distillation Module Channel. *Desalin. Water Treat.* **2009**, No. 6, 177–183.

Clapsaddle, B. J.; Sprehn, D. W.; Gash, A. E.; Satcher Jr., J. H.; Simpson, R. L. A Versatile Sol–gel Synthesis Route to Metal–silicon Mixed Oxide Nanocomposites That Contain Metal Oxides as the Major Phase. *J. Non. Cryst. Solids* **2004**, *350*, 173–181.

Dittus, F. W.; Boelter, L. M. K. University of California Publications on Engineering. *Univ. Calif. Publ. Eng.* **1930**, *2*, 371.

Dorcheh, A. S.; Abbasi, M. Silica Aerogel; Synthesis, Properties and Characterization. *J. Mater. Process. Technol.* **2008**, *199* (1), 10–26.

Doshi, D. a; Shah, P. B.; Singh, S.; Branson, E. D.; Malanoski, A. P.; Watkins, E. B.; Majewski, J.; van Swol, F.; Brinker, C. J. Investigating the Interface of Superhydrophobic Surfaces in Contact with Water. *Langmuir* **2005**, *21* (17), 7805–7811.

Drioli, E.; Ali, a.; Simone, S.; Macedonio, F.; AL-Jlil, S. a.; Al Shabonah, F. S.; Al-Romaih, H. S.; Al-Harbi, O.; Figoli, a.; Criscuoli, a. Novel PVDF Hollow Fiber Membranes for Vacuum and Direct Contact Membrane Distillation Applications. *Sep. Purif. Technol.* **2013**, *115*, 27–38.

Dumée, L. F.; Sears, K.; Schütz, J.; Finn, N.; Huynh, C.; Hawkins, S.; Duke, M.; Gray, S. Characterization and Evaluation of Carbon Nanotube Bucky-Paper Membranes for Direct Contact Membrane Distillation. *J. Memb. Sci.* **2010**, *351*, 36–43.

Dumee, L.; Sears, K.; Schuetz, J.; Finn, N.; Duke, M.; Gray, S. Carbon Nanotube Based Composite Membranes for Water Desalination by Membrane Distillation. *Desalin. Water Treat.* **2010**, *17*, 72–79.

Dumée, L.; Germain, V.; Sears, K.; Schütz, J.; Finn, N.; Duke, M.; Cerneaux, S.; Cornu, D.; Gray, S. Enhanced Durability and Hydrophobicity of Carbon Nanotube Bucky Paper Membranes in Membrane Distillation. *J. Memb. Sci.* **2011**, *376*, 241–246.

Eichhorn, S. J.; Sampson, W. W. Statistical Geometry of Pores and Statistics of Porous Nanofibrous Assemblies. *J. R. Soc. Interface* **2005**, *2* (4), 309–318.

Eichhorn, S. J.; Sampson, W. W. Relationships between Specific Surface Area and Pore Size in Electrospun Polymer Fibre Networks. *J. R. Soc. Interface* **2010**, *7* (45), 641–649.

El-Dessouky, Hisham T., Ettouney, H. M. *Fundamentals of Salt Water Desalination*; Elsevier: Amsterdam, 2002.

Elimelech, M. The Future of Seawater Desalination: Energy, Technology, and the Environment. *Science (80-.).* **2011**, *333*, 712–717.

Essalhi, M.; Khayet, M. Surface Segregation of Fluorinated Modifying Macromolecule for Hydrophobic/hydrophilic Membrane Preparation and Application in Air Gap and Direct Contact Membrane Distillation. *J. Memb. Sci.* **2012**, *417-418*, 163–173.

Essalhi, M.; Khayet, M. Self-Sustained Webs of Polyvinylidene Fluoride Electrospun Nanofibers at Different Electrospinning Times: 1. Desalination by Direct Contact Membrane Distillation. *J. Memb. Sci.* **2013a**, *433*, 167–179.

Essalhi, M.; Khayet, M. Self-Sustained Webs of Polyvinylidene Fluoride Electrospun Nanofibers at Different Electrospinning Times: 2. Theoretical Analysis, Polarization Effects and Thermal Efficiency. *J. Memb. Sci.* **2013b**, *433*, 180–191.

Essalhi, M.; Khayet, M. Self-Sustained Webs of Polyvinylidene Fluoride Electrospun Nano-Fibers: Effects of Polymer Concentration and Desalination by Direct Contact Membrane Distillation. *J. Memb. Sci.* **2014**, *454*, 133–143.

Feng, L.; Zhang, Y.; Xi, J.; Zhu, Y.; Wang, N.; Xia, F.; Jiang, L. Petal Effect: A Superhydrophobic State with High Adhesive Force. *Langmuir* **2008**, *24* (8), 4114–4119.

Field, R. W.; Wu, H. Y.; Wu, J. J. Multiscale Modeling of Membrane Distillation: Some Theoretical Considerations. *Ind. Eng. Chem. Res.* **2013**, *52* (26), 8822–8828.

Findley, M. E. Vaporization through Porous Membranes. *Ind. Eng. Chem. Process Des. Dev.* **1967**, *6* (2),

226–230.

Gash, A. E.; Tillotson, T. M.; Satcher Jr, J. H.; Hrubesh, L. W.; Simpson, R. L. New Sol–gel Synthetic Route to Transition and Main-Group Metal Oxide Aerogels Using Inorganic Salt Precursors. *J. Non. Cryst. Solids* **2001**, *285* (1-3), 22–28.

Geerken, M. J.; van Zanten, T. S.; Lammertink, R. G. H.; Borneman, Z.; Nijdam, W.; van Rijn, C. J. M.; Wessling, M. Chemical and Thermal Stability of Alkylsilane Based Coatings for Membrane Emulsification. *Adv. Eng. Mater.* **2004**, *6* (9), 749–754.

Gingerich, D. B.; Mauter, M. S. Quantity, Quality, and Availability of Residual Heat from United States Thermal Power Generation. *Environ. Sci. Technol.* **2015**, *49* (14), 8297–8306.

Goh, S.; Zhang, Q.; Zhang, J.; McDougald, D.; Krantz, W. B.; Liu, Y.; Fane, A. G. Impact of a Biofouling Layer on the Vapor Pressure Driving Force and Performance of a Membrane Distillation Process. *J. Memb. Sci.* **2013**, *438*, 140–152.

Gryta, M.; Tomaszewska, M. Heat Transport in the Membrane Distillation Process. *J. Memb. Sci.* **1998**, *144* (1-2), 211–222.

Gryta, M.; Tomaszewska, M.; Morawski, A. W. Membrane Distillation with Laminar Flow. *Sep. Purif. Technol.* **1997**, *11* (2), 93–101.

Gustafson, R. D.; Murphy, J. R.; Achilli, A. A Stepwise Model of Direct Contact Membrane Distillation for Application to Large-Scale Systems: Experimental Results and Model Predictions. *Desalination* **2016**, *378*, 14–27.

Haigler, C. H.; White, a R.; Brown, R. M.; Cooper, K. M. Alteration of in Vivo Cellulose Ribbon Assembly by Carboxymethylcellulose and Other Cellulose Derivatives. *J. Cell Biol.* **1982**, *94* (1), 64–69.

Hartnett, J. P.; Rohsenow, W. M. Handbook of Heat Transfer. *Handb. heat Transf. by Hartnett, JP; Rohsenow, Warren M. New York, McGraw-Hill [c1973]* **1973**, *1*.

Hench, L. L.; West, J. K. The Sol-Gel Process. *Chem. Rev.* **1990**, *90* (1), 33–72.

Hitsov, I.; Maere, T.; Sitter, K. De; Dotremont, C.; Nopens, I. Modelling Approaches in Membrane Distillation : A Critical Review. *Sep. Purif. Technol.* **2015**, *142*, 48–64.

Holman, J. P. Heat Transfer. 2002. *McGrawHill, New York, USA*.

Hotaling, N. A.; Bharti, K.; Kriel, H.; Simon, C. G. Biomaterials DiameterJ : A Validated Open Source Nano Fi Ber Diameter Measurement Tool. *Biomaterials* **2015**, *61*, 327–338.

Hwang, H. J.; He, K.; Gray, S.; Zhang, J.; Moon, I. S. Direct Contact Membrane Distillation (DCMD): Experimental Study on the Commercial PTFE Membrane and Modeling. *J. Memb. Sci.* **2011**, *371* (1-2), 90–98.

Iguchi, M.; Yamanaka, S.; Budhiono, A. Bacterial Cellulose — a Masterpiece of Nature's Arts. *J. Mater. Sci.* **2000**, *5*, 261–270.

Imdakm, A. O.; Matsuura, T. A Monte Carlo Simulation Model for Membrane Distillation Processes: Direct Contact (MD). *J. Membr. Sci.* **2004**, *237* (1-2), 51–59.

Incropera, F. P.; Kerby, J. S.; Moffatt, D. F.; Ramadhyani, S. Convection Heat Transfer from Discrete Heat Sources in a Rectangular Channel. *Int. J. Heat Mass Transf.* **1986**, *29* (7), 1051–1058.

Iversen, S. B.; Bhatia, V. K.; Dam-Johansen, K.; Jonsson, G. Characterization of Microporous

Membranes for Use in Membrane Contactors. *J. Membr. Sci.* **1997**, *130*, 205–217.

Izquierdo-Gil, M. A.; Fernandez-Pineda, C.; Lorenz, M. G. Flow Rate Influence on Direct Contact Membrane Distillation Experiments: Different Empirical Correlations for Nusselt Number. *J. Memb. Sci.* **2008**, *321* (2), 356–363.

Jin, H.; Kettunen, M.; Laiho, A.; Pynnönen, H.; Paltakari, J.; Marmur, A.; Ikkala, O.; Ras, R. H. a. Superhydrophobic and Superoleophobic Nanocellulose Aerogel Membranes as Bioinspired Cargo Carriers on Water and Oil. *Langmuir* **2011**, *27* (5), 1930–1934.

Kadoya, K.; Matsunaga, N.; Nagashima, A. Viscosity and Thermal Conductivity of Dry Air in the Gaseous Phase. *J. Phys. Chem. Ref. Data* **1985**, *14* (4), 947–970.

Kakaç, S.; Shah, R. K.; Bergles, A. E. *Low Reynolds Number Flow Heat Exchangers: Advanced Study Institute Book*; Hemisphere publishing corporation, 1983.

Kakaç, S.; Shah, R. K.; Aung, W. *Handbook of Single-Phase Convective Heat Transfer*; Wiley New York et al., 1987.

Kaviany, M. *Principles of Convective Heat Transfer*, 2nd Editio.; Springer Science & Business Media, 2001.

Kaviany, M. Personal Communication. 2015.

Kettunen, M.; Silvennoinen, R. J.; Houbenov, N.; Nykänen, A.; Ruokolainen, J.; Sainio, J.; Pore, V.; Kemell, M.; Ankerfors, M.; Lindström, T.; et al. Photoswitchable Superabsorbency Based on Nanocellulose Aerogels. *Adv. Funct. Mater.* **2011**, *21* (3), 510–517.

Khayet, M. Membranes and Theoretical Modeling of Membrane Distillation: A Review. *Adv. Colloid Interface Sci.* **2011**, *164*, 56–88.

Khayet, M.; Mengual, J. I. Effect of Salt Concentration during the Treatment of Humic Acid Solutions by Membrane Distillation. *Desalination* **2004**, *168*, 373–381.

Khayet, M.; Matsuura, T. *Membrane Distillation: Principles and Applications*; Elsevier B.V.: Amsterdam, 2011.

Khayet, M.; Cojocaru, C. Artificial Neural Network Modeling and Optimization of Desalination by Air Gap Membrane Distillation. *Sep. Purif. Technol.* **2012**, *86*, 171–182.

Khayet, M.; Cojocaru, C. Artificial Neural Network Model for Desalination by Sweeping Gas Membrane Distillation. *Desalination* **2013**, *308*, 102–110.

Khayet, M.; Velazquez, A.; Mengual, J. I. Modelling Mass Transport through a Porous Partition: Effect of Pore Size Distribution. *J. Non-Equilibrium Thermodyn.* **2004**, *29* (3), 279–299.

Khayet, M.; Mengual, J. I.; Matsuura, T. Porous Hydrophobic / Hydrophilic Composite Membranes Application in Desalination Using Direct Contact Membrane Distillation. *J. Membr. Sci.* **2005**, *252*, 101–113.

Khayet, M.; Cojocaru, C.; Garcia-Payo, C. Application of Response Surface Methodology and Experimental Design in Direct Contact Membrane Distillation. *Ind. Eng. Chem. Res.* **2007**, *46*, 5673–5685 ST – Application of response surface me.

Khayet, M.; Imdakm, A. O.; Matsuura, T. Monte Carlo Simulation and Experimental Heat and Mass Transfer in Direct Contact Membrane Distillation. *Int. J. Heat Mass Transf.* **2010**, *53* (7-8), 1249–1259.

Kim, K. H.; Oh, Y.; Islam, M. F. Graphene Coating Makes Carbon Nanotube Aerogels Superelastic and Resistant to Fatigue. *Nat. Nanotechnol.* **2012**, *7* (9), 562–566.

Kimura, S.; Nakao, S.-I.; Shimatani, S.-I. Transport Phenomena in Membrane Distillation. *J. Memb. Sci.* **1987**, *33* (3), 285–298.

Kistler, S. S. Coherent Expanded Aerogels and Jellies. *Nature* **1931**, *127*, 741.

Klemm, D.; Schumann, D.; Udhardt, U.; Marsch, S. Bacterial Synthesized Cellulose - Artificial Blood Vessels for Microsurgery. *Prog. Polym. Sci.* **2001**, *26*, 1561–1603.

Klemm, D.; Schumann, D.; Kramer, F.; Heßler, N.; Koth, D.; Sultanova, B. Nanocellulose Materials – Different Cellulose, Different Functionality. *macro* **2009**, 60–71.

Klemm, D.; Kramer, F.; Moritz, S.; Lindström, T.; Ankerfors, M.; Gray, D.; Dorris, A. Nanocelluloses: A New Family of Nature-Based Materials. *Angew. Chemie* **2011**, *50* (24), 5438–5466.

Korhonen, J. T.; Huhtamäki, T.; Ikkala, O.; Ras, R. H. a. Reliable Measurement of the Receding Contact Angle. *Langmuir* **2013**, *29* (12), 3858–3863.

Kostic, M.; Hartnett, J. P. Heat Transfer to Water Flowing Turbulently through a Rectangular Duct with Asymmetric Heating. *Int. J. Heat Mass Transf.* **1986**, *29* (8), 1283–1291.

Kugland, N. L.; Moody, J. D.; Kozioziemski, B. J.; Rubenchik, a. M.; Niemann, C. Reduction in Helium Thermal Conductivity by 1 Mgcc Silica Aerogel Foam. *Appl. Phys. Lett.* **2008**, *92* (22), 1–4.

Lavoine, N.; Desloges, I.; Dufresne, A.; Bras, J. Microfibrillated Cellulose - Its Barrier Properties and Applications in Cellulosic Materials: A Review. *Carbohydr. Polym.* **2012**, *90* (2), 735–764.

Lawson, K. W.; Hall, M. S.; Lloyd, D. R. Compaction of Microporous Membranes Used in Membrane Distillation. I. Effect on Gas Permeability. *J. Memb. Sci.* **1995**, *101* (1-2), 99–108.

Lawson, K.; Lloyd, D. Membrane Distillation. *J. Membr. Sci.* **1997**, *124* (1), 1–25.

Leitch, M. E.; Li, C.; Ikkala, O.; Mauter, M. S.; Lowry, G. V. Bacterial Nanocellulose Aerogel Membranes: Novel High- Porosity Materials for Membrane Distillation. *Environ. Sci. Technol. Lett.* **2016**, *3*, 85–91.

Lemmon, E. W. Thermophysical Properties of Water and Steam. In *CRC handbook of chemistry and physics*; CRC Press: Boca Raton, FL, 2013.

Li, X.; Wang, C.; Yang, Y.; Wang, X.; Zhu, M.; Hsiao, B. S. Dual-Biomimetic Superhydrophobic Electrospun Polystyrene Nanofibrous Membranes for Membrane Distillation. *Appl. Mater. Interfaces* **2014a**, *6*, 2423–2430.

Li, Z.; Peng, Y.; Dong, Y.; Fan, H.; Chen, P.; Qiu, L.; Jiang, Q. Effects of Thermal Efficiency in DCMD and the Preparation of Membranes with Low Thermal Conductivity. *Appl. Surf. Sci.* **2014b**, *317*, 338–349.

Liao, Y.; Wang, R.; Fane, A. G. Engineering Superhydrophobic Surface on Poly(vinylidene Fluoride) Nanofiber Membranes for Direct Contact Membrane Distillation. *J. Membr. Sci.* **2013a**, *440*, 77–87.

Liao, Y.; Wang, R.; Tian, M.; Qiu, C.; Fane, A. G. Fabrication of Polyvinylidene Fluoride (PVDF) Nanofiber Membranes by Electro-Spinning for Direct Contact Membrane Distillation. *J. Membr. Sci.* **2013b**, *425-426*, 30–39.

Liao, Y.; Loh, C.-H.; Wang, R.; Fane, A. G. Electrospun Superhydrophobic Membranes with Unique

Structures for Membrane Distillation. *ACS Appl. Mater. Interfaces* **2014a**, *6* (18), 16035–16048.

Liao, Y.; Wang, R.; Fane, A. G. Fabrication of Bioinspired Composite Nanofiber Membranes with Robust Superhydrophobicity for Direct Contact Membrane Distillation. *Environ. Sci. Technol.* **2014b**, *48*, 6335–6341.

Liebner, F.; Haimer, E.; Wendland, M.; Neouze, M. A.; Schlufter, K.; Miethe, P.; Heinze, T.; Potthast, A.; Rosenau, T. Aerogels from Unaltered Bacterial Cellulose: Application of scCO 2 Drying for the Preparation of Shaped, Ultra-Lightweight Cellulosic Aerogels. *Macromol. Biosci.* **2010**, *10* (4), 349–352.

Lin, S.; Yip, N. Y.; Elimelech, M. Direct Contact Membrane Distillation with Heat Recovery: Thermodynamic Insights from Module Scale Modeling. *J. Membr. Sci.* **2014**, *453*, 498–515.

Lin, Y.; Ehlert, G. J.; Bukowsky, C.; Sodano, H. A. Superhydrophobic Functionalized Graphene Aerogels. *ACS Appl. Mater. Interfaces* **2011**, *3*, 2200–2203.

Lu, X.; Arduini-Schuster, M. C.; Kuhn, J.; Nilsson, O.; Fricke, J.; Pekala, R. W. Thermal Conductivity of Monolithic Organic Aerogels. *Science* **1992**, *255* (5047), 971–972.

Lu, Y.; Chen, J. Optimal Design of Multistage Membrane Distillation Systems for Water Purification. *Ind. Eng. Chem. Res.* **2011**, *50* (12), 7345–7354.

Ma, Z.; Hong, Y.; Ma, L.; Su, M. Superhydrophobic Membranes with Ordered Arrays of Nanospiked Microchannels for Water Desalination. *Langmuir* **2009**, *25* (10), 5446–5450.

Maidment, D. R. *Handbook of Hydrology*; McGraw-Hill: New York, 1993.

Marrero, T. R.; Mason, E. A. Gaseous Diffusion Coefficients. *Journal of Physical and Chemical Reference Data*. 1972, pp 3–118.

Marťinez, L.; Florido-Ďiaz, F. J.; Herńandez, A.; Pŕadanos, P. Estimation of Vapor Transfer Coefficient of Hydrophobic Porous Membranes for Applications in Membrane Distillation. *Sep. Purif. Technol.* **2003**, *33* (1), 45–55.

Mason, E. A.; Malinauskas, A. P. *Gas Transport in Porous Media: The Dusty-Gas Model*, Volume 17.; Elsevier: Amsterdam, 1983.

McAdams, W. H.; Woods, W. K.; Heroman, L. C. Vaporization inside Horizontal Tubes-II-Benzene-Oil Mixtures. *Trans. ASME* **1942**, *64* (3), 193–200.

McCabe, W. L.; Smith, J. C.; Harriott, P. *Unit Operations of Chemical Engineering*, 6th ed.; McGraw-Hill: New York, 2001.

Mistry, K. H.; McGovern, R. K.; Thiel, G. P.; Summers, E. K.; Zubair, S. M.; Lienhard, J. H. Entropy Generation Analysis of Desalination Technologies. *Entropy* **2011**, *13* (10), 1829–1864.

Moon, R. J.; Martini, A.; Nairn, J.; Simonsen, J.; Youngblood, J. Cellulose Nanomaterials Review: Structure, Properties and Nanocomposites. *Chem. Soc. Rev.* **2011**, *40* (7), 3941–3994.

Morvay, Z. K.; Gvozdenac, D. D. *Applied Industrial Energy and Environmental Management Part III - Toolbox 6: Fundamentals for Analysis and Calculation of Energy and Environmental Performance*; John Wiley & Sons, Ltd, 2008.

Nasir, M.; Matsumoto, H.; Danno, T.; Minagawa, M.; Irisawa, T.; Shioya, M.; Tanioka, A. Control of Diameter, Morphology, and Structure of PVDF Nanofiber Fabricated by Electrospray Deposition. *J. Polym. Sci. Part B Polym. Phys.* **2006**, *44* (5), 779–786.

Nguyen, B. N.; Meador, M. A. B.; Medoro, A.; Arendt, V.; Randall, J.; Mccorkle, L.; Shonkwiler, B. Elastic Behavior of Methyltrimethoxysilane Based Aerogels Reinforced with Tri-Isocyanate. *ACS Appl. Mater. Interfaces* **2010**, *2* (5), 1430–1443.

Nusselt, W. Der W{ä}rmeaustausch Zwischen Wand Und Wasser Im Rohr. *Forsch. auf dem Gebiet des Ingenieurwesens A* **1931**, *2* (9), 309–313.

OECD. *OECD Environmental Outlook to 2050: The Consequences of Inaction*; 2012.

Onsekizoglu, P.; Savas Bahceci, K.; Acar, J. The Use of Factorial Design for Modeling Membrane Distillation. *J. Memb. Sci.* **2010**, *349* (1-2), 225–230.

Pääkkö, M.; Vapaavuori, J.; Silvennoinen, R.; Kosonen, H.; Ankerfors, M.; Lindström, T.; Berglund, L. a.; Ikkala, O. Long and Entangled Native Cellulose I Nanofibers Allow Flexible Aerogels and Hierarchically Porous Templates for Functionalities. *Soft Matter* **2008**, *4* (12), 2492.

Pekala, R. W. Organic Aerogels from the Polycondensation of Resorcinol with Formaldehyde. *J. Mater. Sci.* **1989**, *24*, 3221–3227.

Petersen, N.; Gatenholm, P. Bacterial Cellulose-Based Materials and Medical Devices: Current State and Perspectives. *Appl. Microbiol. Biotechnol.* **2011**, *91* (5), 1277–1286.

Petukhov, B. S. Heat Transfer and Friction in Turbulent Pipe Flow with Variable Physical Properties. *Adv. Heat Transf.* **1970**, *6*, 503–564.

Petukhov, B. S.; Popov, V. N. Theoretical Calculation of Heat Exchange and Frictional Resistance in Turbulent Flow in Tubes of an Incompressible Fluid with Variable Physical properties(Heat Exchange and Frictional Resistance in Turbulent Flow of Liquids with Variable Physical Properti. *High Temp.* **1963**, *1*, 69–83.

Phattaranawik, J.; Jiraratananon, R.; Fane, A. G. Effect of Pore Size Distribution and Air Flux on Mass Transport in Direct Contact Membrane Distillation. *J. Membr. Sci.* **2003a**, *215* (1-2), 75–85.

Phattaranawik, J.; Jiraratananon, R.; Fane, A. G. Effects of Net-Type Spacers on Heat and Mass Transfer in Direct Contact Membrane Distillation and Comparison with Ultrafiltration Studies. *J. Membr. Sci.* **2003b**, *217* (1-2), 193–206.

Phattaranawik, J.; Jiraratananon, R.; Fane, A. G. Heat Transport and Membrane Distillation Coefficients in Direct Contact Membrane Distillation. *J. Memb. Sci.* **2003c**, *212* (1-2), 177–193.

Pitzer, K. S.; Peiper, J. C.; Busey, R. H. Thermodynamic Properties of Aqueous Sodium Chloride Solutions. *J. Phys. Chem. Ref. Data* **1984**, *13* (1), 1–102.

Plueddemann, E. P. *Silane Coupling Agents*; Springer Science & Business Media, 2013.

Pohlhausen, K. Zur N{ä}herungsweisen Integration Der Differentialgleichung Der Iaminaren Grenzschicht. *ZAMM-Journal Appl. Math. Mech. f{ü}r Angew. Math. und Mech.* **1921**, *1* (4), 252–290.

Prausnitz, J. M.; Lichtenthaler, R. N.; de Azevedo, E. G. *Molecular Thermodynamics of Fluid-Phase Equilibria.*, 3rd ed.; Prentice-Hall, Inc.: Upper Saddle River, New Jersey, 1999.

Prince, J. a.; Singh, G.; Rana, D.; Matsuura, T.; Anbharasi, V.; Shanmugasundaram, T. S. Preparation and Characterization of Highly Hydrophobic Poly(vinylidene Fluoride) - Clay Nanocomposite Nanofiber Membranes (PVDF-Clay NNMs) for Desalination Using Direct Contact Membrane Distillation. *J. Memb. Sci.* **2012**, *397-398*, 80–86.

Qtaishat, M.; Matsuura, T.; Kruczek, B.; Khayet, A. Heat and Mass Transfer Analysis in Direct Contact

Membrane Distillation. *Desalination* **2008**, *219*, 272–292.

Qtaishat, M.; Khayet, M.; Matsuura, T. Guidelines for Preparation of Higher Flux Hydrophobic/hydrophilic Composite Membranes for Membrane Distillation. *J. Membr. Sci.* **2009a**, *329*, 193–200.

Qtaishat, M.; Khayet, M.; Matsuura, T. Novel Porous Composite Hydrophobic/hydrophilic Polysulfone Membranes for Desalination by Direct Contact Membrane Distillation. *J. Membr. Sci.* **2009b**, *341*, 139–148.

Qtaishat, M.; Rana, D.; Khayet, M.; Matsuura, T. Preparation and Characterization of Novel Hydrophobic/hydrophilic Polyetherimide Composite Membranes for Desalination by Direct Contact Membrane Distillation. *J. Membr. Sci.* **2009c**, *327* (1-2), 264–273.

Randall, J. P.; Meador, M. A. B.; Jana, S. C. Tailoring Mechanical Properties of Aerogels for Aerospace Applications. *ACS Appl. Mater. Interfaces* **2011**, *3* (3), 613–626.

Rao, G.; Hiibel, S. R.; Childress, A. E. Simplified Flux Prediction in Direct-Contact Membrane Distillation Using a Membrane Structural Parameter. *Desalination* **2014**, *351*, 151–162.

Ross, P.; Mayer, R.; Benziman, M. Cellulose Biosynthesis and Function in Bacteria. *Microbiol. Rev.* **1991**, *55* (1), 35–58.

Ryu, Y. J.; Kim, H. Y.; Lee, K. H.; Park, H. C.; Lee, D. R. Transport Properties of Electrospun Nylon 6 Nonwoven Mats. *Eur. Polym. J.* **2003**, *39* (9), 1883–1889.

Schmidt, F. W.; Newell, M. E. Heat Transfer in Fully Developed Laminar Flow through Rectangular and Isosceles Triangular Ducts. *Int. J. Heat Mass Transf.* **1967**, *10* (8), 1121–1123.

Schneider, C. a; Rasband, W. S.; Eliceiri, K. W. NIH Image to ImageJ: 25 Years of Image Analysis. *Nat. Methods* **2012**, *9* (7), 671–675.

Schofield, R. W.; Fane, a. G.; Fell, C. J. D. Heat and Mass Transfer in Membrane Distillation. *J. Memb. Sci.* **1987**, *33* (3), 299–313.

Schofield, R. W.; Fane, a. G.; Fell, C. J. D.; Macoun, R. Factors Affecting Flux in Membrane Distillation. *Desalination* **1990**, *77*, 279–294.

Semiat, R. Critical Review Energy Issues in Desalination Processes. *Environ. Sci. Technol.* **2008**, *42* (22), 8193–8201.

Shah, R. K.; London, A. L. *Laminar Flow Forced Convection in Ducts: A Source Book for Compact Heat Exchanger Analytical Data*; Academic press: New York, 1978.

Shah, R. K.; Sekulic, D. P. *Fundamentals of Heat Exchanger Design*; John Wiley & Sons, 2003.

Shakaib, M.; Hasani, S. M. F.; Ahmed, I.; Yunus, R. M. A CFD Study on the Effect of Spacer Orientation on Temperature Polarization in Membrane Distillation Modules. *Desalination* **2012**, *284*, 332–340.

Shirazi, M. M. A.; Kargari, A.; Ismail, A. F.; Matsuura, T. Computational Fluid Dynamic (CFD) Opportunities Applied to the Membrane Distillation Process: State-of-the-Art and Perspectives. *Desalination* **2016**, *377*, 73–90.

Sieder, E. N.; Tate, G. E. Heat Transfer and Pressure Drop of Liquids in Tubes. *Ind. Eng. Chem.* **1936**, *28*, 1429–1435.

Silva, T. L. S.; Morales-torres, S.; Figueiredo, J. L.; Silva, A. M. T. Multi-Walled Carbon Nanotube /

PVDF Blended Membranes with Sponge- and Finger-like Pores for Direct Contact Membrane Distillation. *Desalination* **2015**, *357*, 233–245.

Song, L.; Li, B.; Sirkar, K. K.; Gilron, J. L. Direct Contact Membrane Distillation-Based Desalination: Novel Membranes, Devices, Larger-Scale Studies, and a Model. *Ind. Eng. Chem. Res.* **2007**, *46* (8), 2307–2323.

Song, L.; Ma, Z.; Liao, X.; Kosaraju, P. B.; Irish, J. R.; Sirkar, K. K. Pilot Plant Studies of Novel Membranes and Devices for Direct Contact Membrane Distillation-Based Desalination. *J. Membr. Sci.* **2008**, *323* (2), 257–270.

Sonin, A. A. The Physical Basis of Dimensional Analysis. *Dep. Mech. Eng. MIT, Cambridge, MA* **2001**, 1–57.

Soukane, S.; Chelouche, S.; Naceur, M. W. A Ballistic Transport Model for Vacuum Membrane Distillation. *J. Membr. Sci.* **2014**, *450*, 397–406.

Sparrow, E. M. *Analysis of Laminar Forced-Convection Heat Transfer in the Entrance Region of Flat Rectangular Ducts*; Cleveland OH, 1955.

Srisurichan, S.; Jiraratananon, R.; Fane, A. G. Mass Transfer Mechanisms and Transport Resistances in Direct Contact Membrane Distillation Process. *J. Memb. Sci.* **2006**, *277* (1-2), 186–194.

Su, C. I.; Shih, J. H.; Huang, M. S.; Wang, C. M.; Shih, W. C.; Liu, Y. S. A Study of Hydrophobic Electrospun Membrane Applied in Seawater Desalination by Membrane Distillation. *Fibers Polym.* **2012**, *13* (6), 698–702.

Su, C.; Li, Y.; Dai, Y.; Gao, F.; Tang, K.; Cao, H. Fabrication of Three-Dimensional Superhydrophobic Membranes with High Porosity via Simultaneous Electrospraying and Electrospinning. *Mater. Lett.* **2016**, *170*, 67–71.

Suh, D. J.; Park, T. Sol-Gel Strategies for Pore Size Control of High-Surface-Area Transition-Metal Oxide Aerogels. *Chem. Mater.* **1996**, *8* (2), 509–513.

Sun, H.; Xu, Z.; Gao, C. Multifunctional, Ultra-Flyweight, Synergistically Assembled Carbon Aerogels. *Adv. Mater.* **2013**, *25* (18), 2554–2560.

Szentivanyi, A.; Chakradeo, T.; Zernetsch, H.; Glasmacher, B. Electrospun Cellular Microenvironments: Understanding Controlled Release and Scaffold Structure. *Adv. Drug Deliv. Rev.* **2011**, *63* (4), 209–220.

Tamburini, A. Experimental Analysis via Thermochromic Liquid Crystals of the Temperature Local Distribution in Membrane Distillation Modules. In *Chemical Engineering Transactions*; 2013; Vol. 32, pp 2041–2046.

Teichner, S. J.; Nicolaon, G. a.; Vicarini, M. a.; Gardes, G. E. E. Inorganic Oxide Aerogels. *Adv. Colloid Interface Sci.* **1976**, *5* (3), 245–273.

Termpiyakul, P.; Jiraratananon, R.; Srisurichan, S. Heat and Mass Transfer Characteristics of a Direct Contact Membrane Distillation Process for Desalination. *Desalination* **2005**, *177*, 133–141.

Thomas, L. C. *Fundamentals of Heat Transfer*; Prentice-Hall, Inc.: Englewood Cliffs, NJ, 1980.

Thomas, L. C. *Heat Transfer*; PTR Prentice Hall, 1993.

Tijing, L. D.; Chul, Y.; Hasan, A.; Choi, J.; Kyong, H. A Novel Dual-Layer Bicomponent Electrospun Nanofibrous Membrane for Desalination by Direct Contact Membrane Distillation. *Chem. Eng. J.* **2007**, *2*, 3–5.

Tijing, L. D.; Woo, Y. C.; Johir, M. A. H.; Choi, J.-S.; Shon, H. K. A Novel Dual-Layer Bicomponent Electrospun Nanofibrous Membrane for Desalination by Direct Contact Membrane Distillation. *Chem. Eng. J.* **2014a**, *256*, 155–159.

Tijing, L. D.; Choi, J. S.; Lee, S.; Kim, S. H.; Shon, H. K. Recent Progress of Membrane Distillation Using Electrospun Nanofibrous Membrane. *J. Memb. Sci.* **2014b**, *453*, 435–462.

Tijing, L. D.; Woo, Y. C.; Shim, W. G.; He, T.; Choi, J. S.; Kim, S. H.; Shon, H. K. Superhydrophobic Nanofiber Membrane Containing Carbon Nanotubes for High-Performance Direct Contact Membrane Distillation. *J. Memb. Sci.* **2016**, *502*, 158–170.

Tun, C. M.; Fane, A. G.; Matheickal, J. T.; Sheikholeslami, R. Membrane Distillation Crystallization of Concentrated Salts—flux and Crystal Formation. *J. Membr. Sci.* **2005**, *257* (1-2), 144–155.

Wang, C.; Cheng, Y. W.; Hsu, C. H.; Chien, H. S.; Tsou, S. Y. How to Manipulate the Electrospinning Jet with Controlled Properties to Obtain Uniform Fibers with the Smallest Diameter?-a Brief Discussion of Solution Electrospinning Process. *J. Polym. Res.* **2011**, *18* (1), 111–123.

Wang, M.; Anoshkin, I. V; Nasibulin, A. G.; Korhonen, J. T.; Seitsonen, J.; Pere, J.; Kauppinen, E. I.; Ras, R. H. a; Ikkala, O. Modifying Native Nanocellulose Aerogels with Carbon Nanotubes for Mechanoresponsive Conductivity and Pressure Sensing. *Adv. Mater.* **2013**, *25* (17), 2428–2432.

Welty, J. R.; Wicks, C. E.; Rorrer, G.; Wilson, R. E. *Fundamentals of Momentum, Heat, and Mass Transfer*; John Wiley & Sons, 2009.

Wen-Chien, L.; Yi-Hsu, J. Conjugate Leveque Solution for Newtonian Fluid in a Parallel Plate Channel. *Int. J. Heat Mass Transf.* **1986**, *29* (6), 941–947.

Wibulswas, P. Laminar-Flow Heat-Transfer in Non-Circular Ducts., University of London, 1966.

Wu, H. Y.; Wang, R.; Field, R. W. Direct Contact Membrane Distillation: An Experimental and Analytical Investigation of the Effect of Membrane Thickness upon Transmembrane Flux. *J. Membr. Sci.* **2014**, *470*, 257–265.

Wypych, G. *Handbook of Polymers*; ChemTec Publishing: Toronto, 2012.

Xu, Z.; Pan, Y.; Yu, Y. CFD Simulation on Membrane Distillation of NaCl Solution. *Front. Chem. Eng. China* **2009**, *3* (3), 293–297.

Yang, C.; Li, X.-M.; Gilron, J.; Kong, D.; Yin, Y.; Oren, Y.; Linder, C.; He, T. CF4 Plasma-Modified Superhydrophobic PVDF Membranes for Direct Contact Membrane Distillation. *J. Membr. Sci.* **2014**, *456*, 155–161.

Yano, S.; Hatakeyama, H.; Hatakeyama, T. Effect of Hydrogen Bond Formation on Dynamic Mechanical Properties of Amorphous Cellulose. *J. Appl. Polym. Sci.* **1976**, *20* (12), 3221–3231.

Yao, M.; Woo, Y. C.; Tijing, L. D.; Shim, W. G.; Choi, J. S.; Kim, S. H.; Shon, H. K. Effect of Heat-Press Conditions on Electrospun Membranes for Desalination by Direct Contact Membrane Distillation. *Desalination* **2016**, *378*, 80–91.

Yun, Y.; Ma, R.; Zhang, W.; Fane, A. G.; Li, J. Direct Contact Membrane Distillation Mechanism for High Concentration NaCl Solutions. *Desalination* **2006**, *188* (1-3), 251–262.

Zaborowska, M.; Bodin, A.; Bäckdahl, H.; Popp, J.; Goldstein, A.; Gatenholm, P. Microporous Bacterial Cellulose as a Potential Scaffold for Bone Regeneration. *Acta Biomater.* **2010**, *6* (7), 2540–2547.

Zeng, M.; Laromaine, A.; Roig, A. Bacterial Cellulose Films: Influence of Bacterial Strain and Drying

Route on Film Properties. *Cellulose* **2014**, *21* (6), 4455–4469.

Zhang, K. Illustration of the Development of Bacterial Cellulose Bundles/ribbons by Gluconacetobacter Xylinus via Atomic Force Microscopy. *Appl. Microbiol. Biotechnol.* **2013**, *97* (10), 4353–4359.

Zuo, G.; Wang, R. Novel Membrane Surface Modification to Enhance Anti-Oil Fouling Property for Membrane Distillation Application. *J. Membr. Sci.* **2013**, *447*, 26–35.

Aquaver http://www.aquaver.com/ (accessed Apr 2, 2016).

SolarSpring http://www.solarspring.de (accessed Apr 2, 2016).

Web of Science http://apps.webofknowledge.com/.

NIST Chemistry WebBook http://webbook.nist.gov/chemistry/ (accessed Apr 15, 2016).

Polymer Handbook, 89th ed.; Brandrup, J., Immergu, E. H., Abe, A., Bloch, D. R., Eds.; Wiley: New York, 1999.